THE UNIVERSITY *of* EDINBURGH

Activity of comets: Insights from ground-based broadband observations

Daniel Mark Gardener

Doctor of Philosophy
The University of Edinburgh
November 2023

For Mum

Abstract

Comets are the primitive building blocks of the Solar System. In order to understand the extent of the pristine nature of comets, we must understand the mechanisms that affect their surfaces and comae – their activity. Activity can be tracked in a variety of ways, such as observing dust production in the coma using broadband imaging. Activity varies from comet to comet so we must try to distinguish whether these differences in activity are because of ageing or reflect primordial differences. Ageing refers to effects that have chemically or physically altered the nucleus since its formation and cause a change in the activity. I developed a pipeline to calibrate and measure broadband photometry of comets in a consistent way. The pipeline calibrates the brightness to a common photometric system using background stars in the field. I applied this pipeline to ground-based data accompanying the Rosetta mission. The photometry of 67P followed the predictions based on previous apparitions: it showed no obvious change in activity levels from orbit-to-orbit and coma colours remained constant throughout the apparition. I detected an outburst on 2015 August 22 of ~ 0.14 mag. The brightness and estimated mass of this outburst put it in line with the outbursts directly observed on the nucleus by Rosetta. An in situ outburst was observed at the same time as the one seen from the ground; however, linking these two events directly remains challenging. I applied the pipeline to TRAPPIST photometry of 14 comets. I determined that comets of different dynamical classes can be distinguished by their dust activity: dynamically new comets displayed higher dust production rates and greater asymmetries in the dust production rates about perihelion than other comets. There seemed to be no correlation as to whether the peak of activity occurred before or after perihelion. I found strong relationships between dust and gas production which can be used as a rough approximation of gas production rates if one is only presented with broadband data. I found that a decrease in $V-R$ colour is strongly correlated with an increase in gas production pre-perihelion.

Lay summary

Comets are one of the most spectacular astronomical phenomena you can see with the naked eye, bright objects that suddenly appear and bring with them a tail of dust that stretches across large parts of sky. They have captured the imagination of star-gazers for millennia, with evidence of comet sightings throughout almost all of recorded history. These short-lived events were often interpreted as harbingers of doom and destruction, but it was not until relatively recently that the true nature of comets was understood.

Comets are small bodies (1–10 km in diameter) made up of a mixture of rocks and ices. When these objects pass close to the Sun they warm up and the ices within them begin to sublimate (change straight from a solid to a gas). This gas lifts dust off of the surface of the comet as it is ejected into space, this dust reflects sunlight to create a visible atmosphere called the coma. This coma is then pushed by the Sun's radiation into a dust tail. The reflected light from the dust is also accompanied by light directly emitted from the gas molecules themselves which gives the coma a blueish tint, the gas molecules can be pushed by the Solar winds and create a gas tail.

Comets are the leftover building blocks of the Solar System and are made up of the same materials that formed the planets we see today. So, in theory, comets are time capsules of the chemical and physical conditions in the early Solar System. However, comets have not remained unchanged since their formation and have been 'aged' by their encounters with the Sun. Ageing refers to any effect that has chemically or physically altered the comet since its formation. This ageing manifests itself as changes in comet activity. Activity refers to the production of dust and gas by the comet, i.e. the more 'active' a comet is, the more dust and gas it produces. Activity varies from comet to comet so we must try to distinguish whether these differences in activity are because of ageing or reflect inherent differences in their formation.

The best way to learn about a comet is to look at it up close, which only became possible recently. Over the last four decades, huge insights into the composition and structure of comets have been uncovered by space missions sent to a handful of comets. But these missions are few and far between and therefore offer us a very limited sample size of the comet population so the majority of our knowledge of the broader population of comets must come from ground-based telescope observations. Ground-based observations have the advantage of long periods of data collection allowing us to track the activity of comets over long periods and multiple orbits, whereas space missions have only been able to observe a comet within a brief snapshot of time. The easiest way to track activity is by measuring the amount of reflected light off of the dust in the coma. The precise measuring of light is known as photometry.

For this thesis, I developed a data analysis pipeline to consistently calibrate the photometry of comets from ground-based telescope images. The development and testing of this pipeline is described in Chapter 2, as well as a discussion of its strengths and limitations. In Chapter 3, I applied this calibration pipeline to ground-based telescope images of the comet 67P/Churyumov–Gerasimenko, which was the target of the Rosetta mission. The Rosetta mission was the first mission to successfully put a spacecraft in orbit around a comet, and then land a probe on the surface of a comet. I describe the overall activity trends of 67P and search the dense data set for any small-scale change in brightness that I could link to events seen on the comet's surface by the Rosetta spacecraft. I detected an outburst in my data with a brightness that puts it in line with an outburst directly observed by Rosetta; however, linking these two events directly remains challenging. In Chapter 4, I apply my pipeline to a wider survey of 14 comets observed with the TRAPPIST telescopes and I describe the different ways the activity can be used to distinguish different types of comets. In Chapter 5, I compared my dust activity measurements to gas production rates published in literature and I describe the strong relationships between dust and gas production.

Declaration

I declare that this thesis was composed by myself, that the work contained herein is my own except where explicitly stated otherwise in the text, and that this work has not been submitted for any other degree or professional qualification except as specified.

Parts of this work have been published in Gardener et al. (2022).

(*Daniel Mark Gardener, November 2023*)

Acknowledgements

I would like to thank all those who have helped making writing this thesis possible. Firstly, I must thank Colin Snodgrass for his excellent guidance and supervision, without which none of this would have been possible. I am also grateful to my fellow members of the Edinburgh comet and asteroids group for their invaluable support, advice, and company on long observing nights. It was a pleasure to work with the group over the past four years and watch its continual growth as more members were pulled into its orbit.

Special thanks to Nicolas Ligier for reducing and preparing the extensive 67P data set that formed the basis of Chapter 3, which saved me a great deal of time and effort that could have been a whole PhD in and of itself. My gratitude also goes to Cecilia Tubiana for her assistance in the acquisition and comparison of archival OSIRIS and NavCam data (Figures 3.9 and 3.10), as well as her helpful discussion on 67P outbursts. Thanks should also go to Emmanuel Jehin for generously sharing the TRAPPIST data which Chapters 4 and 5 are built upon.

Lastly, I would be remiss in not mentioning my family and friends whose love and emotional support helped me greatly through what was an incredibly challenging time for us all. Words cannot express my gratitude.

Contents

Abstract i

Lay summary iii

Declaration v

Acknowledgements vii

Contents ix

List of Figures xv

List of Tables xix

1 Introduction 1

1.1 Comet classification 3

1.1.1 Division by orbital period 3

1.1.2 Tisserand parameter 3

1.1.3 Levison classification 4

1.1.4 Comet–asteroid continuum 6

1.1.5 Trans-Neptunian objects 6

1.1.6 Interstellar comets 6

1.1.7 Comet naming conventions 7

1.2 Coma and tails 7
1.3 Nucleus 8
1.4 Space missions to comets 12
1.5 Rosetta mission 13
1.5.1 Observing campaign 15
1.6 Comet evolution 17
1.7 Activity 19
1.7.1 Drivers of activity 20
1.7.2 Observing activity 23
1.7.3 Statistical studies of comets 25
1.8 Light curves 28
1.9 Thesis outline 29

2 Methodology 31

2.1 Solar System photometry 31
2.1.1 Coordinate system 31
2.1.2 Time 32
2.1.3 Magnitudes 33
2.1.4 $Af\rho$ 34
2.1.5 Phase functions 36
2.1.6 Colour and photometric systems 37
2.1.7 Spectral slope 40
2.2 Pipeline methodology 40
2.2.1 Astrometry.net 41

2.2.2 JPL Horizons 43

2.2.3 Source Extractor 43

2.2.4 calviacat 44

2.3 Pipeline limitations and testing 49

2.4 Summary 50

3 Searching for outbursts in the ground-based photometry of 67P/Churyumov–Gerasimenko 55

3.1 Introduction 55

3.2 Observations 58

3.2.1 VLT 60

3.2.2 NOT 60

3.2.3 TRAPPIST 60

3.2.4 LT 60

3.2.5 Wendelstein 61

3.2.6 Lowell 61

3.3 Results 61

3.3.1 Summary 61

3.3.2 Offset between telescopes around low phase angles 65

3.4 Analysis 67

3.4.1 Coma colour 67

3.4.2 Searching for outbursts 68

3.5 Discussion 71

3.5.1 Outburst of 2015 August 22 71

3.5.2 Searching for other confirmed outbursts and linking observations to surface changes ... 74

3.5.3 Dust mass estimate ... 75

3.5.4 Comparison to 2021–22 apparition ... 76

3.6 Conclusions ... 78

4 A TRAPPIST survey of the activity of 14 comets 79

4.1 Introduction ... 79

4.2 Observations ... 80

4.2.1 9P/Tempel 1 ... 81

4.2.2 46P/Wirtanen ... 85

4.2.3 88P/Howell ... 92

4.2.4 103P/Hartley 2 ... 95

4.2.5 246P/NEAT ... 99

4.2.6 C/2009 F4 (McNaught) ... 103

4.2.7 C/2009 P1 (Garradd) ... 105

4.2.8 C/2011 L4 (PanSTARRS) ... 110

4.2.9 C/2012 F6 (Lemmon) ... 114

4.2.10 C/2012 K1 (PanSTARRS) ... 117

4.2.11 C/2013 A1 (Siding Spring) ... 120

4.2.12 C/2013 R1 (Lovejoy) ... 124

4.2.13 C/2013 US_{10} (Catalina) ... 127

4.2.14 C/2015 ER_{61} (PanSTARRS) ... 131

4.3 Summary ... 134

4.3.1 Power law index comparisons ... 134

4.3.2 Offset between peak $Af\rho$ and perihelion 138

4.3.3 $Af\rho$ profiles..... 139

4.3.4 Effects on comet colour 140

4.3.5 Dependencies on heliocentric distance..... 140

4.3.6 Time lag between peak dust and gas production 143

4.4 Conclusions 143

5 A comparison between broadband and narrowband observations of gas activity in comets 145

5.1 Dust-to-gas ratio..... 145

5.1.1 46P 146

5.1.2 C/2012 F6 147

5.1.3 C/2013 R1 148

5.1.4 Summary..... 149

5.2 Linking colour change to production rates observed by TRAPPIST 150

5.2.1 46P 150

5.2.2 C/2012 F6 152

5.2.3 C/2013 A1 152

5.2.4 C/2013 R1 152

5.2.5 Summary..... 153

5.3 Afρ vs. gas production rates..... 153

5.4 Production rate change vs. colour change 156

5.5 Comparison to SOHO/SWAN data 158

5.5.1 C/2012 F6 159

5.5.2 C/2013 R1 160

5.5.3 C/2012 K1 160

5.5.4 C/2013 US_{10} 160

5.5.5 Overall trends 161

5.6 Conclusion 163

6 Conclusion 165

6.1 Future work 167

Bibliography 169

List of Figures

1.1 Levison comet classification. 5

1.2 Montage of comet nuclei imaged by space missions. 10

1.3 Diagram of comet formation theories. 11

1.4 Summary of space missions to comets to date. 13

1.5 67P light curve from Snodgrass et al. (2017). 17

1.6 Stages of evolution of a comet nucleus. 18

2.1 Diagram of solar system illustrating the different parameters we can measure for a planetary body. 32

2.2 Composite dust phase function for comets. 36

2.3 Transmission profiles for the HB filters and IHW filters superimposed on comet spectrum. 38

2.4 Broadband filter systems superimposed on a comet spectrum. . . 39

2.5 Flow chart showing the steps in the automatic astrometry and photometry calibration pipeline. 42

2.6 Example output of a calibration slope from CALVIACAT. 46

2.7 Diagrammatic representation of error calibration. 49

2.8 Example output of SExtractor highlighting all sources detected within the frame. 51

2.9 Example SExtractor output with measurement aperture highlighted. 52

2.10 An example of a frame with too small of an FOV which caused Astrometry.net to fail due to a lack of sources. 53

2.11 An example of a bright star lying within the aperture. 53

3.1 Montage of brightest outbursts from 67P seen by Rosetta 56
3.2 Dust arc in the coma of 67P. 57
3.3 r-band light curve of 67P from 2015/16 apparition. 62
3.4 67P light curve around low phase angles. 66
3.5 Colour against time of 67P. 68
3.6 67P light curve with piecewise fit. 69
3.7 67P light curve around perihelion with times of outbursts highlighted. 70
3.8 Trend subtracted light curve of 67P showing outburst of 2015 August 22. 71
3.9 NavCam image of 67P taken 2015 August 22 08:55:01 UTC. . . . 73
3.10 OSIRIS images of 67P taken at the closest times before and after the outburst. 73
3.11 r-band light curve of the 2021–22 67P apparition. 77

4.1 Light curve of 9P/Tempel 1. 82
4.2 $Af\rho$ vs. r of 9P/Tempel 1. 82
4.3 Colour vs. r of 9P/Tempel 1. 84
4.4 Spectral slope vs. r of 9P/Tempel 1. 84
4.5 Light curve of 46P/Wirtanen. 86
4.6 $Af\rho$ vs. r of 46P/Wirtanen. 86
4.7 Colour vs. r of 46P/Wirtanen. 89
4.8 Spectral slope vs. r of 46P/Wirtanen. 89
4.9 Phase angle vs. time of 46P/Wirtanen. 90
4.10 Light curve of 46P/Wirtanen around known outbursts. 91
4.11 Light curve of 88P/Howell. 93
4.12 $Af\rho$ vs. r of 88P/Howell. 93
4.13 Colour vs. r of 88P/Howell. 94
4.14 Spectral slope vs. r of 88P/Howell. 94
4.15 Light curve of 103P/Hartley 2. 97

4.16 $Af\rho$ vs. r of 103P/Hartley 2. 97
4.17 Spectral slope vs. r of 103P/Hartley 2. 98
4.18 Light curve of 246P/NEAT. 100
4.19 $Af\rho$ vs. r of 246P/NEAT. 100
4.20 Colour vs. r of 246P/NEAT. 102
4.21 Spectral slope vs. r of 246P/NEAT. 102
4.22 Light curve of C/2009 F4. 104
4.23 $Af\rho$ vs. r of C/2009 F4. 104
4.24 Spectral slope vs. r of C/2009 F4. 105
4.25 Light curve of C/2009 P1. 107
4.26 $Af\rho$ vs. r of C/2009 P1. 107
4.27 Colour vs. r of C/2009 P1. 109
4.28 Spectral slope vs. r of C/2009 P1 109
4.29 Light curve of C/2011 L4. 111
4.30 $Af\rho$ vs. r of C/2011 L4. 111
4.31 Colour vs. r of C/2011 L4. 113
4.32 Spectral slope vs. r of C/2011 L4. 113
4.33 Light curve of C/2012 F6. 115
4.34 $Af\rho$ vs. r of C/2012 F6. 115
4.35 Spectral slope vs. r of C/2012 F6. 116
4.36 Light curve of C/2012 K1. 118
4.37 $Af\rho$ vs. r of C/2012 K1. 118
4.38 Colour vs. r of C/2012 K1. 119
4.39 Spectral slope vs. r of C/2012 K1. 119
4.40 Light curve of C/2013 A1. 122
4.41 $Af\rho$ vs. r of C/2013 A1. 122
4.42 Spectral slope vs. r of C/2013 A1. 124
4.43 Light curve of C/2013 R1. 126

4.44 $Af\rho$ vs. r of C/2013 R1. 126

4.45 Spectral slope vs. r of C/2013 R1. 127

4.46 Light curve of C/2013 US_{10} 128

4.47 $Af\rho$ vs. r of C/2013 US_{10}. 128

4.48 Spectral slope vs. r for C/2013 US_{10}. 130

4.49 Light curve of C/2015 ER_{61}. 132

4.50 $Af\rho$ vs. r of C/2015 ER_{61}. 132

4.51 Spectral slope vs. r for C/2015 ER_{61}. 133

4.52 $Af\rho$ as a function of aperture radius ρ of fourteen comets. 139

4.53 Heliocentric distance dependence on $Af\rho$ of fourteen comets. . . . 141

4.54 $Af\rho$ dependence on perihelion distance q of all survey comets. . . 141

4.55 The minimum measured $S_{V,R}$ vs. r for all survey comets. 142

5.1 $Af\rho$-to-OH ratios of 46P, C/2012 F6 and C/2013 R1. 147

5.2 $Af\rho$-to-CN ratios of 46P, C/2012 F6 and C/2013 R1. 148

5.3 Gas production rates plotted against colour of 46P, C/2012 F6, C/2013 A1 and C/2013 R1. 151

5.4 C_2 production rates plotted against colour of 46P, C/2012 F6 and C/2013 R1. 153

5.5 Gas production rates plotted against $Af\rho$ of 46P, C/2012 F6 and C/2013 R1. 154

5.6 Pre-production gas production rates plotted against colour of 46P, C/2012 F6 and C/2013 R1. 157

5.7 Post-production gas production rates plotted against colour of 46P, C/2012 F6 and C/2013 R1. 158

5.8 $Af\rho$-to-H_2O ratios of C/2012 F6, C/2013 R1, C/2012 K1 and C/2013 US_{10} 159

5.9 Water production rate plotted against colour of C/2012 F6, C/2013 R1, C/2012 K1 and C/2013 US_{10} 161

5.10 Water production rate plotted against $Af\rho$ of C/2012 F6, C/2012 K1, C/2013 R1 and C/2013 US_{10} 162

List of Tables

1.1 Heliocentric distances and temperature onset of various drivers of activity. 21

2.1 Summary table of the colour terms used during colour calibration to PS1 for each instrument. 47

3.1 Summary of 67P observations. 59

3.2 Summary table of 67P data processed through the pipeline. 62

3.3 Average colour of 67P coma across the observation period measured by different instruments. 67

4.1 Orbital parameters and classifications of comets targeted by TRAPPIST. 80

4.2 Summary of observations of comets made by the TRAPPIST telescopes. 80

4.3 Comparison of $Af\rho$ measurements of C/2011 L4 from this work to literature 112

4.4 Summary of power law indices grouped by dynamical class 135

Chapter 1

Introduction

Comets are small, icy planetesimals left over from the formation of the Solar System. When these objects pass close to the Sun they warm up and the ices within them begin to sublimate into gases. This outgassing lifts dust off of the surface and produces a visible atmosphere called the coma. As a comet gets closer to the Sun the solar radiation pressure and solar winds sculpt the coma into tails. Solar radiation pressure interacts with dust grains to create a dust tail and solar winds accelerate the ionised gas to produce an ion tail. Comets, if sufficiently bright, can be seen from the Earth by eye, and their tails can subtend large angles across the sky. As such, comets are some of the first celestial bodies to be observed and documented by ancient astronomers – the first recorded observations dating back to circa 1000 BC in ancient China (Zhen-Tao et al., 1995).

Edmund Halley computed the orbits of dozens of well observed comets and correctly predicted the periodicity of the comet which now bears his name (Halley, 1705). He postulated that the comets of 1531, 1607 and 1682 were the same object and correctly predicted its return, although he would not live to see it. Many more comets were discovered and categorised in the intervening years, but their physical structure remained elusive. The prevailing theories suggested that comets were not solid bodies but swarms of solid particles. It took until the 1950s before we had a concrete idea of the structure, origin and composition of comets.

The icy-conglomerate or 'dirty snowball' model proposed by Whipple (1950) described the nucleus of the comet as a mixture of dust and ices, which sublimate to create a coma. Sublimation increases as the comet approaches the Sun and the temperature rises. Whipple's model successfully explains many observed phe-

nomena but the idea of a single solid cometary nucleus remained the subject of scientific debate (e.g. Lyttleton, 1951) until it was proven by the spacecraft missions to comet Halley in 1986 (Keller et al., 1986).

Dynamical studies of comets, until recently, demonstrated that there were no original hyperbolic orbits ($1/a < 0$, where a is the semi-major axis of the orbit). Which meant that all comets were coming from within the Solar System and not interstellar space. Oort (1950) proposed that there was a large population of cometary bodies located in the outer Solar System ($\sim 200\,000$ au), later dubbed the Oort cloud. He proposed that comets had their semi-major axis (i.e. orbital energy) increased by perturbations with the planets while their perihelion distance remained the same. Other perturbing forces outside the Solar System (e.g. galactic tides, stars, giant molecular clouds) increased the perihelion distance to outside the planetary region stabilising it in an orbit within the Oort cloud. Recent dynamical studies of Oort cloud comets place constraints on their semi-major axis, and hence the distance to the Oort cloud, of 27 000 to 36 000 au (Dones et al., 2004). Oort originally estimated that this population numbered 2×10^{11} with a total mass of about 0.3 M_{Earth}, modern studies place this number at 7–8 $\times 10^{11}$, with a total mass between 0.5–5 M_{Earth} (Brasser and Morbidelli, 2013; Levison et al., 2010). Tidal forces within the galaxy are thought to be the mechanism for providing new comets from the Oort cloud to the inner Solar System. Hills (1981) later proposed an inner Oort cloud to explain the replenishment of the Oort cloud from the depopulation due to tidal forces. The distance and population of this inner ($< 20\,000$ au) cloud remain uncertain. Recent studies have found Oort cloud comets with semi-major axes of ~ 5000 au, which places an upper limit on Oort cloud population of $\sim 10^{12}$ (Kaib and Volk, 2022). In most theories, Oort cloud comets were formed in the Jupiter–Neptune region before being ejected to the outer Solar System (A'Hearn, 2004; Festou et al., 2004). These ideas still needs to be incorporated with observations of trans-Neptunian objects in the Kuiper belt.

The Kuiper belt, also known as the Edgeworth–Kuiper belt, is a circumstellar disc of icy planetesimals beyond the orbit of Neptune ($a > 30$ au) that were never incorporated into planet formation. The existence of this belt was theorised by Edgeworth (1943, 1949) and Kuiper (1951) and later confirmed by the discovery of the trans-Neptunian object 1992 QB_1 (Jewitt and Luu, 1993). This discovery of the Kuiper belt provided a viable source region of low-inclination short-period comets, which could not be sourced from the Oort cloud but instead from reservoir

a low-inclination Neptune-crossing bodies (Kaib and Volk, 2022). The Kuiper belt extends approximately from $30 < a < 50$ au (Fraser et al., 2022). The number of comet sized bodies within this region is very uncertain, but extrapolating from observed constraints implies a population of $\sim 10^8$ objects with a diameter ~ 2 km or larger (Nesvorný et al., 2017).

1.1 Comet classification

Comets are a broad and varied population of bodies, as such various conventions and taxonomies have been developed over the years to categorise and distinguish different types of comets.

1.1.1 Division by orbital period

Comets can first be divided by their orbital period, a comet with a period greater than 200 years is defined as a long-period comet (LPC), and conversely a comet with a period less than 200 years is classified as a short-period comet (SPC). SPCs are further split into Jupiter-family, Encke-type and Halley-type comets. Jupiter-family comets (JFCs) are SPCs whose orbits are controlled by Jupiter with periods less than 20 years. They are also characterised by low orbital inclination ($< 30°$). An SPC whose orbit is inside that of Jupiter's is known as an Encke-type comet (ETC). Halley-type comets (HTCs) are comets of intermediate period (20–200 years) which have high inclinations ($> 30°$). The source of HTCs and LPCs is thought to be the Oort cloud, as oppose to SPCs which are thought to originate from the Kuiper belt. Of particular interest to cometary scientists are dynamically new comets (DNCs) which are LPCs which have been determined to be making their first pass through the inner Solar System since being scattered to the Oort cloud (Meech, 2017).

1.1.2 Tisserand parameter

A dynamical criterion for distinguishing the orbits of comets and asteroids is the Tisserand parameter which comes from a restricted three-body system of a planet orbiting a central star and a third massless body (Tisserand, 1896). The

parameter is derived from the Jacobi constant, the only conserved quantity in a restricted three-body problem:

$$C_{\mathrm{J}} = 2\left(\frac{\mu_1}{r_1} + \frac{\mu_2}{r_2}\right) + 2n(\xi\dot{\eta} - \dot{\xi}\eta) - (\dot{\xi}^2 + \dot{\eta}^2 + \dot{\zeta}^2) \tag{1.1}$$

where r_1 and r_2 are distances of the massless body from the other two masses, $\mu_x = Gm_x$, n is the mean motion of the masses around the common barycentre, and (ξ, η, ζ) are the sidereal coordinates. Tisserand expressed the Jacobi constant in terms of orbital parameters. The units are chosen to ensure $\mu_1 = 1$ and $n = 1$. The final term $(\dot{\xi}^2+\dot{\eta}^2+\dot{\zeta}^2)$ is the velocity squared and can therefore be expressed as $v^2 = \mu(2/r - 1/a)$, where $\mu = G(\mu_1 + \mu_2) \approx 1$. The Jacobi constant can be further simplified by noticing that $\xi\dot{\eta} - \dot{\xi}\eta$ is the ζ component of the angular momentum $\boldsymbol{h}$, so can be expressed as $h\cos i$ where $h = \sqrt{a(1-e^2)}$. Substituting these back into Equation 1.1, and using the assumptions $\mu_2 << 1$ and $r_1 \simeq r$, gives you the Tisserand parameter:

$$T_{\mathrm{J}} = \frac{1}{a} + 2\sqrt{a(1-e^2)}\cos i \tag{1.2}$$

where a is the semi-major axis of the observed object; e is the eccentricity of the object and i is the inclination of the object. The subscript J indicates this parameter is defined relative to Jupiter, as such the units are expressed in terms of Jupiter's orbital radius. The Tisserand parameter is conserved (at one per cent level) during the encounter of a planet and massless small body. The Tisserand parameter can be related to the relative velocity V_x of the comet as it intersects a planet's orbit with the equation $V_x = \sqrt{3 - T_x}$. Therefore if $T_x > 3$, the orbit of the third body cannot intersect a planet's orbit. As $T_x \to 3$ the influence of the planet on the comet's orbit becomes stronger.

1.1.3 Levison classification

Levison (1996) describes a comet classification system using T_{J}, summarised in Figure 1.1. Active bodies orbiting in the ecliptic plane will have $T_{\mathrm{J}} > 2$, if their $T_{\mathrm{J}} < 3$ then they are a JFC. Bodies with $T_{\mathrm{J}} > 3$ are split depending on whether or not they orbit interior to Jupiter, those within Jupiter's orbit are ETCs and those without are Chiron-type objects, more commonly referred to as

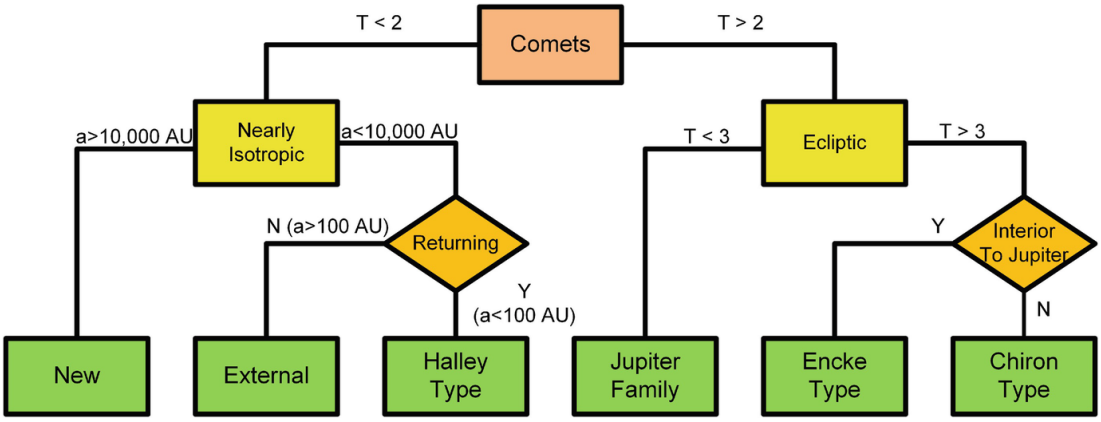

Figure 1.1 Comet classification from Levison (1996), modified by Thomas (2020).

Centaurs. They orbit between Jupiter (5 au) and Neptune (30 au). Scattered disc objects (SDOs) are high inclination, high eccentricity objects thought to have been scattered from the Kuiper belt by the giant planets. The mechanisms that create this disc remains unclear. It is difficult to distinguish SDOs from Centaurs so the Minor Planet Center (MPC) categorises them as the same. Centaurs have short dynamical lifetimes ($\sim$ few Myrs) prompting the idea that SDOs replenish this population. It is thought Centaurs are a transitional object between SDOs and JFCs. The SDOs are perturbed by Neptune and Uranus until they come under the influence of Jupiter and move to a JFC-type orbit. This evolutionary pathway is not guaranteed since it has been shown that Oort cloud objects can directly enter the Centaur orbits. There still remain other objects in the Solar System that do not fall neatly into any category. There remains a discrepancy in the masses and albedos of Centaurs and JFCs, which implies either there are many undetected much smaller Centaurs or the mass loss between these steps is massive (Fraser et al., 2022; Kaib and Volk, 2022).

$T_{\mathrm{J}} < 2$ defines comets that orbit in nearly isotropic inclinations. These are divided into two groups; new and returning, determined by their semi-major axis a. The returning comets are further divided into HTCs or external comets by whether or not their semi-major axis is greater than 100 au. HTCs are believed to have originated in the Oort cloud as external comets that leaked into the planetary domain via perturbation by Saturn or Jupiter. Damocloids are inactive long-period objects with $T_{\mathrm{J}} < 2$ and are assumed to be dormant HTCs. Throughout this thesis I will refer to external comets simply as LPCs, although I will make the distinction between new and returning LPCs.

1.1.4 Comet–asteroid continuum

In recent years there have been increasing numbers of objects in the Solar System observed exhibiting features of both comets and asteroids and the distinction between asteroids and comets has become blurred (Hsieh, 2017; Jewitt and Hsieh, 2022). There are two main types of asteroid–comet continuum objects. First are dormant or extinct comets. These comets have depleted all of their volatiles and do not exhibit any cometary activity and therefore are often confused with asteroids. The second are main-belt comets (MBCs), also known as active asteroids. These bodies orbit within the asteroid belt and have unexpected present-day ice activity and could have played a role in the delivery of water to the terrestrial planets (Jewitt, 2004). A potential third category are 'dark comets', which are seemingly inactive objects that exhibit non-gravitational acceleration that can only be explained by outgassing (Seligman et al., 2023).

1.1.5 Trans-Neptunian objects

Trans-Neptunian objects (TNOs) are any minor planet with a semi-major axis greater than the orbit of Neptune (> 30 au) but not part of the Oort cloud. It is thought that there is a depletion of objects at low eccentricity at $a > 50$ au. It may be caused by such objects being too faint to see since their perihelion distances will be large. This will be solved in the near future by deep surveys, such as LSST, which can probe this region (Bauer et al., 2022).

1.1.6 Interstellar comets

It has long been expected that we would observe interstellar objects, rogue planetesimals ejected from other solar systems that will eventually intercept our own Solar System (McGlynn and Chapman, 1989). This assumption was proved right in 2017 with the discovery of the first interstellar object, 1I/'Oumuamua ('Oumuamua ISSI Team, 2019), and later 2I/Borisov (Guzik et al., 2019). 'Oumuamua drew considerable attention due to its unusual morphology, an elongated ellipsoid shape. 'Oumuamua was also smaller and less active than anticipated. Many expected the interstellar comet to be analogous to an Oort cloud comet since both have been stored in deep space for billions of years. The second interstellar object 2I/Borisov showed much more typical cometary activity. Most

of Borisov's properties are similar to Solar System comets, however, two major differences were observed. First, Borisov had a high abundance ratio of CO/H_2O and second, the elemental abundance of carbon relative to oxygen in its volatiles was nearly six times higher than measured in Solar System comets. This tells us that the comet formed in a different environment with a different CO/H_2O abundance and a system enriched in carbon compared to our Solar System (Bodewits et al., 2020; Cordiner et al., 2020).

1.1.7 Comet naming conventions

Comets are designated using the following conventions. Initially all newly discovered comets are named with the year of discovery followed by a letter indicating the half-month of discovery and a number indicating the order in which they were discovered. For example, the first comet discovered in the first half of January 2024 will be designated C/2024 A1. The letter preceding the numbers stand for the following:

- P/ periodic comets with confirmed multiple perihelion passages
- C/ non-periodic comets, all LPCs regardless of whether or not they have closed orbit are designated as such
- D/ disappeared
- I/ interstellar object
- X/ comet with no established orbit

Periodic comets have a alternative naming convention and are more commonly referred to by the number of the order in which their periodicity was confirmed. This number comes before the 'P' in their designation. Comets are named after the one who discovered it, with the only exception to this rule being the first periodic comet 1P/Halley, which is named after Halley even though he was not the first to discover it.

1.2 Coma and tails

There are four observational components of comets:

- Coma (a.k.a. head)
- Dust tail
- Ion tail (a.k.a. plasma tail)
- Neutral tail

The coma is a round and nebulous cloud composed of both gases and cometary dust. The coma is created by sublimating gases lifting dust off of the surface of the nucleus. This dust is primarily made of silicate and carbon-based material. These solid grains released from the nucleus were incorporated into the comet with little alteration during its formation (Hanner, 1996). The brightness of the coma comes from the reflected sunlight off of dust particles as well as the fluorescence of neutral gas radicals. Radicals and ions observed in cometary comae are not chemically stable, therefore these must be created by photochemistry of stable molecules released from the nucleus. The dust is pushed by solar radiation pressure and extends into a dust tail pointing in the anti-sunward direction, with lengths of 10^4–10^8 km (Fulle, 2004). The dust tail is not necessarily straight and can be curved or structured due to the motion of the comet about the Sun. Photoionisation forms a cometary ionosphere on scales of 10^5–10^6 km, orders of magnitude larger than the nucleus, which interacts with the solar winds forming an ion tail with a length on the order of 10^6–10^7 km (Combi et al., 2004). The ion tail is made up of ionised gas molecules and radicals accelerated by the solar wind. The ion tail also extends in the anti-sunward direction and is a lot straighter than the dust tail due to the difference in speed between the dust and gas particles. A third, neutral tail is sometimes seen composed of gases that are blown away by solar winds before ionisation, atomic sodium is the classic example. However, this neutral tail is difficult to observe even in the brightest comets so is rarely the subject of intense study.

1.3 Nucleus

The nucleus of a comet is a body composed of various rocks and ices. The nucleus morphology can vary quite significantly from comet-to-comet. Figure 1.2 shows a montage of cometary nuclei visited by space missions, each with its own unique structure. Some display a bilobate structure; these bilobate nuclei may have

formed from contact binaries. The typical size of a JFC nucleus ranges $\sim$ 1–10 km in diameter (Snodgrass et al., 2011).

Four ideas of the structure of comet nuclei are depicted in Figure 1.3:

1. Whipple's dirty snowball (Whipple, 1950)
2. Fractal aggregate model (Donn et al., 1985)
3. Rubble pile model (Weissman, 1986)
4. Icy-glue model (Gombosi and Houpis, 1986)

Whipple (1950) described the nucleus of the comet to be a single structure composed of a mixture of ices which sublimate to create a coma. Whipple's model successfully explains many observed phenomena such as large gas production rates, jet structures in the coma, non-gravitational forces due to momentum transfer of gas outflows, comets surviving close encounters with Sun and comets being sources of meteors. This single-body nucleus idea was not confirmed until the observation of 1P/Halley's nucleus in 1986. The images brought back from this and subsequent space missions prompted a re-examination of comet nuclei models. Many of the nuclei observed had elongated shapes with axes ratios of 2:1:1 leading to thoughts that these objects formed via accretion and not a uniform collection of dust and gas around a core (Lamy et al., 2004; Thomas, 2020). Comet nuclei also had low albedo which would not be expected from a 'dirty snowball'. These lead to a rethink in the structure of comet nuclei, with some dubbing them as 'icy dirtballs' (Keller, 1989).

Whipple's model required the comets to form through some form of accretion, and it was unclear whether the cohesion between these cometesimals would be strong enough for the nucleus to be considered one body. Gombosi and Houpis (1986) imagined the nucleus was a single solid body formed of non-volatile chunks 'glued' together by icy material. It is homogeneous on large scale but inhomogeneous on small scales.

Observations of the bilobate nuclei of 103P and 67P threw the concept of a single solid nucleus into doubt, and would suggest several smaller sub-nuclei came together to form the nucleus. This lent credence to the rubble pile theory of Weissman (1986) where the nucleus is formed of many gravitationally bound sub-nuclei. The size distribution, initial composition and bulk density of each

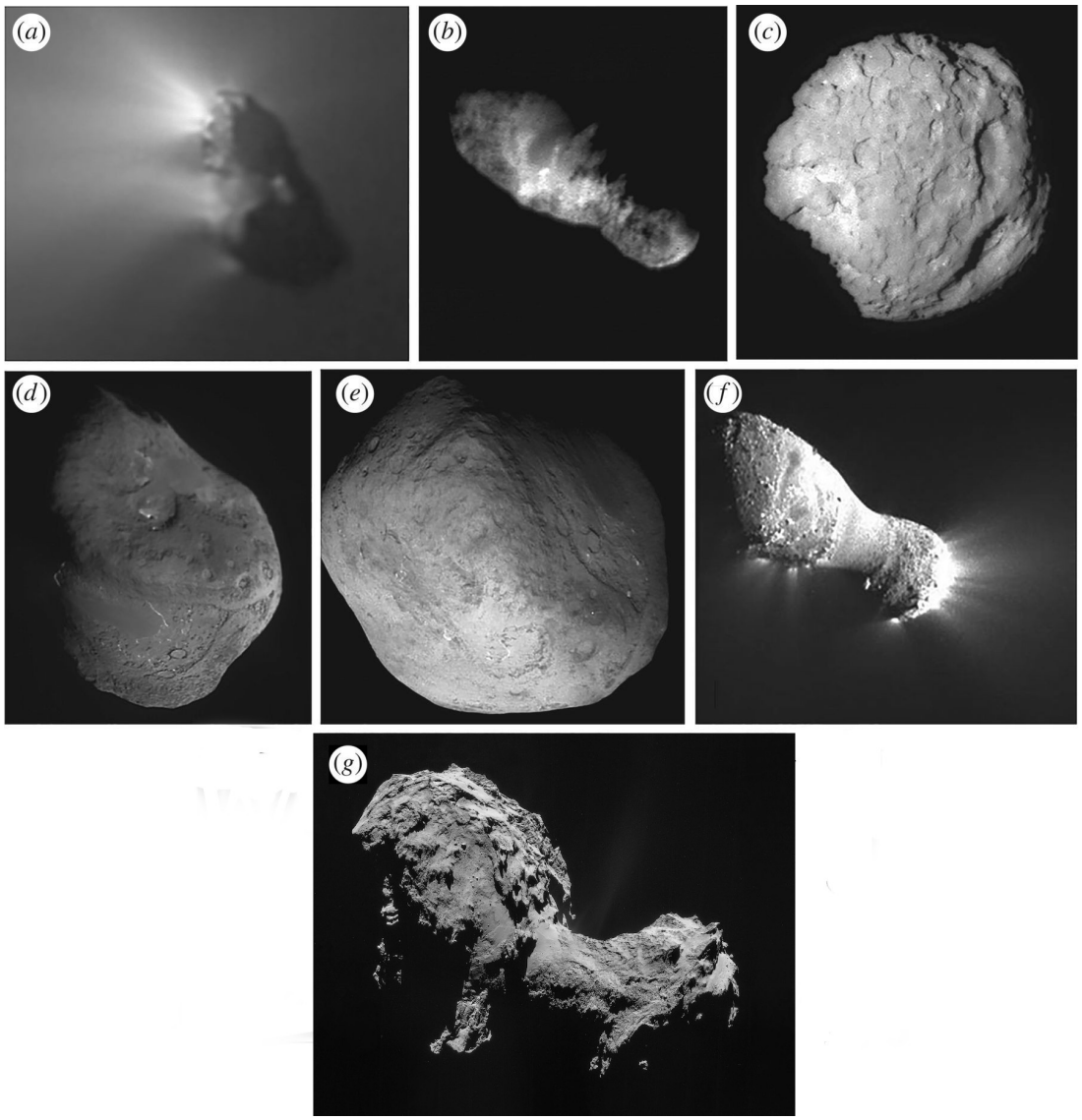

Figure 1.2 Comet nuclei as visited by spacecraft from 1986 to 2014. (a) Nucleus of 1P/Halley obtained by the Giotto spacecraft as it flew through the coma on 1986 March 12 from a distance of 1372 km. Credit:Giotto/MPAe/ESA. (b) 19P/Borrelly as seen at a distance of 3556 km by the Deep Space 1 mission. Credit: NASA/JPL. (c) 81P/Wild 2 viewed at the time of closest approach (238 km) on 2004 January 2 by the Stardust spacecraft. Credit: NASA/JPL. (d) Nucleus of 9P/Tempel 1 as seen from Deep Impact mission on 2005 July 4 from a distance of 500 km. Credit: University of Maryland, JPL/NASA. (e) Reverse side of 9P/Tempel 1 as seen during Stardust-NExT flyby on 2011 February 14 from a distance of 181 km. (f) 103P/Hartley 2 at close approach during the EPOXI mission on 2010 November 4 from a distance of 694 km. Credit: NASA/JPL-Caltech/UMD. (g) 67P/Churyumov–Gerasimenko taken by Rosetta on 2014 September 19 from a distance of 28.6 km. Credit: Rosetta/ESA. Adapted from Meech (2017).

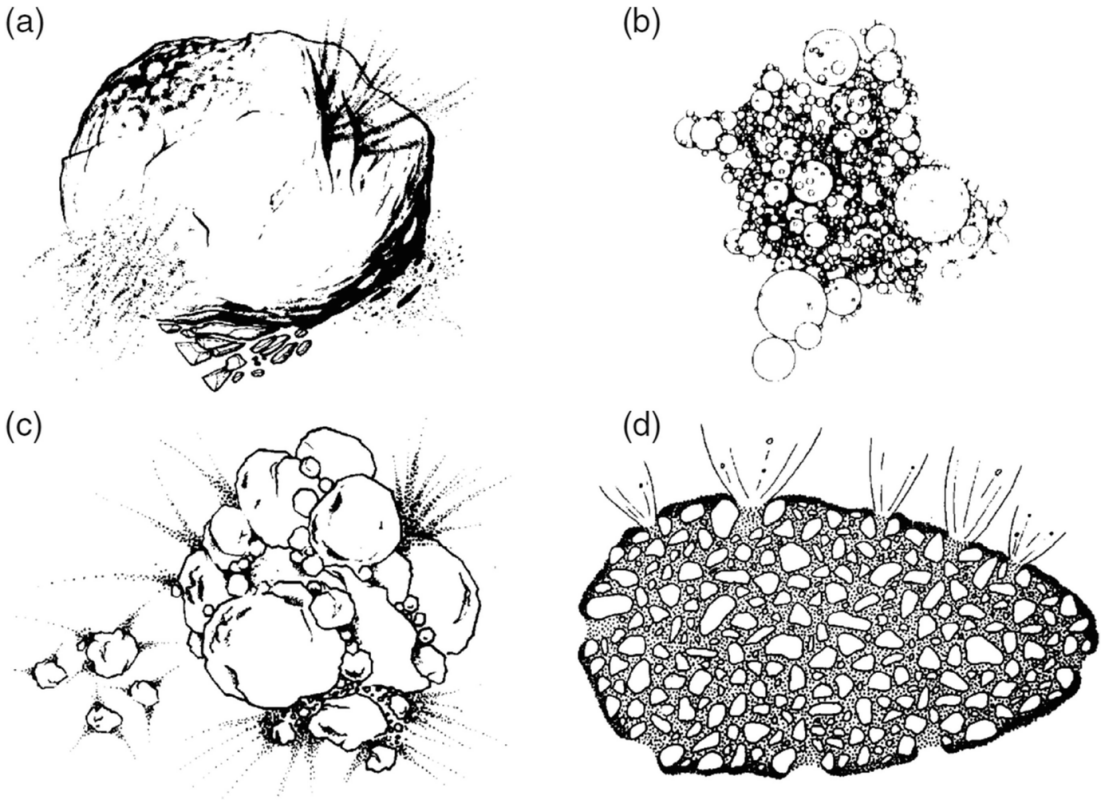

Figure 1.3 Theories of comet formation and structure. (a) Whipple's icy snowball, (b) Donn's fractal aggregate model (Donn et al., 1985), (c) rubble pile model (Weissman, 1986) and (d) icy-glue model (Gombosi and Houpis, 1986). Reproduced from Donn (1989).

sub-nuclei can be different. Comet splitting is seen as evidence for this theory. Models of D/Shoemaker–Levy 9's breakup suggested the nucleus had a tensile strength < 6.5 Pa which provided strong evidence to the loosely bound rubble pile theory. Further splitting seen at 73P/Schwassmann—Wachmann 3 was also seen as evidence for low tensile strength nuclei. Visible observations of 73P found that the largest fragments had the same composition as each other and were consistent with the composition of the nucleus pre-breakup (Schleicher and Bair, 2011). Mid-IR observations found similar mineralogy and grain properties between fragments (Harker et al., 2011). Both of these results imply homogeneous composition and structure between sub-nuclei.

Our picture of the comet nucleus has evolved from the original concept of Whipple's 'dirty snowball' to a porous rubble of low density and low strength (Lamy et al., 2004). The nuclear surface is a compressible layer of dust, which varies in thickness from comet-to-comet but is on the order of 20 cm deep. Beneath this is a hard, possibly icy layer of thickness 0.5–20 cm which itself lies on top of a porous and homogeneous interior (Thomas, 2020). Information of the interior beyond this point remains a mystery.

1.4 Space missions to comets

Our current knowledge of cometary nuclei derives heavily from in situ observations made by space missions. Since the first fly-by missions in the 1980s, there have been several notable missions designed to observe comets up close. Giotto flew by 1P/Halley revealing irregular surfaces, albedo differences and localised surface activity (Reinhard, 1986). The other missions to Halley: VeGa-1 and VeGa-2, Suisei and Sakigake (Grewing et al., 1988), as well as the ISEE-3/ICE mission to comet 21P/Giacobini–Zinner (Von Rosenvinge et al., 1986) led to key advancements in our understanding of the basic properties of the nuclei, chemistry, localisation of surface activity and interactions with solar wind.

In the 21st century we have seen more advanced and specialised missions. Deep Space 1 flew past 19P/Borrelly in 2001 to obtain photometric properties and detailed morphological features (Soderblom et al., 2002). The nucleus was bilobate with terrain including mesas, smooth regions, valleys and depressions (Britt et al., 2004). Stardust was the first sample return mission from a cometary coma (Brownlee et al., 2006), Deep Impact impacted comet 9P/Tempel 1 to eject sur-

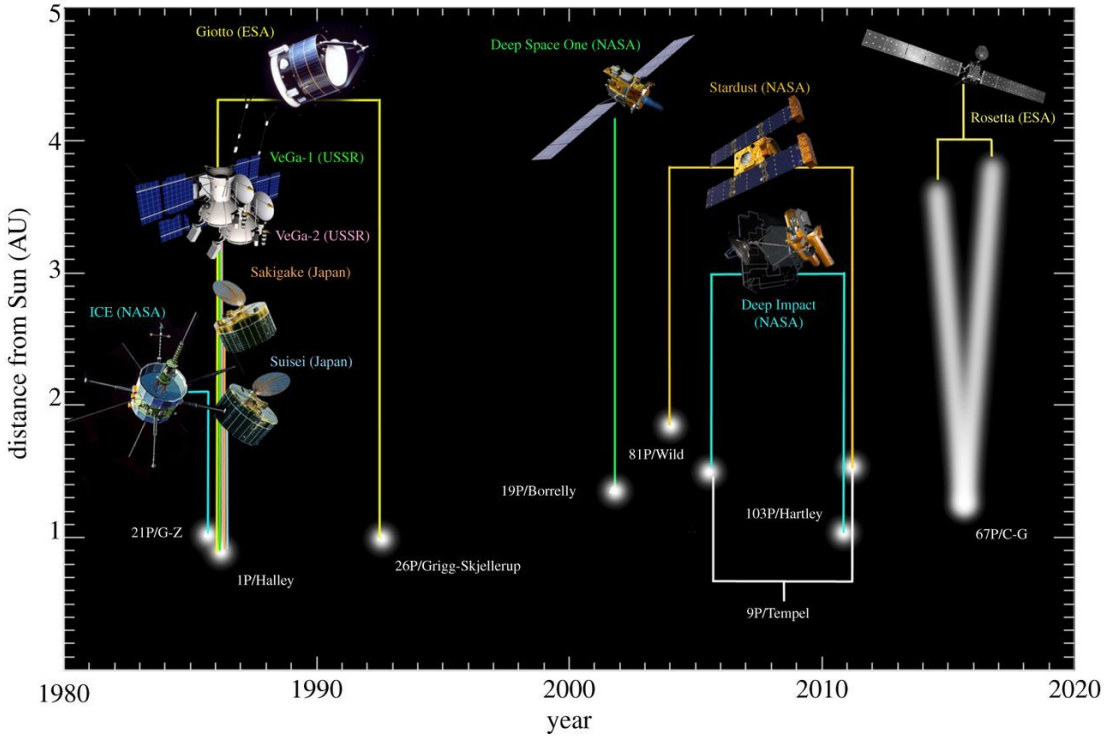

Figure 1.4 All space missions to comets to date showing which missions visited which comets. The continuous line of 67P represents the two years Rosetta spent orbiting the nucleus. Reproduced from Jones et al. (2017)

face material (A'Hearn et al., 2005) which was then analysed by the subsequent Stardust-NExT mission (Veverka et al., 2013). With each new mission came more resolving power to see complex details on the surface as small as even a few metres. It was possible to map the surface and examine geological processes. Deep Impact indicated that CO_2 and H_2O had different distributions around the nucleus suggesting that the nucleus formed through conglomeration of different cometesimals. 103P/Hartley 2, visited by EPOXI (A'Hearn et al., 2011), found that CO_2 was the main driver of activity on the comet. A graphical summary of all comet space missions to date is presented in Figure 1.4.

1.5 Rosetta mission

The Rosetta mission to the JFC 67P/Churyumov—Gerasimenko was a major milestone in cometary science, it was the first mission to rendezvous and then orbit a comet nucleus on its journey through the inner Solar System. The probe monitored the comet continuously over the course of its two years in orbit of

the nucleus. It also launched the Philae lander which made the first successful landing on a comet's surface. Despite a rough landing, it still managed to make in situ measurements of the comet's surface for several days.

From measurements made by the Philae lander we now have evidence that comet nuclei form hard subsurface icy layers (Biele et al., 2015; Boehnhardt et al., 2017; Roll and Witte, 2016). We also observed redeposition of cometary materials, as previously observed on 103P (A'Hearn et al., 2011). Icy patches have been observed previously on the surface of 9P and 103P (Sunshine et al., 2012; Veverka et al., 2013). This was not explained until Rosetta found that some of these patches were frost, condensing overnight, and disappearing after sunrise (De Sanctis et al., 2015; Fornasier et al., 2016). Rosetta observed changes to surfaces as they were happening, such as erosion, fracturing and cliff collapse (El-Maarry et al., 2019; Groussin et al., 2015; Pajola et al., 2017). We now know the depressions on cometary surfaces form and expand radially over timescales of months, which is short compared to the orbital period but longer than some had expected. 67P was found to have a dusty, compressible surface of variable thickness, below which was a hard, possibly icy layer. This layer sits on top of a porous and homogeneous interior. Surface roughness is significant, causing massive temperature differences over short baselines.

67P had a distinctive bilobate morphology, see Figure 1.2g. The planar structures were not aligned between the two lobes, this led to the conclusion that these lobes must have formed independently (Davidsson et al., 2016; Massironi et al., 2015). This has been seen in other comet nuclei (e.g. 19P, 103P) and prompted the idea that these bilobate nuclei might have formed as contact binaries and have compositional differences between the two lobes, as seen in 103P (A'Hearn et al., 2011; Feaga et al., 2011). Observations made by the CONSERT instrument on Rosetta found that the head of 67P is homogeneous on scales larger than a few metres. Measurements of gravity showed no evidence of voids or large scale heterogeneity within the head (Pätzold et al., 2016).

The mass of 67P was $9.982 \pm 0.003 \times 10^{12}$ kg and density was 537.8 ± 0.6 kg m^{-3} with a porosity of 72–74 per cent (Pätzold et al., 2016). The total mass lost during the 2015 perihelion passage was $10.5 \pm 3.4 \times 10^{9}$ kg or 0.1 per cent of the nuclear mass. Assuming a constant rate of mass loss each apparition, the lifetime in this orbit is $\sim$ 6000 yrs. At this mass loss rate, 67P will shrink by about 0.55 m per apparition. The escape velocity was $\sim$ 1 m s^{-1} but was dependent on the location on the nucleus with the neck region having the weakest gravity

($g = 1.4 \times 10^{-4}$ ms^{-2}) and the base of the body the strongest ($g = 2.4 \times 10^{-4}$ ms^{-2}) (Pätzold et al., 2016).

Rosetta gave us a tremendous increase in our knowledge of comet composition from the measurements of cometary grains, including calcium-aluminium (Wooden et al., 2017), one of the earliest condensates of the protoplanetary disc. This far more detailed understanding of cometary grains should lead to constraints on the interpretation of the more limited data on grains in protoplanetary discs generally. An array of new molecules, which were not expected, have been identified including O_2 (Bieler et al., 2015). O_2's correlation with water suggests the O_2 formed on icy grain surfaces in the protoplanetary disc. Grain-surface reactions have been used previously to explain the appearance of other molecules such as CO_2.

The HDO/H_2O ratio was much larger than in any previously observed JFC. This has significant implications on our understanding of the role of comets in the delivery of water to Earth. 67P had an HDO/H_2O ratio three times higher than in the Earth's oceans, which precludes the theory that water on Earth has cometary origins (Altwegg et al., 2015). This large ratio had so far only been found in observations of Oort cloud comets, this changed our theories on comet formation scenarios. Previously it was thought that Oort cloud comets formed in the region of giant planets while JFCs formed in the trans-Neptunian region. It is now clear that both JFCs and Oort cloud comets formed in a largely overlapping region beyond proto-Neptune and were scattered by giant planet migration to their current positions (A'Hearn, 2017; A'Hearn et al., 2012).

1.5.1 Observing campaign

The Rosetta mission was supported by large ground-based observation campaigns (Snodgrass et al., 2013, 2017). Before the mission, Snodgrass et al. (2013) undertook an observing campaign along with analysis of previously unpublished archival data on 67P. This campaign was designed to constrain the start of 67P's activity and predict the pattern of activity over 2014–15 apparition.

Images were taken at the Very Large Telescope (VLT) in *R*-band between 2007 and 2008, this wavelength was chosen as it is free of gas emission lines. The point spread function (PSF) shape was modelled and compared with a radial profile to search for faint activity. It was found that 67P's activity reached a detectable

brightness around 4.3 au in 2007 November. 67P did not appear to have a sudden start in activity but rather a more continuous increase in dust production. Data from different apparitions all fitted onto the same curve implying activity level did not change between apparitions. The shape of the light curve was symmetrical around perihelion, although the comet's brightest point lagged behind perihelion. Snodgrass et al. (2013) proposed that this time could be explained by (1) thermal wave travel time from surface to buried ice, (2) the fact that the production of dust and gas is a two step process or (3) a seasonal effect — 67P reaches equinox around 50 days before perihelion.

The predictions by Snodgrass et al. (2013) were in good agreement with what was observed in the campaign in support of Rosetta (Snodgrass et al., 2017). Observations began in 2013 and early 2014 when 67P was very faint and apparently inactive, although photometry from Rosetta indicated that detectable activity began early in 2014, when the comet was more than 4 au from the Sun. The comet became more visibly active in late 2014 with a 10^{11} km long tail. After passing behind the Sun, it became visible again in 2015, brighter now and still with a long tail. It evolved a broad coma and narrow tail as it retreated from the Sun. 67P faded at about 3.5 au. The nucleus and dust coma of 67P had similar, featureless spectra. The gas coma was more revealing, displaying a composition typical of the carbon-depleted class (A'Hearn et al., 1995). 67P's activity was tracked using broadband photometry in the R-band. The comet's brightness followed the predictions made by Snodgrass et al. (2013) well, with a peak in late August, see Figure 1.5. This observing campaign and the data from it is the focus of Chapter 3.

The dust and CN gas production rates of 67P varied in different ways around perihelion, with the dust production varying symmetrically around perihelion but the CN production was far more asymmetric with a sharp turn-on pre-perihelion, which indicated gas production was dominated by the southern hemisphere (Bockelée-Morvan et al., 2015; Fink et al., 2016; Hässig et al., 2015). However, the dust production rates and CN production rates did not match the in situ observations made by Rosetta (Fougere et al., 2016; Hansen et al., 2016). The seasonal effects implied were not obvious in the Rosetta measurements. One possible explanation was that at distances beyond the sight of Rosetta (> 100 km) was a distributed source of CN (Opitom et al., 2017). This suggested the conclusion that the bright CN band cannot be used as a reliable tracer of total gas production.

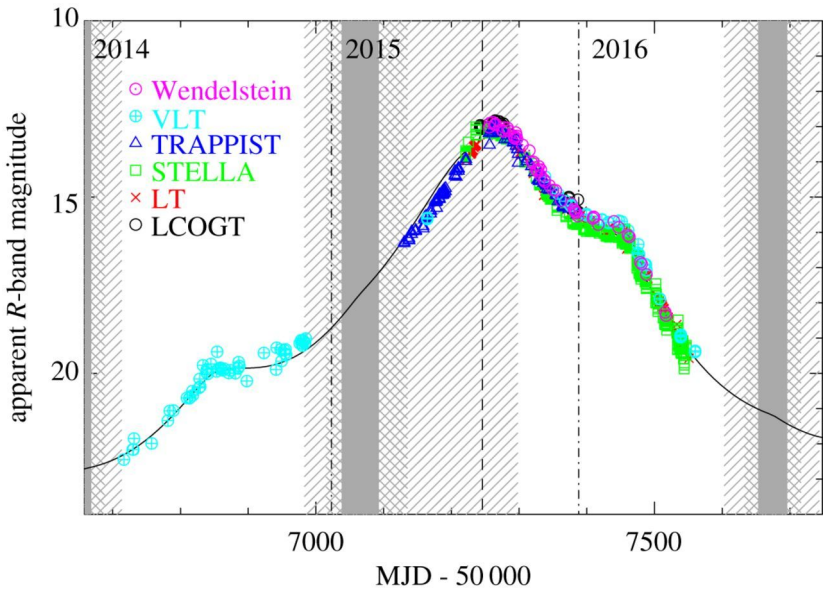

Figure 1.5 Photometry of 67P/Churyumov–Gerasimenko taken in the observation campaign 2014–16. The solid line is the predictions of Snodgrass et al. (2013). Figure taken from Snodgrass et al. (2017).

1.6 Comet evolution

The evolution of a comet's nucleus can be divided into four periods: the pre-cometary phase, the accretion phase, the cold storage phase and the active phase (Meech, 1999).

1. Pre-cometary phase. Interstellar material undergoes significant change in the protostellar clouds from irradiation by cosmic rays. This creates both non-volatile material and highly reactive radicals, which will then potentially be incorporated into comets. This prompts the fundamental question of how much of this primordial material remains in the nucleus after formation (Mumma et al., 1993).

2. Accretion phase. Water-ice is the main constituent of the nucleus however it remains unclear whether this ice is in an amorphous or crystalline form. When water ice condenses at temperatures below 100 K, it does not have sufficient energy to form regular crystalline structure. As the ice condenses it can trap gases within in it (Laufer et al., 1987). The amount of gas that can be trapped is strongly correlated with condensation temperature. More gases can be trapped at lower temperatures because the molecules will have longer residence times in the ice and are therefore more likely to have the pores in the ice sealed before they can escape. Oort cloud comets and other LPCs will have predominantly formed where

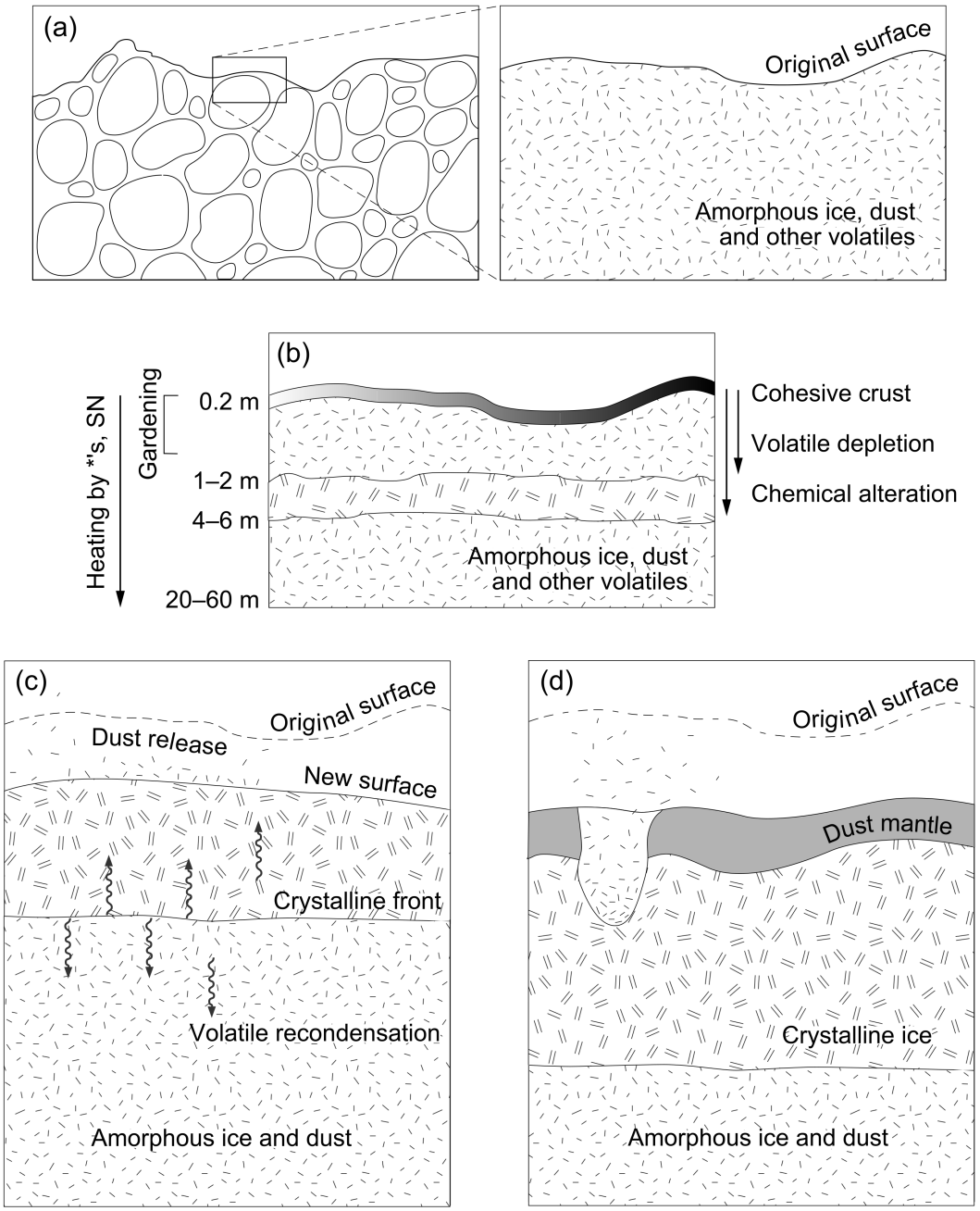

Figure 1.6 Diagram showing the sequence of ageing processes in the upper layers of comet nucleus from (a) the pristine state, (b) alterations it undergoes while stored in the Oort cloud, (c) the changes in surface during active phase and (d) near the end of its lifetime as a dust mantle builds up. Reproduced from Meech and Svoreň (2004).

nebular temperatures may have been between 60 and 100 K. Kuiper belt objects (KBOs) and SPCs formed at temperatures below 30–50 K. This temperature difference is expected to have significant impact on the chemical composition of the comet (Meech and Svoreň, 2004).

3. Cold storage phase Comets may be stored for billions of years in the Oort cloud or the Kuiper belt before passing close to the Sun and entering the active phase. Even during this phase the comets will still be subject to ageing effects. Cosmic rays can bombard the nucleus creating a cohesive crust by depleting the volatiles from and chemically altering the first few metres of the surface.

4. Active phase The active phase is where the majority of the surface and interior evolution of the comet occurs. On its first pass through the Solar System, the surface of the comet will be depleted of volatiles by sublimation. Below this layer, removed in the first passage, will be a layer of pristine amorphous ice. This exposed ice is thought to be the surface of DNCs. Solar insolation will cause the crystallisation of the amorphous ice from the surface inward. Dust redeposition is an important process in cometary evolution discovered by Rosetta. Some of the ejected material falls back onto the comet creating a dust mantle, seen in older periodic comets. This leaves a mystery as to how subsurface sublimation through a porous layer and loss of that layer can be linked. Conduction must play an important role since the lack of abundant water ice on the surfaces of comets suggests that the sublimation comes from below the surface. Figure 1.6 summarises the stages of cometary evolution.

1.7 Activity

In order to understand the extent of the pristine nature of comets, we must first understand the mechanisms that affect their surfaces and comae – in other words, their activity. Activity varies from comet-to-comet so we must try to distinguish whether these differences in activity are because of ageing or reflect primordial differences. Ageing refers to effects that have chemically or physically altered the nucleus since its formation and may cause a change in the activity. Signs of ageing include (1) production of comae and tails, caused by escaping gas and dust lifted off the surface of the comet; (2) non-gravitational effects in the comet's motion, caused by jets of sublimating gas; (3) outbursts, these impulsive increases in mass-loss rate eject material into the coma, causing an

immediate and rapid brightening in telescopic observation; (4) changes in the volatile composition of escaping gases and internal physical nucleus properties; (5) progressive change in cometary brightness; (6) change of physical appearance to that of asteroids, becoming dormant comets, or (7) total disappearance of the nuclei. All processes that physically and chemically alter a cometary nucleus can be regarded as ageing. The ageing processes are too slow and irregular to be detected during a single apparition (Kresák, 1985). It is when comets are observed over a number of Solar System returns that changes will become observable. Because of this, the evolution of comets is best studied on a statistical basis, across multiple apparitions.

1.7.1 Drivers of activity

Activity is driven by solar insolation initiating sublimation of volatile materials. By mass, water is the dominant volatile, these interact with other volatiles like CO_2 to produce the gas emission we see. The temperature at which this begins is dependent on two factors: the latent heat of sublimation of the volatiles and the equilibrium surface temperature of the nucleus. The surface temperature is dependent on heliocentric distance, albedo, surface emissivity, rotation rate, pole direction and thermal diffusivity. A summary of the different processes that drive activity, their heliocentric distances and temperatures is found in Table 1.1.

Water-ice

The main driver of comet activity in the inner Solar System ($r \leq 3$ au) is sublimation of water-ice. Water activity can also come from icy grains that have been ejected in to the coma, which is dependent on the sublimation of other volatiles such as CO_2 or CO (Protopapa et al., 2018). Comets are active far the beyond the water line at $r = 5$ au. There is a distinct change at $r = 4$–6 au but activity does not drop below zero. Meech and Svoreň (2004) solve an energy balance equation and show sublimating water-ice can lift small grains off the surface at distances of $r = 5$–6 au. All-sky surveys find that comets remain active out to large distances post-perihelion, beyond the point where water-ice sublimation can drive this activity. Activity beyond this distance needs to be explained via other mechanisms. It could be sublimation of ices more volatile than water such as CO and CO_2 or it could be crystallisation of water ice ($r < 11$ au). Meech

Table 1.1 Heliocentric distances and temperature onset of various drivers of activity. Reproduced from Meech and Svoreň (2004)

Temp. (K)	Process	r (au)
5	H_2 sublimation	> 3000
22	N_2 sublimation	160
25	CO sublimation	120
31	CH_4 sublimation	80
35–80	High-density amorphous ice anneals	60–10
38–68	High-density $\rightarrow$ low-density amorphous ice	55–15
44	C_2H_6 sublimation	40
57	C_2H_2, H_2S sublimation	24
64	H_2CO sublimation	20
78	NH_3 sublimation	14
80	CO_2 sublimation, low-density amorphous anneal	13
91	CH_3CN sublimation	9
95	HCN sublimation	8
99	CH_3OH sublimation	8
70–120	Low-density amorphous ice anneals	< 18
90–160	Amorphous to crystalline ice phase change	< 11
180	Crystalline ice sublimation	< 11

and Svoreň (2004) argued that distant ($r \geq 7$ au) activity in comets is driven by water-ice undergoing amorphous to crystalline phase changes and releasing of gas (annealing) in water-ice, rather than sublimation of highly volatile materials on the surface. Meech et al. (2009), based on observations of activity in DNCs, propose that activity inbound of a DNC beyond 11 au can only be explained by the annealing of amorphous water ice. Between the ranges of 7–11 au, they suggest activity is driven by a combination of annealing and amorphous-crystalline phase transition. However, the comets C/2017 K2 (Jewitt et al., 2017) and C/2014 UN271 (Farnham et al., 2021) were observed to be active at 23 au, far below the temperature range required for crystallisation to occur. There is considerable debate as to the contribution of amorphous ice to cometary activity (Prialnik and Jewitt, 2022).

CO

CO is one of the most abundant volatiles in comets, although it varies widely from comet to comet. C/2014 Q2 has some of the lowest CO abundances with a CO production rate of 2 per cent with respect to water (de Val-Borro et al., 2017), while on the other hand, the interstellar comet 2I/Borisov had one of the

highest abundances of CO ever detected in a comet of 35–105 per cent (Cordiner et al., 2020). CO rich comets typically have CO/H_2O abundances greater than 8 per cent (Dello Russo et al., 2016), with some having abundances substantially higher, e.g. C/2006 W3 has an abundance in excess of 220 per cent (Bockelée-Morvan et al., 2010). CO is one of the most active volatiles on a comet and can lift dust off of the surface at heliocentric distances as far out as 20 au. Some comets' activity are still dominated by CO even at H_2O sublimating distances, e.g. C/2009 P1 had gas dominated by CO near Sun ($r < 1.5$ au) 5–25 per cent with respect to water (Gicquel et al., 2015). JFCs are typically depleted in CO (< 3 per cent) implying their stores of CO have been fully sublimated away by prolonged exposure to the temperatures in the inner Solar System (Biver et al., 2022).

Jewitt et al. (2021) observed activity in the comet C/2017 K2 at distances of $9 < r < 16$ au and predicted the activity could have begun at distances as far as 35 au. They suggest the activity is driven by sublimation of a super-volatile, such as CO, and that surface temperatures are insufficient for ice crystallisation to be a driver of activity. They argue the ice could still be present and cause a surge of activity at smaller heliocentric distances as the heat travels through the interior. Distant activity post-perihelion can be driven by slow conduction of heat to the interior of the comet or thermal lag, driving activity and outbursts at large distance (Prialnik and Bar-Nun, 1992). Recent pre-perihelion observations of comets show activity at large distances (e.g. Farnham et al., 2021; Jewitt et al., 2021) in which heat transfer cannot be involved and therefore must be driven by some other mechanism such as super-volatile sublimation. Bouziani and Jewitt (2022) modelled the activity of C/2017 K2 and predicted the activity could even occur at very large distances of 150 au. They say free sublimation of super-volatiles is the obvious explanation but is unsatisfactory and suggest that activity is caused by a build-up of pressure due to trapped CO under a dust mantle.

CO_2

Another abundant driver of activity in distant comets is CO_2. It is very difficult to directly observe from the ground and is instead inferred from CO observations made in UV by spacecraft, or O in optical wavelengths. Abundances range from 5–30 per cent with no clear distribution between dynamical ages. It is a major

contributor to activity at $r > 2.5$ au, and can even dominate close to perihelion, e.g. 103P. Strong seasonal effects of CO_2 production were seen in 67P (Bockelée-Morvan et al., 2015; Fink et al., 2016; Hässig et al., 2015).

Studying these drivers of activity or their daughter products will help us understand the underlying mechanisms of activity.

1.7.2 Observing activity

Activity can be tracked in a variety of ways, the easiest of which is observing dust production in the coma and tail. We can study the activity in a quantitative way through broadband photometry of the reflected sunlight, as flux is proportional to the reflecting area of the dust lifted off the comet, and therefore total mass in the coma, and the production rate of dust needed to sustain it. Narrowband photometry can be used to trace the gas production via observations of the specific bandpass of gas fluorescence. Both gas and dust production can be used to constrain the activity levels of a comet.

Gas production

Gas production can be inferred from observations of radicals in the coma such as OH, NH, CH, CN, C_2, C_3 or NH_2, which can be observed at optical wavelengths by the detection of their electronic transition emissions lines. OH is the primary dissociation product of H_2O, which is a dominant volatile in comets and provides a good proxy for total outgassing of comets. The secondary species are produced by the photolysis of their parent species.

The total production rate of a particular species can be determined from the measurement of the total flux from the entire coma measured in a given line or band. If the mean lifetime of the molecule is τ then the coma will contain N molecules of this species at any given time such that:

$$N = Q\tau \tag{1.3}$$

where Q is the production rate of the species. The excitation of the lines is due to resonance fluorescence, so the luminosity of any line or band is proportional to the total number of molecules in the coma and the fluorescence efficiency called

the 'g-factor'. The g-factor represents the probability of scattering a photon per unit time per molecule. The luminosity at wavelength λ is therefore given by:

$$L = gN = gQ\tau \tag{1.4}$$

By expressing the luminosity in terms of the flux F and geocentric distance Δ and rearranging, the production rate is given by:

$$Q = \frac{4\pi\Delta^2 F}{g\tau} \tag{1.5}$$

The production rate can be calculated provided g, τ and F are known. The g-factor has been calculated for many molecules and is available in the literature (e.g. A'Hearn et al., 1995). The lifetime τ cannot directly be inferred from observation. Instead production rates must be derived from the observable column density:

$$N = \frac{4\pi\Delta^2 F}{g} \tag{1.6}$$

From the radial distribution of the gas species in the coma, direct information about their production and destruction mechanisms can be obtained by fitting the radial intensity profiles of gaseous species to a photolytic model. The most commonly used photolytic models are the Haser model (Haser, 1957) and the vectorial model of Festou (1981). The fitting parameters for the Haser model are the scale lengths of the parent and daughter species. The Haser model assumes a simplistic isotropic radial outflow of parent and daughter molecules. The vectorial model is more sophisticated and takes into account the isotropic emission of the daughter species from the parent molecules. The parameters are the lifetimes and velocities of the parent and daughter species. The gas production rates are then determined by comparing the absolute values of the column densities calculated with the model to those derived from observed fluxes.

Dust production

Dust production rate can be determined from the measurement of the $Af\rho$ parameter, the derivation of which is discussed in Section 2.1.4. According to Weaver et al. (1999), the $Af\rho$ parameter can be directly related to the dust mass production rate through:

$$Q = \frac{0.67adv}{A_{\mathrm{P}}} Af\rho \tag{1.7}$$

where Q is the dust mass production rate in kg s^{-1}, a is the average particle radius in μm, d is the particle density in g cm^{-3}, $A_{\rm P}$ is the geometric albedo, v is the outflow velocity of dust grains in km s^{-1}, and $Af\rho$ is the aperture independent measure of dust production rate in m. However, for the vast majority of published literature, and the rest of this thesis, when we refer to dust production we are referring to the quantity $Af\rho$.

Dust is generally favoured as a measurement of activity due to its relative ease of observation compared to gas. However, the presence of a coma or tail does not necessarily imply ongoing activity. Large grains (mm or larger) move away from the nucleus on time-scales of weeks or months due to the fact they are accelerated by solar radiation pressure to a lesser extent than compared to micron sized grains. These large grains can remain visible even when activity is not continuing. Collisions can also create large ejection of dust which create a temporary coma which can be mistaken for activity caused by sublimation. Definitive signs of activity come from observing long-term changes in brightness that cannot be accounted for otherwise. We can compare activity between comets by comparing the variation of their production rates with respect to heliocentric distance r. The easiest way to do this is to measure the gradient, or slope as I will refer to it throughout this thesis, of the $\log Af\rho$ vs. $\log r$ line. The slopes are usually split into pre- and post-perihelion as activity levels tend to vary in a noticeably different way before and after perihelion.

Specific observations that will help distinguish primordial and ageing effects include: (1) searching for activity in very distant comets, such as Centaurs and KBOs. These will significantly enhance our understanding of the drivers of activity. (2) Discovery of comae in KBOs, which will have implications for volatile condensation in the early solar system. Activity in very distant comets, which never come close to the Sun, will create some interesting new ideas and constraints with respect to the condensation and preservation of volatiles in the outer solar nebula. (3) Systematic statistical studies of large numbers of comets to determine and better understand the distinguishing factors between evolutionary and primordial features.

1.7.3 Statistical studies of comets

Several studies have been undertaken into large-scale statistical analysis of comets, mainly focusing on gas activity.

A'Hearn et al. (1995) observed a sample of 85 comets over a period of 17 years. They found that most comets are similar to each other in composition and that the dust-to-gas ratio and coma composition does not vary with dynamical age, however dust and gas production vary significantly from comet to comet. For comets they monitored over multiple orbits, they observed that there was little variation in dust and gas production from one apparition to the next for SPCs. SPCs also displayed steep production rate slopes which the authors suggest is due to the small active fraction of the surface.

A'Hearn et al. (1995) concluded:

1. Comets are uniform when it comes to gas species sampled in their survey (i.e. CN, OH, C_2, C_3, NH).

2. On average, individual comets do not have systematic trends in composition or dust-to-gas ratios with respect to r. Dust-to-gas ratios of the overall comet population generally increased with $r^{0.5}$.

3. On the whole, dust-to-gas ratio was strongly correlated with perihelion distance q. A theory prompted to explain the low dust-to-gas ratios at low q is that older comets have thicker crusts which means gas escapes through pores in the surface and cannot entrap dust, whereas a freely vaporising surface will lift lots of dust. They also note that excess water vaporisation may lead to lower dust-to-gas ratios at higher r.

4. Some comets had variation in abundances of trace species relative to OH, but ratios such as C_2/CN remained constant across the whole population.

5. Comet production of gas and dust was essentially unchanged from orbit-to-orbit, with the exception of external factors such as nuclear breakup.

6. The distribution of active surface area peaked below 1 km^2 which implies the existence of many low activity comets. Dust-to-gas ratio was unaffected by the size of the active area.

7. There was a distinct class of comets with depleted C_2 and C_3. These were nearly all JFCs, but not all the JFCs were carbon depleted.

8. CN, C_2 and C_3 were related to each other much more strongly than OH or NH.

9. JFCs had smaller effective vaporisation areas.

10. JFCs had steeper slopes and larger asymmetries about perihelion than other comets.

11. DNCs had very shallow production rates inbound to perihelion.

12. A halo of H_2O grains was present around DNCs.

Conclusion 5 implies comet nuclei are homogeneous below the surface and the formation materials are unchanged. Conclusions 1 and 3 imply volatile distribution was uniform in the early Solar System.

Fink (2009) conducted a survey of 92 comets over 19 years. They saw that comets display relatively uniform composition.

They describe four classes of comet:

- Typical (70 per cent): showed typical ratios of C_2, NH_2 and CN with respect to H_2O
- Tempel 1 type (20 per cent): depleted in C_2 but not NH_2
- GZ type (6 per cent): deficient in both C_2 and NH_2
- Yanaka: no detectable C_2 or CN

The comets in their survey did not show significant variation in production rates over their observation period. Fragmented comets showed no difference in composition before or after breakup, implying a homogeneous nucleus. Fink (2009) suggested HTCs and hence all Oort cloud comets have different composition to other SPCs; they are C_2 rich and have enhanced C_2/CN ratios. Depleted C_2 comets had higher $Af\rho$ ratios compared to the rest of the survey.

Like A'Hearn et al. (1995), they found $Af\rho/H_2O$ is proportional to q. The $Af\rho$ was linked to the age of the comet. 2P had lowest $Af\rho$ since it was dynamically the oldest comet, whilst Hale–Bopp, a DNC, had the highest $Af\rho/H_2O$. This was caused by loss of fine grain, highly reflective material over many perihelion passages. They suggested C_2 production is inversely proportional to q but CN and NH_2 are not correlated with q.

Langland-Shula and Smith (2011) also saw a carbon depleted subclass of comets in their spectroscopic comet survey, most notably a subset of JFCs observed at

$r > 1.5$ au. They found that $Af\rho$ was not independent of aperture size, except in the dustiest of comets. High dust-to-gas ratios were also observed in comets with large perihelion distances, which suggests dust is released earlier in the coma formation than the gas, contrary to the assumption that comets with smaller perihelion distances are more evolved. The dust-to-gas ratio was found to be evolutionarily independent in comet dynamical families, meaning there was no correlation between dust-to-gas ratio and dynamical type.

The assumptions about dust-to-gas ratios in different dynamical families of comets are:

- Low dust-to-gas ratio (i.e. more gas): it is interpreted that DNCs have more volatiles readily available on their surfaces so sublimate these gases quickly as they pass through perihelion.
- High dust-to-gas ratio (i.e. more dust): as the comets evolve it builds up a dusty crust. This dust is loosely bound to the surface and is lifted up by gas sublimation. Hence older JFCs should have high dust-to-gas ratios.

A population of JFCs with small q were seen to have low dust-to-gas ratios, which challenges the assumption that dynamically older comet have high dust-to-gas ratios. A'Hearn et al. (1995) explained this with the assumption that the loosely bound dust has already been blown away earlier in the comet's lifetime, leaving behind only tightly bound dust; and the fact that sublimation occurs deeper in the comet's interior and therefore not as much dust is lifted off the surface. Both factors decrease the dust production and hence decrease the dust-to-gas ratio.

Cochran et al. (2012) made similar conclusions in their study: the majority of comets were compositionally similar, 9 per cent of their comet population were carbon depleted, there was no depletion in HTCs, and there was no difference in composition with respect to r.

1.8 Light curves

The easiest way to see how the dust activity of a comet changes over time is by plotting a light curve, the brightness of the comet against time or heliocentric distance.

The works of Kamel (1992) and Ferrín (2010) collates photometric light curves for a large variety of comets of different ages and types. Kamel (1992) simply presents the light curves with no interpretation or discussion so is not much more than a useful reference. Ferrín (2010), while impressive in its scope, contains an over-reliance on amateur data and an over interpretation of said data. While an overall pattern in activity is seen in the data, including reasonable estimates for turn on and turn off points in cometary activity, the noisy data makes it difficult to establish a good fit for the light curve. A large scale population study of comets in the same vein, but using professional data, would be more helpful in accurately constraining cometary activity across different populations. Archival searches for comets observed under similar circumstances to data taken with present-day surveys, would also benefit the study of comet behaviour.

Distinguishing the effects of ageing from primordial differences is important since the wide range of formation scenarios should imply significantly different observational qualities such as different volatile and gas abundances. For example, comets formed in the Jupiter–Saturn region are depleted in organic volatiles (Mumma and Charnley, 2011), and being depleted in C_2 is thought to be due to formation in the Kuiper belt and not necessarily due to ageing; more aged comets display higher C_2/CN ratios (Fink, 2009). Signs of ageing include: (1) secular fading due to the build up of a dust mantle or depletion of volatiles, (2) more uniform activity in newer comets due to larger active area, and (3) higher frequency of jets and outbursts on older comets with dust mantle. Once the differences between ageing and primordial effects are established, it will allow us to use the comets as time capsules of the chemical and physical conditions in the early Solar System.

1.9 Thesis outline

For this thesis, I developed a data analysis pipeline to consistently calibrate the photometry of comets from ground-based telescope images. The development, testing and methodology of this pipeline are described in detail in Chapter 2, as well as a discussion of its strengths and limitations.

In Chapter 3, I apply this calibration pipeline to ground-based telescope data of 67P/Churyumov–Gerasimenko. I describe the overall activity trends of 67P and search the data set for any small-scale variations in brightness that I could correlate to events seen on the comet's surface by Rosetta. I detect an outburst

in my data with a brightness that puts it in line with an outburst observed in situ by Rosetta; however, directly linking these two events remains challenging. The results of this work are published in Gardener et al. (2022).

In Chapter 4, I apply my pipeline to a wider survey of 14 comets observed with the TRAPPIST telescopes and I describe the different ways the dust activity can be used to distinguish different dynamical classes of comets. I also investigate the relationship between coma colour and heliocentric distance, and suggest the relationship to gas production.

In Chapter 5, I compare my broadband dust activity measurements to narrowband gas production rates published in the literature. I describe the relationships between dust and gas production, as well as the relationships between coma colour and gas production. This chapter describes a strong correlation between dust production and water production rates measured by SOHO/SWAN.

Finally, in Chapter 6 I summarise my results and use them to evaluate the insights into comet activity that can be gained from ground-based broadband observations of comets. I also discuss the advantages and disadvantages of broadband observations in comparison to other methods such as narrowband photometry and direct observations with space missions. I conclude my thesis by presenting directions for future comet research, with a focus on LSST and Comet Interceptor.

Chapter 2

Methodology

2.1 Solar System photometry

2.1.1 Coordinate system

In cometary science, it is common to express the position of a comet with respect to the Earth and the Sun. The five parameters used to define a comet's position are: (1) the object's distance from the Sun, or heliocentric distance r; (2) the object's distance from Earth, or geocentric distance Δ; (3) the phase angle α, (4) the solar elongation ϵ and (5) the orbital inclination i.

The line drawn from the Sun to the Earth to the object (S-E-O) subtends an angle called the solar elongation ϵ (Figure 2.1). It is the apparent angular distance in the sky between the Sun and a comet. ϵ can be derived from the on-sky coordinates of the Sun and object:

$$\epsilon = \cos^{-1}(\sin \mathrm{Dec}_{\odot} \sin \mathrm{Dec}_{\mathrm{obj}} + \cos \mathrm{Dec}_{\odot} \cos \mathrm{Dec}_{\mathrm{obj}} \cos \Delta\mathrm{RA}) \qquad (2.1)$$

where ΔRA is the difference in right ascension between the Sun and object.

The angle subtended by the line from the Earth to the object to the Sun (E-O-S) is called the phase angle α. An object is at opposition when $\alpha = 0°$ and $\epsilon = 180°$, this means the object is directly opposite the Sun from the point of view of the Earth and would appear fully illuminated. At $\alpha = 180°$ the object is directly

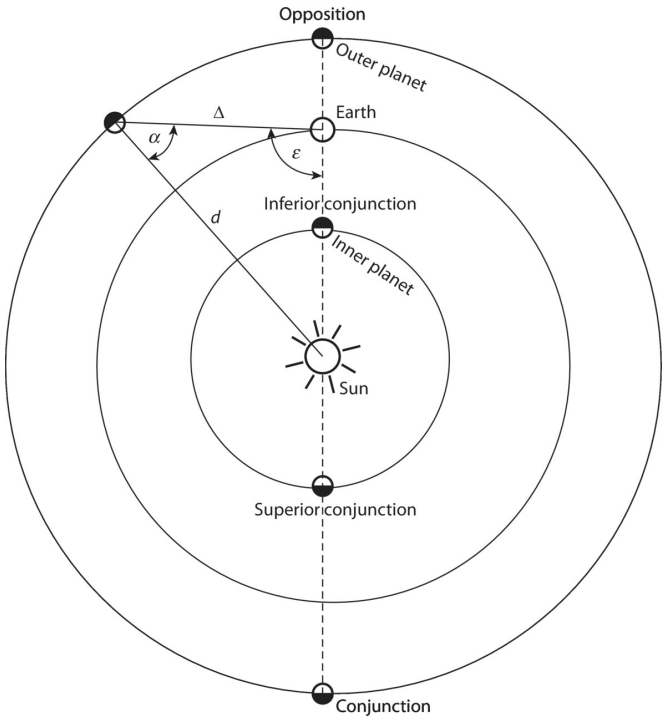

Figure 2.1 Diagram of solar system illustrating the different parameters we can measure for a planetary body. This diagram is for planets, but the same principles apply to comets. In this figure heliocentric distance is denoted with d, in the text I use r to refer to this distance. Reproduced from Shepard (2017)

between the Earth and the Sun, an inferior conjunction. The phase angle can be calculated using the object's geocentric and heliocentric distances in au:

$$\alpha = \cos^{-1}\left(\frac{r^2 + \Delta^2 - 1}{2r\Delta}\right) \tag{2.2}$$

Due to their highly eccentric orbits, most comets are observed between phase angles of 0–110°.

2.1.2 Time

Observations of cometary phenomena take place over timescales of months, days, hours or even minutes. Some things such as rotation period can be accurately measured to the nearest second. As such we need a consistent temporal scale on which to plot these events. The standard Gregorian calendar system used in everyday life is not well suited for astronomical applications. Variable month lengths, leap years, leap seconds, and other quirks of the system make calculating

the exact time interval between two events awkward and prone to mistakes. To avoid this complexity, astronomers use the Julian Date (JD), which is defined as the number of solar days since noon (UTC) on 4713 BC January 1 in the Julian calendar. JDs are fractional which makes calculating the difference between two JDs simple and it is easy to convert to hours, minutes or seconds as required. JDs are often truncated to the Modified Julian Date (MJD), which removes the largely redundant first two digits and sets midnight as the start of the day: MJD=JD$-2\,400\,000.5$.

2.1.3 Magnitudes

The brightness of astronomical objects is measured on the magnitude scale. Magnitude is defined as:

$$m = -2.5\log(F) + \mathrm{ZP} \tag{2.3}$$

where F is the flux and ZP is a constant which sets the zero point of the magnitude scale. But how do we determine what the zero point should be? Historically, the A0V star Vega was selected as the zero point of the magnitude scale. Vega was chosen because it is not variable, it is bright over the whole visible spectrum and is not reddened by interstellar dust. But in the modern day, Vega is too bright to be observed with our sensitive instrumentation, so it is not possible to directly place observed photometry onto the Vega system. The AB system does not use a physical standard source, but instead a hypothetical source of constant frequency flux density. Zero magnitude in this systems corresponds to the flux density f_ν of Vega at the effective wavelength of the Johnson V-band (~ 5500Å). The zero point corresponding to this monochromatic flux density is -48.60, where the f_ν is measured in erg s^{-1} cm^{-2} Hz^{-1}, or 8.90 where f_ν is measured in janskys.

Thanks to historical convention inherited from the ancient Greeks, magnitudes are on a reverse scale where the brighter the object, the smaller the magnitudes. I will not go into the reasoning behind this, a full detailed discussion on the history of the derivation of the magnitude scale can be found in Shepard (2017).

It is necessary to distinguish between several different kinds of magnitudes: apparent, reduced and absolute. The apparent magnitude is the magnitude determined from comparing the flux measured at the telescope to that of standard

stars. This is dependent on multiple factors such as heliocentric and geocentric distance and viewing angles. In order to account for these factors we can define the reduced magnitude. The apparent magnitude can be converted to reduced magnitude by dividing the flux by Δ^2. $m(1, r, \alpha) = m(\Delta, r) - 5 \log \Delta$. Further linearisation of the light curve can be performed by removing the $1/r^2$ dependence: $m(1, 1, \alpha) = m(\Delta, r) - 5 \log \Delta - 5 \log r$. This reduced magnitude is now only dependent on phase angle α.

In planetary science, the absolute magnitude is the magnitude we would see if the body were observed at a theoretical distance of 1 au from the Sun, 1 au from Earth and at a phase angle of $\alpha = 0°$.

2.1.4 $Af\rho$

A'Hearn et al. (1984) defined the widely used $Af\rho$ parameter, which can be used as measure of dust production in comets. In theory, it allows us to compare dust measurements taken at different times, under different circumstances and in different fields of view (FOV). $Af\rho$ is defined as the product of grain albedo A, filling factor of grains within the FOV f and the linear radius of the FOV at the comet ρ. Filling factor f is defined as the ratio of total cross section of grains within the FOV, $N(\rho)\sigma$, and the area of the FOV, $\pi\rho^2$:

$$f = \frac{N\sigma}{\pi\rho^2} \tag{2.4}$$

where σ is the cross-section of a grain, N is the number of particles within the aperture and ρ is the radius of the aperture.

A'Hearn et al. (1984) defines the albedo A as the ratio of total light reflected by cometary particles, $L_{\text{comet}} = 4\pi\Delta^2 F_{\text{comet}}$ to total light absorbed and scattered by cometary particles $F_\odot N\sigma/r^2$:

$$A = \frac{(2\Delta r)^2 \pi F_{\text{comet}}}{N\sigma F_\odot} \tag{2.5}$$

where Δ is the geocentric distance to the comet, r is the heliocentric distance to the comet in au, $F_\odot$ is the solar flux at 1 au and F_{comet} is the observed cometary flux. Albedo here is not to be confused with Bond albedo or geometric albedo.

The albedo A'Hearn et al. (1984) define is a factor of four larger than the geometric albedo, $A_{\mathrm{P}}(\theta)$, defined by Hanner et al. (1981).

While A and f cannot be determined independently, the product Af is an observable quantity:

$$Af = \left(\frac{2\Delta r}{\rho}\right)^2 \frac{F_{\mathrm{comet}}}{F_{\odot}} \tag{2.6}$$

Assuming a spherically symmetric coma and a constant expansion rate of dust grains, f decreases as $1/\rho$ and therefore $Af\rho$ should be independent of aperture size. This therefore creates a straightforward measure of dust production rates and allows for comparison between comets observed under different circumstances, such as instrument effects, image scale and aperture size. $Af\rho$ is usually expressed in units of cm.

Fink and Rubin (2012) discussed some of the shortcomings of $Af\rho$. It requires spherical symmetry of coma with no production or destruction of the dust after it leaves the nucleus and a constant outflow velocity of the dust. These assumptions break down below 20 km where the dust is still coupled to the gas and dust has not reached its terminal velocity. The assumptions are also invalid beyond 10^5 km where the coma is pushed by solar radiation pressure and becomes a tail. The model is not appropriate for receding comets at large heliocentric distances where dust may be comprised of leftover particles that have long residence times in the coma. These assumptions also fail if the coma is asymmetric or has strong jet activity. Fink and Rubin (2012) argued the definition of 'albedo' A defined by A'Hearn et al. (1984) is problematic and should instead be replaced by $q_{\mathrm{sca}}(\lambda)p(g)$, the scattering efficiency of a particle multiplied by its phase function. They consider the particle size dependent velocity, scattering efficiency and phase function to derive a new $Af\rho$. They found that their new definition of $Af\rho$ produced dust-to-gas ratios that are as reliable as those determined by direct observation of infrared emissions of the dust coma, which surprised them since it was assumed that realistic mass loss rates cannot be determined from the visible spectral range. Despite this, the simplicity and straightforward nature of the original $Af\rho$ parameter defined by A'Hearn et al. (1984) means that it is almost universally used today as a measure of comet activity, even if the physical interpretation is simplified and unrealistic.

2.1.5 Phase functions

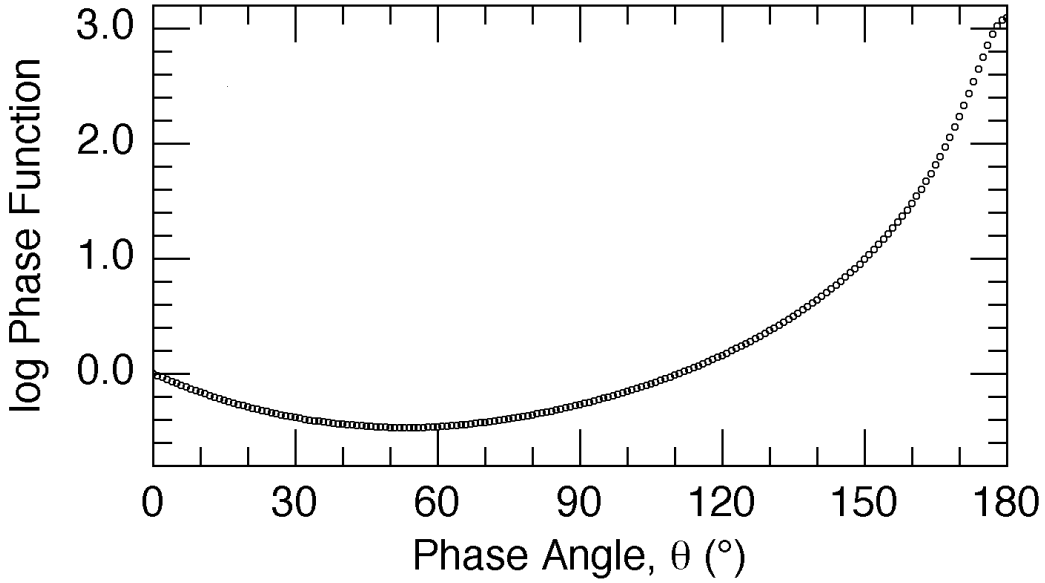

Figure 2.2 Composite dust phase function for comets. Reproduced from Schleicher (2010)

As previously mentioned, the brightness of a comet is dependent on the phase angle α. For a typical planetary body, as the phase angle increases the reduced magnitude increases as less of the observed surface is illuminated by the Sun. But for comets, the diffuse nature of the dust coma means that light is reflected and scattered in a different way than from regular solid planetary bodies. There is a strong increase in the forward direction of scattering, and a much smaller peak at small back scattering angles. Across typical viewing angles of comets ($\alpha = 0$–$110°$), the phase effect varies by up to a factor of three. To compare measurements of dust flux or $Af\rho$ taken at different phase angles, a normalisation needs to applied to adjust for phase angle effects. The scattering of the dust is dependent on properties of dust grains, such as size distribution, roughness and albedo, but measured to first order, the phase angle effects are similar across all comets. As such a single dust phase function can be derived that describes the phase angle correction that needs to be applied to dust measurements. The widely used composite dust phase function derived by Schleicher (2010) (Figure 2.2) is the phase function I have used in my analysis to convert my measurements $A(\theta)f\rho$ to $A(0°)f\rho$. This curve is a composite of two phase function curves, one derived from Halley photometry measured at smaller phase angles (Schleicher et al., 1998), and the second curve fits a Henyey–Greenstein function to mid- and large-phase angle

data sets (Marcus, 2007). A dust phase function of 67P was measured in situ by Rosetta and was found to be consistent with other phase functions found in the literature (Bertini et al., 2017).

2.1.6 Colour and photometric systems

A photometric system is a standardized set of well-characterised colour filters and reference stars that allow astronomers using different telescopes to directly compare their measurements. There are too many different systems to detail all of them, but I will go into two systems that are directly relevant to my thesis.

The *UBVRI* system is the the oldest and one of the most widely used photometric systems in astronomy. It is also named the Johnson–Cousins or Bessell system after its creators (Bessell, 1979; Johnson and Morgan, 1953). An alternative and increasingly common photometric system in recent years is the *ugriz* system, developed for use in the Sloan Digital Sky Survey (SDSS) (Gunn et al., 1998). Many modern observatories and surveys are increasingly using these filters. Other surveys, such as Pan-STARRS and ATLAS used their own versions of the *ugriz* filters (Tonry et al., 2012; Tonry et al., 2018). These surveys are used as the basis for my calibration to give absolute flux values for comets. Using survey stars allows us to link the magnitudes back to a fundamental standard that is well understood.

Colour, or colour index, is the difference in magnitude between two filters, e.g. $B - V$. Objects that emit more blue light will have smaller magnitudes in the B-band than the V-band, so their colour index will be negative, and vice versa for objects that emit more red light.

As previously discussed, gas production can be inferred from observations of secondary species which have emission lines within optical wavelengths. Specialised filters were developed for the specific observations of these emission lines (Figure 2.3). This however does present a problem when trying to determine dust production rate, as the emission lines of these radicals contaminate the broadband spectrum of the dust (Figure 2.4). Separating the contribution of gas from broadband filter is near impossible. Gas contamination depends on dust-to-gas ratios, comets with high dust-to-gas ratio have minimal contamination in R or I-bands (Meech and Svoreň, 2004). As such, dust production rates are usually derived from band-passes at the redder end of the visible spectrum. Distance

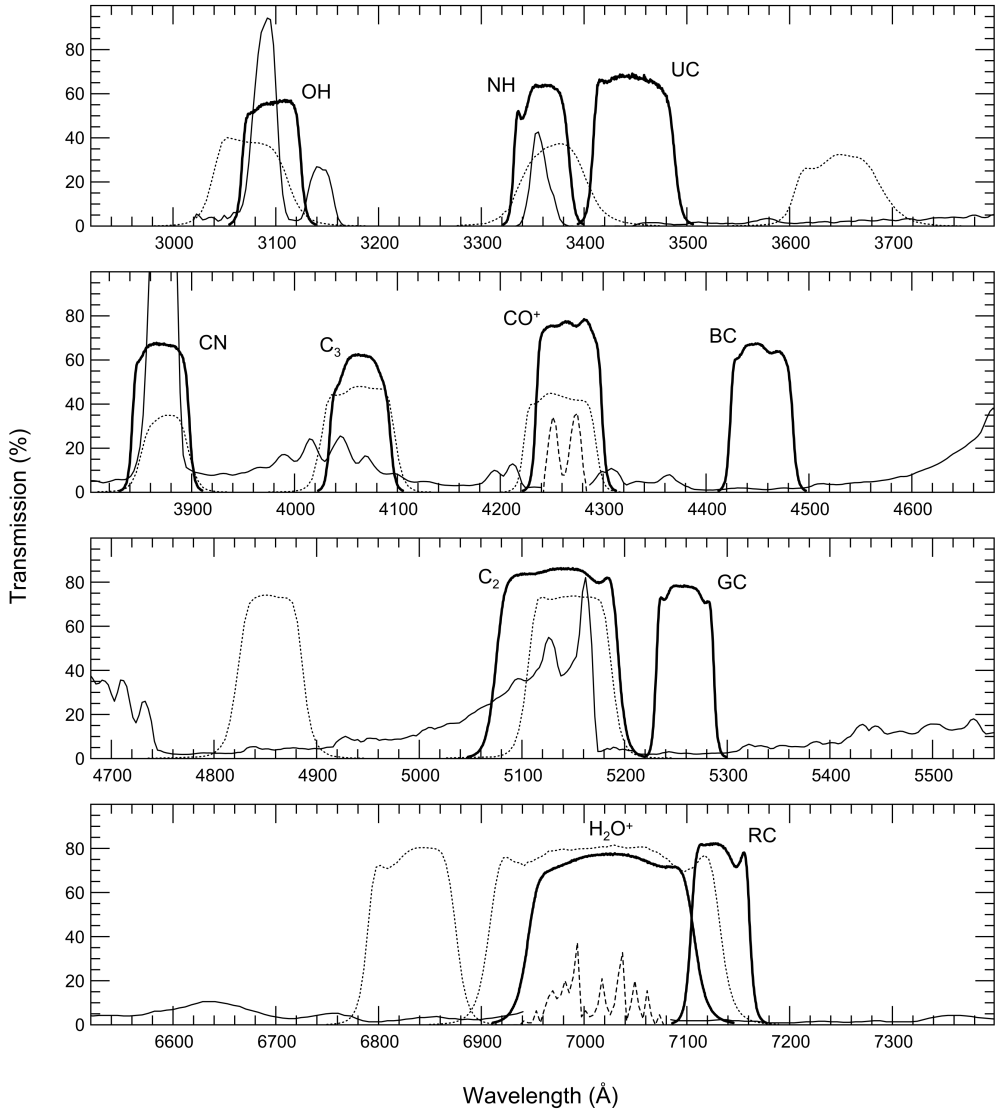

Figure 2.3 Transmission profiles for the HB filters (thick lines) and IHW filters (dotted lines). For comparison, measured comet spectra illustrate the locations of the different emission bands. Reproduced from Schleicher and Farnham (2004).

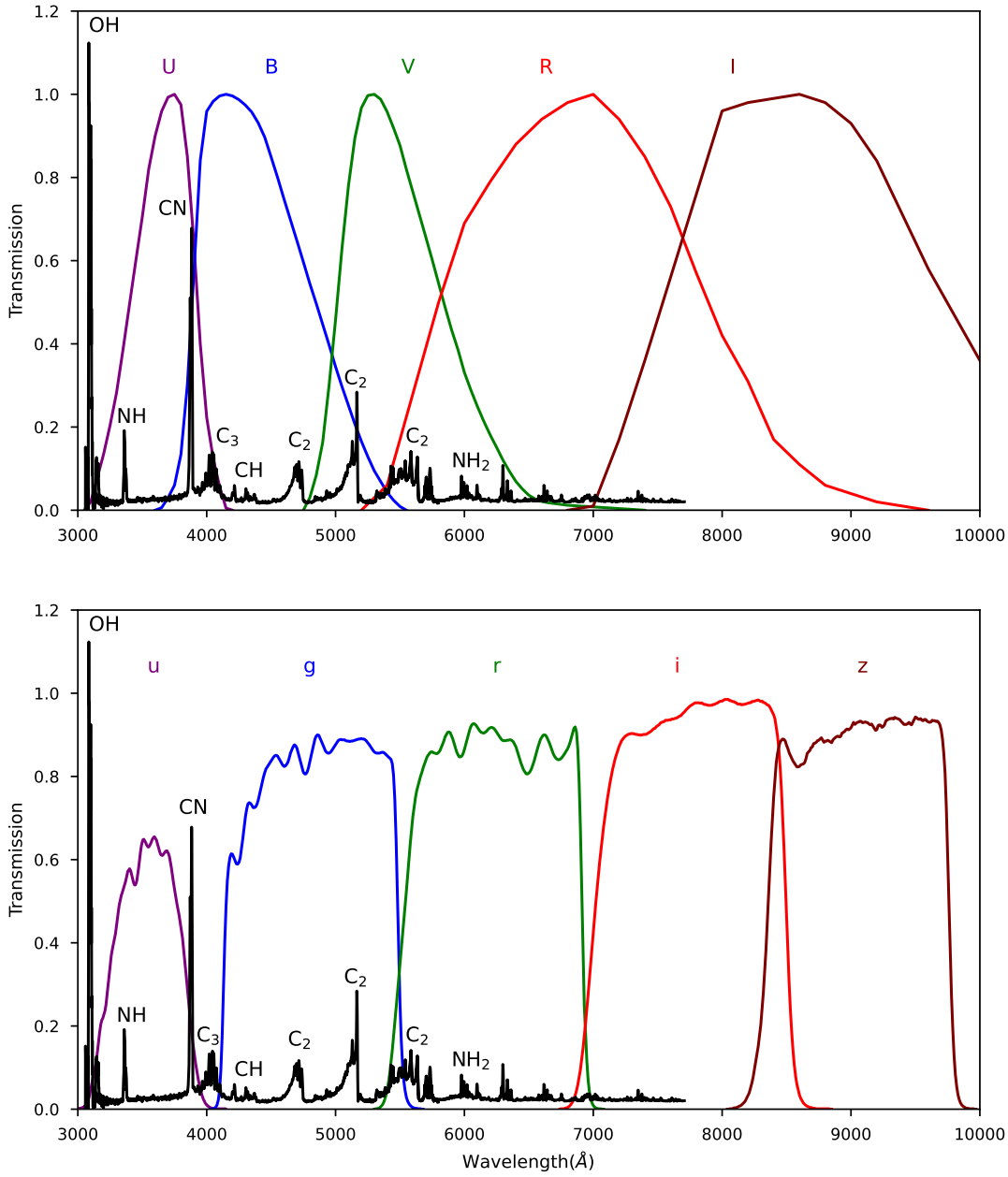

Figure 2.4 Transmission profiles of the (top) Johnson-Cousins U, B, V, R, and I and (bottom) SDSS u, g, r, i and z broadband filters, superimposed on the spectrum of C/2015 ER_{61} (PanSTARRS). Comet spectrum reproduced from Biver et al. (2022).

from the nucleus is also important to consider when accounting for gas contamination. NH_2 drops off rapidly with distance from nucleus whereas CN in the near IR contaminates low dust-to-gas comets at large distances from the nucleus.

The production rate of gas and visual magnitude are closely correlated for comets observed at distances of 0.6–2.8 au (A'Hearn and Millis, 1980; Jorda et al., 1991). CN and C_2 emission lines dominate the visual spectrum so this is unsurprising.

2.1.7 Spectral slope

Measuring the coma in different broadband filters allows us to determine the coma colour. This gives us some very low resolution spectral information and can be used to imply gas production. The colour of the coma corresponds directly to a spectral slope - the gradient of the reflectivity-wavelength curve:

$$S_{\lambda_1,\lambda_2} = \frac{r(\lambda_2) - r(\lambda_1)}{r(\lambda_2) + r(\lambda_1)} \frac{2}{\Delta\lambda} = \frac{\alpha - 1}{\alpha + 1} \frac{2}{\Delta\lambda} \tag{2.7}$$

where $\alpha = 10^{\mathrm{CE}}$ and CE =colour excess, or the difference between coma colour and Solar colour (A'Hearn et al., 1984). $\Delta\lambda = \lambda_1 - \lambda_2$, where λ_1 and λ_2 are the effective wavelengths of the filters. The units of spectral slope are per cent per 100 nm. A positive slope indicates a redder colour and negative slope a bluer colour. This aids inter-comet comparisons.

Throughout this thesis, when calculating spectral slopes, solar colours are taken from Holmberg et al. (2006), and the effective wavelengths of *BVRI* filters taken to be 438, 545, 641 and 798 nm respectively (Bessell, 1990).

2.2 Pipeline methodology

This section will be a detailed methodology of my photometry pipeline which forms the backbone of the analysis in the following two chapters. My data are calibrated through a custom-built pipeline, which incorporates JPL Horizons (Giorgini et al., 1996), Astrometry.net (Lang et al., 2010), SExtractor (Bertin and Arnouts, 1996) and calviacat (Kelley and Lister, 2019). In brief, the steps in the pipeline are:

1. The date from the FITS header is extracted and passed to JPL Horizons to retrieve the ephemeris data of the comet (for my purposes I am interested in position and geocentric distance). The RA and Dec of the target at that date is passed to Astrometry.net.

2. Astrometry of the image is calibrated using Astrometry.net, using the comet RA and Dec as the starting point for its search.

3. SExtractor extracts the instrumental magnitudes of all sources within the field of view using automatic elliptical apertures.

4. The source list is then calibrated by cross-referencing the magnitudes of background stars in the field with a reference catalogue using calviacat.

5. The comet is identified by finding the source with the world coordinate system (WCS) coordinates that most closely match the coordinates from JPL Horizons. Photometry is then measured with a fixed aperture of 10 000 km radius using the geocentric distance from JPL Horizons and appropriate pixel scale from the WCS to calculate the corresponding radius in pixels.

Figure 2.5 shows a flow chart of the steps in the pipeline.

2.2.1 Astrometry.net

Astrometry.net is a calibration software that accurately calibrates the astrometry – the precise positions and motion of celestial bodies in the sky – of a telescopic image. This section will not go into detail as to how the system works as this can be found in Lang et al. (2010), but I will highlight certain aspects of this software that make it ideal for use in my pipeline. As well as providing coordinates for the image it also gives the scale and orientation of the image. This is very useful for calibrating a disparate data set that can have very different conventions and levels of detail in their meta data. The system works blind, working only from the image pixels, meaning it is appropriate to use to solve frames that have no pre-existing astrometry meta data. However, solving blind greatly increases the computation time so I resolve this by feeding it the expected position of the comet at that date and time and using that as the starting point, searching within 1 degree, as any frames outside of that range are definitely pointed in the wrong area of the sky and should be discarded. Astrometry.net calibrates the image's WCS coordinates using the image coordinates of the sources in the field and cross-referencing the

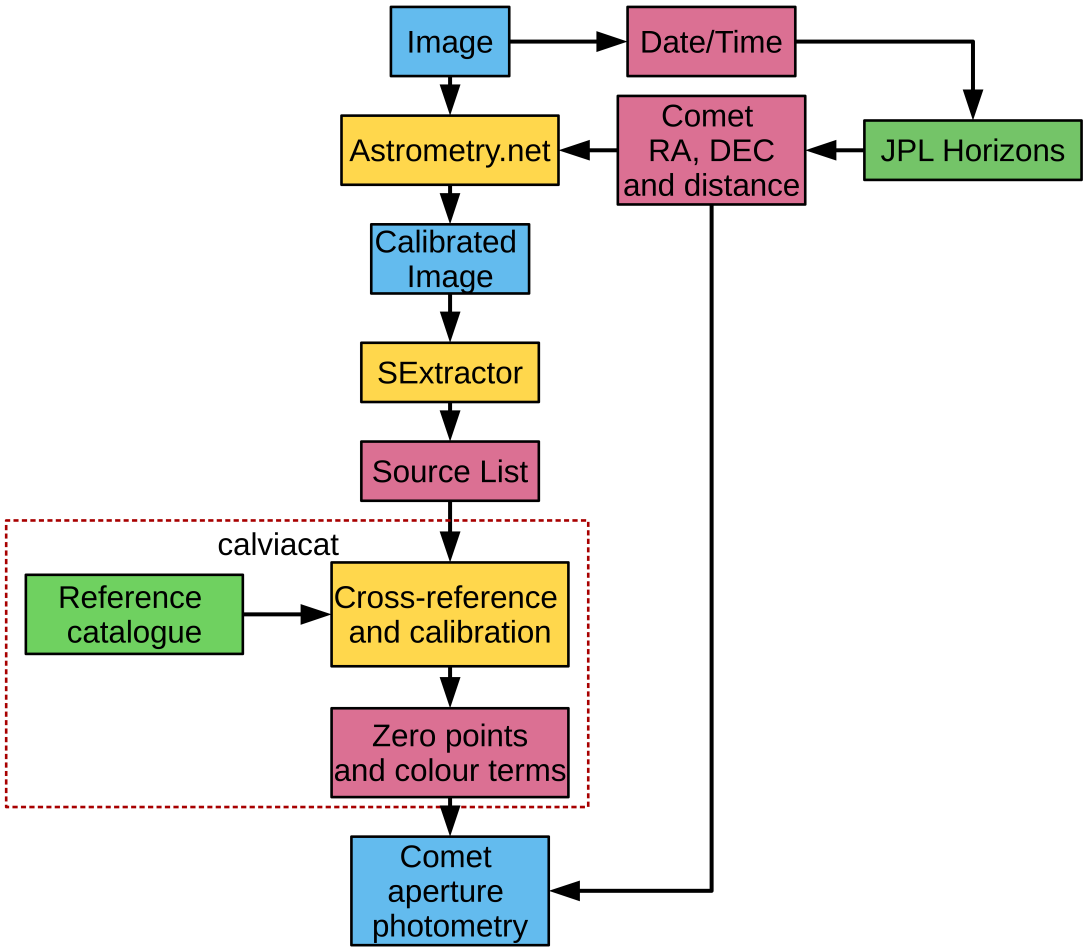

Figure 2.5 Flow chart showing the steps in the automatic astrometry and photometry calibration pipeline.

relative positions with its own catalogue to accurately determine the astrometry of the image. The catalogues used are in varying scales allowing for calibration of instruments with large variations in FOV and pixel scale.

Astrometry.net was the bottleneck in my pipeline and the greatest contributor to increased computation time. It was not flawless and failed occasionally when presented with challenging images. Some data presented an issue with noisy edges left over from the data reduction process. These noisy edges were sometimes incorrectly identified as sources by Astrometry.net causing it to fail to solve. I initially tried masking the edges but the problem persisted even after masking. I concluded that it must have been an issue with the fields of stars themselves. I took the decision to discard these images rather than adapt the pipeline to mask the specific noise pattern since this affected a small amount of the image frames, full discussion of the specific data affected can be found in Chapter 3.3.

2.2.2 JPL Horizons

JPL Horizons is an online database and ephemeris computation service for solar system objects (Giorgini et al., 1996). The pipeline accesses this system through an API to acquire ephemera of the target at the time of observation of each frame. The date and time are extracted from the FITS header and the telescope ID and comet ID are provided by the pipeline. The specific data retrieved and recorded are RA, Dec, geocentric distance, heliocentric distance and phase angle. RA, Dec and geocentric distance are passed on to later steps in the pipeline. The RA and Dec are used as the starting point for the Astrometry.net and then used as a cross reference to identify the comet within the image. The geocentric distance is used to determine the angular size of the aperture.

2.2.3 Source Extractor

Source Extractor (abbreviated to SExtractor) is a software for detection of sources within an image and the measurement of instrumental magnitudes. SExtractor extracts the instrumental magnitudes of all sources within the FOV using automatic elliptical apertures defined so as to contain at least 90 per cent of the source flux around every detected object (Bertin and Arnouts, 1996). SExtractor flags sources that could be problematic during the extraction process;

these warnings can indicate neighbouring sources, saturated pixels or memory overflows. The flagged sources are removed from the source list before passing it to CALVIACAT.

SEXTRACTOR was written with galaxy detection in mind and not comet detection. This is both a help and a hindrance to my pipeline. On the one hand it already has built-in functionality for detection and measurement of the brightness of extended objects. However, the functionality expects elliptical objects to behave similar to galaxies, with their brightest point in the centre and the brightness falling off as you go out radially. It is not designed for the more unusual bright core with an extended tail in one direction typical of a comet. Because of this assumption, the centre of the object is assumed to be the centre of the elliptical aperture used to measure the object, which is not necessarily the centre of the coma. This is a problem since I want to measure the position of the nucleus of the comet which is inside the head of the comet. This sometimes lead to my measured positions of the comet being offset slightly compared to the expected positions from JPL Horizons, especially if the tail is bright significantly beyond the coma. I considered this by allowing some leeway in the measurement of the position and not immediately discarding something if it did not line up exactly. In some cases, the centre of the ellipse was not an adequate measure of the nucleus position and a significant portion of the light fell outside the aperture. I somewhat solved this issue by manual intervention, using the coordinates of the brightest pixels as the centre. While not perfect, it was a lot closer to the actual centre of the coma. This manual case-by-case tinkering is not ideal for a automated pipeline. Ideally, I should have used the coordinates generated from JPL Horizons as the centre of the aperture, instead of relying on SEXTRACTOR functionality not designed for comets.

2.2.4 calviacat

CALVIACAT is a photometry calibration software developed by Kelley and Lister (2019) that calibrates the photometry of raw frames by comparison to a catalogue. It currently allows comparison to four catalogues: Pan-STARRS DR1 (PS1), ATLAS Refcat2, SkyMapper and Gaia DR2. This work makes use of both the PS1 catalogue and Refcat2. The analysis of 67P found in Chapter 3 used PS1 as the comparison catalogue and Chapter 4 used Refcat2. The choice to change reference catalogues was made because Refcat2 had much better coverage of the

southern sky compared to PS1 and since we were using data obtained from a southern telescope it provided many more comparisons stars within each image. In initial tests on TRAPPIST data with the PS1 catalogue, I found frequent frames where there were too few stars to make an accurate calibration.

I found that removing galaxies from the comparison catalogue list improved the accuracy of the calibrations greatly. I did this by removing sources that had a difference greater than 0.05 between the PS1 PSF and Kron magnitudes. PSF magnitudes measure the point-source magnitude by fitting a predefined PSF to each source whereas the Kron (1980) magnitudes are used to measure the magnitude of galaxies and extended sources used elliptical apertures. If the source was a galaxy then there should be a difference between these magnitudes due to the different shapes of apertures and therefore different amount of light. These sources are likely to be galaxies and therefore cannot be used as calibrators. Refcat2 had the added benefit of not having galaxies in it (Tonry et al., 2018) so I could skip this step when using Refcat2 as my reference catalogue. The data from the catalogues is cached locally to allow for quick calibration of the same or similar fields, which was perfect for my uses since I was calibrating multiple frames which were taken in the same or similar field.

CALVIACAT works by cross-referencing the WCS coordinates of sources in the image with catalogue coordinates. I could then establish the difference between the magnitude measured from SExtractor and the catalogue magnitudes. The differences between the magnitudes were plotted against colour to give a colour calibration slope, an example of which can be seen in Figure 2.6.

I put a magnitude limit on the reference stars of $14 < m < 18$; this struck a good balance between the number of reference stars and the reliability of their measured magnitudes. The stars on the brighter and dimmer ends of the range provided less accurate calibration; the bright stars because they might be overexposed and the dim stars because they have less well constrained magnitudes in the reference catalogues. CALVIACAT applied a colour limit of $0.2 < g - i < 3.0$. This was to remove extreme outliers in colour that lie too far from solar colours and would not lie on a linear colour correction fit.

It was necessary to account for the different colour responses of each instruments and to find the zero point of each reference frame. CALVIACAT first determines the colour term, C, for each instrument used in Equation 2.8.

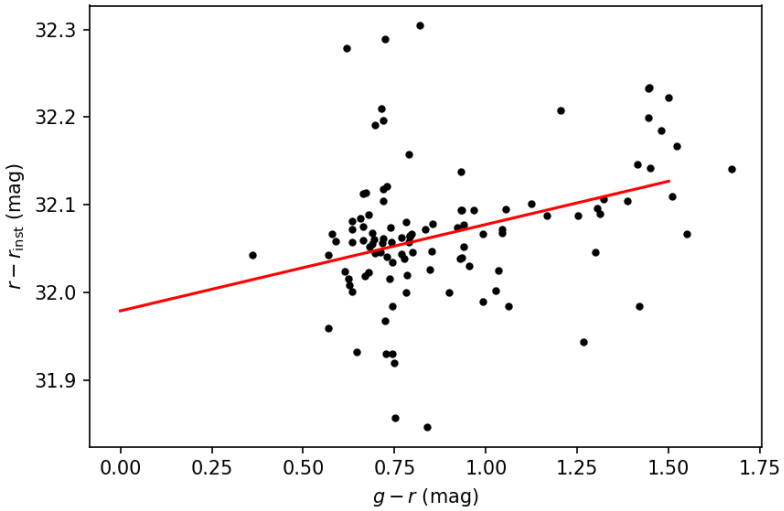

Figure 2.6 Example output of a calibration slope from CALVIACAT. It plots the difference between the measured and catalogue magnitude against the catalogue colour of each source detected in the image. The line is described by the equation 2.8 from which we get the colour term, C, and the zero point, ZP, for calibration.

$$m - m_{\mathrm{inst}} = C(\mathrm{colour\,index}) + ZP \tag{2.8}$$

This varied from frame-to-frame so I took an average of the value C across one data set for each instrument and filter. Once the colour terms for each instrument were determined this was held fixed for all subsequent calibration with that instrument. Table 2.1 displays the colour terms used in the calibrations to the PS1 and Refcat-2 system for each filter and each instrument. Further details of the instrumentation, such as aperture size, FOV and pixel scale, are found in Table 3.1.

The different comets in the TRAPPIST survey did not have clean spectra, free of gas emission lines, like that of 67P. This issue was highlighted early on by 46P/Wirtanen, a particularly active comet with notable gas emissions (Moulane et al., 2023). This comet had C_3 emissions in its spectra which appears in the B-filter but not in the g-filter which leads to differing colours when comparing $g - r$ measured directly from g and r filters and $g - r$ measured from converting B and R measurements to g and r.

Table 2.1 Summary table of the colour terms used during colour calibration to PS1 for each instrument. The colour terms used in the calibration of TRAPPIST data to Refcat2 is listed at the bottom.

Telescope/instrument	Filter	Colour	Colour term
NOT/ALFOSC	V	g–r	0.45±0.08
	R	g–r	0.14±0.09
OGS/SDC	visible	g–r	−0.41±0.04
TRAPPIST-South/CCD	B	g–r	−0.55±0.09
	V	g–r	0.48±0.04
	R	g–r	0.14±0.05
	I	r–i	0.23±0.04
VLT/FORS	R	g–r	0.22±0.08
WHT/ACAM	r	g–r	−0.04±0.03
	i	r–i	0.04±0.03
STELLA/WIFSIP	g	g–r	−0.15±0.10
	r	g–r	−0.02±0.08
	i	r–i	0.07±0.24
	z	i–z	−0.20±0.26
LT/IO:O	g	g–r	−0.01±0.03
	r	g–r	−0.02±0.02
	i	r–i	0.04±0.03
	z	i–z	0.13±0.06
LOT	B	g–r	−0.28±0.06
	V	g–r	0.43±0.05
	R	g–r	0.16±0.03
LCOGT/Merope	g	g–r	0.03±0.05
	r	g–r	0.01±0.03
	i	r–i	0.04±0.02
	z	i–z	−0.07±0.10
Rozhen BNAO 2-m/FoReRo-2	R	g–r	0.21±0.17
CA 2.2-m/CAFOS	R	g–r	0.22±0.07
CA 3.5-m/MOSCA	R	g–r	0.10±0.03
Lowell 0.8-m/NASAcam	R	g–r	0.08±0.07
TNG/DOLoRes	B	g–r	−0.52±0.08
	V	g–r	0.42±0.03
	R	g–r	0.14±0.03

continued on next page

Table 2.1 – *continued from previous page*

Telescope/instrument	Filter	Colour	Colour term
Wendelstein 2-m/WWFI	g	g–r	-0.02 ± 0.10
	r	g–r	0.02 ± 0.06
	i	r–i	0.05 ± 0.09
OSN 1.5-m/CCD	R	g–r	0.20 ± 0.05
INT/WFC	B	g–r	-0.45 ± 0.07
	r	g–r	0.04 ± 0.01
	i	r–i	0.08 ± 0.05
BTA/SCORPIO2	r	g–r	0.01 ± 0.02
LCOGT/SBIG	r	g–r	0.01 ± 0.04
OSN 0.9-m/CCD	R	g–r	0.09 ± 0.02
LCOGT/Sinistro	r	g–r	0.01 ± 0.03
Gemini N/GMOS	g	g–r	-0.08 ± 0.12
	r	g–r	0.10 ± 0.14
	i	r–i	0.15 ± 0.04
	z	i–z	-0.27 ± 0.11
TRAPPIST/CCD	B	B–V	-0.32 ± 0.05
(Refcat2)	V	B–V	-0.10 ± 0.02
	R	V–R	0.05 ± 0.03
	I	R–I	-0.002 ± 0.018

For this reason I decided to change the pipeline so that the magnitudes of calibrator stars were converted to B, V, R and I, the native filters of the TRAPPIST telescope, instead of converting the comet magnitudes to g, r, i and z, the inbuilt filters of CALVIACAT. This decision was made so as to be more consistent to the raw data and the fact I did not need to compare different data taken with different telescopes and different filters. Converting the stars' magnitudes was more likely to be accurate than converting comet magnitudes since I could use well-established conversion formulas (Jester et al., 2005) that are written for the black body spectra of stars and not the variable spectra of comets.

I found that the errors provided by CALVIACAT were overestimates since CALVIACAT assumed every point as equally weighted and did not exclude obvious outliers. So I recalculated the errors by excluding sources that were over 3 sigma away from the average colour calibration trend. Once I excluded the outliers, I subtracted the trend and then measured the average distance of points away from that trend

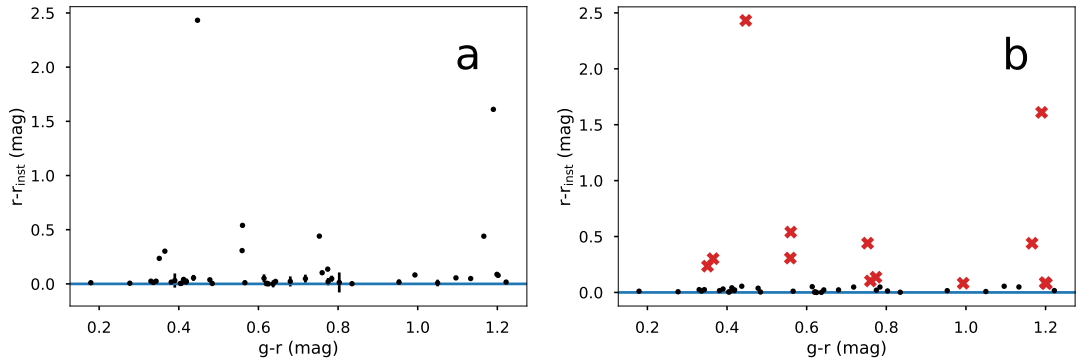

Figure 2.7 Figures demonstrating my new error calculation method, (a) represents a colour calibration curve with the trend subtracted leaving, (b) the outliers above 3 sigma are excluded, and the error is recalculated by measuring the average distance of points above the trend line.

line to find the average error (Figure 2.7).

Once calibration was complete, the photometry of the comet was then measured with a fixed aperture of 10 000 km radius (Figures 2.8 and 2.9) using the geocentric distance from JPL Horizons and appropriate pixel scale from Astrometry.net to calculate the corresponding radius in pixels. If other catalogue sources were found within the aperture, the pipeline raised a flag and recorded their catalogue magnitudes.

2.3 Pipeline limitations and testing

The uncertainties in the instrumental magnitudes measured by SExtractor were generally small, on the order of a thousandth of a magnitude. For bright objects, this is not a significant contribution to the error budget. This uncertainty increases by a factor of ten when measuring objects of brightness less than 19 mag. Errors in calibration from calviacat are larger than those found by the instrumental magnitudes, on the order of a hundredth of a magnitude, and are usually the biggest contributor to the overall error budget. The only time they are not is when they are outweighed by the uncertainties in the colour terms used during colour calibration, as shown in Table 2.1.

The pipeline did have limitations. In order to perform automatic astrometry and magnitude calibration, the pipeline needed a large sample of background stars

which could be lacking in some frames, particularly from instruments with a relatively small FOV (Figure 2.10). The pipeline did not take into account bright field stars that could contribute to the background level inside the aperture, or completely outshine the comet, even if their centres were outside the comet aperture (Figure 2.11). This lead to a target being artificially brightened, especially when the target was dimmer and more likely to be outshone by field stars. These points had to be removed manually.

I used the VLT data on 67P as a test bed for the pipeline. It highlighted the limitation of detecting dim targets. Due to a large observing window I had a complete range of brightnesses from across the perihelion. When the comet was dim it was found that it was difficult to identify the comet automatically. Bright sources near or on top of the comet were often mistaken for the comet. It also highlighted some limitations with crowded fields since at the time of observation 67P was crossing the Galactic Plane so it was in a busy field, meaning the chances of a background source overlapping with the aperture were increased. I mitigated this by flagging sources that were found within the aperture, so this could be removed from the data set before analysis. The sources that were found within the aperture had their magnitudes recorded. Observations where background sources were within 2 mag of the comet were removed from the final data set analysis. This was decided on a case-by-case basis as to whether or not a source was bright enough to have a significant impact on the recorded brightness of the comet. Often near perihelion, the comet was so bright it outshone the majority of field stars.

2.4 Summary

I have developed a pipeline for calibration of broadband data using the consistent calibration system of CALVIACAT. The testing of the pipeline was mostly successful with the handful of failures mainly being a result of poor input data. These still had to be removed manually from the final data set before analysis, this is a point that could be improved upon in future versions of the pipeline. The pipeline calibrated the brightness by cross-referencing with stellar catalogues, initially Pan-STARRS 1 and then later ATLAS Refcat-2. These catalogues provided a firm foundation on which to calibrate my data. Referencing these catalogues also allowed me to calibrate each image individually using the background stars within the same frame, therefore providing me with a more accurate calibration

specific to each image. Calibrating all the data using the same method and to a consistent standard allowed me to build up a complete picture of a comet's activity by combining data from different telescopes and instruments.

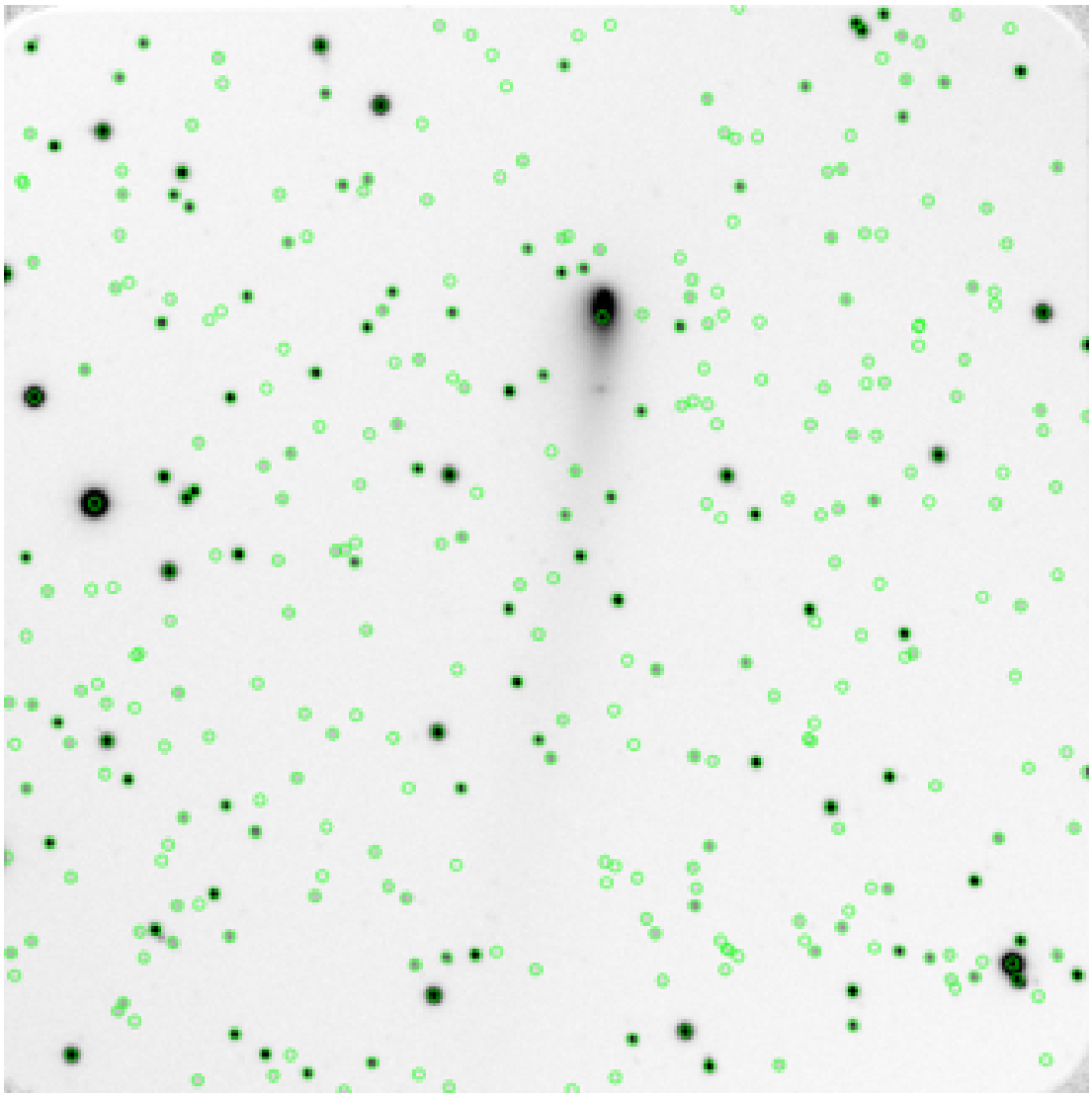

Figure 2.8 Example output of SExtractor highlighting all sources detected within the frame. These points just indicate the positions of detected sources and are not representative of the actual size of the apertures used in the calibration. 67P taken with NOT/ALFOSC on 2015 July 26.189 with a 6.4'×6.4' FOV.

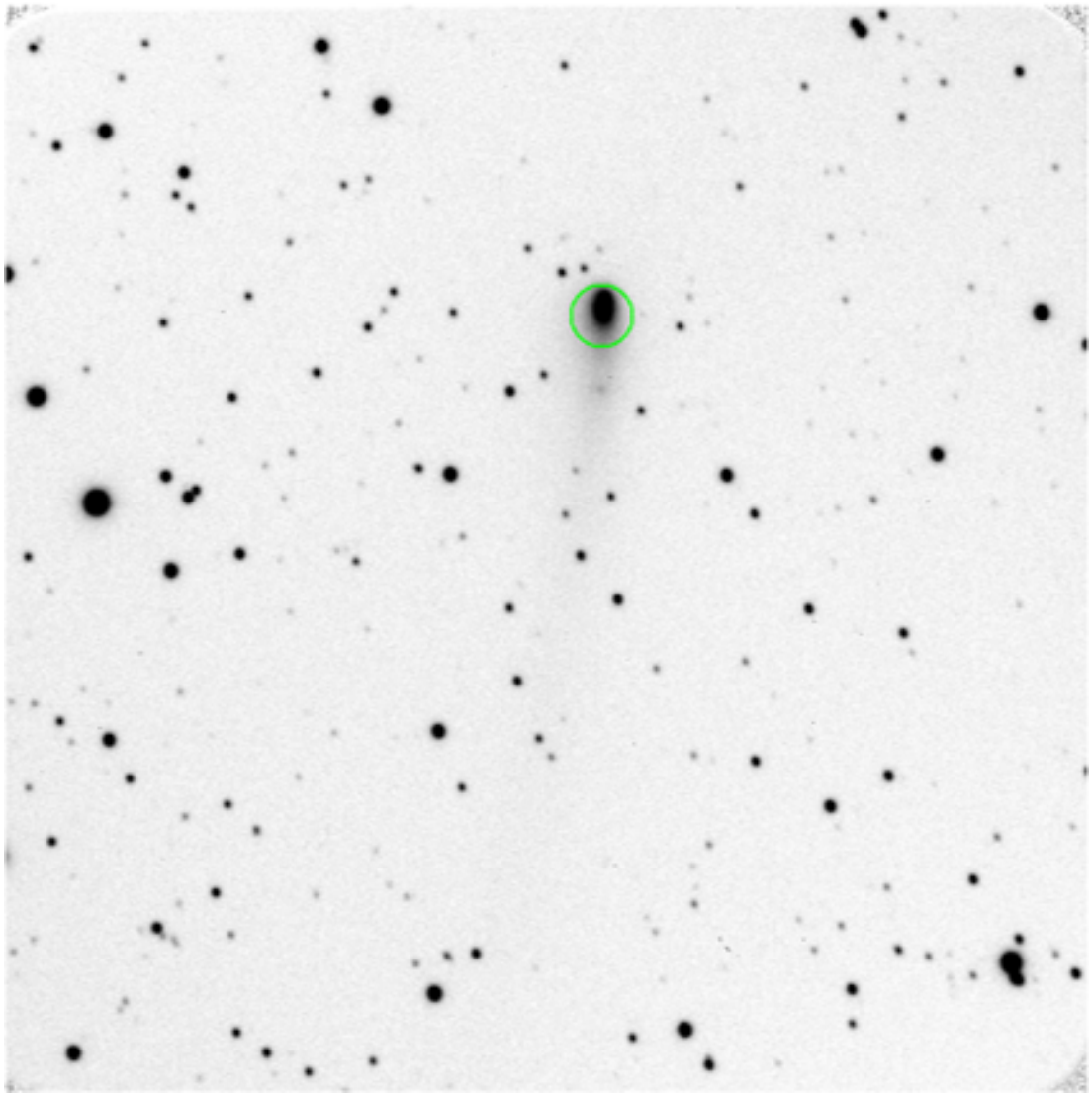

Figure 2.9 The same frame as Figure 2.8 with the comet highlighted. This is the aperture used in calibrations, in this frame it is clear to see the offset caused by SExtractor's extended object centering. The aperture is 10 000 km in size. In this case, the majority of the light is within the aperture but in other cases where the coma was much more extended, the aperture did not include all of the light.

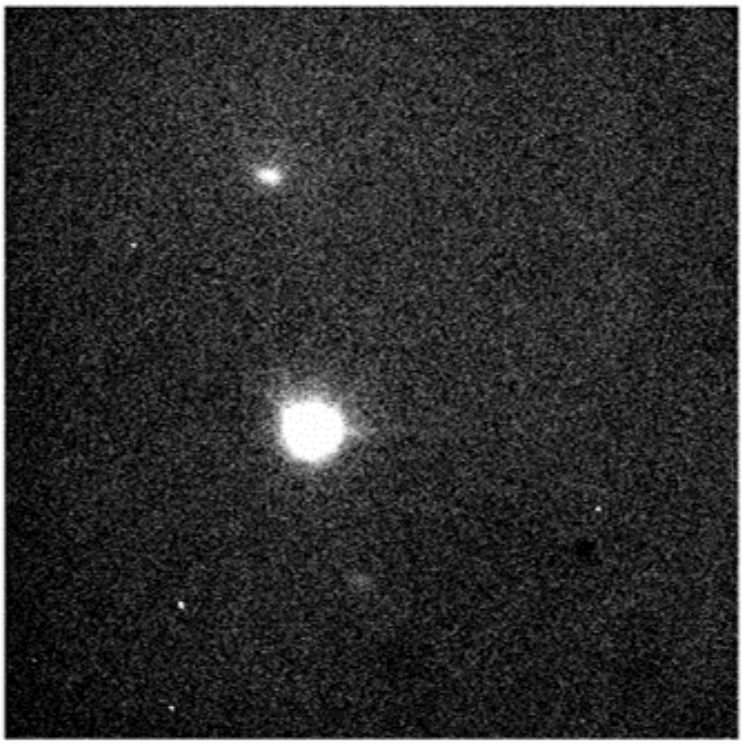

Figure 2.10 An example of a frame with too small of an FOV which caused Astrometry.net to fail due to a lack of sources. 67P taken with IRTF/MORIS on 2016 March 14.349 with a 1'×1' FOV.

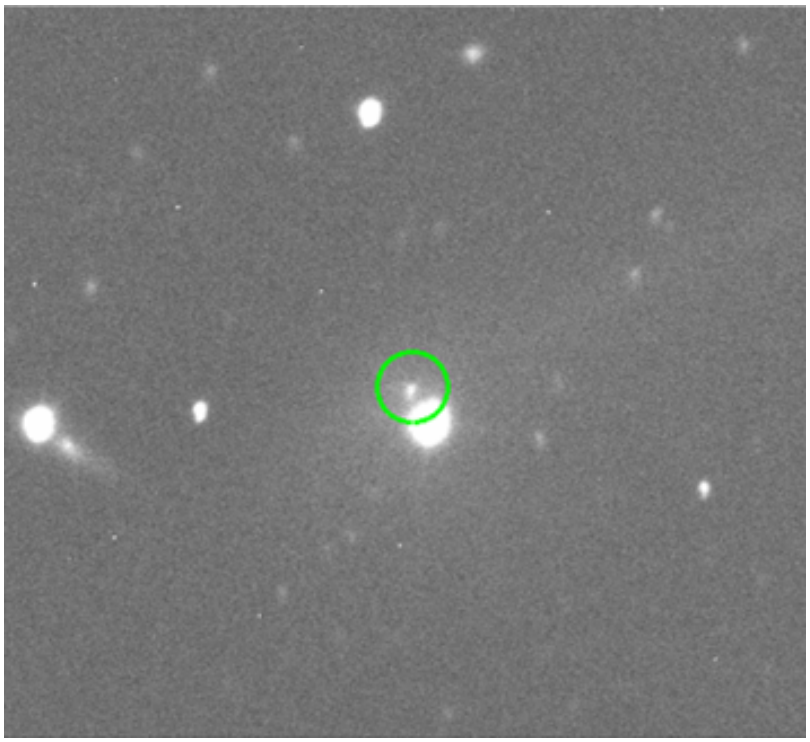

Figure 2.11 An example of a bright star lying within the aperture. Cropped frame of 67P taken with NOT/ALFOSC on 2015 August 21.247 with a 6.4'×6.4' FOV.

Chapter 3

Searching for outbursts in the ground-based photometry of 67P/Churyumov–Gerasimenko

3.1 Introduction

The Rosetta mission was backed up by a large ground-based observing campaign of comet 67P/Churyumov–Gerasimenko (Snodgrass et al., 2017) that followed the activity through its perihelion passage. This data set is one of the most detailed and comprehensive data sets ever taken of a comet, with coverage across almost all of the comet's inward and outward journeys, so provides an ideal treasure trove for detailed analysis.

The Rosetta mission provided us with an opportunity to link ground-based observations with events observed in situ in orbit around the comet's nucleus. Instruments began monitoring 67P in 2014 March while inbound to the comet. At this time the comet was already active and an outburst was detected in April (Tubiana et al., 2015). The comet was regularly monitored as the spacecraft approached between July and August, with no further outbursts seen. Once in orbit around the comet an outburst was seen in 2015 February (Knollenberg et al., 2016). Over the next few months, the Rosetta probe had to retreat to a safe distance from the comet due to high dust content in the coma; during this time some smaller outbursts on the comet's surface could have been missed. Between 2015 July and

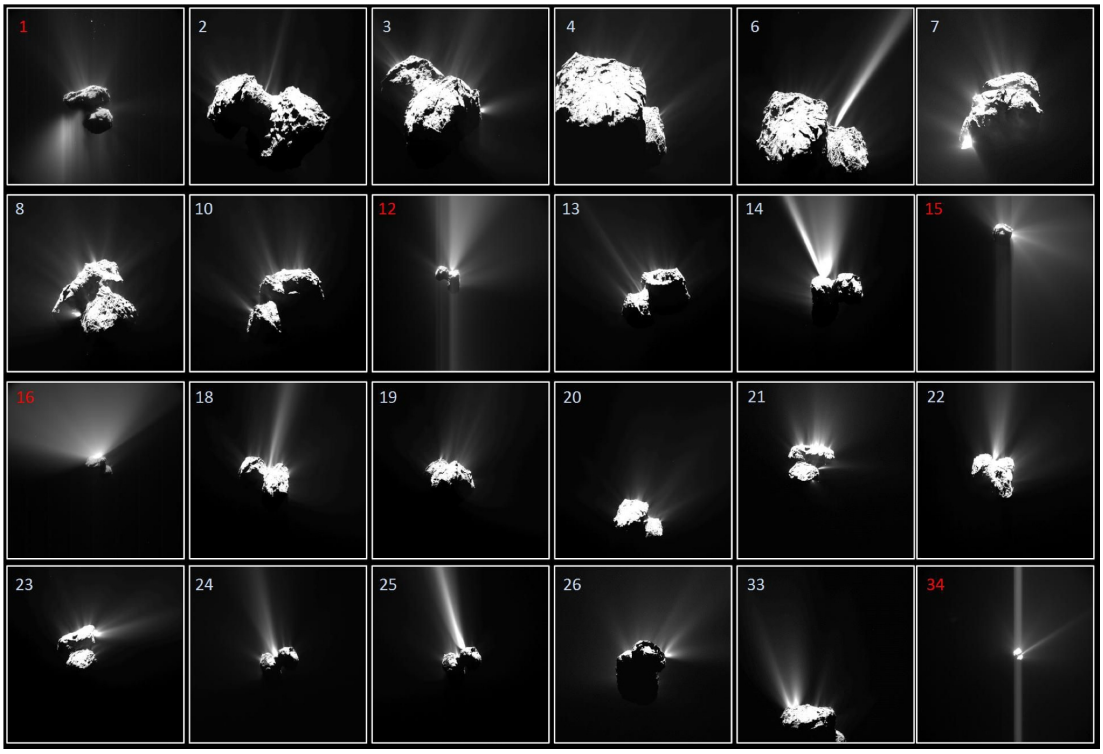

Figure 3.1 A selection of the brightest outbursts from 67P seen by Rosetta. White numbers indicate images taken with OSIRIS and red numbers indicate images from NavCam. Reproduced from Vincent et al. (2016)

September, as the comet passed perihelion, 34 individual outbursts were observed as detailed in Vincent et al. (2016) (Figure 3.1).

During this time, Boehnhardt et al. (2016) saw a large dust ejection event in the coma morphology in images acquired at the 2-m Wendelstein telescope on 2015 August 22–23 Figure 3.2), but they do not make a link between this observation and any outbursts seen by Rosetta. Knight et al. (2017), observing from the 0.8-m Lowell telescope, also saw the same outburst in their photometry on 2015 August 22. They make a tentative link to an outburst observed by Rosetta. They also report a possible outburst occurring on 2015 September 19 but they do not match it with any other known outbursts of 67P. Another notable outburst was seen by multiple instruments on Rosetta on 2016 February 19 (Grün et al., 2016). Initial analysis of TRAPPIST observations over this period by Grün et al. (2016) claim to show an increased and sustained brightness correlating to this outburst. A final notable outburst was seen by Agarwal et al. (2017) on 2016 July 3, while the comet was well on its outward journey, which was thought to be driven by sub-surface energy storage.

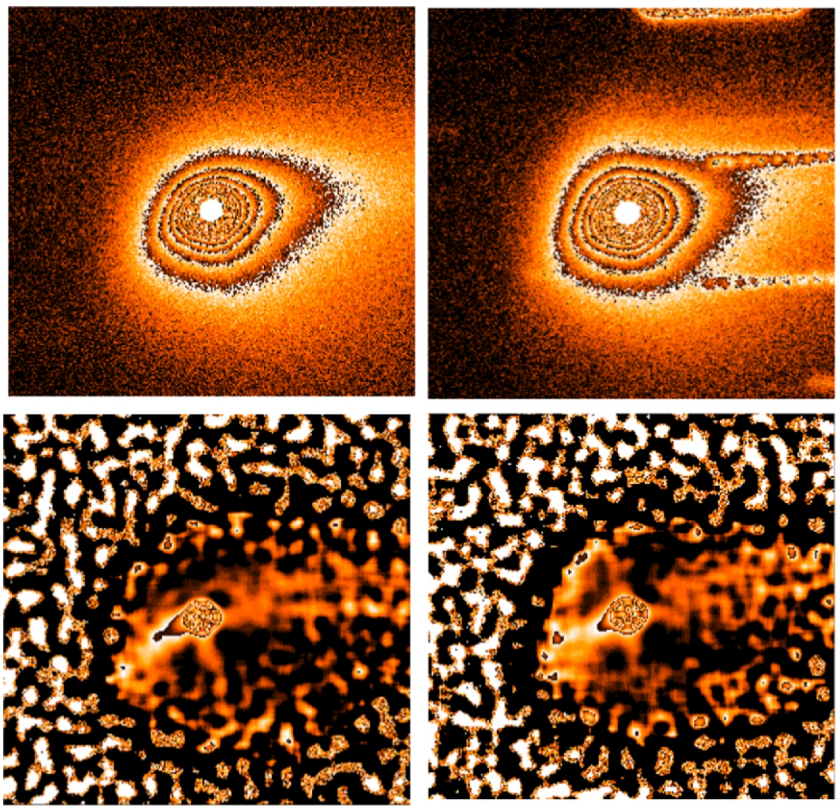

Figure 3.2 Dust arc in the coma of 67P. The two top images show the isophote (lines of equal brightness) pattern of the comet on 2015 August 22 (top left panel) and on 2015 August 23 (top right panel). The bottom images show the respective adaptive Laplace-filtered versions of the comet image on both observing dates. The Laplace-filtered image of 2015 August 23 displays a straight short jet-like structure at near-nucleus PA 20 deg and an arc-let structure at the end of the jet, extending into southeastern direction. Neither features are present in the coma the day before. Image orientation is north up, East to the left. Reproduced from Boehnhardt et al. (2016)

Aside from searching for these small-scale transient events, tracing activity can give us an insight into the ageing processes that affects a comet. Predictions of the dust activity were made by Snodgrass et al. (2013) by fitting a physical model (Meech et al., 1986) based on sublimation from the nucleus to the three previous apparitions of 67P. They described the dust flux with single power law fits and found $Af\rho \propto r^{-3.2}$ pre-perihelion and $\propto r^{-3.4}$ post-perihelion. Using these relationships, they predicted the dust flux around the next perihelion, with a peak R-band magnitude of ~ 13 expected in 2015 August. The observations have shown the comet followed these predictions well, having $Af\rho \propto r^{-3.7}$ and a peak R-band magnitude just under 13 (Snodgrass et al., 2017). This leads us to believe that the activity of 67P remains largely unchanged from orbit-

to-orbit and therefore results from Rosetta can be applied more generally to help constrain models of comet activity evolution and scale results to different comets and apparitions. The activity analysis performed in Snodgrass et al. (2017) was made using an approximate calibration; in this chapter I detail results of a precise calibration method using my own pipeline which was applied across the majority of the Snodgrass et al. (2017) campaign data. In this chapter I search the broadband photometry to find small-scale variations that could be linked to outbursts. The large pool of data allows me to confirm the brightening across multiple data sets, paying attention to events seen by Rosetta to see if any links could be made. I also look to see if I can confirm the outbursts seen by Vincent et al. (2016), Boehnhardt et al. (2016), Knight et al. (2017), Grün et al. (2016) and Agarwal et al. (2017). I aim to constrain the detectability of small-scale events from ground-based observations. These constraints will help future interpretations of ground-based observations of comets and link them to changes in the nucleus, the majority of which we will not visit directly.

3.2 Observations

Table 3.1 summarises the broadband imaging observations of 67P made between 2013 and 2017. The whole data set covers a total on-target observing time of ∼640 hrs with 9606 individual frames from 27 telescopes across nine countries. The data at the beginning and end of the campaign offered limited use due to my pipeline's limitation in detecting dim targets in crowded fields and therefore are not suitable for automatic photometry analysis. Nordic Optical Telescope (NOT) observations, for example, cover a period in 2014 when the comet was visible at low altitudes in the northern sky. These data however, due to the comet's faintness and the high airmass during observation, are not suitable for automatic processing. Analysis of the 2014 NOT data was performed by Zaprudin et al. (2015) and analysis of the remaining 2014 data can be found in Snodgrass et al. (2016a). In this chapter I focus my analyses on the data between 2015–16, which covers the majority of the comet's inner Solar System passage and the main phase of the Rosetta mission. It was during this phase that the majority of the telescopes were observing the comet regularly, providing almost 24/7 coverage at some points. The early portion of this data were afflicted by less favourable viewing conditions due to the small solar elongation in the early months of observation, including during the perihelion on 2015 August 13. After

2015 October it became more favourable to view.

I highlight data that have unique coverage or significance in the following subsections.

Table 3.1 Summary table of 67P observations. Filters in letters for standard bands, with lowercase (*g,r,i,z*) indicating Sloan Digital Sky Survey (SDSS)-type filters and upper case (*B,V,R,I*) indicating Johnson–Cousins types. The raw data are available from individual observatory archive facilities as indicated, those not indicated are proprietary data. All of the original imaging data will eventually be made publicly available at the ESA Planetary Science Archive (`http://www.cosmos.esa.int/web/psa`).

Telescope/instrument	Filter	FOV	Pixel scale	Dates (YY/MM/DD)
NOT/ALFOSC[a]	*V,R*	6.4'x6.4'	0.2138	13/05/13-16/08/10
NOT/StanCam[a]	*V,R*	3'x3'	0.176	14/04/05-16/05/22
OGS/SDC	visible	42.5'x42.5'	0.62	14/09/21-16/07/04
TRAPPIST-South/CCD	*B,V,R,I*	22'x22'	0.6	15/04/18-16/06/07
NTT/EFOSC[b]	*r*	4.1'x4.1'	0.12	15/04/22-16/07/29
VLT/FORS[b]	*R*	7.1'x7.1'	0.25	15/05/21-17/03/25
WHT/ACAM[c]	*R,I*	8.3' diameter	0.25	15/07/06-16/06/28
STELLA/WIFSIP	*g,r,i,z*	22'x22'	0.32	15/07/18-16/06/08
LT/IO:O[d]	*g,r,i,z*	10'x10'	0.15	15/07/18-16/06/11
LOT	*B,V,R*	13.08'x13.08'	0.39	15/08/02-15/11/07
LCOGT/Merope[e]	*g,r,i,z*	5'x5'	0.278	15/08/07-15/09/21
Rozhen BNAO 2-m/FoReRo-2	*B,R*	7.6'x7.6'	0.89	15/08/11-16/11/06
CA 2.2-m/CAFOS[f]	*R*	16' diameter	0.53	15/08/14-16/06/05
CA 3.5-m/MOSCA[f]	*R*	11'x11'	0.33	15/08/18-15/08/25
Lowell 0.8-m/NASAcam	*R*	15'	0.45	15/08/18-15/12/01
TNG/DOLoRes[g]	*B,V,R*	8.6'x8.6'	0.252	15/08/18-16/03/17
Wendelstein 2-m/WWFI	*g,r,i*	26.6'x29.0'	0.199	15/08/21-16/05/08
OSN 1.5-m/CCD[h]	*R*	7.8'x7.8'	0.23	15/09/21-16/04/30
INT/WFC[c]	*B,r,i*	34.2'	0.33	15/10/13-16/06/23
BTA/SCORPIO2	*r,g*	6.1'x6.1'	0.18	15/11/07-16/04/01
LCOGT/SBIG[e]	*r*	15.8'x15.8'	0.464	15/12/14-16/01/30
OSN 0.9-m/CCD[h]	*R*	13.2'x13.2'	0.38	16/01/13-16/01/16
LCOGT/Sinistro[e]	*r*	26'x26'	0.389	16/01/27-16/03/30
Gemini N/GMOS[i]	*g,r,i,z*	5.5'x5.5'	0.08	16/02/16-16/05/28
IRTF/MORIS[j]	*r*	1'x1'	0.117	16/03/14-16/03/28
LT/IO:O	*g,r,i,z*	10'x10'	0.15	21/07/06-22/06/11

[a] Data available from: `https://www.not.iac.es/archive/`
[b] Data available from: `https://archive.eso.org/eso/eso_archive_main.html`
[c] Data available from: `http://casu.ast.cam.ac.uk/casuadc/ingarch/`
[d] Data available from: `https://telescope.livjm.ac.uk/cgi-bin/lt_search`
[e] Data available from: `https://archive.lco.global/`
[f] Data available from: `https://caha.sdc.cab.inta-csic.es/calto/index.jsp`
[g] Data available from: `http://archives.ia2.inaf.it/tng/`
[h] Data available from: `https://arch.osn.iaa.csic.es:8443/ada/fitsSearch.htm`
[i] Data available from: `https://archive.gemini.edu/`
[j] Data available from: `https://irtfdata.ifa.hawaii.edu/search/`

3.2.1 VLT

The 8-m European Southern Observatory VLT in Chile provided the longest observing period from start to end; the VLT began observing 67P in 2013 to measure the astrometry of the comet before the spacecraft's arrival and constrain the start of activity (Snodgrass et al., 2016a). It also extended beyond the observing windows of most other telescopes with observations made until 2017 March 25 providing unique coverage of the comet's outward journey as it dimmed to below 22 mag, after which it became undetectable.

3.2.2 NOT

Similarly to the VLT, the NOT started observing 67P in 2013. Despite being located on La Palma in the northern hemisphere, the 2.56-m telescope is capable of observing at very low altitudes meaning it started observing before its northern hemisphere counterparts. However, these early observations were of limited use because of the difficulty of detecting the faint comet. The NOT provided regular coverage over the course of the perihelion passage, it observed once or twice a week between 2015 July 1 and 2016 August 10 in both R- and V-bands. More details of these observing runs can be found in Zaprudin et al. (2015) and Zaprudin et al. (2017).

3.2.3 TRAPPIST

The robotic 60-cm TRAPPIST-South telescope in La Silla (Jehin et al., 2011) provided regular coverage across all of the perihelion passage including a unique period between 2015 April 18 and June 27 when the comet was difficult to observe from northern hemisphere observatories. TRAPPIST provided observations in B-, V-, R- and I-bands across the whole passage. For more details see Snodgrass et al. (2016b).

3.2.4 LT

The robotic 2-m Liverpool Telescope (LT) on La Palma provides some of the most regular coverage in r-band across the majority of the perihelion passage

between 2015 July 18 and 2016 June 11 and measurements in the g-, i- and z-bands between 2015 July 18 to August 31 and 2016 February 10 to June 11. This run was also detailed in Snodgrass et al. (2016b).

I undertook regular monitoring of 67P with the LT during 67P's subsequent apparition between 2021 July 6 and 2022 June 11 covering both inbound and outbound journeys. These observations are discussed in Section 3.5.4.

3.2.5 Wendelstein

The 2-m telescope at the Wendelstein observatory in Germany provided over 90 hours of regular post-perihelion coverage between 2015 August 22 and 2016 May 9 and showed initial evidence for an outburst (Boehnhardt et al., 2016).

3.2.6 Lowell

The 0.8-m telescope at the Lowell Observatory made regular observations post-perihelion between 2015 August 18 and December 1. It observed the same outburst seen by the Wendelstein telescope as well as a second potential outburst (Knight et al., 2017).

3.3 Results

3.3.1 Summary

Data reduction was performed using my pipeline detailed in Chapter 2 using the PS1 catalogue (Tonry et al., 2012) as the reference catalogue. Table 2.1 displays the colour terms used in the calibrations for each filter in each data set. Figure 3.3 shows the r-band light curve of 67P, calibrated to the PS1 photometric system, compiling all the data processed through my pipeline. Table 3.2 present a summary of the data processed. In this sub-section I briefly describe specific results from specific data sets.

The VLT provided a high quality data set that ran with few issues. As such it was used as the test data for the initial development of the pipeline. The VLT data

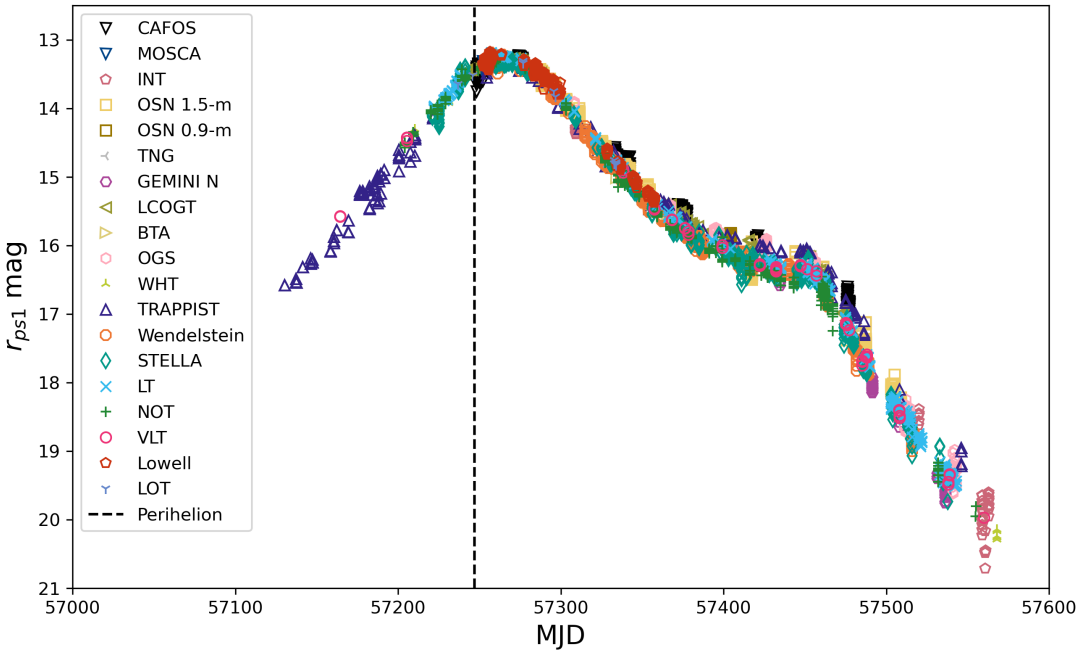

Figure 3.3 Light curve of 67P/Churyumov–Gerasimenko measured within 10 000 km aperture. Photometry has been calibrated and scaled to the PS1 r-band. The vertical dotted line shows time of perihelion on 2015 August 13.

Table 3.2 Summary table of 67P data processed through the pipeline. Frames input is the original number of images passed to the pipeline. Frames processed is the number of frames successfully calibrated by the pipeline, images causing the pipeline to fail or images manually removed from the final data are not included in this number.

Telescope/instrument	Frames input / successfully processed															
	B		*V*		*R*		*I*		*g*		*r*		*i*		*z*	
NOT/ALFOSC	–	–	489	460	667	459	–	–	–	–	–	–	–	–	–	–
NOT/StanCam	–	–	51	0	56	0	–	–	–	–	–	–	–	–	–	–
OGS/SDC	–	–	–	–	258	192	–	–	–	–	–	–	–	–	–	–
TRAPPIST-South/CCD	63	59	247	217	74	72	69	61	–	–	–	–	–	–	–	–
NTT/EFOSC	–	–	–	–	–	–	–	–	–	–	24	0	–	–	–	–
VLT/FORS	–	–	–	–	53	52	–	–	–	–	–	–	–	–	–	–
WHT/ACAM	–	–	–	–	–	–	–	–	–	–	9	9	3	3	–	–
STELLA/WIFSIP	–	–	–	–	–	–	–	–	25	25	745	645	25	25	35	35
LT/IO:O	–	–	–	–	–	–	–	–	109	100	355	317	109	100	109	100
LOT	4	3	5	5	14	13	–	–	–	–	–	–	–	–	–	–
LCOGT/Merope	–	–	–	–	–	–	–	–	28	28	32	32	14	14	14	14
Rozhen BNAO 2-m/FoReRo-2	5	0	–	–	13	2	–	–	–	–	–	–	–	–	–	–
CA 2.2-m/CAFOS	–	–	–	–	912	690	–	–	–	–	–	–	–	–	–	–
CA 3.5-m/MOSCA	–	–	–	–	22	22	–	–	–	–	–	–	–	–	–	–
Lowell 0.8-m/NASAcam	–	–	–	–	354	318	–	–	–	–	–	–	–	–	–	–
TNG/DOLoRes	48	48	74	74	69	64	–	–	–	–	–	–	–	–	–	–
Wendelstein 2-m/WWFI	–	–	–	–	–	–	–	–	45	44	1619	1245	41	38	–	–
OSN 1.5-m/CCD	–	–	–	–	1499	1473	–	–	–	–	–	–	–	–	–	–
INT/WFC	37	34	–	–	–	–	2	2	–	–	90	86	–	–	–	–
BTA/SCORPIO2	–	–	–	–	–	–	–	–	6	0	15	13	–	–	–	–
LCOGT/SBIG	–	–	–	–	–	–	–	–	–	–	51	42	–	–	–	–
OSN 0.9-m/CCD	–	–	–	–	78	78	–	–	–	–	–	–	–	–	–	–
LCOGT/Sinistro	–	–	–	–	–	–	–	–	–	–	42	36	–	–	–	–
Gemini N/GMOS	–	–	–	–	–	–	–	–	17	17	42	42	12	12	12	12
IRTF/MORIS	–	–	–	–	–	–	–	–	–	–	113	0	–	–	–	–

also helped me constrain the limitations of the automatic detection, with its wide observing window it observed the comet at its faintest. As 67P dimmed below 20 mag, and down to 22 mag, the automatic pipeline calibration became increasingly unreliable. The brighter background stars outshone the fainter comet leading the pipeline to often misidentify the stars as 67P. Even when the comet was correctly identified, the instrumental magnitudes determined by SExtractor had larger errors than when measuring a brighter comet, which lead to significant variation in brightness between individual measurements. From this, I determined that the pipeline works best when observing a comet brighter than 20 mag.

The regular observations by the LT were well suited for my pipeline producing well calibrated and consistent results in g-, r-, i- and z-bands. These data formed the backbone of my comparison and I used this as a 'true' representation of the light curve. The colours obtained from the LT were also used as my starting point when approaching colour calibration of the remaining data.

The NOT/ALFOSC data presented an issue; noisy edges left over from the data reduction process. These noisy edges were sometimes incorrectly identified as sources by Astrometry.net causing it to fail to solve. I initially tried masking the edges but the problem persisted even after masking. I concluded that then it must have been an issue with the fields of stars themselves. I took the decision to discard these images rather than adapt the pipeline to mask the specific noise pattern since this affected only around 12 per cent of the images in the NOT data, and even fewer in the data set as a whole. Despite this, it is one of the most well calibrated and comprehensive data sets in both r- and g-bands. 32 images taken by CAFOS on the Calar Alto Observatory (CA) 2.2-m telescope had noisy artefacts, similar to the NOT, which caused the pipeline to fail. Again, I took the decision to simply discard these frames. The calibration of some of these data had wide variations within nights due to the small number of calibration stars within the FOV. This led to some differing estimations of the zero point in each frame as calviacat tried to fit a line to a small number of points. The large number of exposures taken each night allowed me to remove outliers in the calibration. While this data set is large it is concentrated on small groups of consecutive nights separated by weeks rather than long-term monitoring.

The Lowell data set had good coverage around perihelion, but somewhat inconsistent calibration due to varying quality between frames. Several frames contained dead pixels which sometimes would lie on top of a star, making the calibration less accurate. The 43 frames where the dead pixels lay within the comet aperture

were discounted.

The European Space Agency (ESA) Optical Ground Station (OGS) data contained 18 frames which were discounted due to being pointed towards the wrong area of the sky. Another 37 frames did not have enough background stars to perform calibration.

The pipeline failed to run on Infrared Telescope Facility (IRTF), New Technology Telescope (NTT) and NOT/StanCam data due to the small FOV in the images. There were few stars within the field which meant astrometry and photometry calibrations failed.

It is worth mentioning the William Herschel Telescope (WHT), Lulin Observatory One-Meter Telescope (LOT), Telescopio Nazionale Galileo (TNG), Isaac Newton Telescope (INT) and Bolshoi Teleskop Alt-azimutalnyi (BTA). They are well calibrated data but have sparse coverage having only 3 to 5 nights of observations in each set. The consistent calibrations made possible due to the larger data set they are a part of meant that they are still useful in the final data to fill in gaps and aid in confirming outbursts.

Any data not mentioned above ran through my pipeline successfully and was generally well calibrated. A common issue in these data were the occasional lack of background stars to use for photometric calibration but this typically affected less than 10 per cent of images.

Overall the pipeline worked well and processed the majority ($\sim$ 83 per cent) of the data and produced well calibrated and consistent results across the different data sets. The pipeline works best when the comet is brighter than mag 20 brightness and in a well-exposed, but not too crowded, field of stars. Without these conditions the comet identification and calibration becomes increasingly inaccurate.

A limitation highlighted by the NOT/ALFOSC and CA/CAFOS data is that the pipeline has no way of adjusting for any noisy edges or artefacts that may remain after data reduction. This noise often was misidentified as sources by SExtractor and Astrometry.net which caused them either to fail or give inaccurate results. The other limitation is the pipeline only does simple aperture photometry around the comet and does not take into account any contribution of the background flux from nearby bright stars that are outwith the aperture. I decided against implementing a fix for both of these issues because of the small

proportion of images they affect.

3.3.2 Offset between telescopes around low phase angles

A peculiar effect I see in my data is a significant shift in r-band magnitudes at low phase angles between different telescopes (Figure 3.4). The TRAPPIST data is the best example of this, it follows the overall brightness trend but is shifted relative to the curve around low phase angles, the bump in the light curve around MJD 57450 when the comet was at opposition in 2016. Initially I thought it was an effect of the slight bandpass differences between the r and R filters. Some other data sets that use Johnson–Cousins filters, e.g. OSN, OGS and CAFOS, appear to align better with TRAPPIST however this is not true of all data taken in this filter, for example the NOT data does not have an offset and follows the trend of the majority of the data. This offset persisted after colour calibration. I looked at $r-i$ colours around low phase angles to see if there was a change in the colour but this was not seen, see section 3.4.1. I also investigated if there was any correlation between colour and geocentric distance, airmass or seeing. I did not see any correlation so it remains a mystery as to what is causing this offset. Some of the telescopes in Figure 3.4 have a large scatter of points over one night, e.g. STELLA, OSN, Wendelstein and CAFOS. This scatter arises from uncertainties in the measurements or calibrations and is not indicative of any activity change over small time-scales. I chose not to plot the uncertainties of each individual point for the sake of visual clarity. The changes are also over a time-scale that is too short to be an effect of the rotation of the nucleus. In order to aid in meaningful comparisons between the data I needed to correct these offsets and line the points up with the rest of the curve. To correct for these offsets I first subtracted the overall trend of the light curve leaving me with a scatter of points around the average. For each data set that was offset from the average, I modelled the offset as a function of time using a simple straight-line fit. Each fit was then subtracted from their respective data so the averages of each data set followed the average of the overall curve.

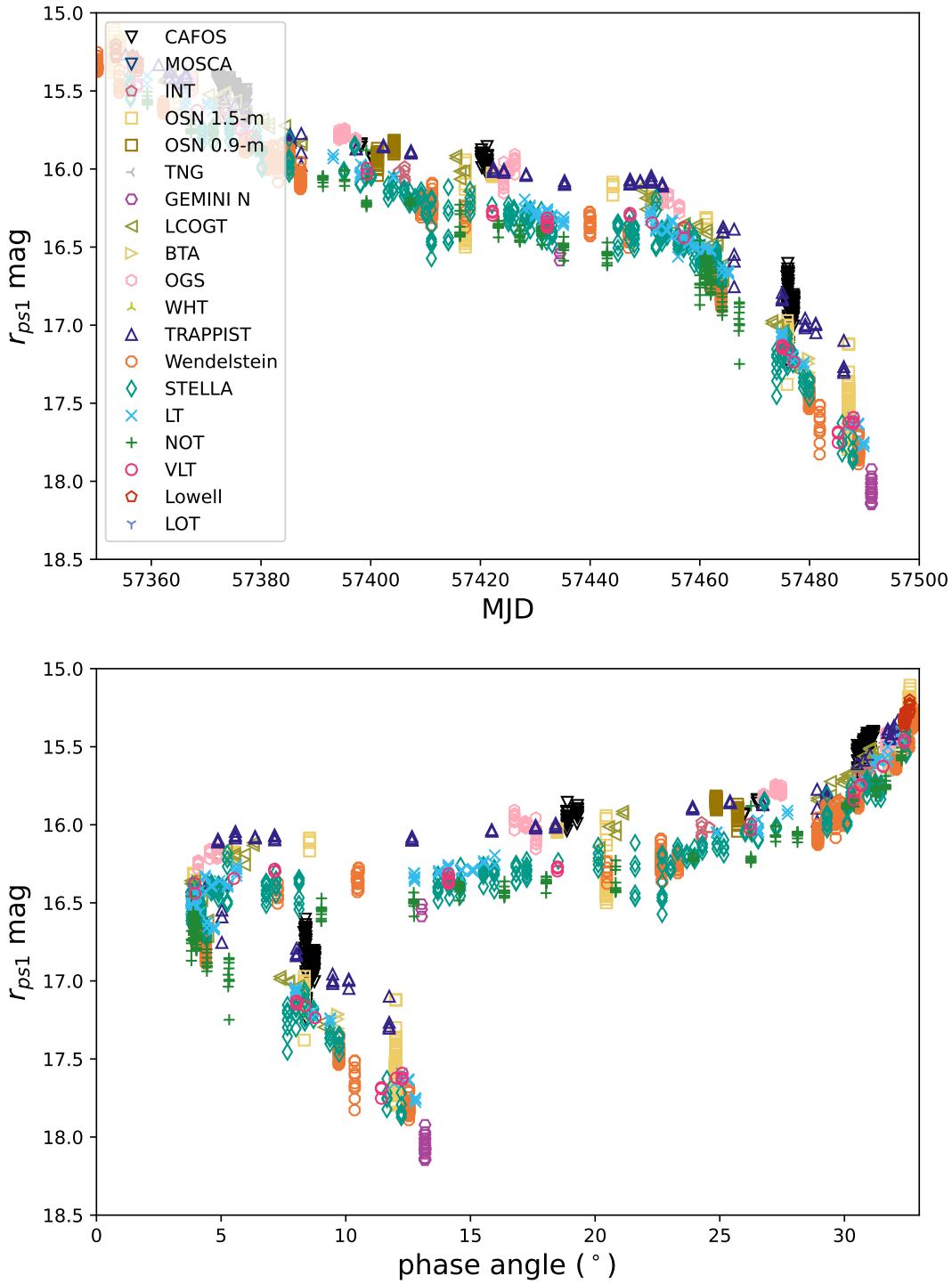

Figure 3.4 Light curve around low phase angles, plotted against time (top) and phase angle (bottom). All points have been calibrated to PS1 r-band. A clear offset is seen in the TRAPPIST (blue triangles), OSN (yellow squares), OGS (pink hexagons) and CAFOS (black downward-triangles) points which were measured in Johnson–Cousin R filter. The majority of the other points were measured in SDSS r type filters.

3.4 Analysis

3.4.1 Coma colour

Table 3.3 Average colour of 67P coma across the observation period measured by different instruments. All instruments are calibrated to the Pan-STARRS magnitude system.

Telescope/instrument	Filter range	Colour index
Gemini N/GMOS	g–r	0.65 ± 0.04
	r–i	0.26 ± 0.03
	i–z	0.03 ± 0.06
LT/IO:O	g–r	0.61 ± 0.004
	r–i	0.27 ± 0.004
	i–z	0.08 ± 0.01
NOT/ALFOSC	g–r (from V and R)	0.61 ± 0.004
STELLA/WIFSIP	g–r	0.64 ± 0.02
	r–i	0.24 ± 0.03
	i–z	0.08 ± 0.05
TRAPPIST-South/CCD	g–r (from B, V and R)	0.60 ± 0.004
	r–i (from R and I)	0.20 ± 0.004
Wendelstein 2-m/WWFI	g–r	0.59 ± 0.02
	r–i	0.22 ± 0.02

The coma colour remains more or less constant throughout the apparition (Figure 3.5) indicating no significant change in the gas production relative to dust production around perihelion, which would be expected to cause a decrease in $g - r$, for example. Table 3.3 summarises the average colours measured by six different instruments during the campaign in $g - r$, $r - i$ and $i - z$. The colours for the NOT/ALFOSC and TRAPPIST-South have been converted from *B, V, R, I* to *g, r, i* (Jester et al., 2005).

The g–r colour of 67P is consistent with what we would expect the dust from a comet to look like at these heliocentric distances (Jewitt and Meech, 1986) and compared to ensemble properties measured in SDSS-style filters (Solontoi et al., 2012). Boehnhardt et al. (2016) reports a minor $g - r$ colour change from 0.56 to 0.62 measured within a 10 000 km apertures between 2015 September 10 and 2016 May 7. They report this from a sample of just four data points from across their data. I do not see the same trend in my calibrations of the Wendelstein data, in fact I see a slight opposite trend, however this discrepancy could be explained by the differences in calibration methods between our works. Since I have access

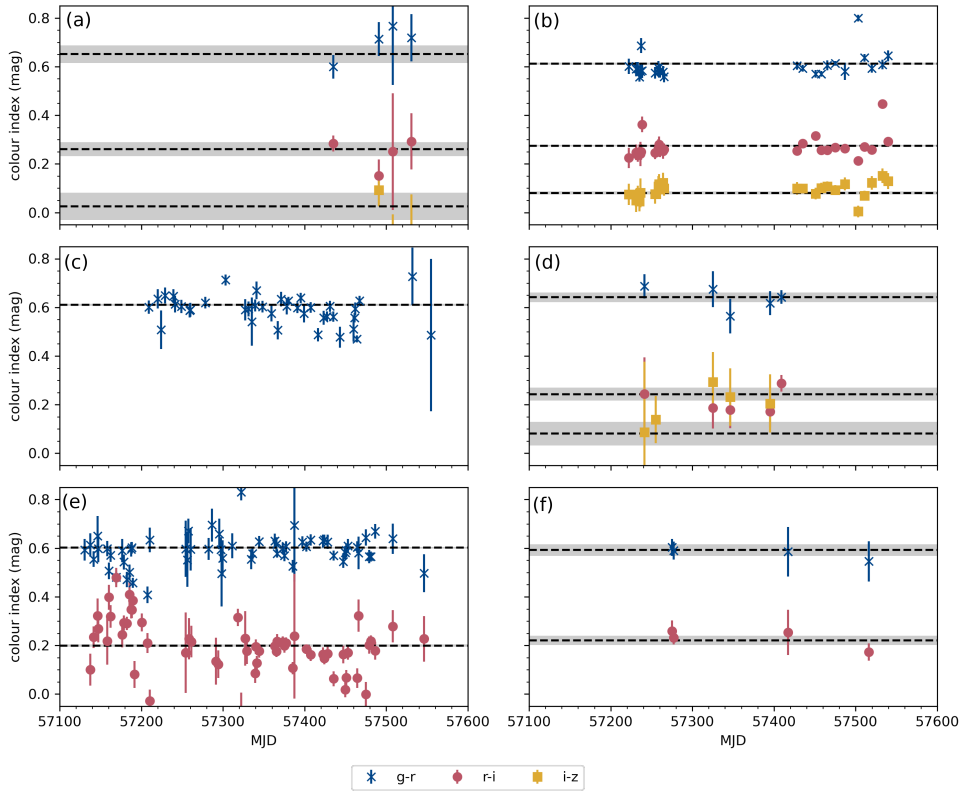

Figure 3.5 Colour against time between 2015 March 19 and 2016 July 31 for comet 67P/Churyumov-Gerasimenko measured with (a) Gemini-North, (b) the Liverpool Telescope, (c) the Nordic Optical Telescope, (d) STELLA, (e) TRAPPIST-South and (f) the Wendelstein 2-m telescope in the *g*-, *r*-, *i*- and *z*-bands. The weighted mean colours are shown with the horizontal dotted lines and uncertainties as the shaded areas.

to colour data from a much wider span of time I can say that I do not see this subtle colour change in any of my data.

3.4.2 Searching for outbursts

67P was observed in *r*-band filters for almost its entire perihelion passage. I measured the maximum brightness of the comet as ∼13.2 within a 10 000 km aperture for the period of late August to early September 2015. The light curve (Figure 3.3) follows the predictions (Snodgrass et al., 2013) well and does not show any large-scale deviations from the expectations, which indicates the activity level remained more or less constant between apparitions. A brightness increase

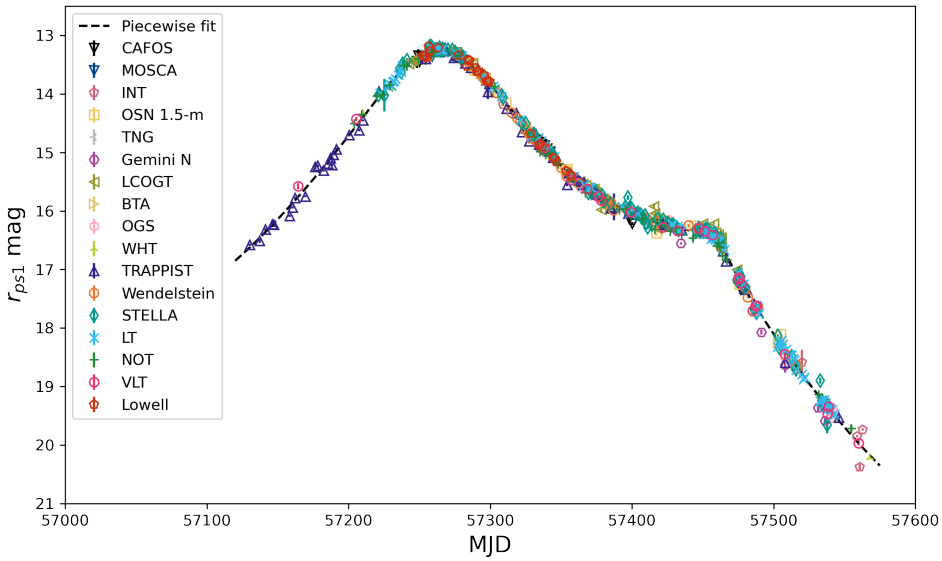

Figure 3.6 Light curve of 67P/Churyumov–Gerasimenko measured within 10 000 km aperture. Photometry has been calibrated and scaled to the r-band. A piecewise fit trend line has been plotted.

of ∼0.14 mag was obvious in multiple data sets on 2015 August 22, indicated in Figure 3.7, confirming the outburst seen by Boehnhardt et al. (2016) with the Wendelstein telescope. The number of telescopes pointed at 67P that night allowed me to constrain the event to within a few hours. The last observation taken by the LT at 05:51:25 UTC measured a brightness of 13.34±0.03, then about five hours later it was observed by the Lowell telescope between 11:17:19 and 11:46:24 UTC which measured an average brightness of 13.20±0.02. This increase in brightness is seen by the LT and Wendelstein the following night. LT measured 13.19±0.02 and Wendelstein measured 13.22±0.03.

In order to properly characterise these outbursts and discover others missed by manual inspection I removed the underlying photometric trend. I modelled the trend as a simple polynomial piecewise fit. The data are scaled and shifted to fit to the curve as described in section 3.3.2. This was done because of subtle offsets between the data sets remaining after the colour calibration. Figure 3.6 shows the light curve with the offsets between data removed and the piecewise fit plotted underneath. Figure 3.8 shows the outburst of 2015 August 22 with the trend removed. I modelled an exponential fit to the outburst, peaking at 0.14 ± 0.02 mag brighter than the baseline and falling off as $m \propto e^{-0.59t}$, where t is measured in days. No further outbursts were seen after the removal of the

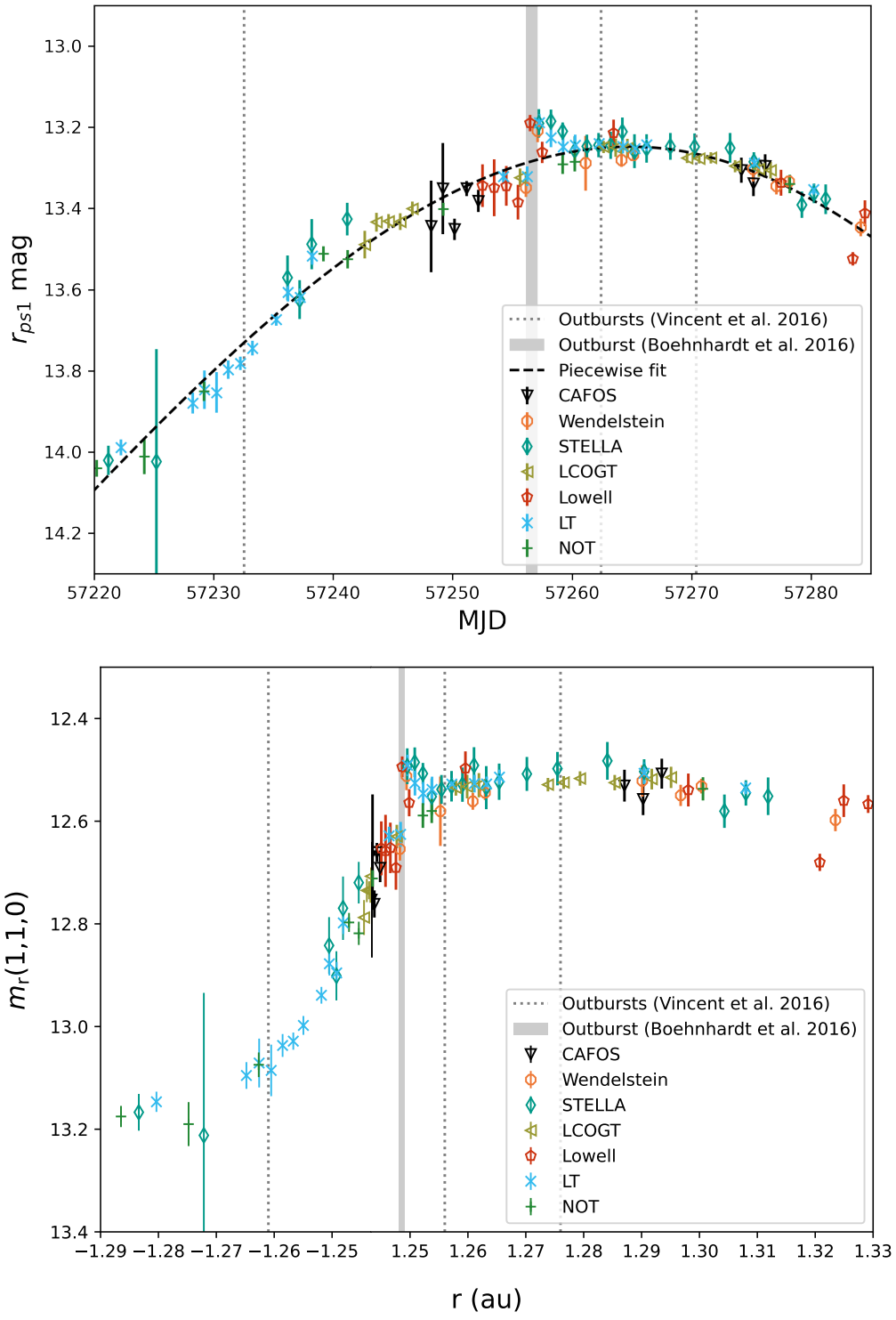

Figure 3.7 Light curve of 67P/Churyumov–Gerasimenko around perihelion between 2015 July 17 and 2015 September 25, plotted against time (top) and heliocentric distance (bottom). A piecewise fit trend line has been plotted (top) and the time of the outburst seen in Boehnhardt et al. (2016) has been highlighted. The grey dotted line show the times of the brightest outbursts seen by Vincent et al. (2016).

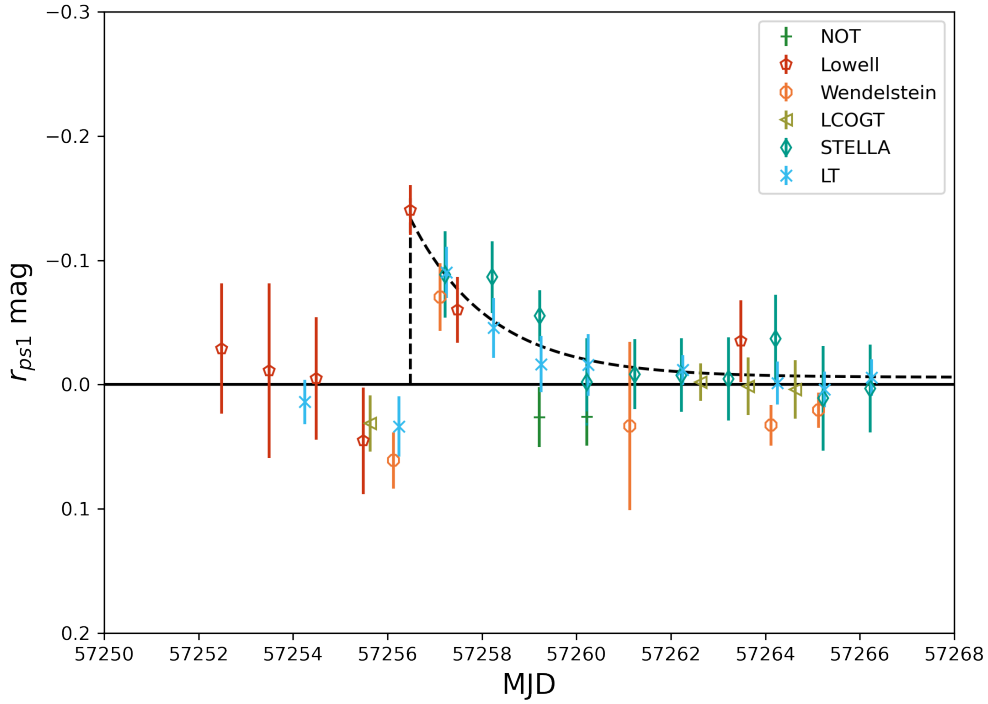

Figure 3.8 Light curve around 2015 August 22 with the baseline photometric trend removed. An anomalous increase in the brightness is obvious. The Lowell points have been shifted to match the trend. The anomaly shows signs of being an outburst with a rapid brightening with an exponential fall-off. I estimate a brightening of 0.14 mag

baseline trend. I tried to find evidence in the photometry of outbursts seen on 2016 February 19 (Grün et al., 2016) and 2016 July 3 (Agarwal et al., 2017) but could not find anything convincing. I also looked to see if we could confirm the potential outburst seen from the ground on 2015 September 19 (Knight et al., 2017) but I could not find convincing evidence of brightening within the other data at this time.

3.5 Discussion

3.5.1 Outburst of 2015 August 22

I can confirm the outburst seen in the comet coma morphology by Boehnhardt et al. (2016) in my analysis of the 67P photometry. The date and time of this event

corresponds to an outburst seen by the NavCam instrument onboard Rosetta: outburst #16 from Vincent et al. (2016), which was observed on 2015 August 22 06:47:04 UTC. Outburst #16 could be connected to my outburst, it is bright and occurs immediately before the brightness increase seen in the ground-based data at 2015 August 22 11:17:19 UTC. The data taken with NavCam is uncalibrated so I do not know exactly how bright it is compared to the other outbursts seen with OSIRIS. Judging the images by eye we can see that the outburst is as bright as, if not brighter than, the other outbursts and shares morphological similarities with the brightest outbursts seen with OSIRIS.

Looking at NavCam images from ESA's Planetary Science Archive (PSA), the first image taken ∼2 hours following the outburst seems to show increased activity; it has an increased brightness in the inner coma compared with other images taken around that time (Figure 3.9). This indicates a possible longer term event compared to typical events seen from the spacecraft, which appear only in single frames. However, the comet was observed from a different orientation in the image following the outburst, and activity level varies depending on the part of the surface that is illuminated so it is difficult to make a direct comparison and make a clear statement about the longevity of the outburst. OSIRIS did not acquire images at the time of the outburst, the images that were closest in time to the outburst were taken 2015 August 22 05:55:43 UTC and 2015 August 23 05:08:20 UTC (Figure 3.10). These images taken before and after the outburst do not show any significantly increased activity (C Tubiana 2022, personal communication, 22 July).

The Boehnhardt outburst looks different in morphology to the Vincent outburst, the former is a jet-like structure while the latter is much broader and fan-like in its appearance, although it is essential to point out that these two structures are very different in scale. The outbursts photographed by Rosetta are of the order of 10 km in size whereas the Boehnhardt event is approximately 5000 km in length. The source locations estimated for these events also differ, Boehnhardt et al. (2016) suggests the feature originated from latitudes between +5° and +10° on the nucleus whereas Vincent et al. (2016) see their outburst coming from a latitude of -40°. This discrepancy may be due to differing coordinate systems, since Boehnhardt et al. (2016) uses a simplified spherical planetocentric model to estimate the source location and Vincent et al. (2016) uses more accurate planetographic coordinates. Planetocentric latitude refers to angle between the equatorial plane passing through the centre of the body, planetographic latitude

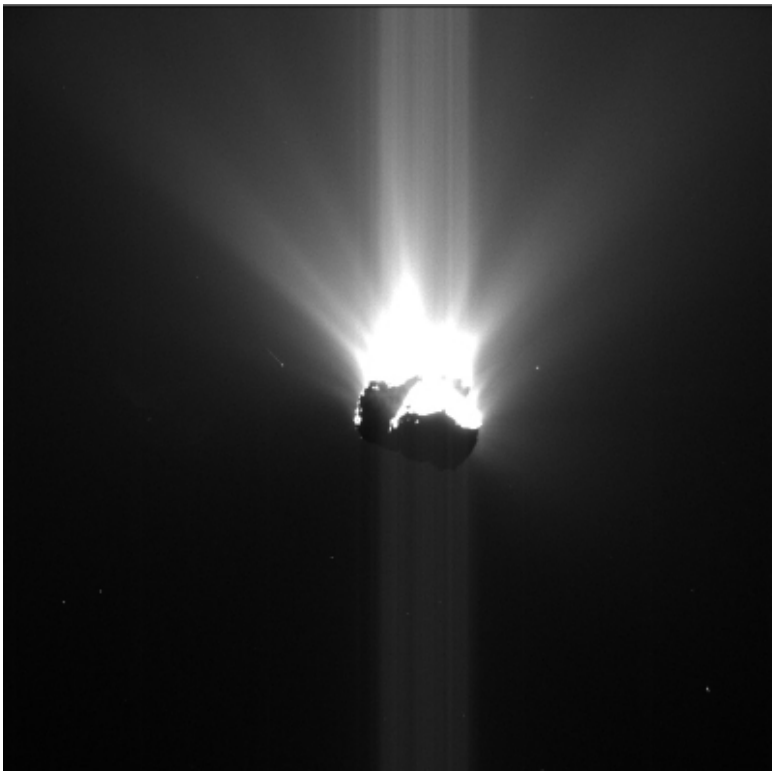

Figure 3.9 NavCam image of 67P taken 2015 August 22 08:55:01 UTC, $\sim$ 2 hours after #16, Figure 3.1. It shows increased brightness in the inner coma hinting that the outburst could have caused sustained activity for an extended period of time. However, the comet was observed from a different orientation and the activity levels varies depending on surface illumination so it is hard to say for sure this is the same activity event.

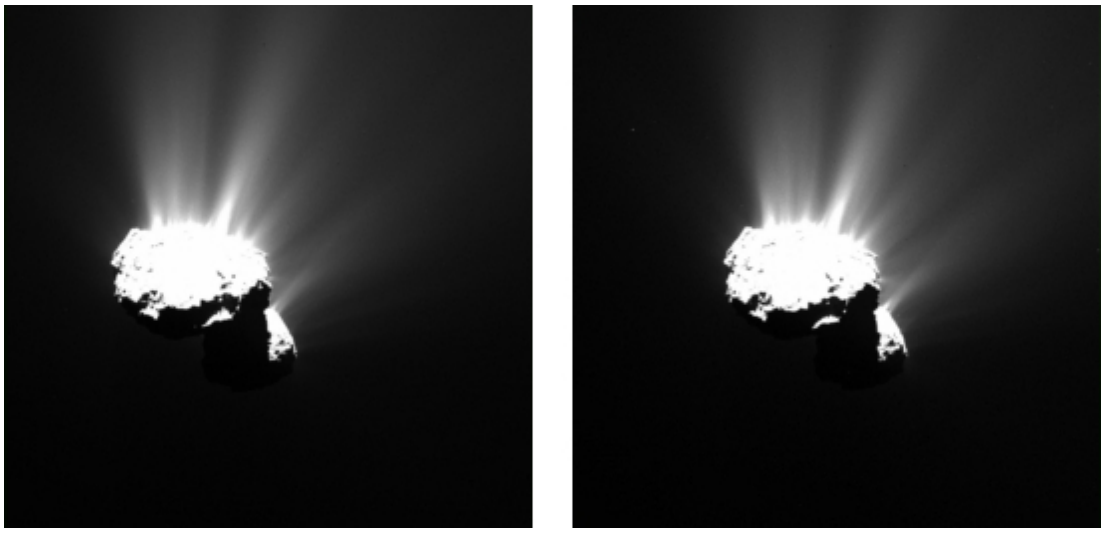

Figure 3.10 OSIRIS images of 67P taken at the closest times before and after the outburst. The images were taken 2015 August 22 05:55:43 UTC (left) and 2015 August 23 05:08:20 UTC (right). No significantly increased activity can be seen, implying the outburst occurred on a much shorter timescale than the cadence of OSIRIS images.

is defined as the angle between equatorial plane and a vector through the point of interest that is normal to the reference surface of the body. With 67P's unusual shape it is anticipated that there will be discrepancies between the two systems measuring from the same point. The angles measured by the two systems could produce significantly different results. However, it would not be enough to explain the discrepancy I see, especially since the two events originate from different hemispheres which would not change between coordinate systems. Since the scales of these outbursts differ by orders of magnitude, it could be possible that outburst #16 is but one of many small outbursts that contribute to this larger coma change. Outburst #15 (Figure 3.1) was seen about 24 hours before #16 and could be contributing to the brightening but there was no brightening seen in the data when outburst #15 happened. It could be possible a larger outbursting event was missed by the in situ instruments, however this is unlikely since during that time the probe was regularly monitoring the nucleus, taking images with an average separation of 12 minutes and some as short as 5 minutes (Vincent et al., 2016). All of this uncertainty makes it difficult to draw a definitive connection between the Boehnhardt event and in situ observations.

3.5.2 Searching for other confirmed outbursts and linking observations to surface changes

The outburst of 2015 August 22 is on the smaller side of outbursts typically seen from the ground in other comets. While this outburst was easily spotted, it is possible it could have been missed had I not known where to look. It was noticed due to its connection with the morphology change seen by Boehnhardt et al. (2016). Other outbursts seen by the spacecraft were not seen on the ground. Grün et al. (2016) reports a sustained increase in $Af\rho$, using a 5000 km aperture, of the comet around the event of 2016 February 19 (MJD 57437.4), based on TRAPPIST data. However this sustained brightness increase is not seen in my magnitude data. This could be due to the low phase angle at the time of observations, meaning the phase angle effects masked any potential signal from the data. It is worth noting that my magnitudes are not phase-corrected whereas Grün et al. (2016) presents phase corrected data. Also this sustained brightness could have been subtracted from the data during detrending. I do not detect the brightening independent of the spacecraft data.

A major goal of this study was to see if any surface changes seen by Rosetta could

be connected to observations made from the ground. One of the most notable surface changes on the comet was the Aswan cliff collapse (Pajola et al., 2017). This collapse was linked to a bright outburst seen by NavCam on 2015 July 10 (MJD 57213.1). There is unfortunately a gap of several days in the ground-based data that coincides with this event meaning any increase in brightness would have been missed so it is impossible to say if this event could have been visible from the ground. El-Maarry et al. (2019) summarises and maps the major nuclear surface changes observed by Rosetta. I compared these observations to the estimated source positions of both the Vincent and Boehnhardt outbursts but I found no obvious signs of a surface change that corresponded to either position.

3.5.3 Dust mass estimate

In order to create more meaningful comparisons to physical quantities I estimate the mass of the 2015 August 22 outburst. This is done by multiplying the geometric cross-sectional area of the outburst by the dust grain density. I assume a dust r-band geometric albedo of $A_{\mathrm{P}} = 0.04$ (Keller et al., 1986) and a total geometric cross-sectional area, G, defined in Kelley et al. (2021b) as:

$$G = \frac{\pi r^2 \Delta^2}{A_{\mathrm{P}} \Phi(\theta)} 10^{-0.4(m - m_{\odot})} \tag{3.1}$$

where r is the heliocentric distance in km, Δ is the observer-comet distance in km, $\Phi(\theta)$ is the coma phase function evaluated at phase angle θ, m is the apparent magnitude of the total dust coma and $m_{\odot}$ is the apparent magnitude of the Sun at 1 au in the same bandpass and magnitude system. G is an area measured in km^2 so in order to convert G into an estimate of dust mass we need to make an assumption of the grain density and grain size distribution. I assume a grain density of 500 kg m^{-3}, to match the nuclear bulk density of Jorda et al. (2016), and a grain size distribution of $dn/da = a^{-2.6}$, constrained between dust grain radii of 1 μm and 10 μm. The choice of grain size distribution and constraints are chosen to match those of Vincent et al. (2016). To calculate the mass of the outburst I subtract the coma mass after the outburst from the coma mass before the outburst. Using these, I estimate the mass of my outburst to be 2.0×10^5 kg ($\sim$12 per cent of the total coma), which puts it in agreement with the mass estimates made by Vincent et al. (2016), who puts a constraint of 10^4 kg on the typical dust mass of outbursts seen by Rosetta, with 10^5 kg being the largest seen.

Grün et al. (2016) claim to observe an outburst of mass 10^3 kg from the ground, with such sensitivity I would expect to see many more outbursts than I do. My estimate is also in line with similar scale outbursts seen on other comets observed from the ground; Kelley et al. (2021b) estimates that the mass of outbursts from 46P/Wirtanen lie between 3×10^4 kg to 5 $\times10^6$ kg. It is encouraging to see that the outburst I see is of the same mass as the ones seen by Rosetta as this implies that the outburst seen from the ground is, if not one observed directly by Rosetta, an outburst of a similar scale to the largest seen. However, this raises the question as to why apparently none of the other similarly large outbursts were seen from the ground. The other brightest outbursts, including outburst #12, the brightest seen by Vincent et al. (2016), go unseen in the photometry. Perhaps this is due to the challenging viewing conditions that were present during the early part of the campaign when 67P was most active.

3.5.4 Comparison to 2021–22 apparition

I made a comparison to data taken during the 2021–22 apparition, where the viewing conditions were a lot more favourable. Despite the better viewing conditions, there was not as an intensive monitoring campaign for this apparition. Sharma et al. (2021) observed two outbursts using the 70-cm GROWTH-India Telescope on 2021 October 29 and 2021 November 17. The second outburst was also observed and confirmed by the LCO Outbursting Objects Key (LOOK) Project (Kelley et al., 2021a; Lister et al., 2022). These outbursts came 4 days before and 15 days after perihelion respectively. This lends credence to the fact that activity levels remain similar between orbits since it was at this point around perihelion in the 2015–16 apparition where Rosetta detected the highest rate of outbursts. The outburst I saw on 2015 August 22 occurred 9 days after perihelion. The Sharma outbursts were measured to have masses of 5.3 $\times10^5$ kg and 1.3 $\times10^6$ kg respectively. This is consistent with the mass I estimated for my outburst but it is still an order of magnitude larger than the typical outburst seen by Rosetta.

I observed 67P with the LT during its 2021–22 apparition, the r-band light curve is shown in Figure 3.11. As with the previous apparition, the comet follows the predictions well. The predictions of the dust flux were created based on the simple power law dependencies on heliocentric distance derived by Snodgrass et al. (2013). These were based on the three previous apparitions of 67P prior

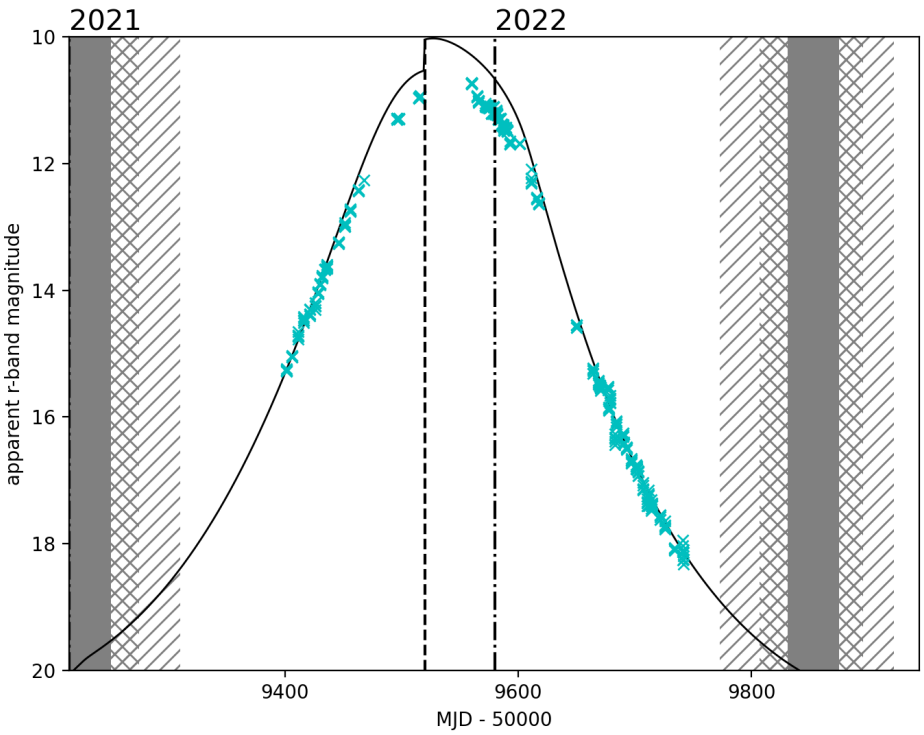

Figure 3.11 r-band light curve of the 2021–22 67P apparition. Observations were taken at the LT. The solid black curve is the predicted brightness of the comet. The step in the curve between pre- and post-perihelion is not a real feature and is due to the simplistic power law functions used in the prediction. The vertical dashed line shows the time of perihelion. The hatched patterns shows when solar elongation below 50° (hatched), 30° (cross-hatched) and 15° (solid grey). The dash-dotted line shows the division between years.

to 2016, but since the activity did not change significantly between them these still can be used to give a good first-order description of the dust brightness. The discrepancy around perihelion is due to the simplification of the models and should not be seen as a deviation from predictions. A more thorough prediction could have been created to more accurately predict the activity around perihelion using the detailed sublimation models of Snodgrass et al. (2013), but this was not my indention and these power laws merely served as a rough estimate of the overall trends. Excluding the discrepancies around perihelion due to oversimplification of the model, the data is a good match for the predictions pre- and post-perihelion which suggests no difference in activity levels between apparitions. No outbursts were seen in this data. This data was unfortunately marred by extended periods of telescope downtime due to a volcanic eruption on La Palma. As luck would

have it, the eruption coincided with perihelion and the two outbursts that were seen by Sharma et al. (2021), which meant I was unable to independently confirm these outbursts using the LT.

All of this highlights the fact that characterising small-scale outbursts of a comet and linking it to nuclear activity is still challenging, even when I have direct comparisons from spacecraft data.

3.6 Conclusions

I developed a pipeline for the consistent calibration of the multitude of disparate data from the ground-based observing campaign accompanying the Rosetta mission. The pipeline worked well with a processing success rate of ∼83 per cent across the data. The photometry of 67P followed the predictions based on previous apparitions: it showed no obvious change in activity levels from orbit-to-orbit and coma colours remained constant throughout the apparition. The calibrated data allowed for a careful search for outbursts through the perihelion period between 2015 April and 2016 August. I discovered one outburst on 2015 August 22 with a magnitude increase of ∼0.14 mag. This event confirms that the brightening seen in Boehnhardt et al. (2016) was a sign of an outburst. The brightness and estimated mass of this outburst put it in line with the outbursts directly observed on the nucleus by Rosetta. Linking this event with in situ outbursts proved challenging: while an in situ outburst was seen within the same time period as the brightening event, discrepancies in the surface origin estimates and the differences in scale of the in situ outbursts compared to the large-scale coma morphology made it hard to prove that there was a direct link between them. No other outbursts were seen in my data despite the many in situ events observed. I conclude that events of this scale are extremely challenging to observe from the ground and bridging the gap between large-scale coma changes and small-scale nuclear activity remains to be understood.

Chapter 4

A TRAPPIST survey of the activity of 14 comets

4.1 Introduction

Several studies have been undertaken into a large-scale statistical analysis of comets, mainly focusing on narrowband photometry (e.g. A'Hearn et al., 1995; Cochran et al., 2012; Fink, 2009; Langland-Shula and Smith, 2011). While I am not able to match these studies in terms of pure numbers, what this study offers is a study of how the activity changes over a broader timescale. This study is focused purely on broadband photometry, which is more commonly used for long-term monitoring. I aim to compare the long-term activity trends of these comets, how they vary from comet-to-comet and how they vary between families. This chapter is focused on applying my previously developed pipeline to existing TRAPPIST survey data. TRAPPIST is a pair of small robotic telescopes, one at La Silla observatory in Chile in the southern hemisphere, and the other at Oukaïmeden Observatory in Morocco in the northern hemisphere, meaning it can observe comets continuously with more or less identical instrumentation (Jehin et al., 2011). I focus on fourteen comets that were observed extensively by TRAPPIST in broadband *BVRI* filters. They were selected so as to include a representative sample of each of the dynamical families. I want to compare how the long-term trends vary from comet-to-comet and between families. Understanding activity will help us distinguish dynamically ages, compositional differences and select targets for space missions, ground-based surveys and detailed spectroscopic study.

4.2 Observations

Table 4.1 lists the 14 comets targeted by TRAPPIST in this survey and summarizes their orbital parameters. Details of the observations of each comet are summarised in Table 4.2 which include the range of dates and heliocentric distances at which the comets were observed as well as the filters used in the observations.

Table 4.1 Orbital parameters and classifications of comets targeted by TRAPPIST. Orbital parameters obtained from JPL Horizons. Classification obtained from CODE catalogue (Królikowska and Dybczyński, 2020).

Name	Class.	a (au)	q (au)	e	i(°)	Period (y)	$T_{\rm J}$
9P/Tempel 1	JFC	3.1465	1.5424	0.5098	10.5	5.5816	2.969
46P/Wirtanen	JFC	3.0927	1.0554	0.6588	11.7	5.4390	2.818
88P/Howell	JFC	3.1087	1.3582	0.5631	4.38	5.4811	2.948
103P/Hartley 2	JFC	3.4698	1.0587	0.6949	13.6	6.4635	2.641
246P/NEAT	JFC	4.0280	2.8798	0.2851	16.0	8.0843	2.913
C/2009 F4	DNC	–	5.4549	1.0018	79.3	–	—
C/2009 P1	DNC	–	1.5505	1.0010	106.2	–	-0.432
C/2011 L4	DNC	–	0.3015	1.0000	84.2	–	—
C/2012 F6	LPC	487.1	0.7312	0.9985	82.6	10 752	0.147
C/2012 K1	DNC	–	1.0546	1.0002	142.4	–	—
C/2013 A1	DNC	–	1.3998	1.0001	129.0	–	-0.919
C/2013 R1	LPC	515.5	0.8118	0.9984	64.0	11 705	0.499
C/2013 US_{10}	DNC	–	0.8230	1.0003	148.9	–	2.210
C/2015 ER_{61}	LPC	382.9	1.0421	0.9973	6.35	7494	1.271

Table 4.2 Summary of observations of comets made by the TRAPPIST telescopes.

Target	TS/TN	Filters	Date range	r range (au)		Perihelion date
			(YY/MM/DD)	Pre-perihelion	Post-perihelion	(YY/MM/DD)
9P	TS	*B,V*	11/02/09 – 12/01/21	—	1.536–3.296	11/01/10
	TS	*B,V,R,I*	16/01/20 – 16/09/25	2.337–1.553	1.543–1.632	16/08/02
46P	TS	*B,V,R,I*	18/06/15 – 18/12/19	2.317–1.056	1.056–1.058	18/12/12
	TN	*B,V,R,I*	18/08/17 – 19/05/09	1.795–1.055	1.055–2.052	18/12/12
88P	TS	*B,V,R,I*	15/03/15 – 17/02/03	1.380–1.359	1.361–4.463	15/04/06
	TN	*B,V,R,I*	17/02/15 – 20/09/09	4.494–1.366	—	20/09/28
103P	TS	*B,V*	10/12/10 – 12/04/30	—	1.211–4.630	10/10/28
246P	TS	*B,V,R,I*	12/01/24 – 14/09/06	3.440–2.998	2.886–3.982	13/01/28
C/2009 F4	TS	*B,V,R,I*	11/03/09 – 15/02/16	5.874–5.457	5.460–9.588	11/12/31
C/2009 P1	TS	*B,V,R,I*	10/12/09 – 13/05/09	4.705–1.771	2.320–5.807	11/12/23
C/2011 L4	TS	*B,V,R,I*	12/01/24 – 13/02/08	5.795–0.856	—	13/03/10
C/2012 F6	TS	*B,V,R,I*	12/11/18 – 13/06/06	2.259–0.819	1.063–1.538	13/03/24
C/2012 K1	TS	*B,V,R,I*	13/03/28 – 15/12/14	6.208–1.382	1.067–5.812	14/08/27
C/2013 A1	TS	*B,V,R,I*	13/03/10 – 15/03/21	6.662–1.401	1.400–2.446	14/10/25
C/2013 R1	TS	*B,V,R,I*	13/09/11 – 14/10/14	1.920–1.057	1.256–4.211	13/12/22
C/2013 US_{10}	TS	*B,V,R,I*	14/05/16 – 16/01/01	6.649–1.339	1.001–1.184	15/11/15
	TN	*B,V,R,I*	16/09/01	—	4.159	15/11/15
C/2015 ER_{61}	TS	*B,V,R,I*	16/02/18 – 17/12/11	5.564–1.046	1.050–3.223	17/05/09
	TN	*B,V,R,I*	17/07/28	—	1.642	17/05/09

4.2.1 9P/Tempel 1

9P/Tempel 1 was discovered by Wilhelm Tempel on 1867 April 3 (Yeomans et al., 2005). It is a JFC with an orbital period of 5.6 years and comes to perihelion at a distance of 1.5 au from the Sun.

9P was the target of NASA's Deep Impact mission, which intentionally crashed a spacecraft into the surface of the comet on 2005 July 4. The mission revealed a nucleus that was different in shape and topography to the two JFCs previously visited by other spacecraft (Borrelly and Wild 2, Figs. 1.2b & c). This called into question the definition of a typical comet nucleus, or if a typical nucleus even existed. The topography featured suspected impact craters and distinct layers; frequent small outbursts from the surface of the comet were also seen. The surface itself was not icy but the presence of volatiles in the ejecta implied ice deposits near the surface. The impact excavated a large volume of very fine particles, too numerous to have been created by the impact alone, suggesting that fine material covered the surface to a depth of tens of metres. The impact also excavated organic molecules such as HCN and CH_3CN (A'Hearn et al., 2005).

9P was visited again on 2011 February 14 by NASA's Stardust-NExT mission. This mission increased imaging coverage to almost two-thirds of the nuclear surface, including the 2005 impact site, which left behind a 50-m deep crater, but it is possible the crater was initially larger. The nucleus had an average radius of 2.83±0.1 km. 30 per cent of the surface was covered in smooth flow-like deposits, suspected to be deposits from eruptions after the nucleus gained its current shape. The craters thought previously to be from impacts are instead from volatile outbursts. Comparing the surface from the Deep Impact images, most of the surface remained unchanged, the only change was seen along a 10–15 m thick deposition, which had retreated by up to 50 m in some places. Overall, activity was lower in 2011 than 2005, with most of the jets coming from an eroding scarp (Veverka et al., 2013).

9P was observed by the TRAPPIST-South telescope between 2011 February 9 and 2012 January 21 in B- and V-bands and between 2016 January 20 and September 25 in B-, V-, R- and I-bands; this covers both the 2011 and 2016 apparitions of 9P.

The light curves of the two observed apparitions of 9P are plotted in Figure 4.1, with the filled and unfilled points representing the first and second apparition re-

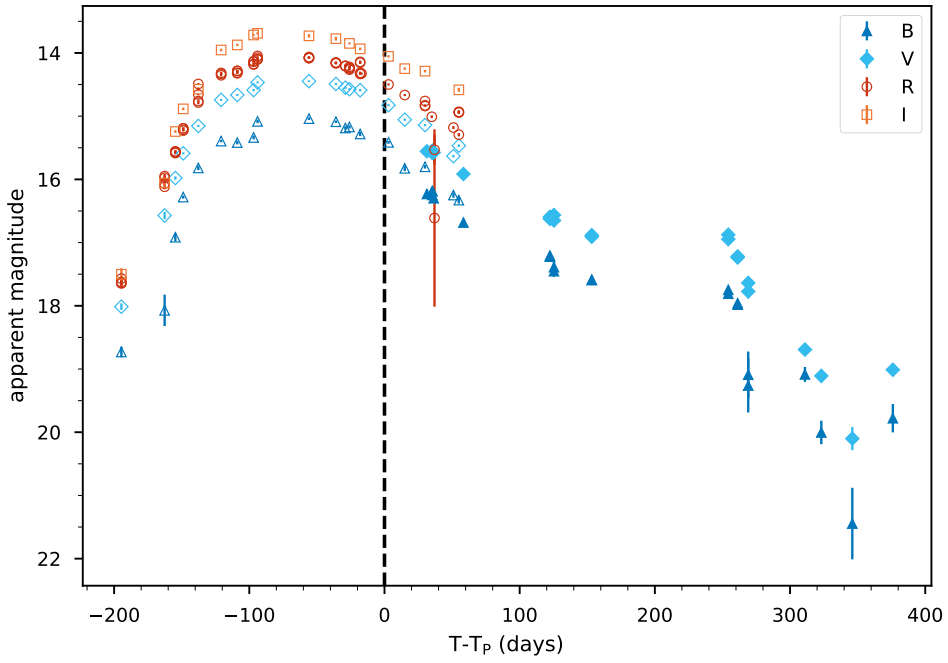

Figure 4.1 Light curve of 9P/Tempel 1 measured in B-, V-, R- and I-bands by the TRAPPIST-South telescope in $\rho = 10\,000$ km apertures. Data from both apparitions are plotted against time from perihelion ($T - T_P$), with filled and unfilled points representing the first and second apparitions respectively.

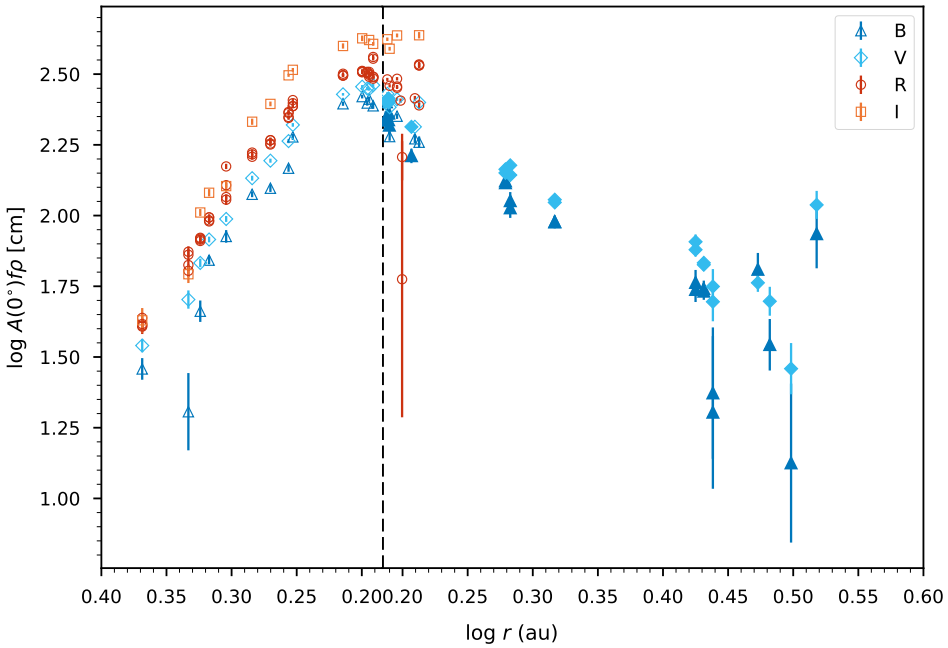

Figure 4.2 $Af\rho$ vs r of 9P/Tempel 1 measured in B-, V-, R- and I-bands by the TRAPPIST-South telescope in $\rho = 10\,000$ km apertures. The vertical dotted line indicates the perihelion distance of $r = 1.54$ au. Data from both apparitions are plotted, with filled and unfilled points representing the first and second apparitions respectively.

spectively. The first apparition was observed 30 days after perihelion and followed 9P out to a distance of 3.3 au, measuring a peak brightness of 16.19 ± 0.06 in B-band and 15.55 ± 0.04 in V-band. During its second apparition, 9P was observed inbound from 2.3 au and was followed through to its perihelion at 1.54 au; observations continued for a short period post-perihelion, following it out to $r = 1.6$ au post-perihelion. Its brightness peaked about 2 months before perihelion with an R-band magnitude of 14.08 ± 0.03.

The heliocentric dependence of $Af\rho$, the dust production parameter, is plotted in Figure 4.2, from this I can measure the power law slope between $Af\rho$ and heliocentric distance r using simple least square linear fitting. In the first apparition, $Af\rho$ steadily decreases with heliocentric distance post-perihelion, following a relationship of $Af\rho \propto r^{-2.21 \pm 0.20}$ in V-band. By looking at Figure 4.2, I can assume that all the optical emission is from dust due to the fact that the $Af\rho$ measurements are larger in the redder filters than the bluer filters. The $Af\rho$ parameter assumes that dust is the only source of light and the spectra of dust is red so we would expect the I- and R-bands to give us larger measurements of $Af\rho$ than those derived from B- and V-bands. If the $Af\rho$ derived from B- and V-bands were larger than from the I and R-bands, that would imply there were other emissions in those bands which could not be coming from the dust. For the second apparition, the pre-perihelion power law slope, measured in R-band, was -4.88 ± 0.17 and post-perihelion the slope was -3.15 ± 1.36. In its second apparition, 9P shows an asymmetry between $Af\rho$ slopes about perihelion; the slope pre-perihelion is steeper than the slope post-perihelion. The two apparitions have broadly similar post-perihelion power law slopes, although the few points measured post-perihelion in the second apparition leads to a larger uncertainty in its slope. However, a visual inspection of both Figures 4.1 and 4.2, reveals that the brightness and $Af\rho$ trends of both apparitions broadly align, suggesting that the activity of 9P does not vary significantly between apparitions. I cannot confirm if the asymmetry is present in both apparitions since I do not have pre-perihelion measurements for the first, but since the post-perihelion slopes of both apparitions match it is logical to assume that the pre-perihelion slope of the first apparition would be similar to the second orbit if it had been measured. Meech et al. (2011a) saw this asymmetry between 9P's dust production slopes during the 2005 apparition, and looking at Yoshida's light curve[1] of the 2011 apparition while sparse, shows a steeper slope pre-perihelion to post-perihelion. This seems to be a common trend across all of its apparitions. Schleicher (2007)

[1] `http://www.aerith.net/comet/catalog/0009P/2011.html`

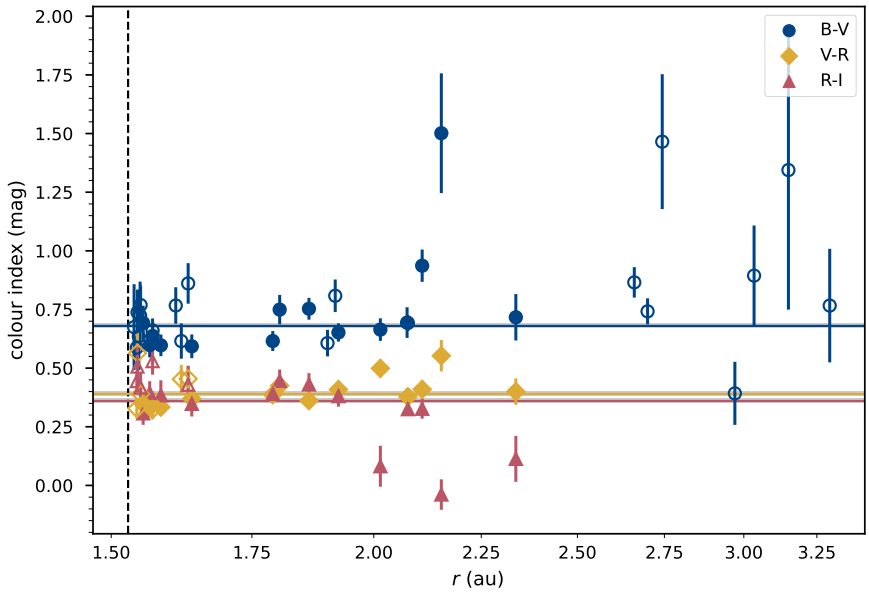

Figure 4.3 Colour index vs. r of 9P/Tempel 1 measured by TRAPPIST-S in the B-, V-, R- and I-bands. The filled and unfilled points represent pre- and post-perihelion measurements respectively. The means and uncertainties are drawn as horizontal lines and shaded areas respectively. The mean is a sigma-clipped mean, hence the shaded are may be too small to be visible and not encapsulate all the points. The vertical dotted line indicates the perihelion distance of $r = 1.54$ au.

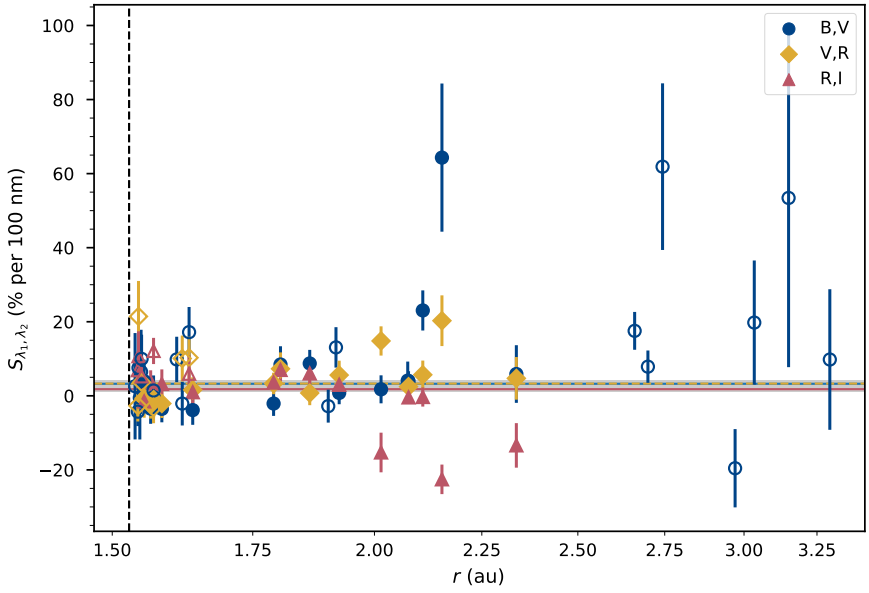

Figure 4.4 Spectral slope vs. r of 9P/Tempel 1 measured by TRAPPIST-S in the B-, V-, R- and I-bands. The filled and unfilled points represent pre- and post-perihelion measurements respectively. The means and uncertainties are drawn as horizontal lines and shaded areas respectively. The vertical dotted line indicates the perihelion distance of $r = 1.54$ au.

observed a 20 per cent decrease in dust production from 1994–2005, there is not much overlap in heliocentric distance in our data to confirm whether or not this decrease in activity is also seen between the 2011 and 2016 apparitions.

The colours of 9P (Figure 4.3) remain constant across both orbits, however I only have colour measurements in $B-V$ for the first orbit so I do not know how colours in $V-R$ or $R-I$ changed. I measured colours of $B-V = 0.68 \pm 0.01$, $V-R = 0.39 \pm 0.01$ and $R-I = 0.36 \pm 0.01$, which correspond to average spectral slopes (Figure 4.4) of $S_{B,V} = 3.3 \pm 0.9$ per cent per 100 nm, $S_{V,R} = 3.3 \pm 0.9$ per cent per 100 nm and $S_{R,I} = 1.8 \pm 0.7$ per cent per 100 nm. This uniform spectral slope across the *B-, V-* and *R*-bands, indicates a red spectrum with little or no variation in the gas production relative to dust production. Spectra of 9P measured during the 2005 apparition detected CN, C_2, C_3, NH and OH emission lines (Meech et al., 2011a; Picazzio et al., 2014). The CN and C_3 emissions are present in the *B*-band, the C_2 is in *B*- and *V*-band. These do not seem to have affected the colour.

9P does not show variation in activity between apparitions. There is asymmetry in dust activity pre- and post-perihelion with a steeper $Af\rho$ power law slope before perihelion compared to after. The colours of the comet remain consistent between apparitions, in $B-V$ at least, and do not vary across the course of the inner orbit. The lack of variation in $V-R$ across the second perihelion indicates little variation in gas production relative to dust production. The dust activity of the first apparition peaked about two months before perihelion at $r = 1.64$ au. The consistency of the dust activity between orbits indicates this is a dynamically old comet; the majority of its volatiles have been depleted and it has a small portion of active area that sublimates each orbit.

4.2.2 46P/Wirtanen

46P/Wirtanen was discovered by Carl Wirtanen on 1948 January 17 (van Biesbroeck, 1948). 46P is a JFC with an orbital period of 5.4 years. 46P is notable since it was selected as the original target for the Rosetta mission, as such it is a well studied comet. 46P is a hyperactive comet, one that produces more H_2O per unit time than is possible purely from sublimation of their small surface area, and outbursts regularly (Kelley et al., 2021b).

46P was observed in *B-, V-, R-* and *I*-bands by the TRAPPIST-South telescope

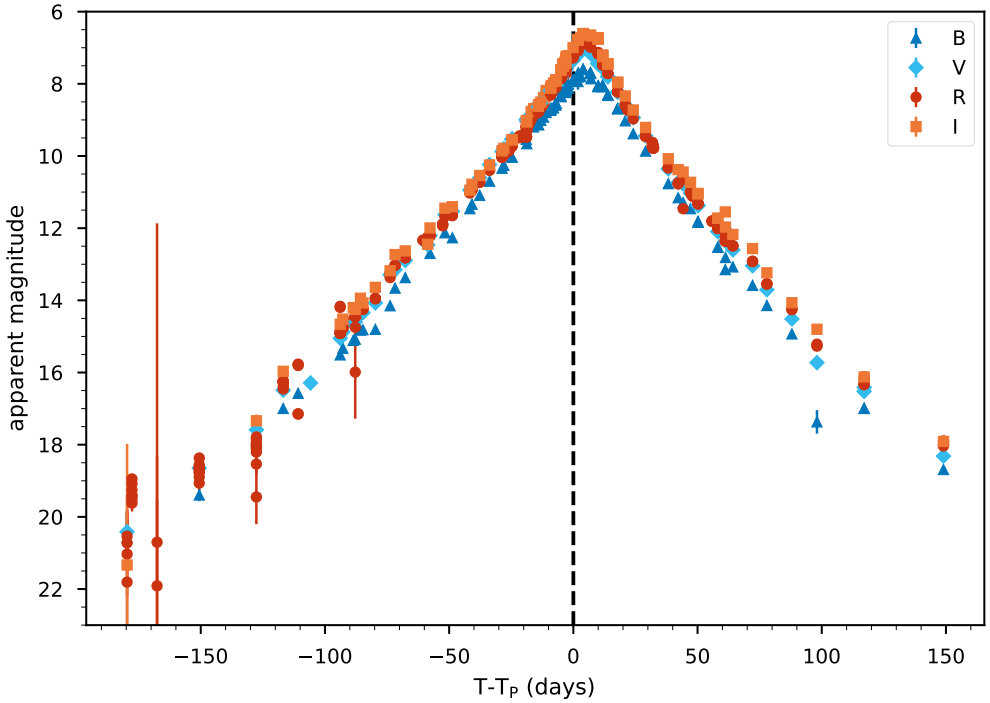

Figure 4.5 Light curve of 46P/Wirtanen measured by the TRAPPIST-South and TRAPPIST-North telescope in B-, V-, R- and I-bands in $\rho = 10\,000$ km aperture. Time is measured in days from perihelion ($T - T_P$).

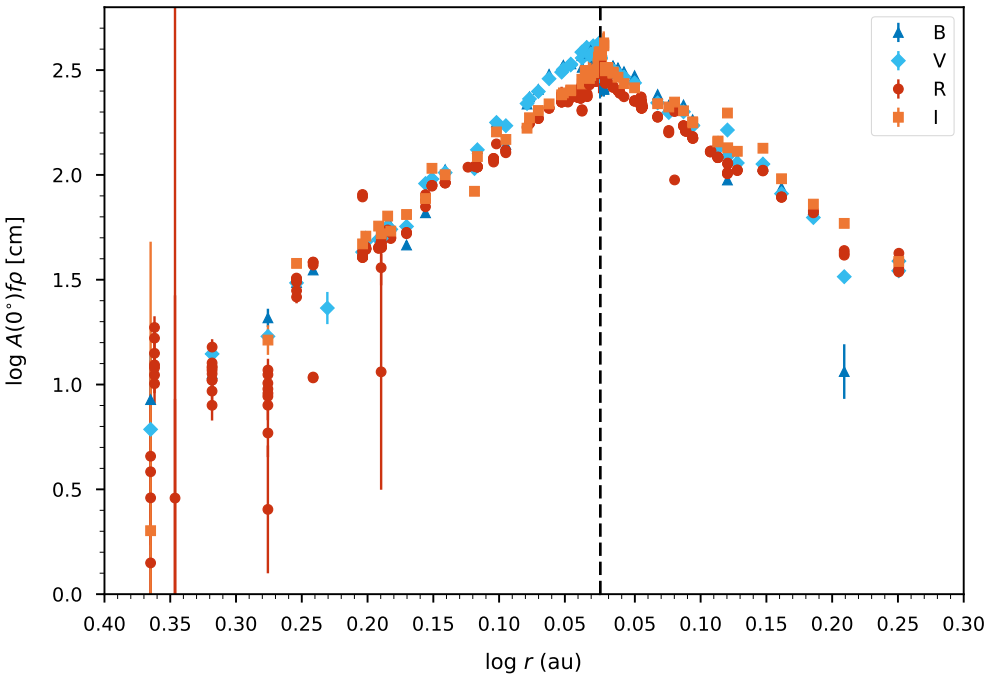

Figure 4.6 $Af\rho$ vs. r of 46P/Wirtanen measured in B-, V-, R- and I-bands by the TRAPPIST-South telescope in $\rho = 10\,000$ km apertures. The vertical dotted line indicates the perihelion distance of $r = 1.05$ au.

between 2018 June 15 and December 19 and by the TRAPPIST-North telescope between 2018 August 17 and 2019 May 9. The comet was observed continuously from an inbound distance of 2.3 au to perihelion at 1.06 au and then outbound to 2.0 au. The light curve of 46P is plotted in Figure 4.5. The brightness peaks just above 7 mag in the R-band approximately three days after perihelion at a heliocentric distance of 1.06 au.

The dependence of $Af\rho$ with heliocentric distance is plotted in Figure 4.6. It is in good agreement with published sources (Kelley et al., 2021b; Moulane et al., 2023). Pre-perihelion, $Af\rho$ follows a power law slope of -5.33 ± 0.09 and post-perihelion, it follows a slope of -4.03 ± 0.05. 46P demonstrates an asymmetry in pre- and post-perihelion $Af\rho$ slopes with a steeper slope pre-perihelion compared to post-perihelion. Moulane et al. (2023) also publishes this broadband TRAPPIST data alongside narrowband data. This asymmetry is also seen in dust production by Moulane et al. (2023) and in the water production by Combi et al. (2020). Our measurements of $Af\rho$ differ slightly than those obtained by Moulane et al. (2023), despite using the exact same data. Both our methods measure $Af\rho$ in a 10 000 km aperture but the difference probably lies in the difference of calibration methods, they calibrated off of standard stars whereas I cross-referenced catalogue magnitudes with field stars hence leading to subtly different magnitude values.

Rosenbush et al. (2021) do not see asymmetry in the dust production before and after perihelion and measure a power law slope of $r^{-3.4\pm0.4}$ both pre- and post-perihelion. Combi et al. (2020) measured the water production rate and found pre-perihelion power law slope of 17.8 ± 2.7 and post-perihelion slope of 8.6 ± 0.7. Knight et al. (2021) found that gas production symmetric around perihelion with a slope of -3.8 for carbon species (i.e. CN, C_3 and C_2) but they saw OH and NH fall off post perihelion, this fall-off was also seen by Moulane et al. (2023). Knight et al. (2021) and Moulane et al. (2023) suggest OH and NH production came predominantly from a source of icy grains in the coma. Carbon species exhibited coma morphology that varied with rotation which implied an active area 30 per cent, this higher active area suggests 46P is a 'young' JFC.

Protopapa et al. (2021) and Kareta et al. (2023) question the assumption of icy grain as the primary source of water activity and investigate the production rates purely from icy grains in the coma. They find a lack of ice signatures in the coma of 46P and no evidence for morphology change in different wavelengths that would appear in ice sublimation. Kareta et al. (2023) find that icy grains

alone cannot account for the water production rate observed and instead suggest that 46P has a much larger active surface fraction of 64 per cent.

The colours of 46P are plotted in Figure 4.7. It has average colours $B - V = 0.53 \pm 0.01$ and $R - I = 0.22 \pm 0.01$. The $V - R$ colour varies significantly across the course of the orbit so an average is not measured.

My colours are similar to the colours found in Kelley et al. (2021b). Using the conversion in Jester et al. (2005), $g - r = 0.49$ becomes $B - V = 0.45$ and $r - i = 0.13$ becomes $R - I = 0.36$, while not an exact match I am willing to put the discrepancy down to using conversions for stellar magnitudes not properly designed for comets. Rosenbush et al. (2021) measured colours of $B - V$ between 0.76 and 0.87 and $V - R$ between 0.38 and 0.50. They find no variation in $V - R$ at the same point I do, however they are observing in a much smaller aperture of an angular size of 2×FWHM, meaning the physical radii varied from 270 to 3000 km – significantly smaller than my apertures. Zheltobryukhov et al. (2020) found that contamination of gas emission in the V-band flux of 46P is only ~ 5.4 per cent for a small near-nucleus aperture with a diameter of about 200 km. As such, Rosenbush et al. (2021) state the gas contribution to the dust flux is negligible.

The spectral slopes measured each night are shown in Figure 4.8. 46P has an average spectral slope of $S_{B,V} = -10.6 \pm 1.1$ per cent per 100 nm and $S_{R,I} = -6.7 \pm 0.7$ per cent per 100 nm across the orbit. This shows a bluer colour typical of gas emissions in comets, which would be expected in $S_{B,V}$ but not $S_{R,I}$ which should theoretically be free of gas contamination. $S_{V,R}$ varies significantly through the passage and reaches a minimum of −60 per cent per 100 nm 24 days ($r = 1.1$ au) before perihelion. This trend is not seen in other colour bands indicating that the colour change is caused by increased production of gases that have their emissions within the B- and V-bands. Knight et al. (2021) finds emission lines of CN, C_3 and C_2, all of which have their emission lines in either the B- or V-bands. This implies gas production is at its peak just before perihelion. This is offset from the peak R-band brightness and peak in $Af\rho$ dust production which comes 3 days after perihelion. It would appear that the dust and gas production are not synchronised.

I see an apparent reddening in both $S_{B,V}$ and $S_{V,R}$ in Figure 4.8 just after perihelion. The phase angle of 46P across the observing window is plotted in Figure 4.9, you can see that the phase angle is at its lowest immediately after perihelion and therefore the contribution of dust (i.e. red) to the spectra is increased, which

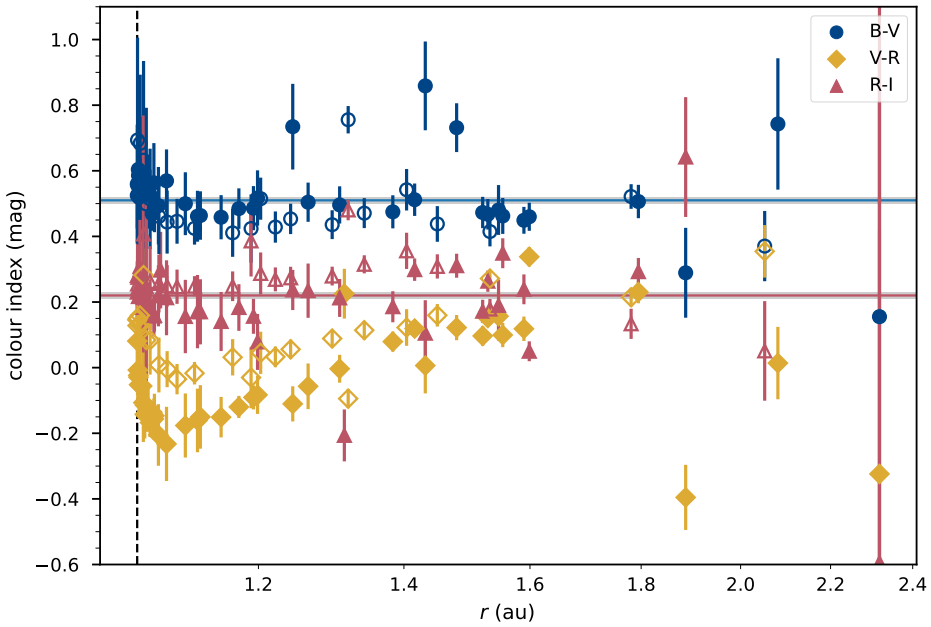

Figure 4.7 Colour index vs. r of 46P/Wirtanen measured with TRAPPIST-S and TRAPPIST-N photometry in the B-, V-, R- and I-bands. The filled and unfilled points represent pre- and post-perihelion measurements respectively. The means and uncertainties are drawn as horizontal lines and shaded areas respectively. The vertical dotted line indicates the perihelion distance of $r = 1.05$ au.

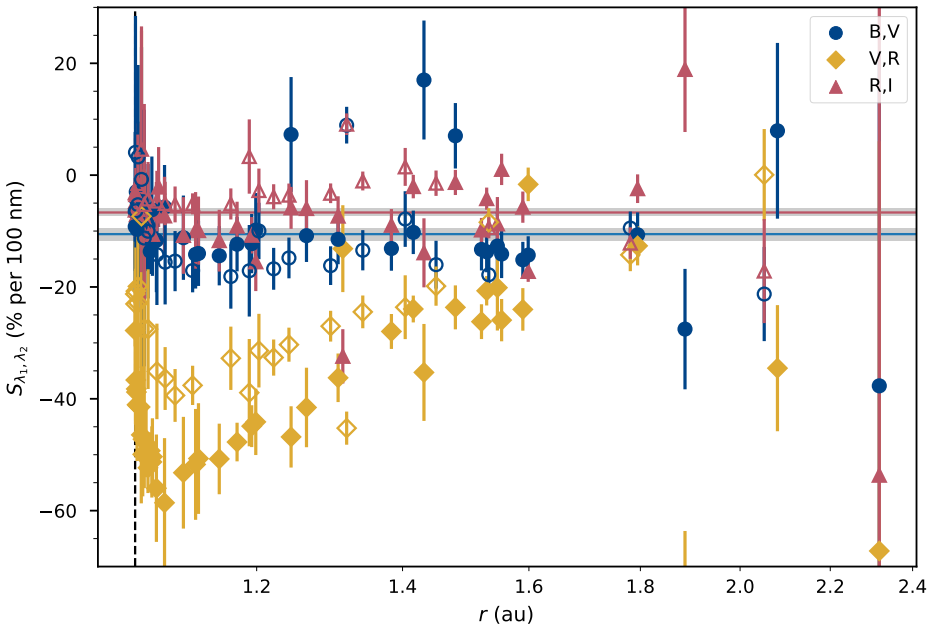

Figure 4.8 Spectral slope vs. r of 46P/Wirtanen measured with TRAPPIST-S and TRAPPIST-N photometry in the B-, V-, R- and I-bands. The filled and unfilled points represent pre- and post-perihelion measurements respectively. The means and uncertainties are drawn as horizontal lines and shaded areas respectively. The vertical dotted line indicates the perihelion distance of $r = 1.05$ au.

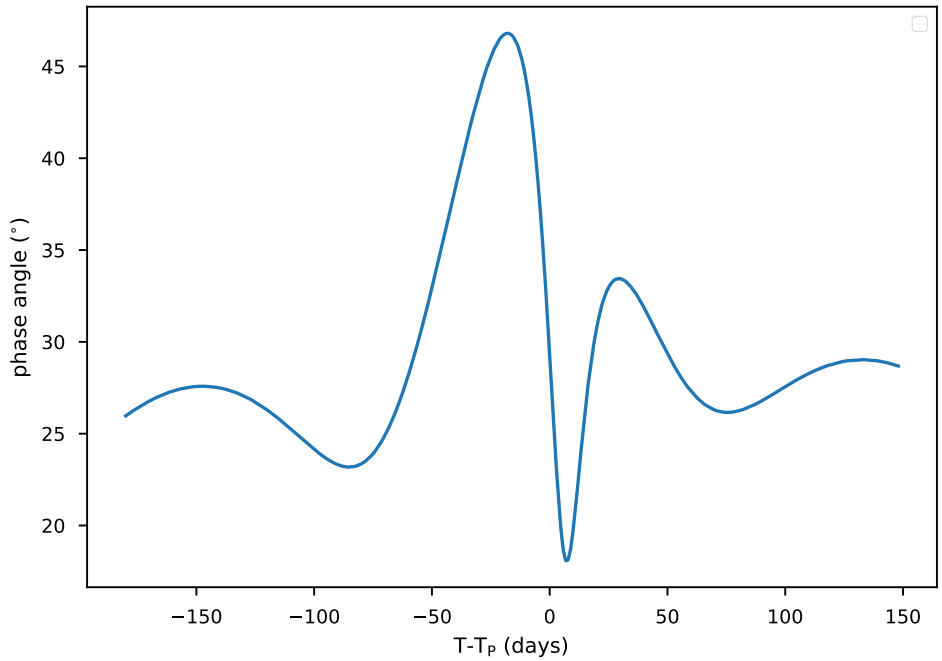

Figure 4.9 Phase angle of 46P/Wirtanen vs. time from perihelion ($T - T_P$) during the 2018–19 apparition.

would cause a reddening to occur in the spectral slopes. Therefore this peak in the slopes probably does not correspond to an actual sudden reddening but is instead a phase angle effect on the dust. Since the gas is emitting light and not reflecting it, it is not affected by phase angle so the change in brightness purely comes from dust contributions, hence the dramatic change in $V - R$ as the dust contribution to the R-band increases much quicker than gas contribution.

Zheltobryukhov et al. (2020) measured spectral slopes of $S_{V,R} = -16.4 \pm 7.1$ per cent per 100 nm and $S_{R,I} = -8.7 \pm 8.4$ per cent per 100 nm on 2019 February 8. On February 7 I measured slopes of $S_{V,R} = -27.0 \pm 2.6$ per cent per 100 nm and $S_{R,I} = -3.24 \pm 1.76$ per cent per 100 nm, which are broadly in agreement since they also see blue slopes. Rosenbush et al. (2021) measures to spectral slopes $S_{V,R} = 14.7 \pm 2.4$ per cent per 100 nm and $S_{R,I} = 9.3 \pm 2.6$ per cent per 100 nm across the whole orbit, measuring redder slopes than both myself and Zheltobryukhov et al. (2020).

46P is a hyperactive comet showing significant brightening in B- and V-bands about 20 days before perihelion relative to R-band, implying increased gas production relative to dust production. The R-band and hence dust production does

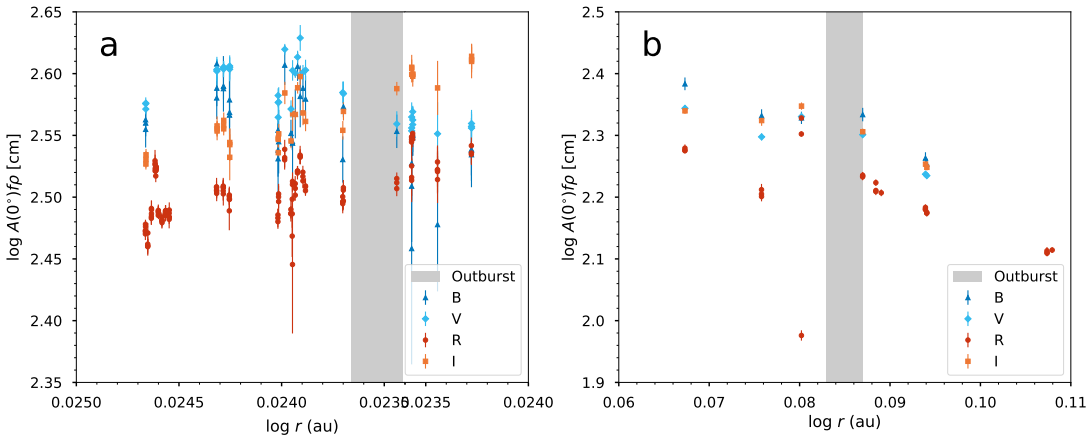

Figure 4.10 Light curve of 46P/Wirtanen around the outbursts of (a) 2018 December 12 and (b) 2019 January 28. The grey boxes span the constraints of the onset of the outbursts detected by Kelley et al. (2021b). No sign of the outburst is seen in (a). In (b) the light curve shows a deviation that occurs just before the lower constraint on the time of outburst. However, with the lack of data around this point, I am hesitant to draw a direct connection.

not peak until later, coming 3 days after perihelion. This discrepancy in peak gas and dust production is explained by the difference in expansion speeds between dust and gas. The dust expansion speed is far slower than the gas so remains within the viewing aperture longer. The dust activity slopes show an asymmetry in pre- and post-perihelion slopes with the inbound slope being steeper than the outbound slope. We do not see any outbursts in our data, four of the six outburst seen by Kelley et al. (2021b) are missed in my data. Two outbursts on 2018 December 12 and 2019 January 28 do coincide with my data set but I do not see any clear signs of outburst on preliminary investigation of either the light curve or coma morphology in my images. Kelley et al. (2021b) puts constraints on the onset of the December 12 outburst to occur any time between MJD 58462.249 and 58464.861. The only observation taken in this period was at MJD 58463.874, which did not show any obvious signs of brightening, suggesting the outburst seen by Kelley et al. (2021b) occurred before or after this time (Figure 4.10a). The constraints on the onset of the January 28 outburst are between MJD 58509.367 and 58511.165, looking at magnitudes we see no obvious increase but when converted to $Af\rho$, a slight deviation from the trend at this time does seem to be present (Figure 4.10b). I tentatively confirm that this outburst is seen in my data although it is not as clear as the one seen by Kelley et al. (2021b).

4.2.3 88P/Howell

88P/Howell was discovered by Ellen Howell at Palomar Mountain Observatory on 1981 August 29 (Howell and Kowal, 1981). It is a CO_2 rich (Reach et al., 2013) JFC with a period of 5.48 years, semi-major axis of 3.1 au and comes to perihelion at 1.4 au.

88P/Howell was observed over two apparitions in *B, V, R* and *I*-bands, the first by the TRAPPIST-South telescope between 2015 March 15 and 2016 February 24 and the second by the TRAPPIST-North telescope between 2017 February 15 and 2020 September 9. In its first apparition 88P was observed prior to perihelion at 1.38 au and was then followed through to its perihelion at $q = 1.36$ au and then out to a distance of 4.46 au. Early stages of 88P's second apparition were observed at large heliocentric distances of about 4.5 au, however the comet was below 20 mag in brightness, which I had previously determined to be the limit below which data becomes unsuitable for the automatic pipeline processing. As such, this early data was discarded in this analysis. The second apparition was later observed inbound from 1.88 au with observations ending just before perihelion at 1.36 au.

The light curve of 88P is plotted in Figure 4.11 with the filled and unfilled points representing observations from the first and second apparitions respectively. The *R*-band magnitude of 88P peaked about a week ($r = 1.37$ au) after perihelion with a brightness of about 13.1 mag. The last measurement made by TN on the second apparition measured an *R*-band brightness of 12.86 mag nineteen days before perihelion which, if the trend continued, would suggest that it would have reached a slightly brighter peak in its second perihelion. However, when converting the brightness to $Af\rho$ (Figure 4.12), the second apparition lines up much better with the first. At a distance of $r = 1.38$ au pre-perihelion, $Af\rho = 1017 \pm 9$ cm in the first apparition, and at a distance of $r = 1.37$ au, $Af\rho = 1020 \pm 9$ cm for the second apparition. The difference in brightness is due to different observing geometry and not a change in activity. I measure a pre-perihelion $Af\rho$ in *R*-band power law slope of -9.59 ± 1.62 during the first apparition and a slope of -3.41 ± 0.18 during the second apparition. It should be noted that in the first apparition there are only a handful of pre-perihelion data points at $r < 1.4$ au to work with, so the second apparition with many measurements covering a greater span of distance should be taken as a far more representative measure of the $Af\rho$ slope across the whole pre-perihelion orbit. The second apparition's slope

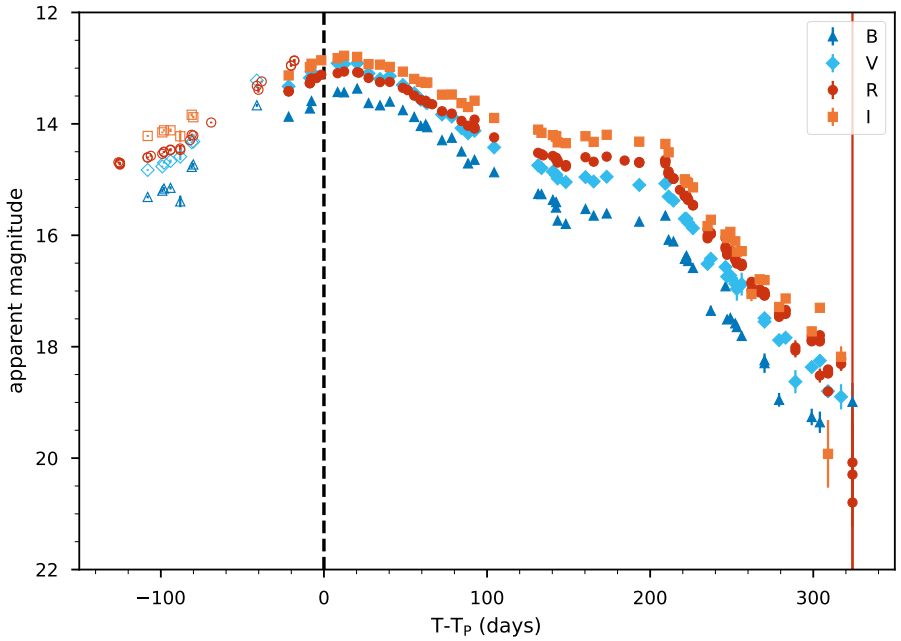

Figure 4.11 Light curve of 88P/Howell measured in B-, V-, R- and I-bands by the TRAPPIST-South and -North telescopes in $\rho = 10\,000$ km apertures. Data from both apparitions are plotted against time from perihelion ($T-T_{\rm P}$), with filled and unfilled points representing the first and second apparitions respectively.

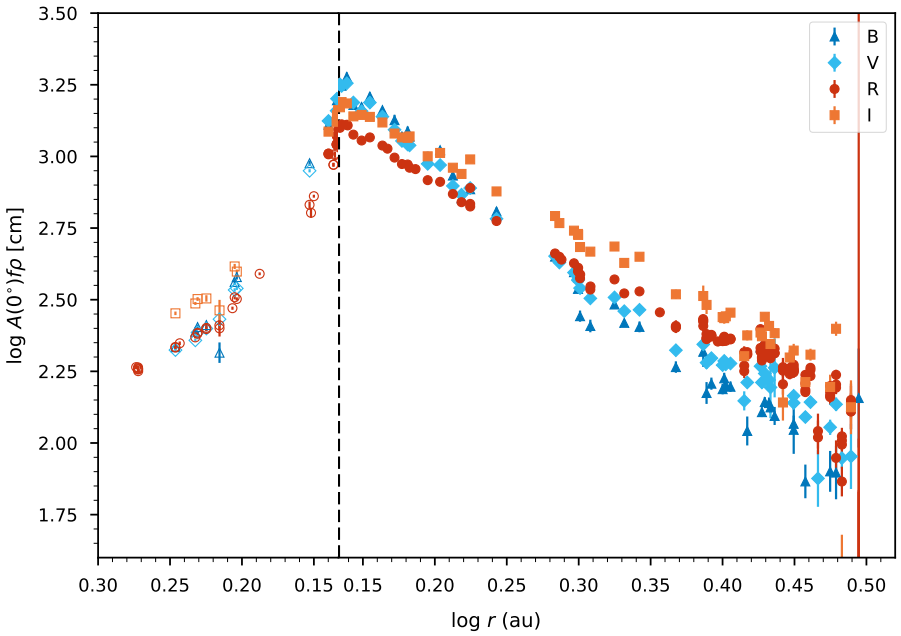

Figure 4.12 $Af\rho$ vs. r of 88P/Howell measured in B-, V-, R- and I-bands by the TRAPPIST-South and -North telescopes in $\rho = 10\,000$ km apertures. The vertical dotted line indicates the perihelion distance of $r = 1.36$ au. Data from both apparitions are plotted, with filled and unfilled points representing the first and second apparitions respectively.

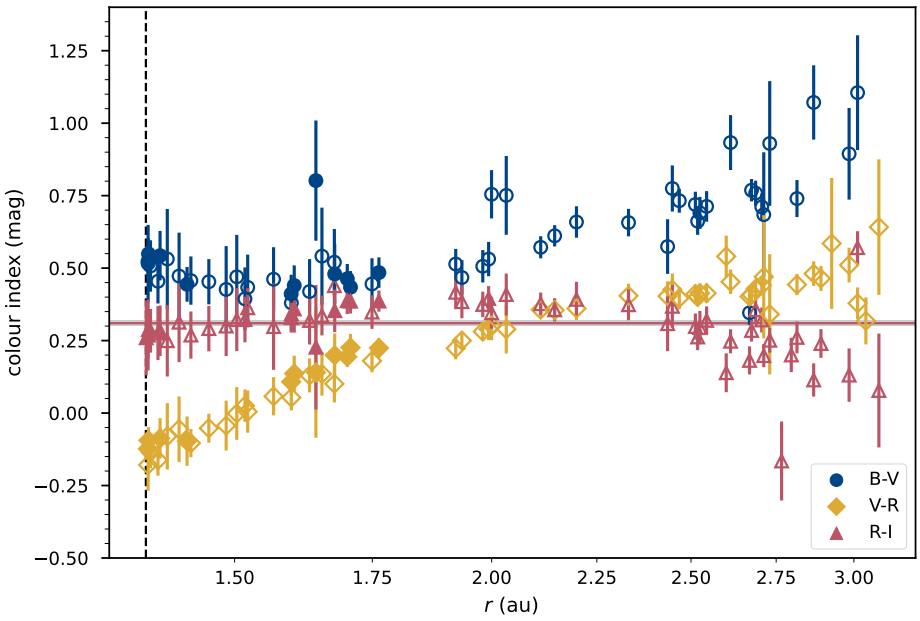

Figure 4.13 Colour index vs. r of 88P/Howell measured with TRAPPIST-S and TRAPPIST-N photometry in the B-, V-, R- and I-bands. The filled and unfilled points represent pre- and post-perihelion measurements respectively. The means and uncertainties are drawn as horizontal lines and shaded areas respectively. The vertical dotted line indicates the perihelion distance of $r = 1.36$ au.

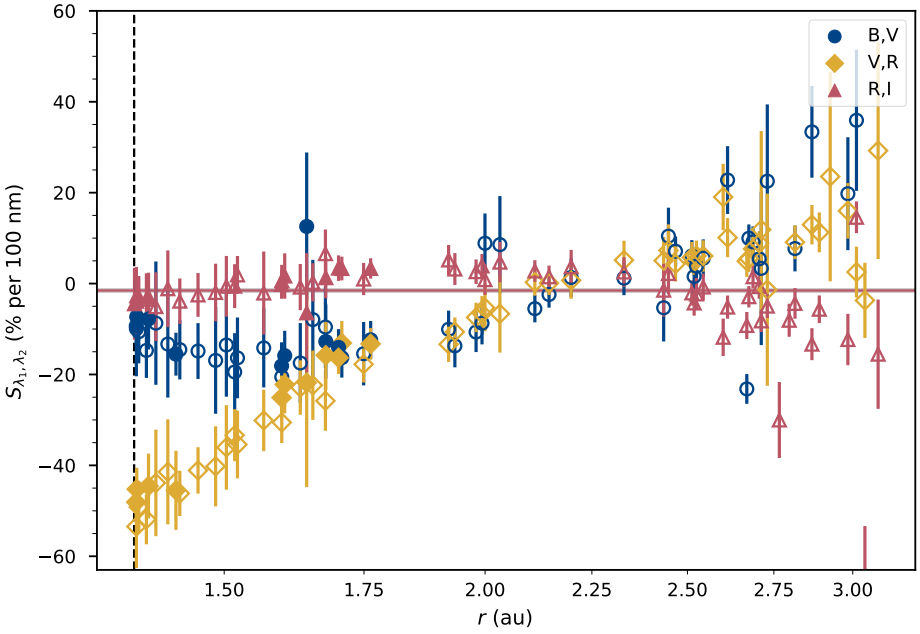

Figure 4.14 Spectral slope vs. r of 88P/Howell measured with TRAPPIST-S and TRAPPIST-N photometry in the B-, V-, R- and I-bands. The filled and unfilled points represent pre- and post-perihelion measurements respectively. The means and uncertainties are drawn as horizontal lines and shaded areas respectively. The vertical dotted line indicates the perihelion distance of $r = 1.36$ au.

increases quite dramatically before perihelion to -10.0 ± 0.9 between 1.42 au and 1.37 au, which matches the first apparition's measurements. The post-perihelion slope was only measured for the first apparition and was found to be -3.05 ± 0.05 after perihelion, then the slope flattens slightly beyond 2.27 au to -2.77 ± 0.17. If one assumes the post-perihelion slope of the second apparition to be similar to the first apparition, then 88P shows the same asymmetry with steeper incoming than outgoing slopes as seen in other JFCs.

Colours measured for 88P are plotted in Figure 4.13. It is immediately clear that the colour of 88P does not remain constant across the orbit. Both $B-V$ and $V-R$ are at their bluest around perihelion, this then becomes redder as 88P retreats further into the Solar System. $R-I$ does not seem to show as a significant change as $B-V$ or $V-R$, staying more or less constant throughout and, if anything, getting bluer. We can see that the trend is repeated in the second apparition since $V-R$ looks to be on a downward trend prior to perihelion. When converting to spectral slope (Figure 4.14), the trends become more pronounced. It looks like $V-R$ is inversely proportional to heliocentric distance outgoing from perihelion, this suggests decreasing gas production with respect to to heliocentric distance. $S_{V,R}$ peaks around -50 per cent per 100 nm about a week ($r = 1.37$ au) after perihelion. This matches the dust production peak. I measure average colours of $R - I = 0.30 \pm 0.01$ and corresponding spectral slopes of $S_{R,I} = -1.5 \pm 0.5$ per cent per 100 nm.

4.2.4 103P/Hartley 2

103P/Hartley 2 was discovered on 1986 March 15 by Malcolm Hartley with the UK Schmidt Telescope at Siding Spring observatory (Hartley, 1986). 103P is a Jupiter-family comet with a period of ~ 6.5 years and a perihelion distance of $q \sim 1.06$ au.

103P was selected as the target of NASA's Extrasolar Planet Observation and Deep Impact Extended Investigation (EPOXI), which repurposed the Deep Impact flyby spacecraft (A'Hearn et al., 2011). The spacecraft made its closest approach (694 km) to 103P's nucleus on 2010 November 4, one week after perihelion at a distance of 1.064 au. Observations of the comet began two months before encounter and continued for three weeks after. 103P had a distinctive bi-lobed shape with a long edge length of 2.33 km. The nucleus had two distinct types of terrain, rough 'knobby' terrain and smooth terrain on the 'waist' between the

two lobes. Outgassing jets were seen in all terrain but were clustered in the rough terrain of the smaller lobe, as seen in Figure 1.2f. 103P is a hyperactive comet, like 46P, CO_2 is the primary driver of activity in 103P, this super-volatile lifts pure water-ice, which then sublimate in the coma. A'Hearn et al. (2011) also notice that sublimation was much less on the smooth 'waist' region and suggest that this is a region of redeposition but the mechanism of this remains unclear.

As 103P was a space mission target, it made for a compelling target for ground-based observers. Meech et al. (2011b) details the results of the large ground-based observing campaign of 103P made in support of the EPOXI mission. They find that 103P became active at $r \sim 4.4$ au, and that just before perihelion CO_2 becomes the dominant driver of activity. This CO_2 activity lasts out to aphelion and remains active after aphelion. 103P is normal in terms of the abundance of C-chain species. The active nucleus area was estimated to be ~ 2 per cent with the remaining water production rate being from icy grain halo. They suggest 103P might be a relatively new JFC due to its unusual physical properties and abundance of CO_2 ice.

103P/Hartley 2 was observed by the TRAPPIST-South telescope between 2010 December 10 and 2012 April 30 in B- and V-bands. Observations started 43 days after perihelion on 2010 October 28, covering heliocentric distances from $r = 1.21$ au out to $r = 4.53$ au.

Figure 4.15 plots the light curve of 103P against time. The peak measured brightness in the B-band is 11.35 mag but as the measurements started post-perihelion it is impossible to say if this was the peak brightness across the whole passage. Estimating from Yoshida's light curve [2] of the 2010 apparition, it would seem activity peaked about a month before perihelion.

Figure 4.16 plots the $Af\rho$ dependence with respect to heliocentric distance. I measure an $Af\rho$ post-perihelion slope of -2.20 ± 0.10. It should be noted that I am measuring $Af\rho$ from V-band observations so they may be contaminated with gas, unfortunately I am only presented with B- and V-bands which both contain several prominent gas emission lines. I cannot make a direct comparison to R- or I-band to infer the amount of gas present in the coma relative to the dust. 103P is well within distances at which we see gas sublimation in other comets so gas contamination could well be a possibility.

[2] `http://www.aerith.net/comet/catalog/0103P/2010.html`

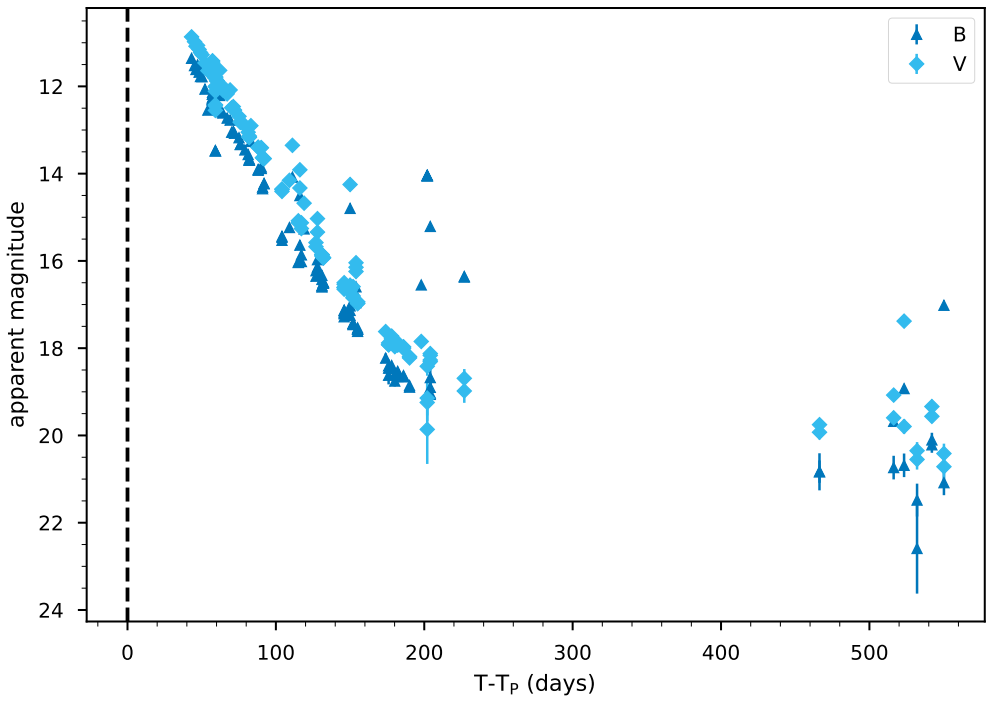

Figure 4.15 Light curve of 103P/Hartley 2, measured in B- and V-bands by the TRAPPIST-South telescope in $\rho = 10\,000$ km apertures. Time is measured as days from perihelion ($T - T_P$).

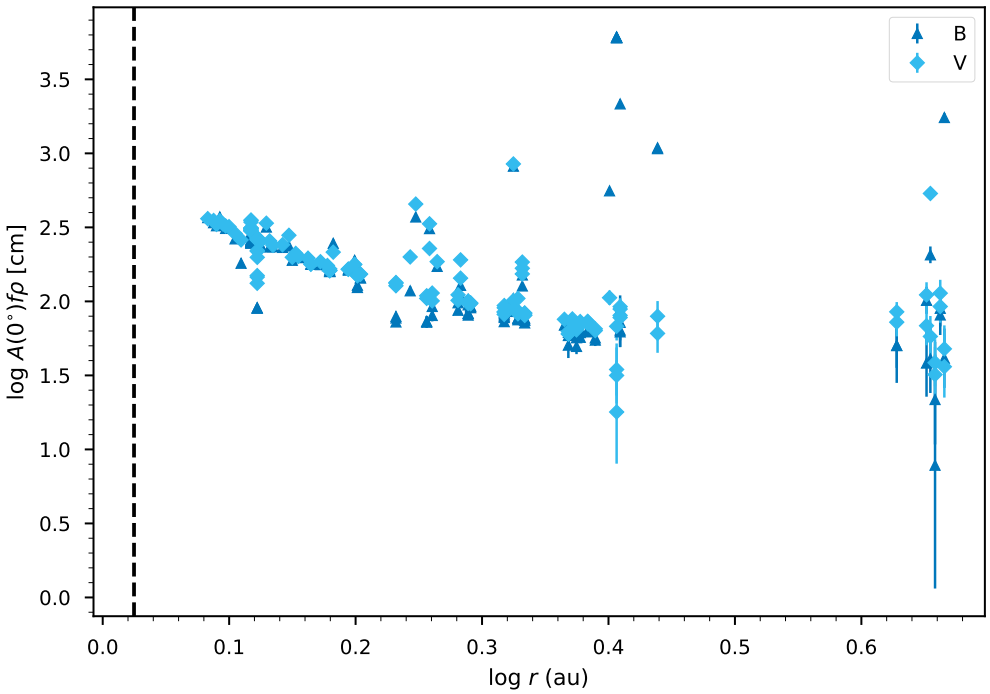

Figure 4.16 $Af\rho$ vs. r of 103P/Hartley 2 measured in B- and V-bands by the TRAPPIST-South telescope in $\rho = 10\,000$ km apertures. The vertical dotted line indicates the perihelion distance of $r = 1.06$ au.

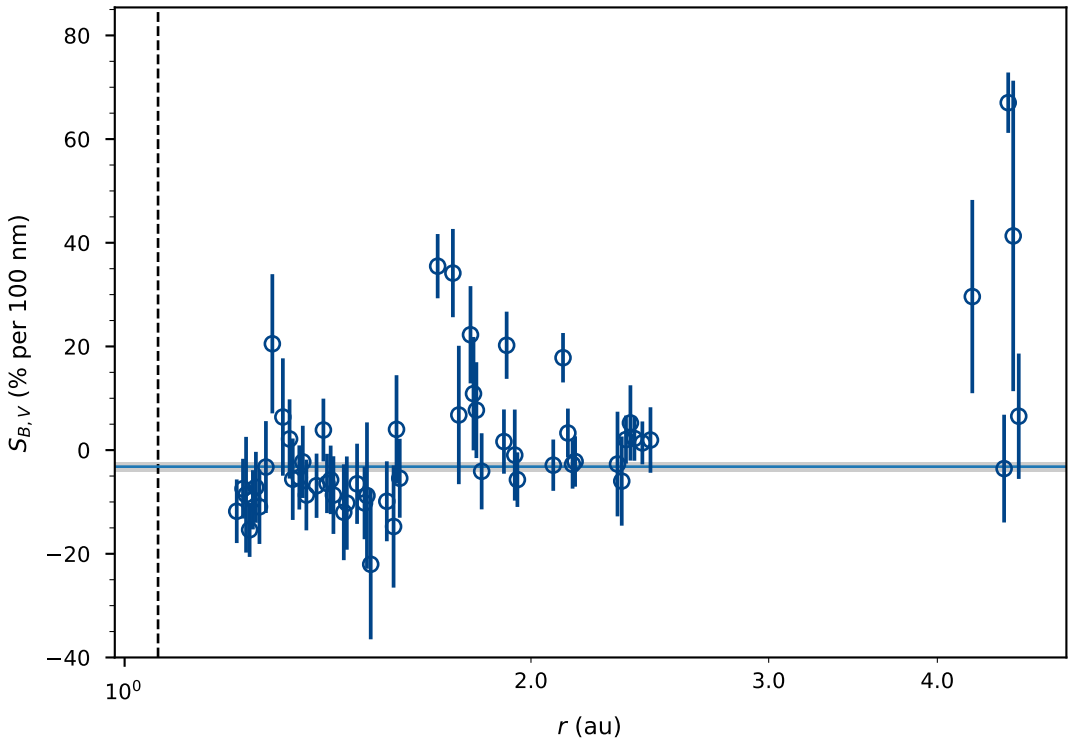

Figure 4.17 Spectral slope vs. r post-perihelion of 103P/Harley 2 measured with TRAPPIST-S photometry in the B- and V-bands. The means and uncertainties are drawn as horizontal lines and shaded areas respectively. The vertical dotted line indicates the perihelion distance of $r = 1.06$ au.

Knight and Schleicher (2013) finds dust production slopes of $r^{-3.4}$ to $r^{-4.1}$ pre-perihelion and $r^{-1.68}$ to $r^{-1.91}$ post-perihelion. It is an adequate match for my measurement of post-perihelion slope and slight differences are likely due to the fact they measure $Af\rho$ from a narrowband green continuum filter. It also confirms the pattern we have seen in JFCs so far, that the pre-perihelion slope is steeper than the post-perihelion slope.

The average colour remains constant at $B-V = 0.56\pm0.01$ and the corresponding spectral slope is $S_{B,V} = -3.2 \pm 0.9$ per cent per 100 nm. 103P seems to be far bluer than the average JFC, which has a typical colour of $B - V = 0.74$ (Jewitt, 2015). This suggests gas contamination could be present in these bands and 103P has a gas rich coma. An anomalous increase in CN was seen between 2010 September 9 and 17 (A'Hearn et al., 2011) but this was not seen in the ground based data (Meech et al., 2011b). CN has emission in the blue bands so might be the cause of this unusually blue colour.

It is difficult to make as many conclusions about this comet's activity as previous

comets in my sample due to lack of data. Its post-perihelion activity seems typical of JFCs with a shallow slope consistent with other outbound JFCs, but we cannot make any comment on the asymmetry from my data since we have no pre-perihelion measurements. However, other observations do see an asymmetry with a steeper pre-perihelion slope to post-perihelion slope (Knight and Schleicher, 2013). The gas production does not vary between B- and V-bands but we do not know how it varies relative to R-band. The $B - V$ colour is bluer than the average active JFC implying gas production.

4.2.5 246P/NEAT

246P/NEAT was discovered on 2004 March 28 by the Near-Earth Asteroid Tracking (NEAT) programme using the 1.2-m reflector at Haleakala (Hormuth et al., 2004). It is a Jupiter-family comet with semi-major axis 4.03 au and period of 8.08 years. It came to perihelion at distance $q = 2.88$ au – the largest for any JFC in my sample – on 2013 January 28.

246P/NEAT was observed by the TRAPPIST-South telescope between 2012 January 24 and 2014 September 6 in B-, V-, R- and I-bands. It was observed inbound from $r = 3.44$ au through perihelion at $q = 2.88$ au then back out to $r = 3.98$ au.

The light curve of 246P is plotted in Figure 4.18. The measured brightness peaks in the R-band at 14.3 mag about 5 months after perihelion at a distance of $r = 3.2$ au, but this was due to phase angle effects and not a change in activity – the variation in phase angle over the course of the observations is plotted over the light curve in Figure 4.18. The peaks in brightness corresponding to points of minimum phase angle. Correcting for the phase angle and plotting the heliocentric dependence of the $Af\rho$ parameter gives us Figure 4.19. Immediately we see a different light curve than seen in other JFCs, the curve is much flatter without a steep brightness slope pre- or post-perihelion. Pre-perihelion, the $Af\rho$ has a slope of -5.16 ± 0.2 which then flattens off at about 3 au to 1.69 ± 0.99 before reaching perihelion however I am missing data immediately prior to the perihelion so I am unsure if the trend continues. Judging from the mismatch in $Af\rho$ in the B- and V-bands pre- and post-perihelion it would seem that the activity decreases significantly before reaching perihelion. Post-perihelion, the light curve has a slope of 1.14 ± 0.24 out to about 3 au after which the slope steepens to -3.50 ± 0.10. Initially I assumed the variations in slope were due to underlying phase effects but the peaks in $Af\rho$ do not line up with the points

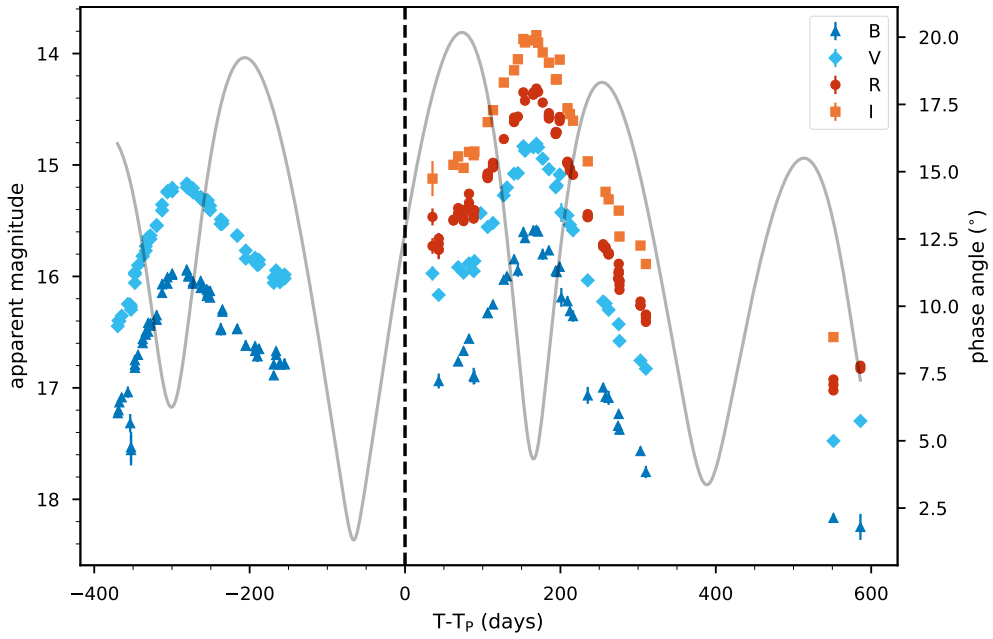

Figure 4.18 Light curve of 246P/NEAT measured in B-, V-, R- and I-bands by the TRAPPIST-South telescope in $\rho = 10\,000$ km apertures. Time is measured as days from perihelion. The phase angle is superimposed as the solid line.

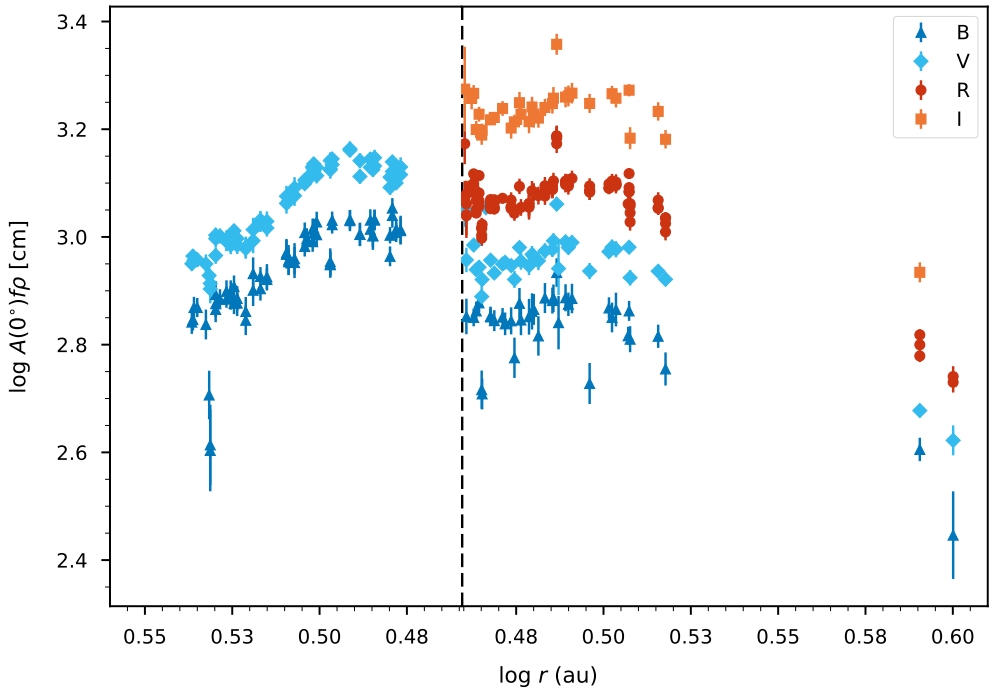

Figure 4.19 $Af\rho$ vs. r of 246P/NEAT measured in B-, V-, R- and I-bands by the TRAPPIST-South telescope in $\rho = 10\,000$ km apertures. The vertical dotted line indicates the perihelion distance of $r = 2.88$ au.

of minimum phase angle which would suggest these effects arise elsewhere. The fact that the turning points in the slopes occur roughly at the same heliocentric distance, 3 au, suggest a turn-on or turn-off of a specific volatile, probably water (Meech and Svoreň, 2004). There are no spectroscopic studies into gas production on this comet so I can only go off of the broadband data. What remains to be explained is the mismatch between the pre- and post-perihelion curves, clearly the activity decreases approaching perihelion.

246P is the only JFC in my sample to observed at distances beyond 3 au so provides unique, but limited, insight into the activity of JFCs at larger heliocentric distances. It would suggest the change in activity is quite drastic beyond these distances. Within 3 au, 246P displays activity not seen in the other JFCs in my sample, with much flatter activity slopes indicating little change in its activity once it crosses the 3 au threshold. The $Af\rho$ values are higher than the other JFCs in my sample, despite the large heliocentric distance. The different activity behaviour displayed in this comet compared to its peers in the Jupiter-family is likely due to its large perihelion distance compared to the other JFCs in the sample.

The colours of 246P are plotted in Figure 4.20. The colours remain constant across its orbit, this is probably due to the large perihelion distances at which the relevant volatiles that would produce colour change are sublimating at a lower level. However, the high $Af\rho$ relative to other JFCs would indicate there is significant activity on this comet. The average colour index over the orbit is: $B-V = 0.79 \pm 0.01$, $V-R = 0.49 \pm 0.01$ and $R-I = 0.48 \pm 0.01$.

The spectral slopes are plotted in Figure 4.21. The average of the spectral slopes are $\mathrm{S}_{B,V} = 11.4 \pm 0.7$ per cent per 100 nm, $\mathrm{S}_{V,R} = 14.3 \pm 1.0$ per cent per 100 nm and $\mathrm{S}_{R,I} = 9.2 \pm 0.8$ per cent per 100 nm.

246P is an outlier in my sample being a JFC with a larger perihelion distance. The increase of activity inbound to perihelion is interesting but I do not have data all the way up to perihelion to see if this trend continues, however judging by post-perihelion trends it would seem that a decrease in activity immediately before perihelion would seem likely and that any increase in activity would not match up with what we see post-perihelion. There is not much, if any, gas contamination in the coma of 246P shown by the unchanging spectral slopes across the whole orbit; which is unusual given the large $Af\rho$ implies increased activity. Perhaps dust-to-gas ratios are so large that any contribution of the gas is swamped by

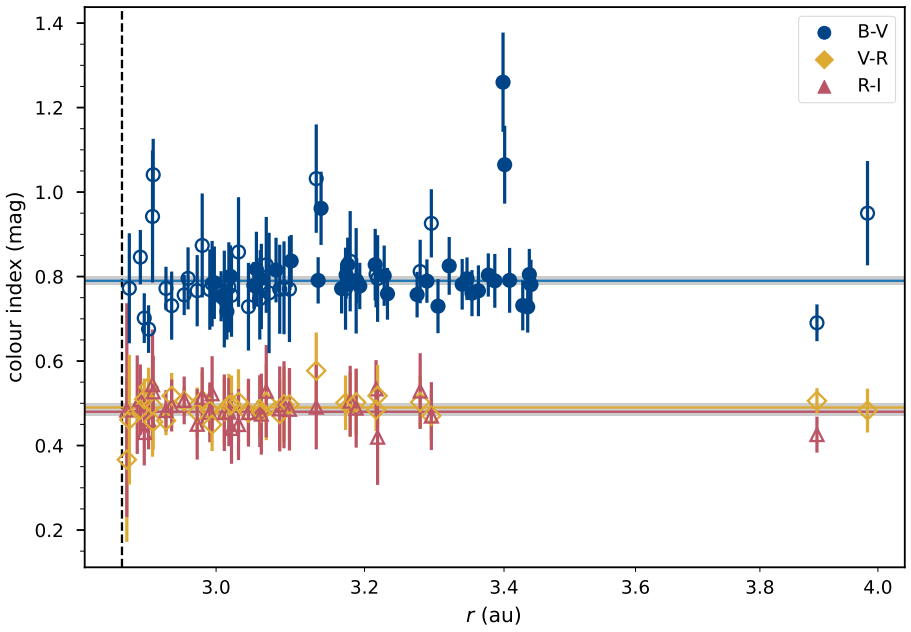

Figure 4.20 Colour index vs. r of 246P/NEAT measured with TRAPPIST-S photometry in the B-, V-, R- and I-bands. The filled and unfilled points represent pre- and post-perihelion measurements respectively. The means and uncertainties are drawn as horizontal lines and shaded areas respectively. The vertical dotted line indicates the perihelion distance of $r = 2.88$ au.

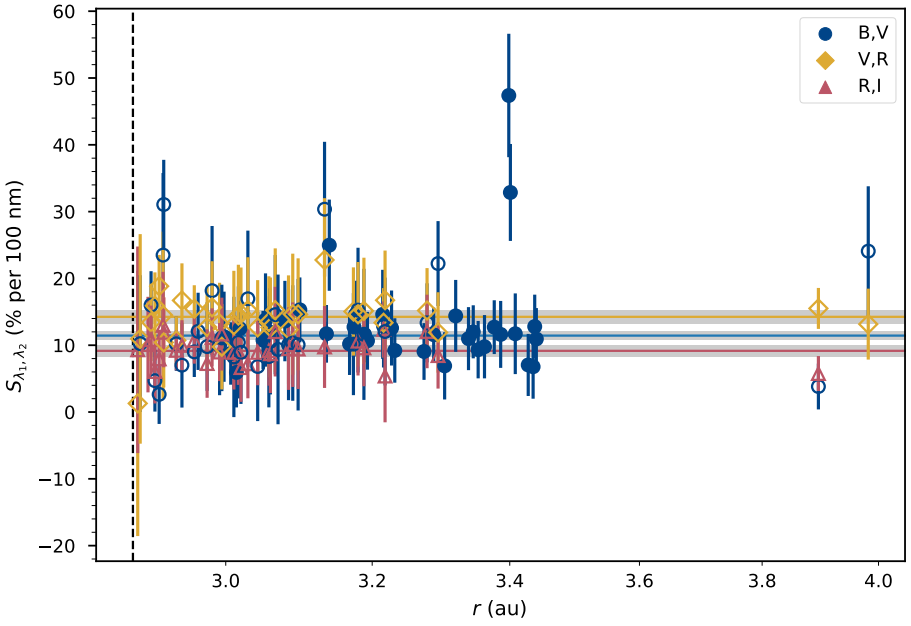

Figure 4.21 Spectral slope vs. r of 246P/NEAT measured with TRAPPIST-S photometry in the B-, V-, R- and I-bands. The filled and unfilled points represent pre- and post-perihelion measurements respectively. The means and uncertainties are drawn as horizontal lines and shaded areas respectively. The vertical dotted line indicates the perihelion distance of $r = 2.88$ au.

dust contributions.

4.2.6 C/2009 F4 (McNaught)

C/2009 F4 (McNaught) was discovered by Robert McNaught on 2009 March 19 in images taken with the 0.5-m Uppsala Schmidt telescope at Siding Spring observatory (McNaught et al., 2009). With an eccentricity of 1.0018 and an orbital inclination of 79.3° and reciprocal original semi major axis of $1/a$ of -3.32×10^{-4} au^{-1}, this comet is the first DNC in my survey.

C/2009 F4 (McNaught) was observed by the TRAPPIST-South telescope between 2011 March 9 and 2015 February 16 in B-, V-, R- and I-bands. It was observed from $r = 5.87$ au inbound and followed through to perihelion at $q = 5.45$ au and then all the way out to $r = 9.58$ au. C/2009 F4 has by far the largest perihelion distance of all the comets in my sample. The first portion of the orbit was only observed in B- and V-bands with R- and I-band observations beginning 2012 October 29, after which observations were made in all four bands.

The light curve of C/2009 F4 is plotted in Figure 4.22. The peak brightness in the V-band is 15.8 mag, measured about 200 days before perihelion. Although with a gap in the observations it is difficult to determine if this was the peak brightness of the entire orbit, by eye it would seem the peak would be around this point as, after the gap, the comet has decreased in brightness and the curve is on a clear downward trend, therefore, the peak probably happened 100–200 days before perihelion. $Af\rho$ is plotted against heliocentric distance in Figure 4.23. The pre-perihelion slope is very shallow with a power law slope of -0.82 ± 0.37, it becomes steeper outgoing with a power law slope of -4.88 ± 0.41 out to 6 au then the slope decreases to -2.40 ± 0.76 beyond 6 au. It is hard to judge due to the gaps in the data, but it would seem that the dust activity peaked some time within the four months before perihelion, however as mentioned the activity pre-perihelion was flat indicating sustained activity levels inbound to perihelion. This is the first DNC in our sample and displays a distinctly different and much larger asymmetry in the dust activity than JFCs.

The colours across the course of the orbit of C/2009 F4 remain constant, measuring average colours: $B - V = 0.78 \pm 0.01$, $V - R = 0.44 \pm 0.01$ and $R - I = 0.40 \pm 0.01$. Figure 4.24 plots the spectral slopes of C/2009 F4. The average slopes are: $S_{B,V} = 10.6 \pm 0.6$ per cent per 100 nm, $S_{V,R} = 8.7 \pm 0.7$ per cent per 100 nm

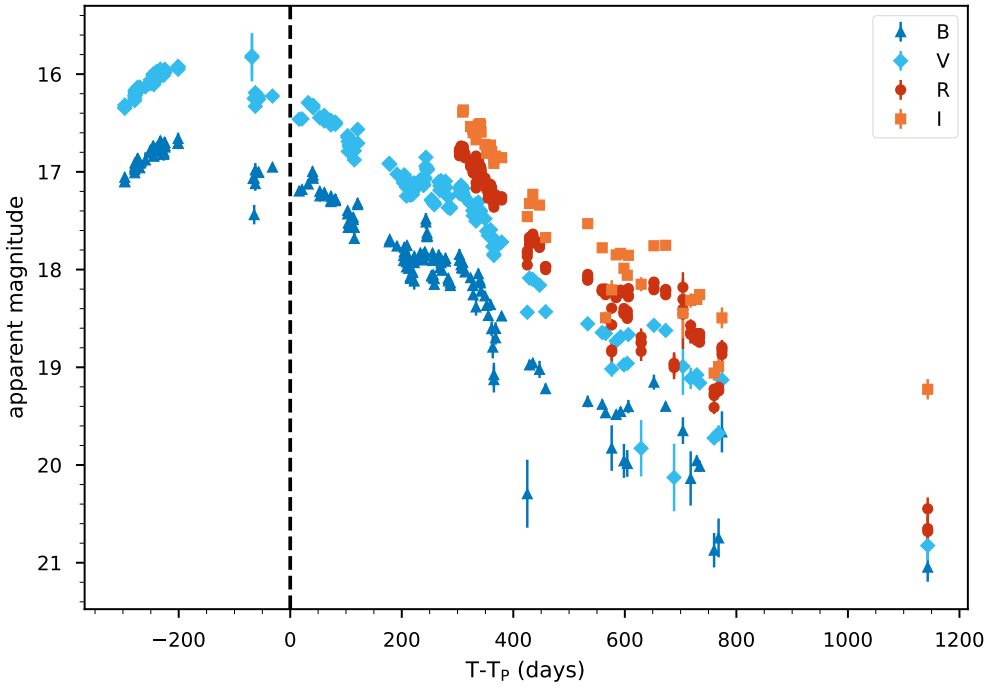

Figure 4.22 Light curve of C/2009 F4 measured in B-, V-, R- and I-bands by the TRAPPIST-South telescope in $\rho = 10\,000$ km apertures. Time is measured as days from perihelion.

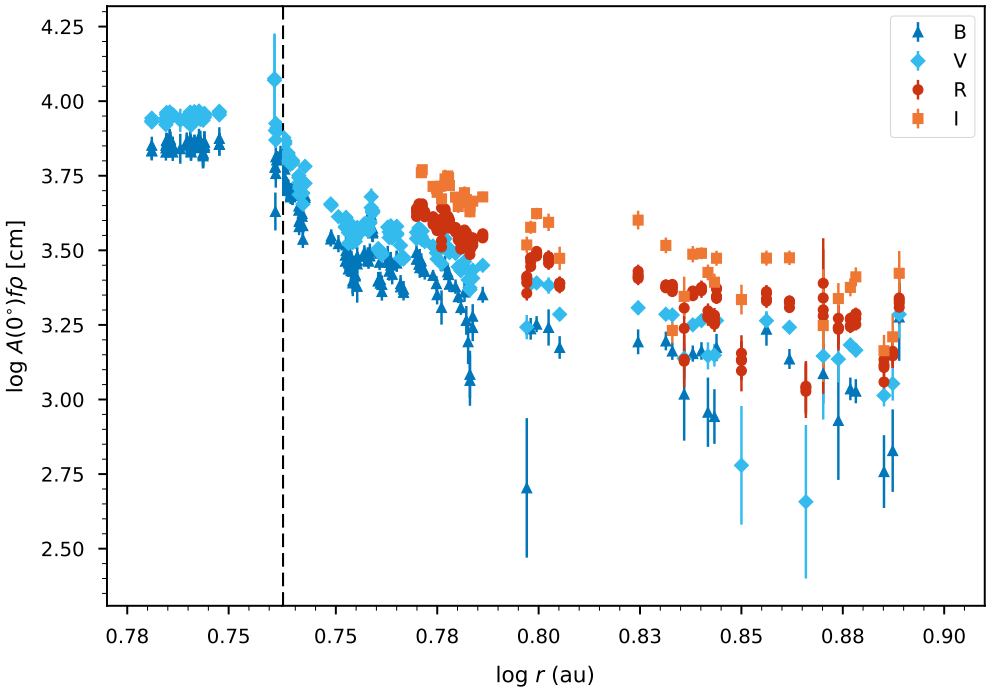

Figure 4.23 $Af\rho$ vs. r for C/2009 F4 measured in B-, V-, R- and I-bands by the TRAPPIST-South telescope in $\rho = 10\,000$ km apertures. The vertical dotted line indicates the perihelion distance of $r = 5.45$ au.

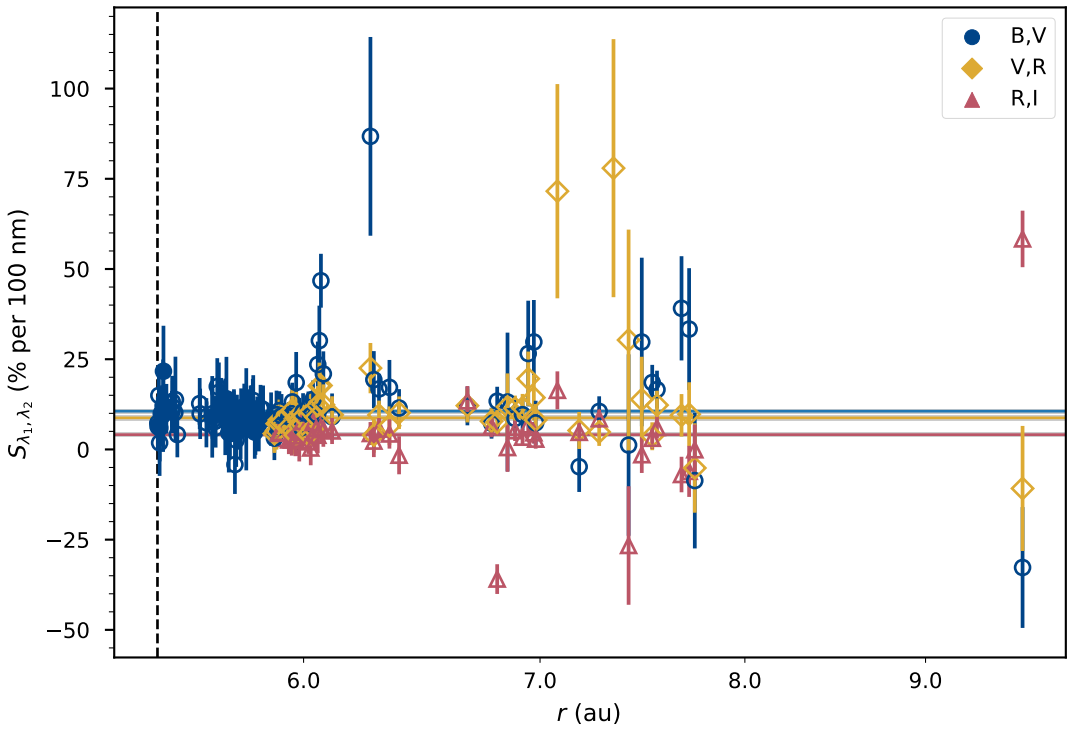

Figure 4.24 Spectral slope vs. r of C/2009 F4 measured with TRAPPIST-S photometry in the B-, V-, R- and I-bands. The filled and unfilled points represent pre- and post-perihelion measurements respectively. The means and uncertainties are drawn as horizontal lines and shaded areas respectively. The vertical dotted line indicates the perihelion distance of $r = 5.45$ au.

and $S_{R,I} = 4.1 \pm 0.6$ per cent per 100 nm. We do not have any $V - R$ or $R - I$ colour information around perihelion but judging by the typical comet colours, spectral slopes measured later in the orbit and the large perihelion distance we can assume there was minimal gas contamination in the B- and V-bands and that the measurements $Af\rho$ taken in the V-band are a good measure of the dust production of C/2009 F4.

4.2.7 C/2009 P1 (Garradd)

C/2009 P1 (Garradd) was discovered on 2009 August 13 by Gordon Garradd using the 0.5-m Uppsala Schmidt telescope at Siding Spring Observatory (McNaught and Garradd, 2009). Its orbital parameters of eccentricity of 1.0018, inclination of 79.3° and $1/a = 4.06 \times 10^{-4}$ au^{-1} lead us to determine that it is a DNC.

Remote observations using the Deep Impact Fly-by spacecraft detected H_2O,

CO_2 and CO in the coma of C/2009 P1. H_2O production rates show a post-perihelion decrease, however it showed a continuing increase in CO outgassing through perihelion (Feaga et al., 2013; Gicquel et al., 2015; McKay et al., 2015). This uncorrelated volatile behaviour has been attributed to a seasonal effect, where one hemisphere is more enriched in CO than the other, or possibly that this is activity typical of dynamically young comets. Ivanova et al. (2017) found emission bands of neutral molecules such as C_2, C_3, CN, CH, and NH_2 as well as CO+ and H_2O+ ions together with very strong continuum were identified in the spectra of C/2009 P1.

C/2009 P1 was observed by the TRAPPIST-South telescope between 2010 December 9 and 2013 May 9 in *B-, V-, R-* and *I*-bands. It was observed from $r = 4.70$ au to perihelion at 1.55 au then back out to $r = 5.81$ au. Figure 4.25 shows peak brightness of about 11 mag in V-band about four months before perihelion but this is due to phase effects, compare this to Figure 4.26 in which $Af\rho$ seems to have a slight upward trend before perihelion, so the peak in activity comes in the two months before perihelion.

Pre-perihelion, the $Af\rho$ slope is steep at distances beyond 3 au measuring a power law slope of -1.85 ± 0.06 which then flattens to -0.14 ± 0.02 within 3 au. The post-perihelion slope is steep measuring a gradient of -3.03 ± 0.06. C/2009 P1 displays sustained activity before perihelion then is followed by a steep fall-off post-perihelion. It is clear the activity gradually increases with heliocentric distance before reaching some sort of limit at 3 au where the activity levels off. This turn on point is not mirrored post-perihelion with activity already on the decline before 3 au. Seasonal effects have already been used to explain the CO production, perhaps this seasonal effect is also causing the levelling off and drop off of dust production.

Mazzotta Epifani et al. (2016) measures R-band $Af\rho$ of 3693±156 cm and 6368±412 cm in 2010 August ($r \sim 6$ au) and 2011 July ($r \sim 2.5$ au) respectively. Velichko and Andreev (2018) measure $Af\rho$ that varied from 1000 to 5500 cm and Ivanova et al. (2014) see $Af\rho$ that varied from 900 to 5500 cm across the whole orbit. My $Af\rho$ varied from 400 cm to 13 000 cm in V-band. The large discrepancy in the upper values of $Af\rho$ could come down gas contamination as we know that C/2009 P1 has significant carbon species emissions which pollute the B- and V-bands.

Combi et al. (2013) sees water production rate rise rapidly from first observation 130 days before perihelion (2011 August 13, $r \sim 2.3$ au) for about a month. The

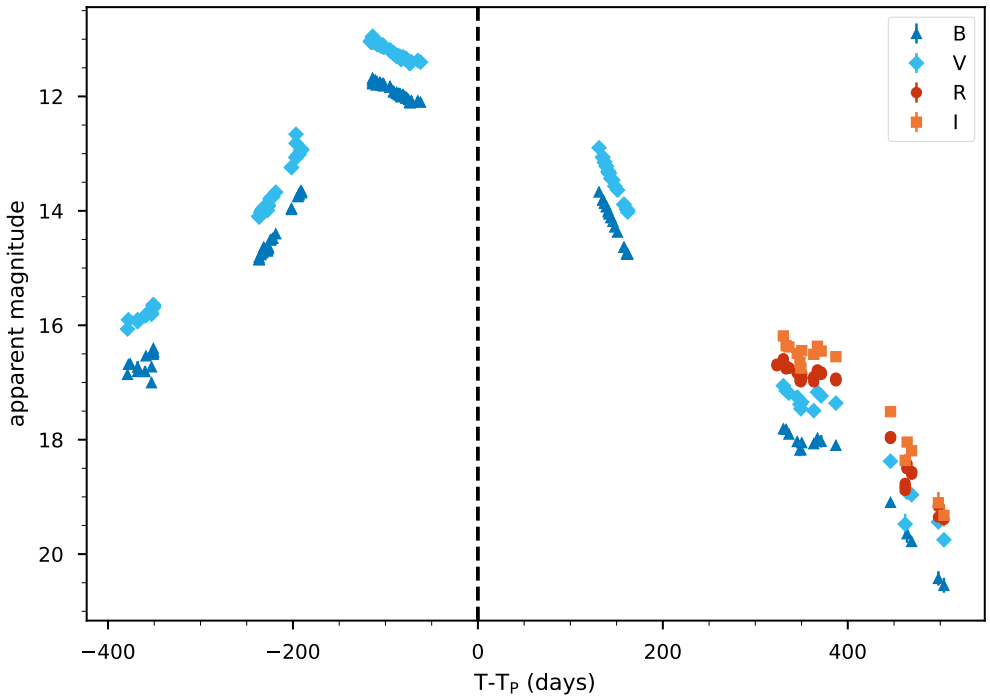

Figure 4.25 Light curve of C/2009 P1 measured in B-, V-, R- and I-bands by the TRAPPIST-South telescope in $\rho = 10\,000$ km apertures. Time is measured as days from perihelion.

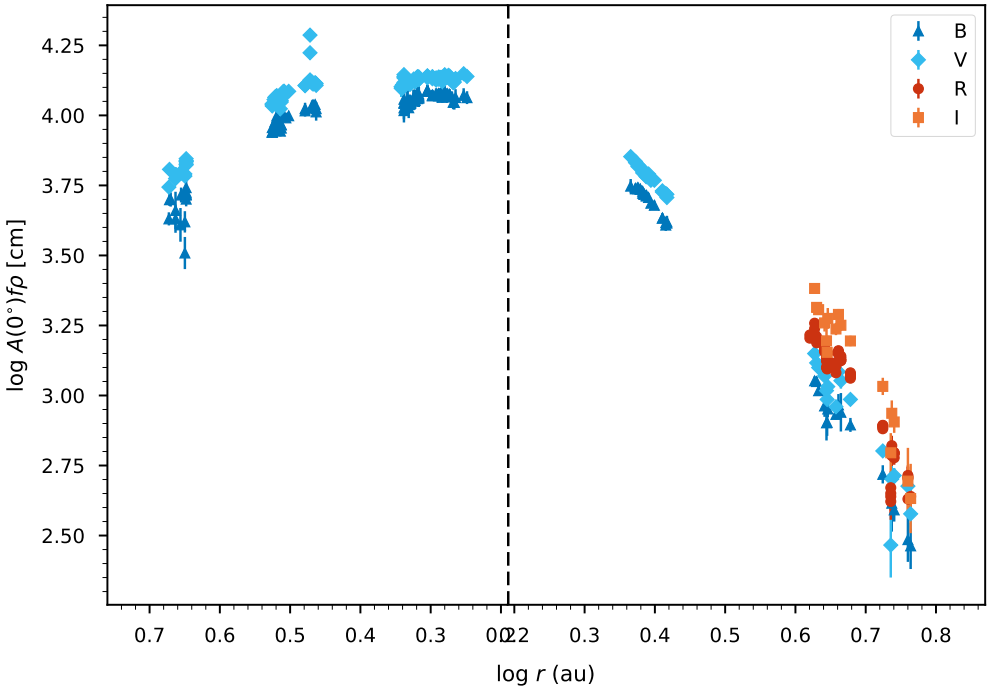

Figure 4.26 $Af\rho$ vs. r of C/2009 P1 measured in B-, V-, R- and I-bands by the TRAPPIST-South telescope in $\rho = 10\,000$ km apertures. The vertical dotted line indicates the perihelion distance of $r = 1.55$ au.

activity then decreases gradually but irregularly to perihelion, after perihelion the water production rate decreases uniformly. They measure a pre-perihelion power law of -0.47 and post-perihelion power law of -3.2 for water production. The unusual pre-perihelion variation is thought to be a seasonal effect or an extended source of an icy grain halo, or a combination of both. This idea is also supported by Paganini et al. (2012) and Villanueva et al. (2012). Bodewits et al. (2014) saw a very steep increase in water production of r^{-6} before perihelion peaking 100 days before perihelion, decreasing at lower rate of r^{-4} post-perihelion. They suggest an active area of 75 km^2 to explain water production. They also support the icy halo theory, finding that 200 days before perihelion, H_2O was produced in the coma.

The water production and dust production are not exactly correlated, but it is clear to see that the peak in activity of both water and dust production comes around the same time – about two to three months before perihelion. Combi et al. (2013) sees a similar asymmetry in water production that I see in the dust production, but this is not seen by Bodewits et al. (2014), they report a steeper incoming slope than outgoing. The difference comes from the different boundary conditions on the measurement of the slope. Combi et al. (2013) measured the slope for all pre-perihelion activity whereas Bodewits et al. (2014) only measured the slope prior to the peak in activity which did not include the subsequent fall-off before perihelion.

Figure 4.27 shows that C/2009 P1 has uniform colours across its orbit, measuring average colours: $B-V = 0.72 \pm 0.01$, $V-R = 0.42 \pm 0.01$ and $R-I = 0.40 \pm 0.02$. The corresponding spectral slopes against time are plotted in Figure 4.28, which shows flat spectral slopes across the orbit. The average of the spectral slopes are: $S_{B,V} = 6.3 \pm 0.8$ per cent per 100 nm, $S_{V,R} = 7.1 \pm 1.1$ per cent per 100 nm, $S_{R,I} = 4.1 \pm 1.0$ per cent per 100 nm, however we are lacking R- and I-bands around perihelion so I can glean little detail about gas production near perihelion, all I can say is that gas production does not change relative to the V- and B-bands but this is not uncommon among my data set so does not rule out the possibility that there is gas production from the nucleus. Mazzotta Epifani et al. (2016) measures an average of $V-R = 0.46 \pm 0.06$ and $R-I = 0.45 \pm 0.05$ between two measurements in 2010 August ($r \sim 6$ AU) and 2011 July ($r \sim 2.5$ au). Velichko and Andreev (2018) measures redder continuum, a spectral slope of 10 per cent per 100 nm. Ivanova et al. (2014) measured the colour of the comet in BC, GC and RC filters. They found spectral slope of reflectance varied from 0–20

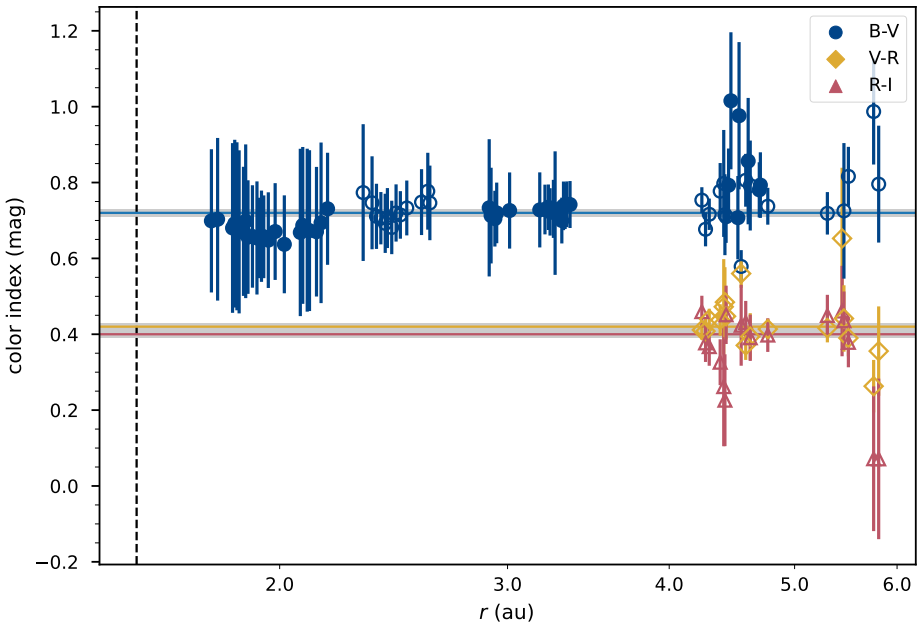

Figure 4.27 Colour index vs. r of C/2009 P1 measured with TRAPPIST-S photometry in the B-, V-, R- and I-bands. The filled and unfilled points represent pre- and post-perihelion measurements respectively. The means and uncertainties are drawn as horizontal lines and shaded areas respectively. The vertical dotted line indicates the perihelion distance of $r = 1.55$ au.

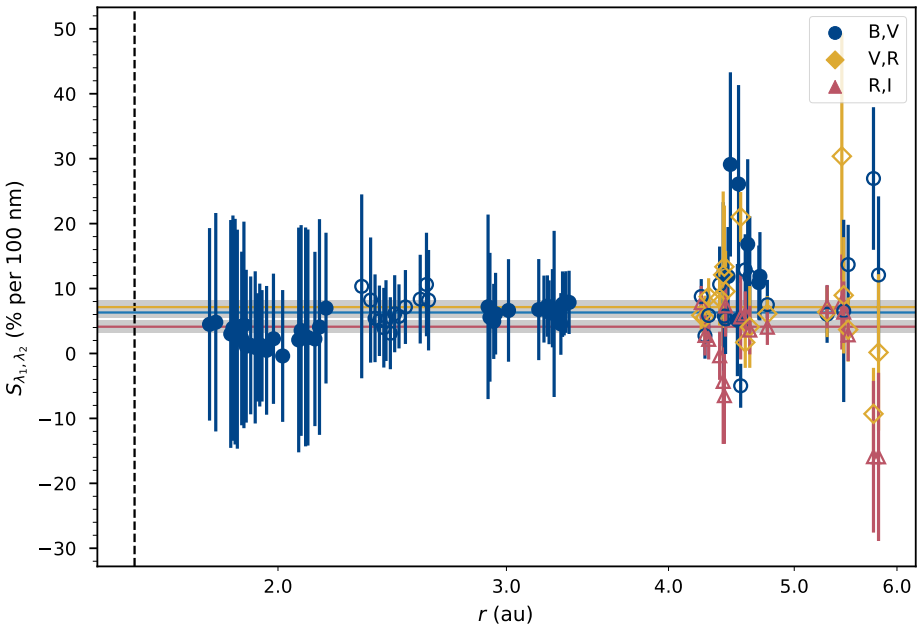

Figure 4.28 Spectral slope vs. r of C/2009 P1 measured with TRAPPIST-S photometry in the B-, V-, R- and I-bands. The filled and unfilled points represent pre- and post-perihelion measurements respectively. The means and uncertainties are drawn as horizontal lines and shaded areas respectively. The vertical dotted line indicates the perihelion distance of $r = 1.55$ au.

per cent per 100 nm. These measurements of colours are all in broad agreement with mine.

C/2009 P1 comes to perihelion well within gas sublimation range judging from the previous comets so it would seem likely that there would be colour change between bluer bands and redder bands due to any increased gas production. We should consider this when interpreting the $Af\rho$ slopes since the values were derived from the V-band, as this was the only available colour across the entire orbit. Given the gas species detected by other observations, I cannot rule out gas contamination in these bands so the $Af\rho$ in those bands might not be an accurate representative of the dust production of C/2009 P1.

4.2.8 C/2011 L4 (PanSTARRS)

C/2011 L4 (PanSTARRS) was discovered by Wainscoat et al. (2011) in images taken on 2011 June 6 with the 1.8-m Pan-STARRS 1 telescope at Haleakala. It was detected at a heliocentric distance of 7.9 au (Williams, 2011a). It had an inclination of 84.2° and a reciprocal semi-major axis, $1/a = -8.9 \times 10^{-5}$ au (Williams, 2013). The high inclination and small reciprocal semi-major axis indicated that this was a dynamically new comet from the Oort cloud. C/2011 L4 came to perihelion at a distance $q = 0.3015$ au – the closest in our sample – on 2013 March 10. This close encounter with the Sun also made it a challenging target to observe due to its low solar elongation near perihelion. As such most of the observations of this comet were focused on periods of long before or long after perihelion.

C/2011 L4 was observed by the TRAPPIST-South telescope between 2012 January 24 and 2013 February 8 in B- and V-bands. It was observed inbound from $r = 5.79$ au through to $r = 2.9$ au. Unfortunately, the low solar elongation around perihelion meant there was little data following the comet at the time of perihelion, but one additional measurement was taken at $r = 0.85$ au, 30 days prior to perihelion, in B-, V-, R- and I-bands.

The light curve of C/2011 L4 is plotted in Figure 4.29. It measures a peak R-band brightness of 7.83 ± 0.05 mag. $Af\rho$ is plotted as a function of heliocentric distance in Figure 4.30. We can see immediately that $Af\rho$ does not have a linear dependence on r, it increases non-linearly and plateaus after about $r = 4$ au. After following to $r = 2.9$ au, viewing geometry becomes to challenging

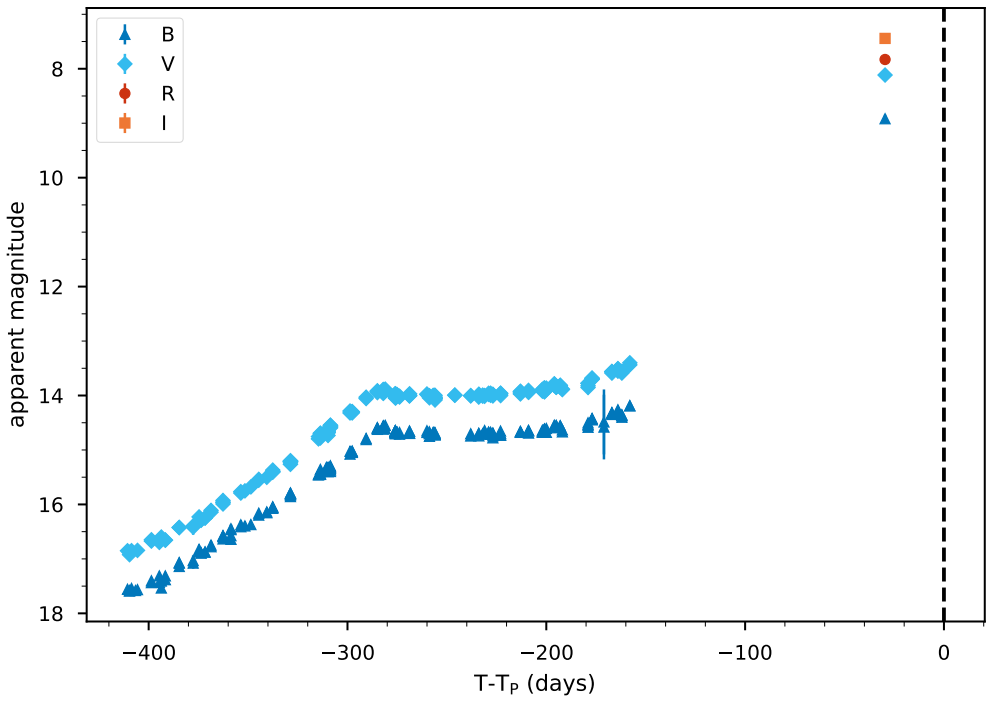

Figure 4.29 Light curve of C/2011 L4 measured in B-, V-, R- and I-bands by the TRAPPIST-South telescope in $\rho = 10\,000$ km apertures. Time is measured as days from perihelion.

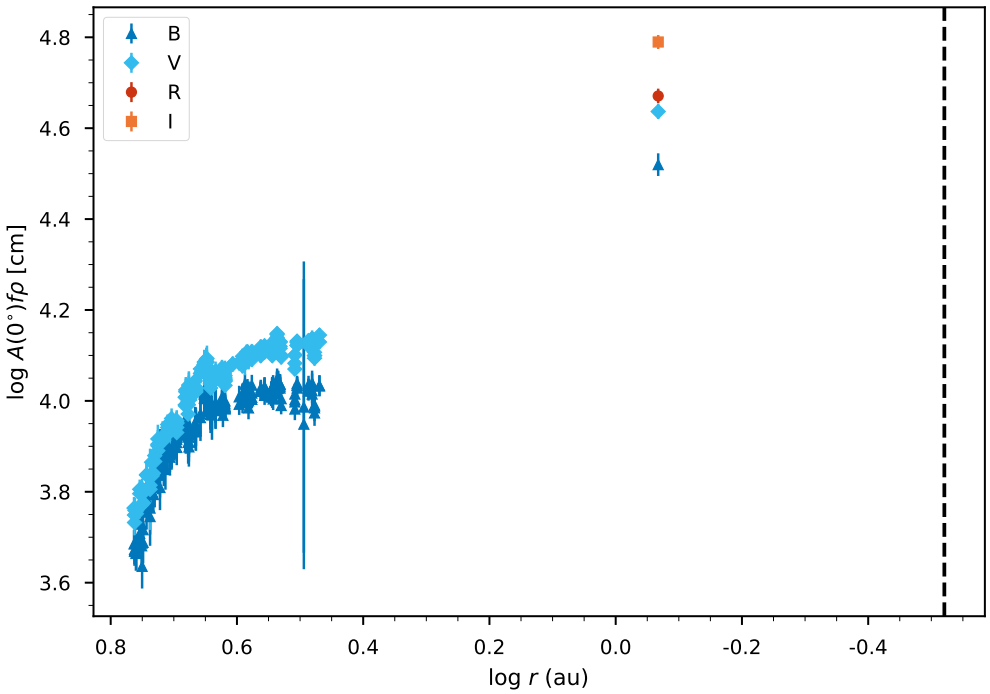

Figure 4.30 $Af\rho$ vs. r of C/2011 L4 measured in B-, V-, R- and I-bands by the TRAPPIST-South telescope in $\rho = 10\,000$ km apertures. The vertical dotted line indicates the perihelion distance of $r = 0.30$ au.

Table 4.3 Comparison of $Af\rho$ measurements of C/2011 L4 from this work to literature. Literature observations were taken on the same night as mine unless otherwise noted, time of literature observation is shown in brackets after $Af\rho$.

Date	$Af\rho$ (cm)		Reference
	This work	Literature	
2012 Apr 29	10185 ± 262	11020 ± 800 (Apr 22)	Yang et al. (2014)
2012 May 15	11065 ± 238	11690 ± 800	Yang et al. (2014)
2012 Jun 1	12331 ± 31	~ 14000 (May 31)	Ivanova et al. (2014)
2012 Jun 22	11758 ± 188	~ 11000 (Jun 21)	Ivanova et al. (2014)
2012 Jul 12	12119 ± 200	12890 ± 900	Yang et al. (2014)

for regular observations and there is a large gap before the next observation at $r = 0.85$ au. It would seem there is significant increase in activity in this gap as the point measured near perihelion is significantly brighter in both B- and V-bands. It is difficult to judge from just one point if this is indeed a true representation of the activity trend, however all four bands do show this increased brightness leading me to suspect it is not just an outlier. Ferrín (2014) collects amateur data for C/2011 L4, including observations around perihelion, showing that C/2011 L4 does show a further increase in brightening before perihelion. As I do not have post-perihelion observations, I cannot make any judgement about the asymmetry of the activity however Combi et al. (2014) measured the water production rates of C/2011 L4 pre- and post-perihelion. While not an exact proxy to dust production, this still gives us an idea of how the activity changes. Combi et al. (2014) found the activity to be greater pre-perihelion than post-perihelion, which is in agreement with the observational evidence that DNCs have greater pre-perihelion activity compared to post-perihelion.

Table 4.3 compares my $Af\rho$ with literature results. My results have good agreement with the literature on comet C/2011 L4.

Figure 4.31 seems to show $B - V$ on an upward trend before perihelion but the error bars are so big that conclusive statements about the colour evolution cannot be made with my data alone. The observations taken 30 days before perihelion show a similar colour to the rest of the orbit, within the error bars, so it would seem $B - V$ colour does not vary. I measure an average colour of $B - V = 0.71 \pm 0.01$ across the whole orbit. For the one measurement near perihelion I measure $V - R = 0.29 \pm 0.22$ and $R - I = 0.39 \pm 0.22$. The corresponding spectral slopes are $S_{B,V} = 5.1 \pm 1.0$ per cent per 100 nm, $S_{V,R} = -7.0 \pm 22.5$ per cent per 100 nm and $S_{R,I} = 3.4 \pm 13.5$ per cent per 100 nm. C/2011 L4 has a bluer

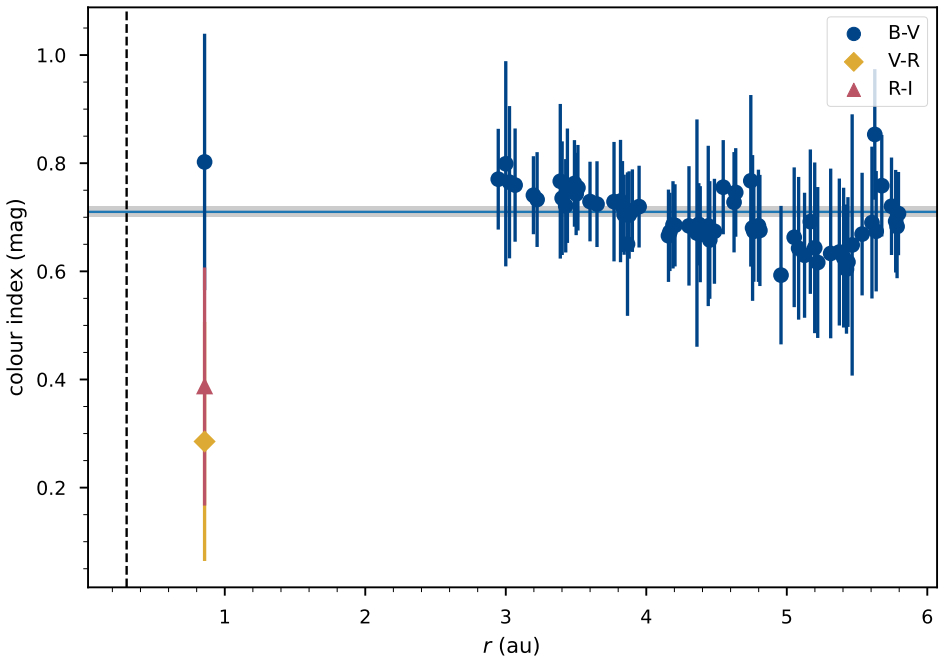

Figure 4.31 Colour index vs. r pre-perihelion of C/2011 L4 measured with TRAPPIST-S photometry in the B-, V-, R- and I-bands. The means and uncertainties are drawn as horizontal lines and shaded areas respectively. The vertical dotted line indicates the perihelion distance of $r = 0.30$ au.

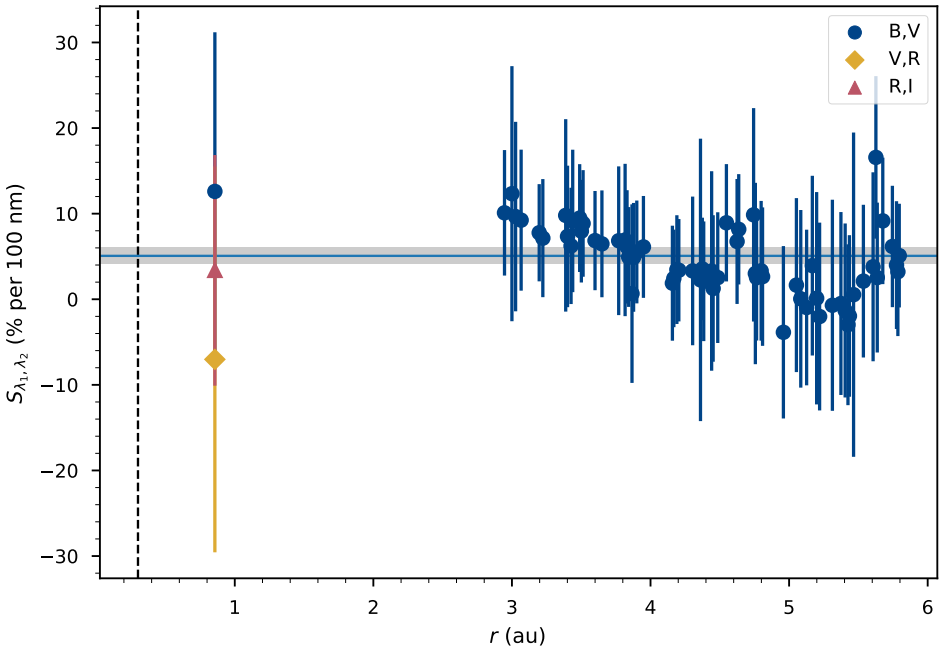

Figure 4.32 Spectral slope vs. r pre-perihelion of C/2011 L4 measured with TRAPPIST-S photometry in the B-, V-, R- and I-bands. The means and uncertainties are drawn as horizontal lines and shaded areas respectively. The vertical dotted line indicates the perihelion distance of $r = 0.30$ au.

spectral slope between V and R around perihelion, perhaps indicating increased gas production, but since I do not have R- or I-band measurements for the rest of the orbit I do not know if this blue colour is a sustained trend or just appearing around perihelion. Ivanova et al. (2014) observed the comet at distances of 4.4 and 4.2 au and observed high levels of activity far beyond the water sublimation zone. They observed redder than solar colours, and suggested that C_2 emission was absent from, or made an insignificant contribution to, the spectra. This is reassuring for me as this means my measurements for $Af\rho$ are likely to be free from gas contamination. Yang et al. (2014) finds the comet to be dust rich with a dust to gas ratio of 4. They also do not report gas contamination in the dust continuum. The dust coma became redder with decreasing r between 4.9 and 4.0 au, which I saw evidence for but could not conclude due to the large errors, they suggest this is caused by increasing size of coma dust grains.

4.2.9 C/2012 F6 (Lemmon)

C/2012 F6 (Lemmon) was discovered by Alex Gibbs on 2012 March 23 using the Mt Lemmon Survey at a heliocentric distance of 5 au (Williams, 2011b). Its orbital dynamics classify it as a returning LPC (period $\sim 10\,000$ years) from the Oort cloud. This comet has visited the inner Solar System many times. C/2012 F6 came to perihelion at $q = 0.7312$ au on 2013 March 24.

C/2012 F6 (Lemmon) was observed by the TRAPPIST-South telescope between 2012 November 18 and 2013 June 6 in B-, V-, R- and I-bands. It was monitored from $r = 2.25$ au through to perihelion at $q = 0.73$ au then back out to $r = 1.54$ au.

The light curve is plotted in Figure 4.33. The magnitude peaks at around 8 mag 10 days before perihelion. The true peak could be later but looking at the trend of the brightness it would seem this is a good estimate. The $Af\rho$ curve is plotted in Figure 4.34, it has power law slopes of -2.57 ± 0.02 incoming and -1.29 ± 0.13 outgoing. Combi et al. (2014) finds water activity to be lower before perihelion than after, measuring water production slopes of $r^{-3.0}$ and $r^{-2.3}$. They see peaks in water activity 20 days before, the day of and 22 days after perihelion. I do not have coverage of this time but checking Yoshida's light curve[3] does not show this small scale variation but does show the general trend and asymmetry

[3] `http://www.aerith.net/comet/catalog/2012F6/2012F6.html`

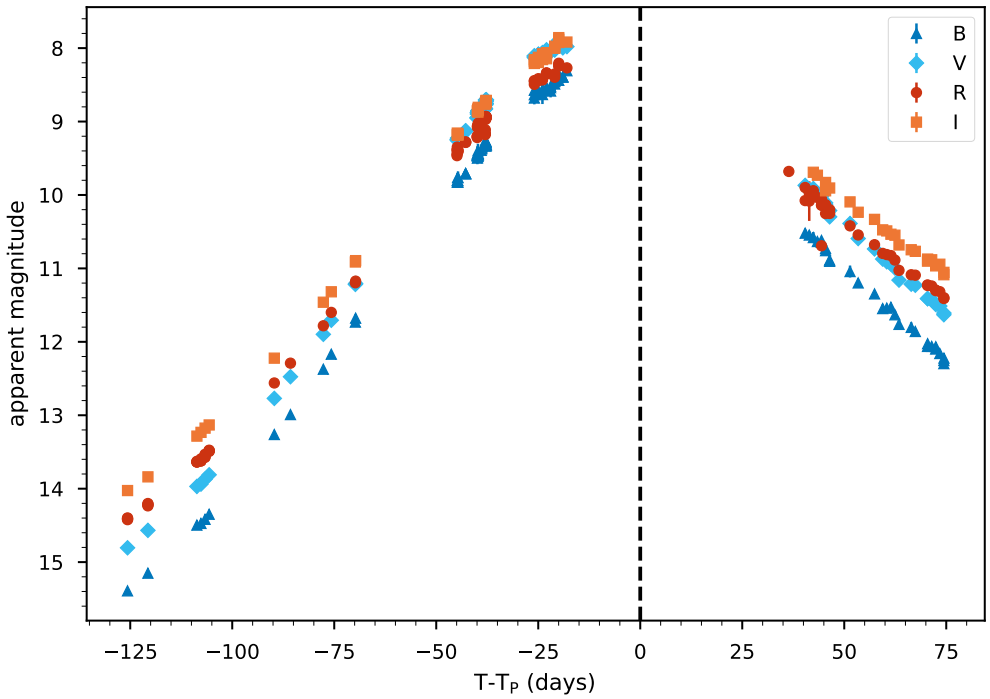

Figure 4.33 Light curve of C/2012 F6 measured in B-, V-, R- and I-bands by the TRAPPIST-South telescope in $\rho = 10\,000$ km apertures. Time is measured as days from perihelion.

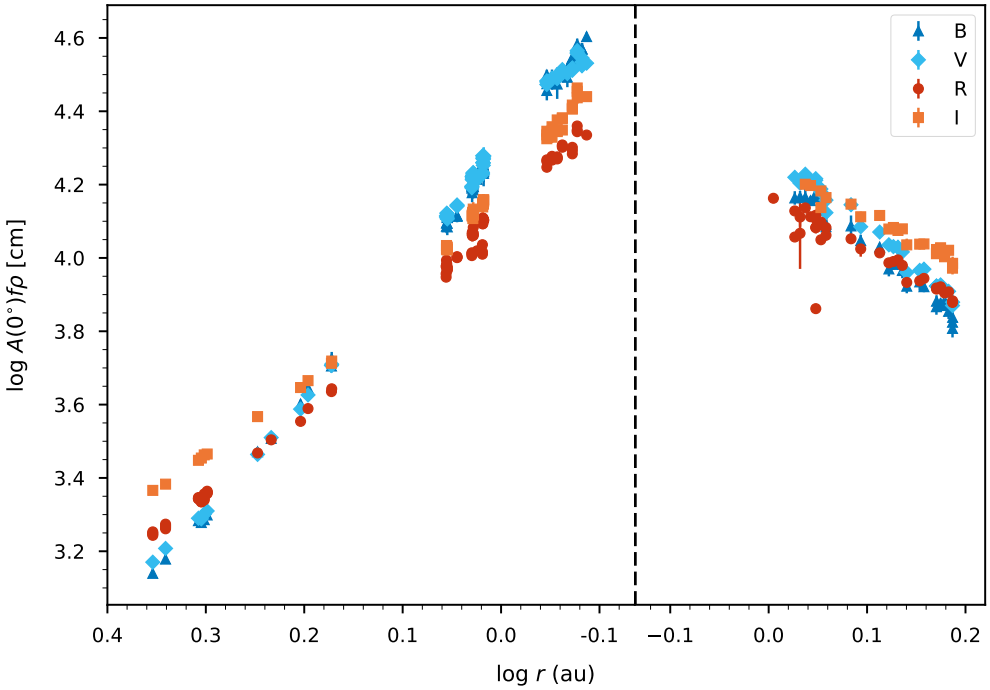

Figure 4.34 $Af\rho$ vs. r for C/2012 F6 measured in B-, V-, R- and I-bands by the TRAPPIST-South telescope in $\rho = 10\,000$ km apertures. The vertical dotted line indicates the perihelion distance of $r = 0.73$ au.

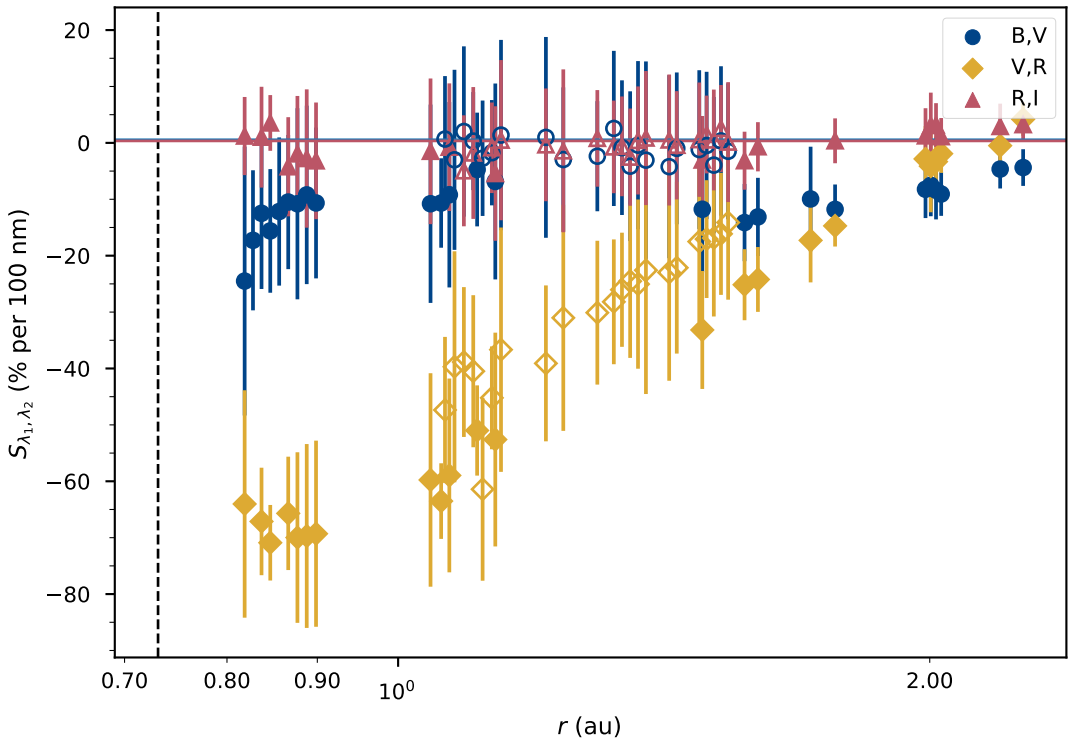

Figure 4.35 Spectral slope vs. r of C/2012 F6 measured with TRAPPIST-S photometry in the B-, V-, R- and I-bands. The filled and unfilled points represent pre- and post-perihelion measurements respectively. The means and uncertainties are drawn as horizontal lines and shaded areas respectively. The vertical dotted line indicates the perihelion distance of $r = 0.73$ au.

in activity about perihelion. This LPC displays slopes that are more in line with the asymmetry we see in JFCs than DNCs, hence indicating that this is a dynamically older comet that is returning to the Solar System multiple times.

Spectral slopes are plotted in Figure 4.35 show us that this comet is not as smooth and uniformly active as I thought at first glance. The average spectral slopes are $S_{B,V} = -6.9 \pm 1.2$ per cent per 100 nm and $S_{R,I} = 0.9 \pm 1.0$ per cent per 100 nm across orbit. There is a deep trough in the spectral slope $S_{V,R}$ and a smaller $S_{B,V}$ trough is also seen. $S_{V,R}$ dips to about -70 per cent per 100 nm, these slopes are signifiers of active gas production. We even see a decrease in $B - V$ around perihelion which is not seen in most comets in our sample, however the error bars on the spectral slopes are such that the points could still lie within the average spectral slope and I cannot be certain that this decrease is real.

Opitom et al. (2015a) published narrowband observations obtained at the same time with TRAPPIST. They find significant differences between dust and gas

production. They found the dust and gas activity not to be correlated, showing different trends pre- and post-perihelion. The gas slopes were much steeper pre-perihelion than post-, the opposite trend is seen in the dust slopes. Evidence of this was also present in the coma morphology with features seen in the RC filter not seen in other filters. They also see no colour change, however they are using narrowband filters so direct comparison to broadband colours cannot be made. They do see some change in the RC−UC colour which they attribute to gas contamination in the UC filter, probably from OH.

4.2.10 C/2012 K1 (PanSTARRS)

C/2012 K1 (PanSTARRS) was discovered on 2012 May 17 by Larry Denneau and Richard Wainscoat in images taken by the 1.8-m Pan-STARRS 1 telescope on Haleakala (Sato et al., 2012). This dynamically new comet came to perihelion at $q = 1.05$ au on 2014 August 27.

C/2012 K1 (PanSTARRS) was observed by the TRAPPIST-South telescope between 2013 March 28 and 2015 December 14 in *B-, V-, R-* and *I*-bands. It was monitored from 6.21 au to perihelion at 1.05 au then out to 5.8 au. The light curve is plotted in Figure 4.36. The comet peaks in brightness at around 10.5 mag in *R*-band about 75 days after perihelion. This unusual shape of light curve is due to viewing geometry so this peak in brightness does not correspond to a peak in activity. Figure 4.37 shows the measured peak in activity is actually 10 days after perihelion at $r = 1.07$ au. It is possible that peak activity could have occurred just before perihelion since the time immediately prior to perihelion was not observed due to low solar elongation.

The $Af\rho$ power law slopes are shallow inbound. The slope is initially -0.56 ± 0.12 flattening to -0.08 ± 0.02 at distances $r < 3$ au. Outbound, the slope is -1.74 ± 0.05 out to 1.3 au, -0.83 ± 0.05 between 1.4 au and 1.8 au, -1.34 ± 0.06 between 1.9 au and 2.7 au, and then finally -2.31 ± 0.15 beyond 3 au. C/2011 K1's activity displays similar characteristics to those that were seen in earlier DNCs in the sample, specifically C/2009 P1, i.e. a high and sustained level activity pre-perihelion, with the only significant change occurring about 3 au. The post-perihelion activity falls off sharply but not continuously, indicating different volatiles with different turn on points. After 3 au its activity decreases more rapidly probably due to the turn off of water.

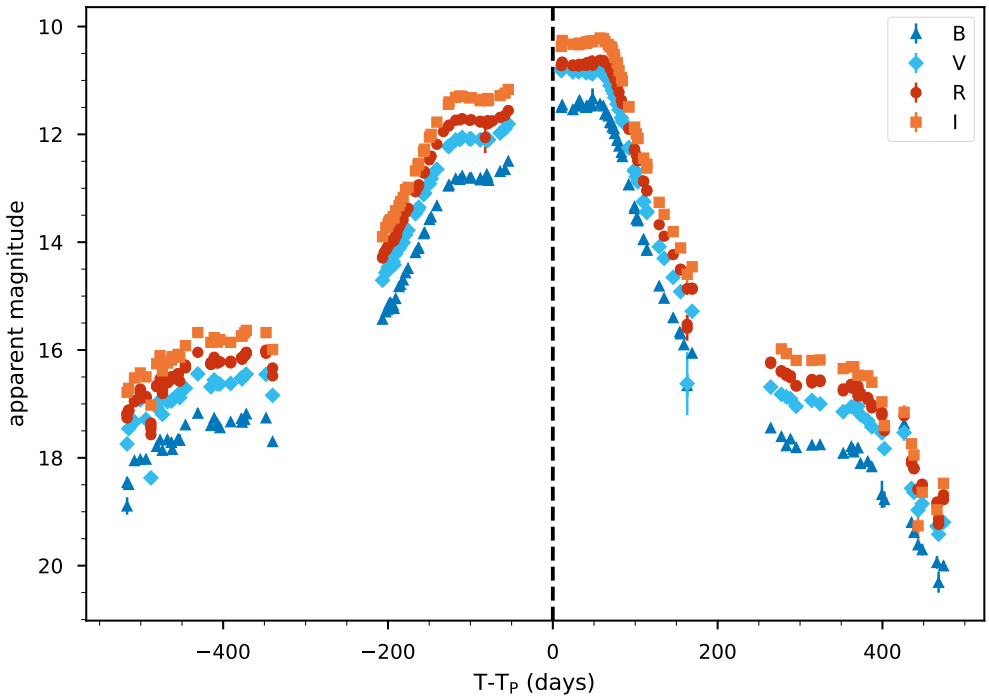

Figure 4.36 Light curve of C/2012 K1 measured in B-, V-, R- and I-bands by the TRAPPIST-South telescope in $\rho = 10\,000$ km apertures. Time is measured as days from perihelion.

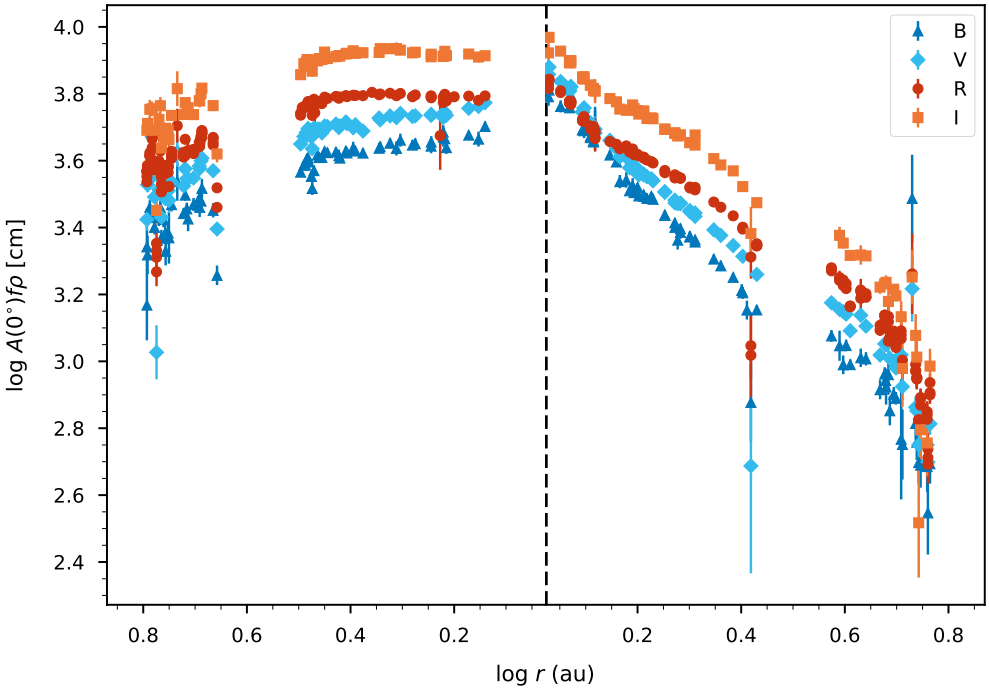

Figure 4.37 $Af\rho$ vs. r of C/2012 K1 measured in B-, V-, R- and I-bands by the TRAPPIST-South telescope in $\rho = 10\,000$ km apertures. The vertical dotted line indicates the perihelion distance of $r = 1.05$ au.

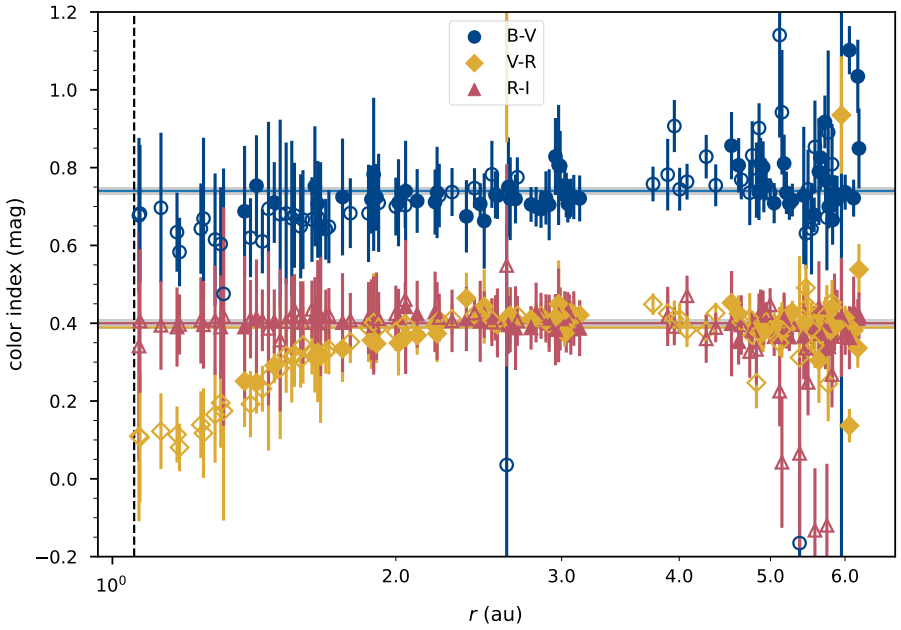

Figure 4.38 Colour index vs. r of C/2012 K1 measured with TRAPPIST-S photometry in the B-, V-, R- and I-bands. The filled and unfilled points represent pre- and post-perihelion measurements respectively. The means and uncertainties are drawn as horizontal lines and shaded areas respectively. The vertical dotted line indicates the perihelion distance of $r = 1.05$ au.

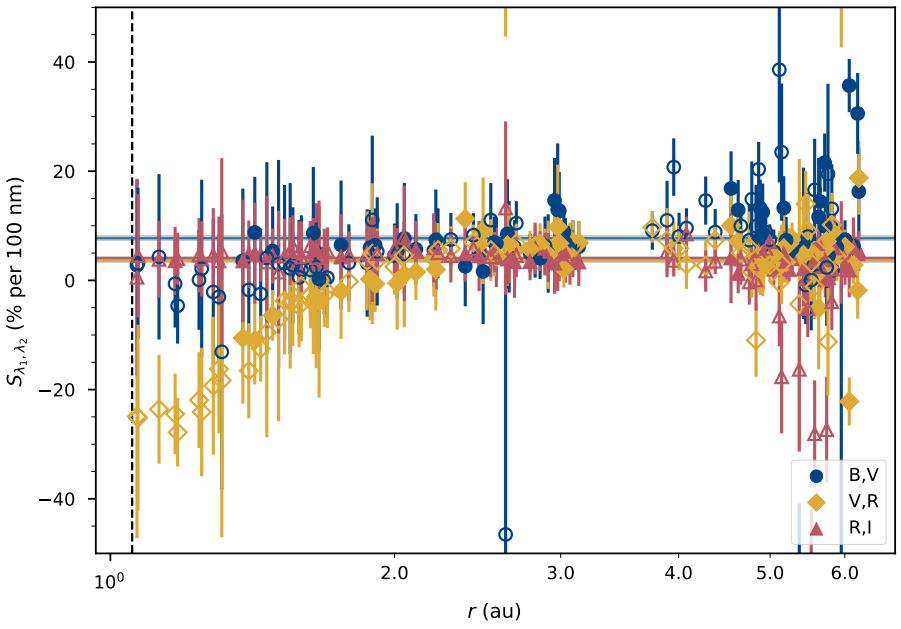

Figure 4.39 Spectral slope vs. r of C/2012 K1 measured with TRAPPIST-S photometry in the B-, V-, R- and I-bands. The filled and unfilled points represent pre- and post-perihelion measurements respectively. The means and uncertainties are drawn as horizontal lines and shaded areas respectively. The vertical dotted line indicates the perihelion distance of $r = 1.05$ au.

Woodward et al. (2015) find average dust production rate at distance of 1.70 au of $Af\rho = 5340$ cm, I measure $Af\rho = 6140$ cm at the same point. Woodward et al. (2015) also find the dust grains of C/2012 K1 are dominated by carbon and have bulk properties similar to other nearly isotropic comets. Garcia and Gil-Hutton (2021) measured a V magnitude of 17.27 and $Af\rho = 622.30 \pm 6.71$ cm. This is much dimmer and less active than I measure. It remains unclear why they observe such a dim magnitude especially since they use the same aperture size as me. They see twisted structures in morphology and posit the idea of active polar regions. Combi et al. (2018) measures water production rates of $r^{-0.8}$ pre-perihelion and $r^{-2.4}$ post-perihelion. They also draw a comparison to C/2009 P1 showing similarities in the production rate pre-perihelion inside 2.1 au and the more steady drop after perihelion. These similarities to C/2009 P1 I also see in the dust activity. They also see an extended source thought to be an icy grain halo.

Figure 4.38 shows the colours of C/2012 K1 remain constant across most of the orbit but show variation near perihelion. The average colours across the whole orbit are $B - V = 0.74 \pm 0.01$, $V - R = 0.39 \pm 0.004$ and $R - I = 0.40 \pm 0.01$. $V - R$ reaches a minimum around 10 days after perihelion which corresponds to the peak in $Af\rho$. The spectral slopes are plotted in Figure 4.39. The average slopes are $S_{B,V} = 7.7 \pm 0.5$ per cent per 100 nm, $S_{V,R} = 3.6 \pm 0.5$ per cent per 100 nm and $S_{R,I} = 4.1 \pm 0.4$ per cent per 100 nm. $S_{V,R}$ reaches a minimum around -30 per cent per 100 nm indicating increased gas production around perihelion after r=2.2 au and ceasing at the same point post perihelion. Betzler et al. (2020) find between 2014 April 4 and May 8 the average $S_{440,647} = 8 \pm 7$ per cent per 100 nm and average $B - R = 1.17 \pm 0.17$ which agrees with the colours I measure, from my data I get $B - R = 1.09 \pm 0.10$.

4.2.11 C/2013 A1 (Siding Spring)

C/2013 A1 (Siding Spring) was discovered on 2013 January 3 by McNaught et al. (2013) with the 0.5-m Southern Uppsala Schmidt telescope at the Siding Spring Observatory at $r = 7.2$ au. Orbital parameters define it as a DNC coming to perihelion at 1.40 au on 2014 October 24, and its orbital solution put it on a trajectory for a close encounter with Mars at a distance of 141 000 km on 2014 October 19. This made it an interesting target for astronomers and presented a unique opportunity to observe the nucleus of a DNC using spacecraft in orbit of

Mars, however the scientific insights of this seem limited. Farnham et al. (2017) observed the nucleus in MRO HiRISE images, revealing a ~ 1 km non-spherical body and activity modulation with a period of 8.1 hr. There clearly was a plan to perform a detailed analysis, constraining the size, shape, orientation, albedo and phase dependence of the nucleus, however these results seem to have never been published as there is no follow-up paper. It was thought that high-velocity ($\sim$ 56 ms^{-1}) dust grains from the comet's coma could pose a serious risk to instruments both in orbit and on the surface of the planet, but various hazard analyses (Farnocchia et al., 2014; Kelley et al., 2014; Tricarico et al., 2014; Ye and Hui, 2014) determined that these risks were minimal. Kiss et al. (2015) estimate that activity started about a month before discovery at ~ 8 au. On 2013 March 31, 6.4 au, they measured $Af\rho = 185 \pm 25$ cm and a dust production rate of 1.5 ± 0.5 kg s^{-1} indicating a slower increase than expected for an Oort cloud comet. Observations made by instruments orbiting Mars can be found in Benna et al. (2015); Crismani et al. (2015, 2018); Espley et al. (2015); Gurnett et al. (2015); Restano et al. (2015); Schneider et al. (2015); Sánchez–Cano et al. (2020).

C/2013 A1 (Siding Spring) was observed by the TRAPPIST-South telescope between 2013 March 10 and 2015 March 21 in *B-, V-, R-* and *I*-bands. Monitored from 6.66 au through perihelion at 1.4 au and out to 2.44 au. The light curve is plotted in Figure 4.40. The brightness peaks in *R*-band about 11.5 mag about 50 days before perihelion but then has a sudden brightening immediately after perihelion – an outburst. The $Af\rho$ curve in Figure 4.41 paints a clearer picture, flattening out the phase angle effects, and making the outburst even more prominent.

Even without the outburst, this comet has a strange activity pattern, seemingly oscillating in activity as it approaches perihelion. Its activity initially climbs steadily inbound, with a slope of -0.25 ± 0.07, then begins to decrease interior to 4 au with a slope of 1.85 ± 0.07. At some point within interior to 3 au, its activity starts rising again to a slope -1.01 $\pm$ 0.10, but it then plateaus and starts to decrease again with a slope 0.49 ± 0.05 interior to 2 au as it approaches perihelion. This pattern is subtle and could be attributed to phase angle effects but this pattern is also seen in Opitom et al. (2016). They present broadband *R*-band and narrowband TRAPPIST data of C/2013 A1 and see outburst two weeks after perihelion on 2014 November 10. The shallow dependence of gas activity is consistent with the theory of a dust mantle which may be partially blown off during the outburst, which is typical of DNCs. They also see similarities between

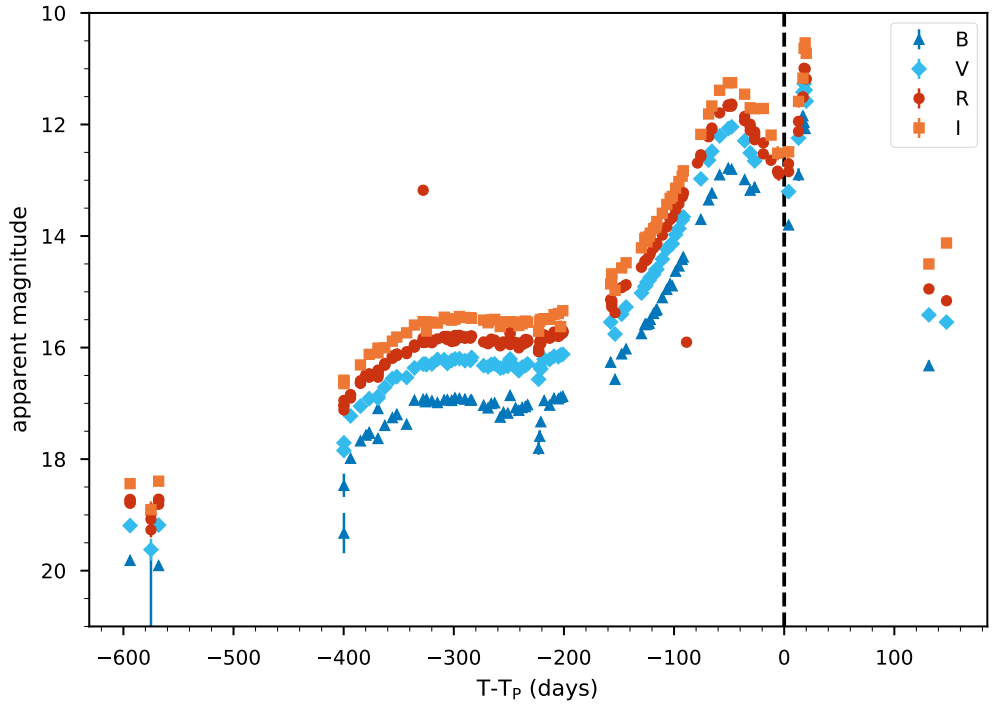

Figure 4.40 Light curve of C/2013 A1 measured in B-, V-, R- and I-bands by the TRAPPIST-South telescope in $\rho = 10\,000$ km apertures. Time is measured as days from perihelion.

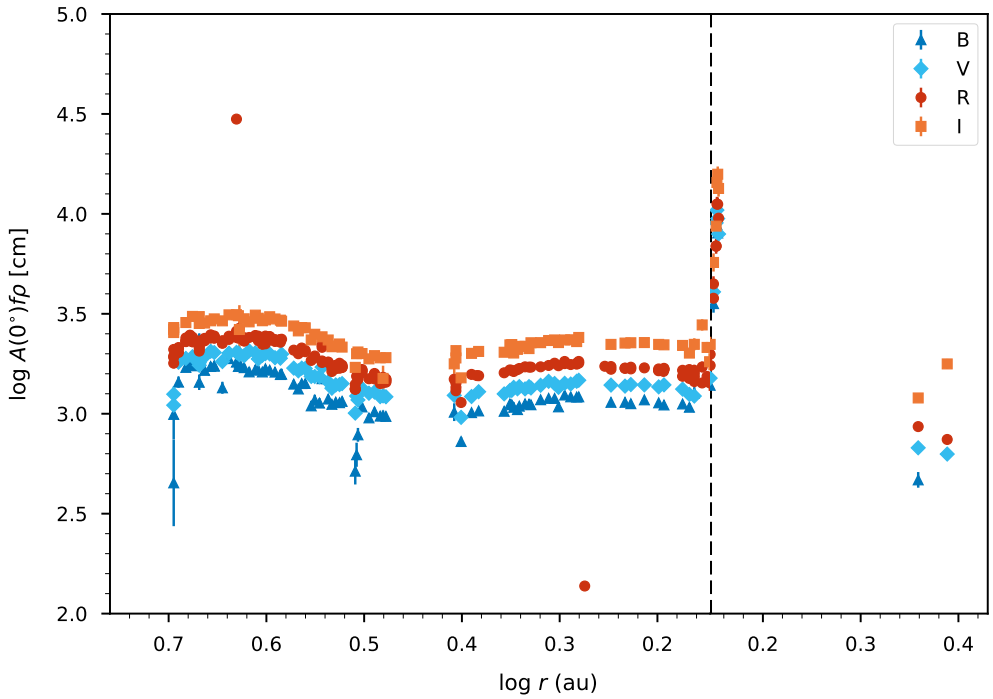

Figure 4.41 $Af\rho$ vs. r for C/2013 A1 measured in B-, V-, R- and I-bands by the TRAPPIST-South telescope in $\rho = 10\,000$ km apertures. The vertical dotted line indicates the perihelion distance of $r = 1.40$ au.

C/2009 P1 and C/2013 A1 at same heliocentric distances.

Li et al. (2014) observed C/2013 A1 with Hubble Space Telescope at 4.58, 3.77 and 3.28 au measuring $Af\rho$ of 2500, 2100 and 1700 cm respectively. My data is in good agreement measuring 2316 cm at 4.6 au, 2080 cm at 3.72 au, and 1703 cm at 3.3 au. Stevenson et al. (2014) measure $Af\rho = 432\pm21$ cm at 3.82 au on 2014 January 16; $Af\rho$=726±40 cm at 1.88 au on 2014 July 28; $Af\rho$=724±40 cm at 1.48 au on 2014 September 21. They suggest the decrease in activity between July and September is due to depletion of volatiles. I measure $Af\rho$ of 2359 on 2014 January 14, 1791 on 2014 July 25 and 1663 on 2014 September 24. Andrienko et al. (2016) measure $Af\rho$ is 1550 cm on 2013 December 12, 1750 cm on 2013 December 13 compared to my measurement of 2407 cm on 2013 December 14.

Bodewits et al. (2015) suggest seasonal and evolutionary effects on the nucleus to explain the pre-perihelion activity pattern. Increases in water production between 2.46 and 2.06 au suggest onset of sublimation of icy grains in the coma, driven by CO_2. For $r > 2.5$ au, CO_2 sublimation from a constant area on nucleus, H_2O production is too low to account for all activity. At distances $2.5 < r < 2$ au, there is an increased sublimation rate of icy grains and increased water production. At $r < 2$ au, there is a rapid change of sub-solar latitude, resulting in insolation of new parts of the surface, water sublimation begins and CO_2 production decreases which is similar to what was seen in C/2009 P1.

The colours of C/2013 A1 remain relatively constant at $S_{V,R} = -38.6 \pm 2.2$ per cent per 100 nm, $S_{B,V} = 6.0 \pm 0.6$ per cent per 100 nm and $S_{R,I} = 30.5 \pm 1.4$ per cent per 100 nm, until perihelion when there is a sudden drop in $V - R$ immediately post-perihelion corresponding to the outburst, curiously $R - I$ increases around this time too. $R-I$ in general, is unusually high as well, C/2013 A1 seems to be a very red comet. Perhaps there is an emission line in the infrared contained in the outburst. Li et al. (2014) measured colour is $S_{B,V} = 5\pm0.3$ at 4.58 au and 3.77 au and 9±0.3 per cent per 100 nm at 3.28 au. They say temporal evolution of the dust colour are most consistent with icy grains in the coma. The slopes measured by Li et al. (2014) are mostly consistent with mine. Andrienko et al. (2016) measured colours of $V - R = 0.49 \pm 0.03$ and corresponding slope of 13.2 ± 0.03 per cent per 100 nm on 2013 December 12, and $V - R = 0.41 \pm 0.02$ with slope of 5.1 ± 0.65 per cent per 100 nm on 2013 December 13. This is very different to my measured colours on 2013 December 14 of $V - R = -0.13 \pm 0.23$ corresponding to $S = -49 \pm 24$ per cent per 100 nm.

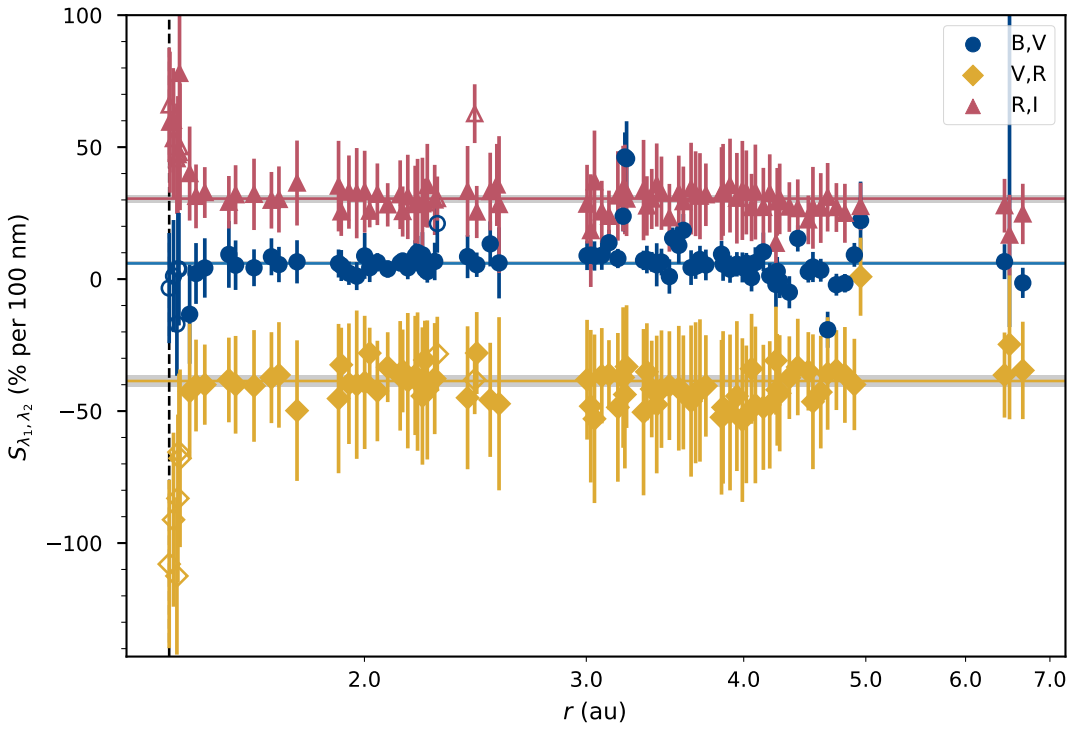

Figure 4.42 Spectral slope vs. r of C/2013 A1 measured with TRAPPIST-S photometry in the B-, V-, R- and I-bands. The filled and unfilled points represent pre- and post-perihelion measurements respectively. The means and uncertainties are drawn as horizontal lines and shaded areas respectively. The vertical dotted line indicates the perihelion distance of $r = 1.40$ au.

We cannot see if this follows the pattern of other DNCs as there is limited post-perihelion data so it is hard to judge if there is any asymmetry in the slopes pre- and post-perihelion. Looking at the light curve of Yoshida[4], it seems that there is steep decrease in brightness post-perihelion after the outburst. The shallow incoming slope does indicate the pre-perihelion trend is at least true.

4.2.12 C/2013 R1 (Lovejoy)

C/2013 R1 (Lovejoy) was discovered by amateur astronomer Terry Lovejoy on 2013 September 7 at a distance of 1.97 au from the Sun (Guido et al., 2013). It came to perihelion at $q = 0.8$ au on 2013 December 22, its inclined ($i = 64°$) and highly eccentric ($e = 0.9924$) orbit indicates this is a long-period comet from the Oort cloud. It has a period of $\sim$ 11 500 yrs making it a dynamically old

[4] `http://www.aerith.net/comet/catalog/2013A1/2013A1.html`

comet. Narrowband TRAPPIST data has already been published by Opitom et al. (2015b).

C/2013 R1 (Lovejoy) was observed by the TRAPPIST-South telescope between 2013 September 11 and 2014 October 14 in *B*-, *V*-, *R*- and *I*-bands. It was monitored from $r = 1.92$ au inbound coming to perihelion at $q = 0.81$ au then out to $r = 4.2$ au outbound. The light curve of C/2013 R1 is plotted in Figure 4.43, peaking in brightness of about 8 mag in the *R*-band about 50 days before perihelion. The $Af\rho$ curve (Figure 4.44) reveals the activity is more symmetrical than the light curve would suggest, the peak dust activity is measured 60 days after perihelion although I miss the crucial perihelion measurements so it is likely the activity peaked between the two points measured pre- and post-perihelion. The $Af\rho$ slopes measure -3.52 ± 0.07 pre-perihelion and -2.76 ± 0.09 post-perihelion. This is similar to the characteristics seen in C/2012 F6, another LPC, indicating a shared characteristic between them.

Opitom et al. (2015b) shows dust slopes of $r^{-3.92}$ pre-perihelion and $r^{-3.01}$, the discrepancies are probably due to narrowband vs. broadband filters. Combi et al. (2018) sees similar activity trends in the water production of C/2013 R1 with steeper inbound slope than outbound. They measured slopes of $r^{-2.2}$ pre-perihelion and $r^{-1.6}$ post-perihelion. Paganini et al. (2014) and Opitom et al. (2015b) also see similar trends in water production albeit being a factor of two smaller than in Combi et al. (2018).

Looking at the colours in Figure 4.45, the colours are flat overall with average spectral slopes of $S_{R,I} = 0.3 \pm 0.8$, $S_{B,V} = -1.1 \pm 1.2$ and $S_{V,R} = -3.0 \pm 1.2$ per cent per 100 nm. Although $S_{V,R}$ is not constant and seems to have a downward trend pre-perihelion reaching a minimum around -30 per cent per 100 nm ($r = 1.06$ au) which would be suggestive of increased gas activity pre-perihelion which is not present post-perihelion. Opitom et al. (2015b) measures a constant colour between 6 and 14 per cent per 100 nm, in RC and GC filters. This constant nature is not seen in ours, showing the difference between broadband imaging and using narrow filters designed specifically to separate dust and gas. H_2O, CO, CH_4, HCN, C_2H_6 and CH_3OH are detected by (Paganini et al., 2014). C_2, NH and OH production rates are strongly correlated with dust production, while CN and C_3 are not (Opitom et al., 2015b).

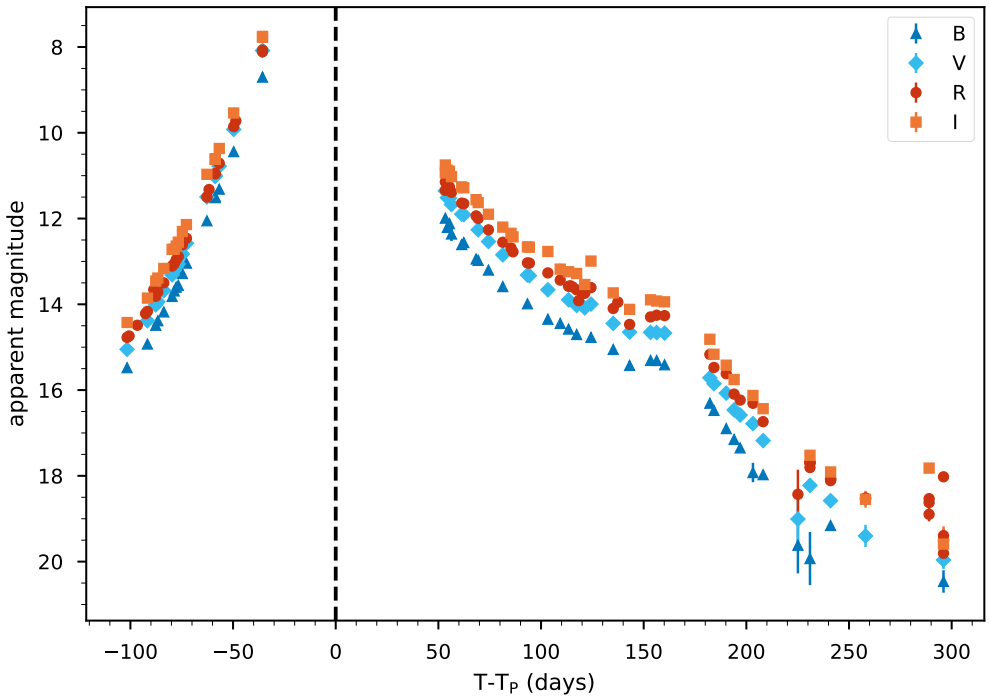

Figure 4.43 Light curve of C/2013 R1 measured in B-, V-, R- and I-bands by the TRAPPIST-South telescope in $\rho = 10\,000$ km apertures. Time is measured as days from perihelion.

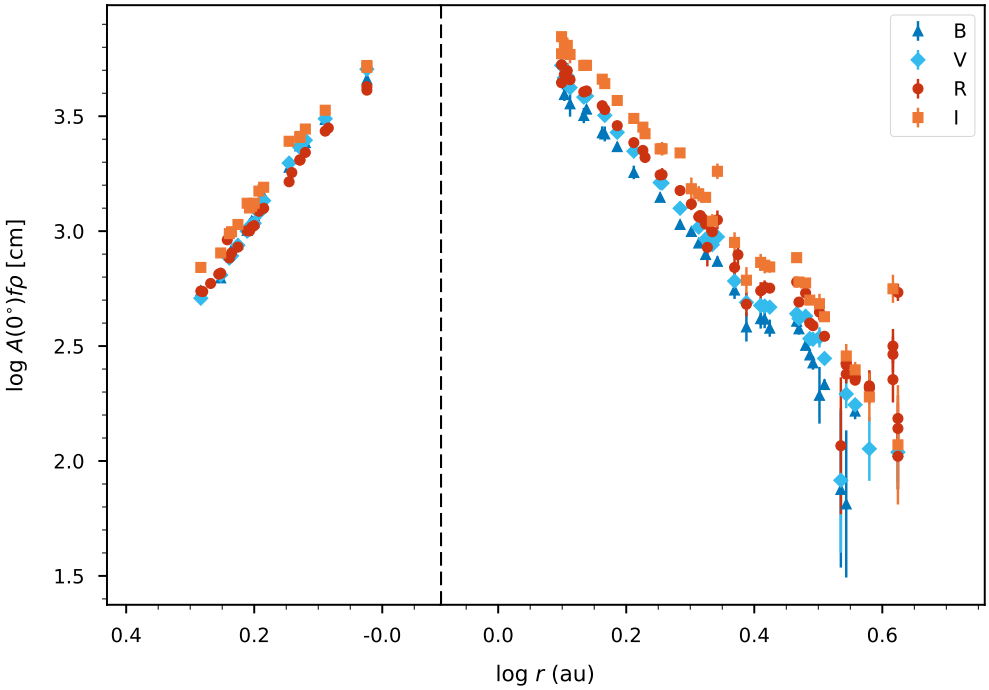

Figure 4.44 $Af\rho$ vs r for C/2013 R1 measured in B-, V-, R- and I-bands by the TRAPPIST-South telescope in $\rho = 10\,000$ km apertures. The vertical dotted line indicates the perihelion distance of $r = 0.81$ au.

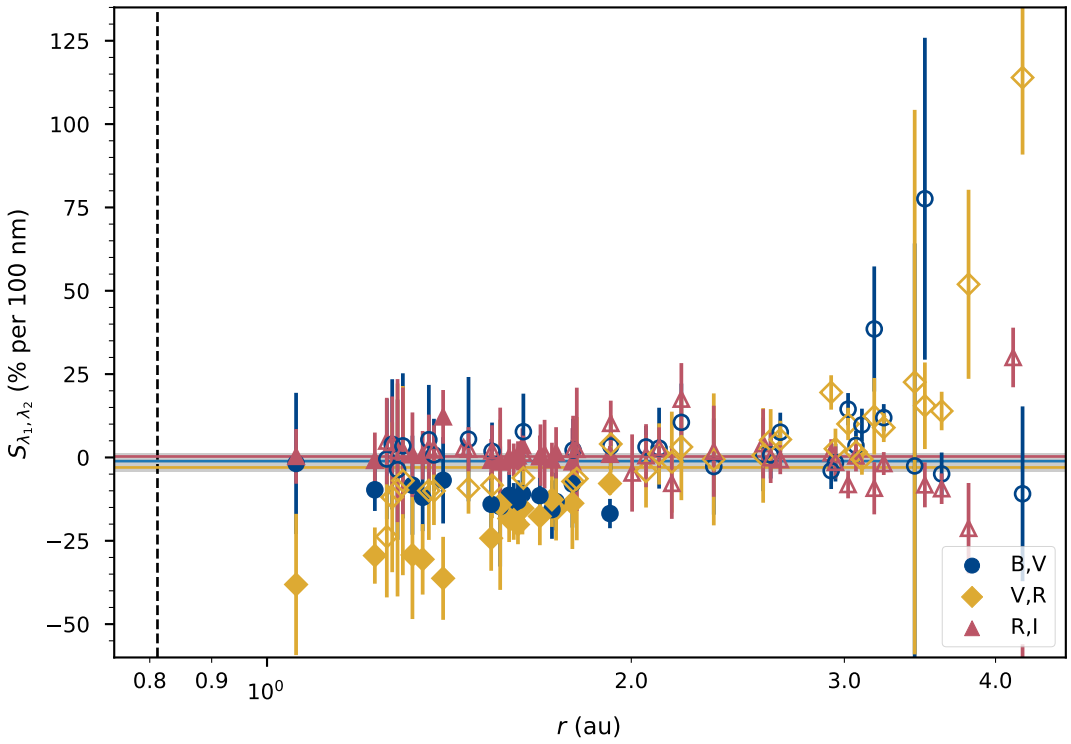

Figure 4.45 Spectral slope vs. r of C/2013 R1 measured with TRAPPIST-S photometry in the B-, V-, R- and I-bands. The filled and unfilled points represent pre- and post-perihelion measurements respectively. The means and uncertainties are drawn as horizontal lines and shaded areas respectively. The vertical dotted line indicates the perihelion distance of $r = 0.81$ au.

4.2.13 C/2013 US$_{10}$ (Catalina)

C/2013 US$_{10}$ was discovered by the Catalina Sky Survey on 2013 October 31 at $r = 8$ au (Honkova et al., 2013). With $e = 1.0003$, $i = 148.9$, $1/a = 5.3 \times 10^{-6}$ au^{-1}, this is a dynamically new carbon rich (Woodward et al., 2021) comet coming from the Oort cloud for the first time. It came to perihelion at $q = 0.8230$ au on 2015 November 15. Protopapa et al. (2018) noted the coma of C/2013 US$_{10}$ is made of water-ice grains with sizes on the order of ~ 1 μm containing no more than 1 per cent refractory material. They suggest it is a hyperactive comet but this is reliant on the size of its nucleus which is not well constrained.

C/2013 US$_{10}$ was observed in B-, V-, R- and I-bands by the TRAPPIST-South telescope between 2014 May 16 and 2016 January 1 covering $r = 6.65$ au to perihelion at $q = 0.82$ au then a few observations back out to $r = 1.18$ au. It was also observed by the TRAPPIST-North telescope on 2016 September 1 at

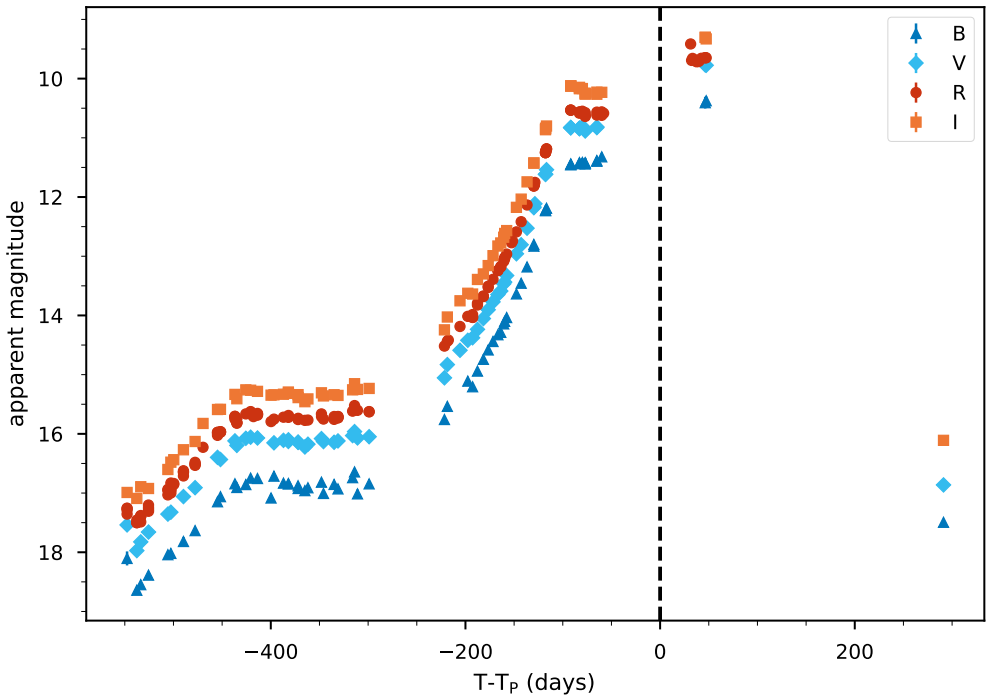

Figure 4.46 Light curve of C/2013 US_{10} measured in B-, V-, R- and I-bands by the TRAPPIST-South and TRAPPIST-North telescopes in $\rho = 10\,000$ km apertures. Time is measured as days from perihelion..

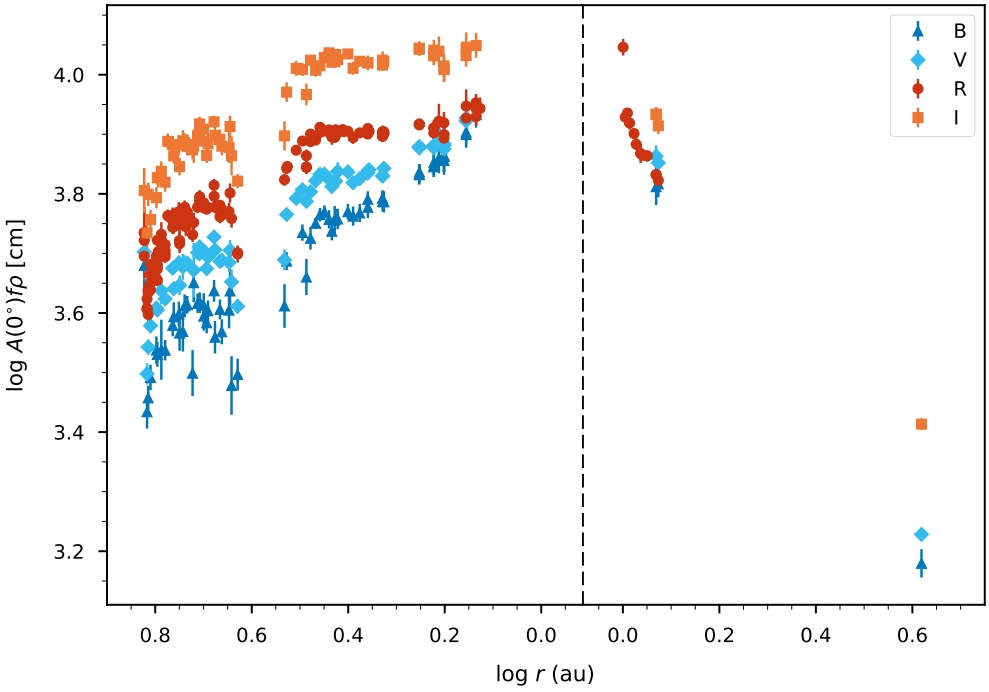

Figure 4.47 $Af\rho$ vs. r for C/2013 US_{10} measured in B-, V-, R- and I-bands by the TRAPPIST-South and TRAPPIST-North telescope in $\rho = 10\,000$ km apertures. The vertical dotted line indicates the perihelion distance of $r = 0.82$ au.

$r = 4.16$ au outbound.

The light curve is plotted in Figure 4.46 which shows the brightness peaking at around 9.5 mag in R-band about 30 days after perihelion, looking at amateur data taken around perihelion confirms this[5]. Figure 4.47 shows that the change in brightness is largely a viewing geometry effect and the dust activity is much flatter than the light curve would suggest, also the dust activity would appear to peak 60 days before perihelion instead of after although the activity is very similar to the post-perihelion. The geometry also masks the significant decrease in activity post perihelion. The pre-perihelion slope is not uniformly continuous so I have split the curve into sections to measure the power law slopes. The first section ($r > 5.6$ au) has a slope of -1.68 ± 0.26 which then shallows to -0.48 ± 0.03 after the comet passes $r = 5.6$ au, this then flattens again to -0.01 ± 0.02 around 3 au. The slope then steepens approaching perihelion within 1.8 au to -0.28 ± 0.07. This is like what we see in 88P. Post-perihelion, the slope is -1.58 ± 0.10. Combi et al. (2018) found the water production rates of C/2013 US_{10} to be $r^{-1.6}$ incoming and $r^{-1.9}$ outgoing. Like me, they see production rates higher pre-perihelion than post-perihelion. They suggest that C/2013 US_{10} might not be a DNC and is instead a returning LPC due to its semi-major axis of $a = 14\,000$ au, which is close to the cut-off for DNCs of $a > 10\,000$ au. For my analysis I will still classify it as a DNC. Garcia et al. (2020) observed on 2015 July 18, at distance of $r = 2.16$ au, an $Af\rho = 6331 \pm 20$ cm with a 10 000 km aperture. This the same order of magnitude of my observations, I measure $Af\rho = 7891 \pm 45$ cm on 2015 July 20.

Figure 4.48 plots the spectral slopes for C/2013 US_{10}. The comet has an average spectral slope across the orbit of $S_{V,R} = 4.9 \pm 0.6$ per cent per 100 nm, $S_{B,V} = 5.3 \pm 0.7$ per cent per 100 nm and $S_{R,I} = 3.8 \pm 0.5$ per cent per 100 nm. But the colour begins to shift toward the blue end of the spectrum about 100 days before perihelion ($r \sim 1.8$ au) before reaching a minimum pre-perihelion at $S_{V,R} = -15$ per cent per 100 nm and $S_{B,V} = -5$ per cent per 100 nm ($r = 1.36$ au). Post perihelion seems to show a continued decrease to $S_{V,R} \sim -25$ per cent per 100 nm. However $S_{B,V}$ has increased since perihelion. It is hard to say since we only have a few points post-perihelion so this makes it difficult to draw any conclusion regarding the offset of the peaks in gas and dust activity.

C/2013 US_{10} shows activity similar to other DNCs with a flat incoming slope and very steep outgoing. The only unusual characteristic of this curve is the

[5] `http://www.aerith.net/comet/catalog/2013US10/2013US10.html`

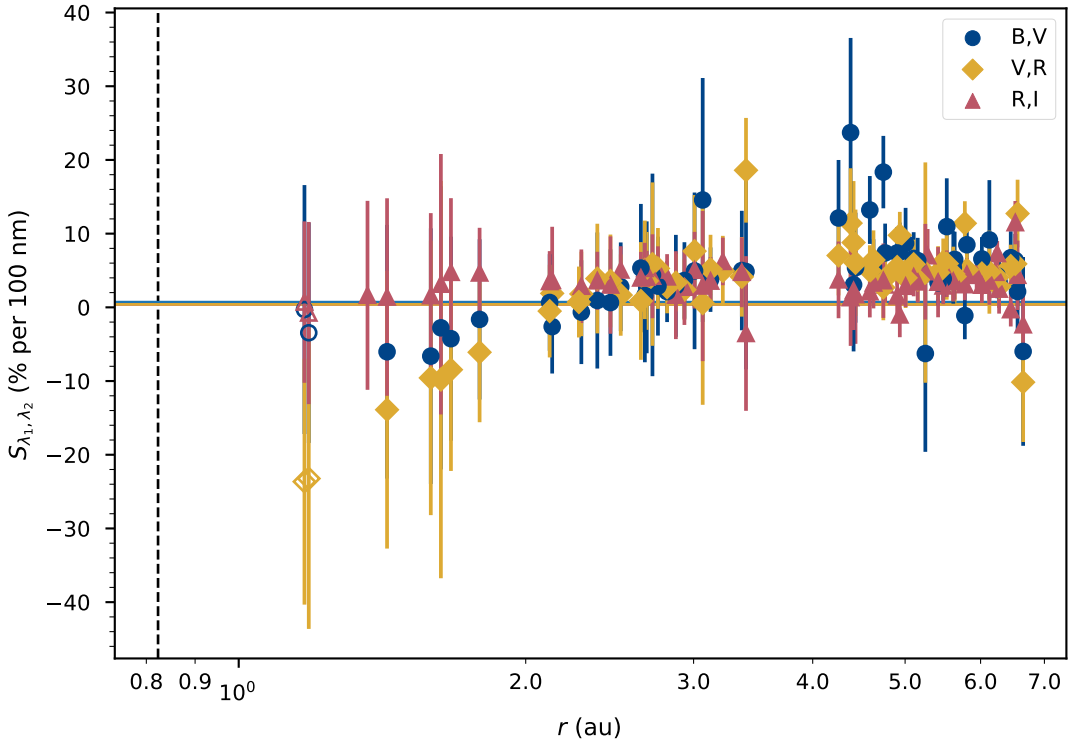

Figure 4.48 Spectral slope vs. r of C/2013 US_{10} measured with TRAPPIST-S photometry in the B-, V-, R- and I-bands. The filled and unfilled points represent pre- and post-perihelion measurements respectively. The means and uncertainties are drawn as horizontal lines and shaded areas respectively. The vertical dotted line indicates the perihelion distance of $r = 0.82$ au.

steep curve before 5.6 au, measuring a slope steeper than the outgoing slope. It is possible that this unusual characteristic suggests that this comet is in fact a returning LPC as theorised by Combi et al. (2018). Although relative to the JFCs and LPCs the slope is not that steep so still suggests possible DNC like activity. This suggests there is some activity driver which plateaus after 6 au. The curve shows another flattening around 3 au corresponding to the water line. Although the dust activity has flattened, the gas has not; the colours show that production of gas are still increasing up to perihelion. A threshold is then again passed at 1.8 au, although increase is relatively minor. Perhaps this represents an exposure of a new volatile, this threshold corresponds to the decrease in $V - R$ and $B - V$.

4.2.14 C/2015 ER$_{61}$ (PanSTARRS)

C/2015 ER$_{61}$ (PanSTARRS) was discovered by the Pan-STARRS 1 survey telescope on Haleakala on 2015 March 14 at $r = 8.45$ au. The orbital parameters point to it originating from the Oort cloud, but its small semi-major axis and defined period mean it is not dynamically new but instead a returning long-period comet. Meech et al. (2017) report large nucleus $R \sim 9$ km. They report activity began at $r = 8.8$ au in early 2015, driven by CO_2 sublimation, peaking in 2016 April at $r = 5.1$ au. Their model suggests that water sublimation began at 5 au. They show water sublimation area 1 per cent and thermal models suggest CO_2 ice at depth of 0.4 m. If CO_2 ice was on surface, then the comet would be active further out, as much as 20 au.

C/2015 ER$_{61}$ (PanSTARRS) was observed in *B-, V-, R-* and *I*-bands by the TRAPPIST-South telescope between 2016 February 18 and 2017 December 11 and by the TRAPPIST-North telescope on the 2017 July 28. This covers a passage from $r = 5.56$ au inbound coming to perihelion at $q = 1.04$ au and then out to $r = 3.22$ au. Figure 4.49 shows the light curve of C/2015 ER$_{61}$. The brightness peaks around 10 mag in the V-band 35 days before perihelion, this maximum brightness is extremely sudden and causes a discontinuity in the light curve, this is a large outburst from the surface of the comet implying a large mass of dust was ejected from nucleus. Outside of this discontinuity, the slopes seem smooth and continuous. To get a clearer picture of the nature of this outburst we can look at Figure 4.50, the $Af\rho$ curve. Immediately we can see the outburst is even more prominent and does not follow the trend of the pre-perihelion curve. The dust production rate increased by a factor of 4 compared to pre-outburst levels. The pre-perihelion slope follows a power law slope of -0.27 ± 0.02 before the outburst. Post-perihelion the power law slope is initially -2.56 ± 0.10 but this could still be within the dimming of the outburst, after 1.4 au it shallows to -1.16 ± 0.01. Unlike the other two LPCs in my survey this comet has a relatively flat pre-perihelion slope which would make it more similar to the DNCs I have studied. C/2015 ER$_{61}$ has a similar orbital period to the other LPCs which would suggest it should have undergone the same amount of processing, but this assumes a close perihelion distance at previous apparition, so perhaps despite its LPC designation, it is traveling to the inner Solar System for the first or second time, exposing new volatiles for the first time and hence displaying activity more similar to a dynamically young comet.

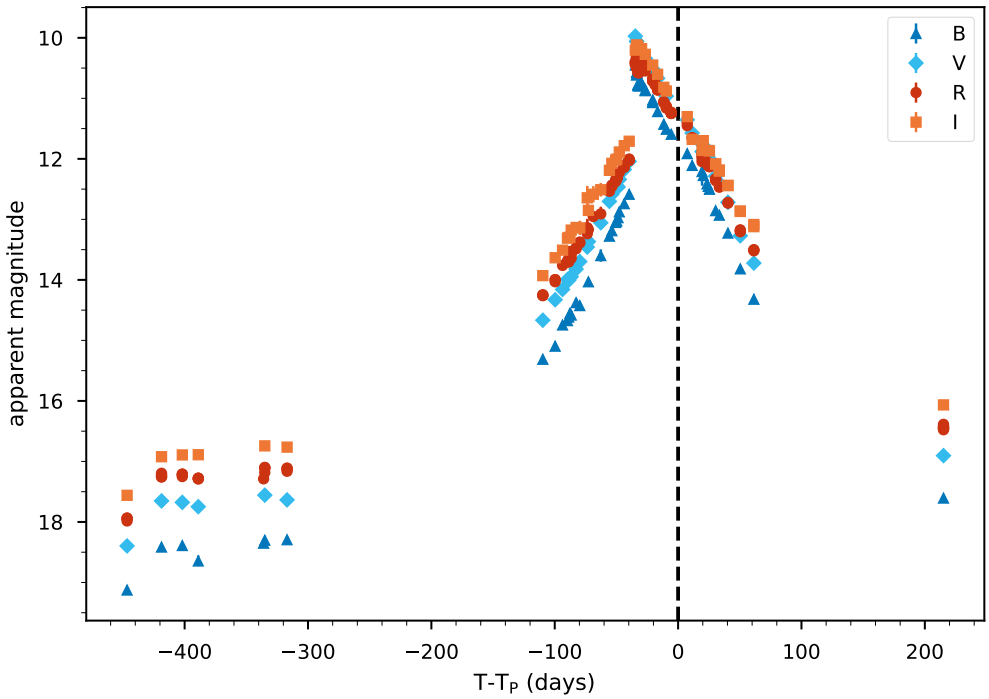

Figure 4.49 Light curve of C/2015 ER_{61} measured in B-, V-, R- and I-bands by the TRAPPIST-South telescope in $\rho = 10\,000$ km apertures. Time is measured as days from perihelion.

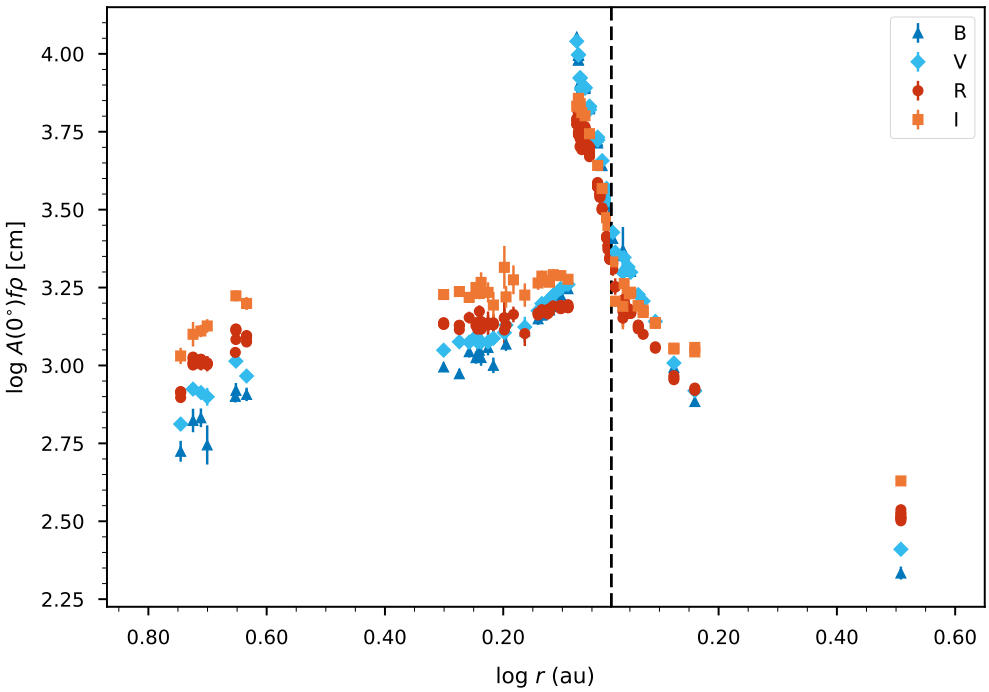

Figure 4.50 $Af\rho$ vs. r for C/2015 ER_{61} measured in B-, V-, R- and I-bands by the TRAPPIST-South telescope in $\rho = 10\,000$ km apertures. The vertical dotted line indicates the perihelion distance of $r = 1.04$ au.

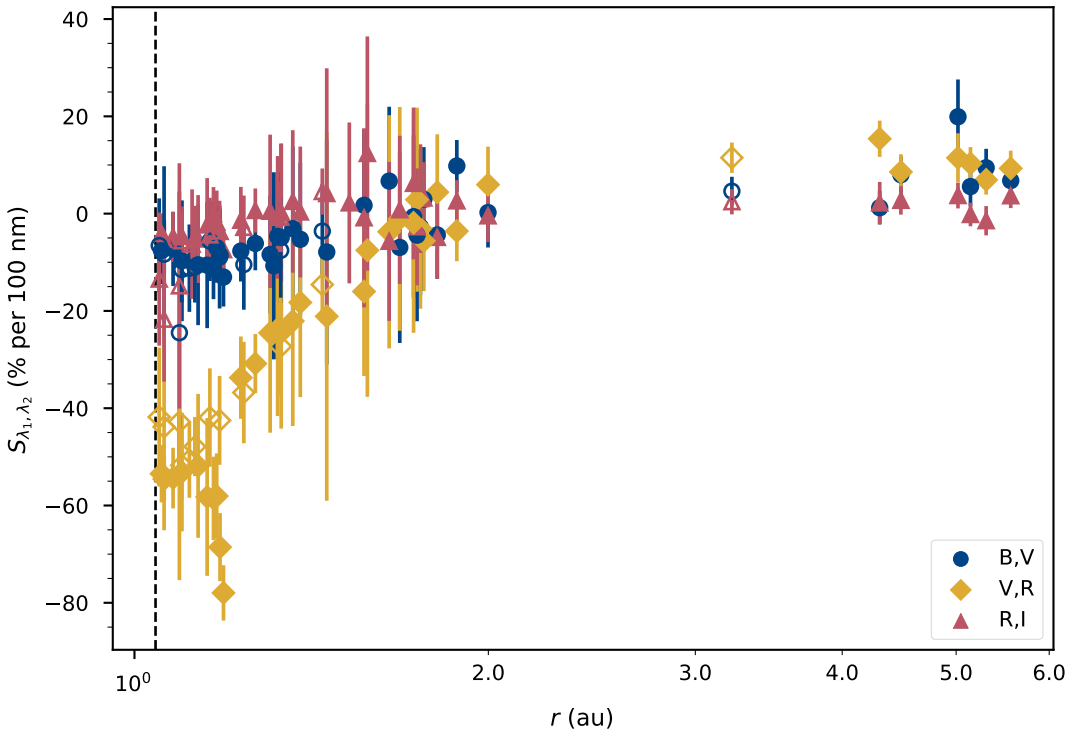

Figure 4.51 Spectral slope vs. r of C/2015 ER_{61} measured with TRAPPIST-S photometry in the B-, V-, R- and I-bands. The filled and unfilled points represent pre- and post-perihelion measurements respectively. The means and uncertainties are drawn as horizontal lines and shaded areas respectively. The vertical dotted line indicates the perihelion distance of $r = 1.04$ au.

Figure 4.51 shows the spectral slope of C/2015 ER_{61} measured on each night. There is a clear trough in spectral slopes across all the spectral ranges around perihelion, especially between V and R-band, reaching a minimum around $S_{V,R} \sim -60$ per cent per 100 nm, $S_{B,V} \sim -15$ per cent per 100 nm, $S_{R,I} \sim -15$ per cent per 100 nm. There is also a secondary trough in $S_{V,R} \sim -80$ per cent per 100 nm about 35 days ($r = 1.19$ au) before perihelion which would line up with the timing of the outburst seen in Figure 4.50. This peak is not seen in either $S_{R,I}$ or $S_{B,V}$ indicating an excess of a gas present only in B- and V-band. Also intriguing is that this is the only comet where we see a change in $S_{R,I}$ indicating perhaps there is increased production in R-band relative to I-band, although the errors are large enough that the scatter of points is encapsulated by the upper and lower bounds of the errors.

Yang et al. (2018) obtained high-resolution spectra of the outburst of C/2015 ER_{61} using UVES/VLT. It had typical isotopic ratios to other comets, which supports the theory that JFCs and Oort cloud comets originate in a largely over-

lapping region beyond Neptune. Opitom et al. (2019) find different morphology between dust and gas. NH_2 has different radial profile to other gases indicating an extended source, probably an icy grain halo. These morphological features are due to non-uniformly active nucleus, with different active areas. Different gas and dust morphology was also seen in C/2013 R1 (Opitom et al., 2015b) and 103P/Hartley 2 (Knight and Schleicher, 2013). Morphological differences between gas species or between dust and gas are linked to compositional differences on the surface such as the surface inhomogeneities seen by EPOXI (A'Hearn et al., 2011). Saki et al. (2021) and Roth et al. (2021) found C/2015 ER_{61} to be enriched in CH_3OH but depleted in HCN and CO. Other species are consistent with other comets. They see short-period variations in the production rates attributed to diurnal effects or effects of the outburst. They suggest decrease in post-perihelion production rates are due to seasonal effects.

4.3 Summary

4.3.1 Power law index comparisons

The power law indices measured for each comet are summarised in Table 4.4. It is clear there are distinct differences in the activity between the dynamical classes of comets. With the exception of 246P, all the JFCs in our sample follow the pattern of a steep pre-perihelion $Af\rho$ slope and then a shallower post-perihelion slope. This pattern in slopes is also seen in other studies of JFCs (e.g. Gillan et al., 2024; Whipple, 1978). The JFCs have an average pre-perihelion $Af\rho$ power law index of -4.5 ± 1.0 and post-perihelion index of -2.9 ± 0.7 giving an asymmetry, the difference between slopes, of -1.6 ± 1.2. This pattern is seen over a heliocentric distance range of 1.5 and 3 au. Gillan et al. (2024) found slopes of -6.5 ± 5.5 pre-perihelion and -3.6 ± 3.4 post-perihelion. Whipple (1978) measured pre-perihelion slope of 5.0 ± 1.4 and post-perihelion slope of 4.61 ± 0.91 for JFCs. Whipple measured the intrinsic brightnesses, not $Af\rho$, so the power law indices are not directly comparable, but it is still a worthwhile comparison of the underlying pattern of slopes. Both Gillan et al. (2024) and Whipple (1978) found a large range of slopes pre-perihelion in JFCs. At heliocentric distances less than 1.5 au, 46P and 88P showed an increase in their pre-perihelion power law indices. 46P's slope increased to -5.33 ± 0.09 and 88P measured slopes of -9.6 ± 1.6 and -10.0 ± 0.9 for the first and second apparitions respectively. This

Table 4.4 Summary of power law indices measured for each comet, grouped by dynamical class.

		Pre-perihelion		Post-perihelion	
Class	Comet	r range (au)	Power law index	r range (au)	Power law index
JFC	9P/Tempel 1 (2011)	—	—	1.54–3.30	-2.21 ± 0.20
	9P/Tempel 1 (2016)	1.55–2.34	-4.88 ± 0.17	1.54–1.63	-3.15 ± 1.36
	46P/Wirtanen	1.06–2.32	-5.33 ± 0.09	1.06–2.05	-4.03 ± 0.05
	88P/Howell (2015)	1.36–1.38	-9.59 ± 1.62	1.36–2.20	-3.05 ± 0.05
		—	—	2.27–3.12	-2.77 ± 0.17
	88P/Howell (2020)	1.37–1.42	-10.0 ± 0.90	—	—
		1.54–1.88	-3.41 ± 0.18	—	—
	103P/Hartley 2	—	—	1.21–2.75	-2.20 ± 0.10
	246P/NEAT	3.00–3.08	1.69 ± 0.99	2.89–3.13	1.14 ± 0.24
		3.10–3.44	-5.16 ± 0.20	3.17–3.98	-3.50 ± 0.10
LPC	C/2012 F6	0.82–2.26	-2.57 ± 0.02	1.01–1.54	-1.29 ± 0.13
	C/2013 R1	1.06–1.92	-3.52 ± 0.07	1.26–4.21	-2.76 ± 0.09
	C/2015 ER_{61}	1.23–5.56	-0.27 ± 0.02	1.05–1.44	-2.56 ± 0.10
		—	—	1.44–3.22	-1.16 ± 0.01
DNC	C/2009 F4	5.65–5.87	-0.82 ± 0.37	5.46–6.11	-4.88 ± 0.41
		—	—	6.27–9.59	-2.40 ± 0.76
	C/2009 P1	1.77–3.31	-0.14 ± 0.02	2.32–5.81	-3.03 ± 0.06
		3.32–4.70	-1.86 ± 0.06	—	—
	C/2011 L4	2.90–5.79	non-linear	—	—
	C/2012 K1	1.38–3.14	-0.08 ± 0.02	1.08–1.31	-1.74 ± 0.05
		4.55–6.21	-0.56 ± 0.12	1.40–1.79	-0.83 ± 0.05
		—	—	1.87–2.69	-1.34 ± 0.06
		—	—	3.75–5.81	-2.31 ± 0.15
	C/2013 A1	1.40–2.00	0.49 ± 0.05	—	—
		2.02–2.56	-1.01 ± 0.10	—	—
		3.00–4.02	1.85 ± 0.07	—	—
		4.06–6.66	-0.25 ± 0.07	—	—
	C/2013 US_{10}	1.34–1.79	-0.28 ± 0.07	1.00–1.18	-1.58 ± 0.10
		2.12–2.72	-0.01 ± 0.02	—	—
		2.75–5.64	-0.48 ± 0.03	—	—
		5.78–6.65	-1.68 ± 0.26	—	—

steep slope within 1.5 au was not seen in the post-perihelion slopes of the JFCs. This could suggest the presence of a volatile which turns on at 1.5 au or perhaps more likely a seasonal effect, however we only have these two examples to draw from so I am cautious to draw too many conclusions from such a limited sample.

246P is unique in the sample of JFCs due to its large perihelion distance of $q = 2.88$ au, as such it does not display the same activity pattern as the other JFCs. 246P had steep slopes beyond 3 au pre-perihelion but then it flattened out around 3 au. The activity then decreased some point before perihelion before flattening off again, after which the post-perihelion activity decreased after 3 au. This raises the question as to what is causing the flattening of this slope. The other comets in the JFCs increase in their activity at this point so we might

expect to see that pattern repeated here. Could it be that 246P has an extremely processed nucleus compared to the other JFCs? 246P was the only JFC observed which had most of its perihelion passage outside of 3 au but since this is the only comet like this in its classification I do not know if this is a representative object and cannot make any generalisations about JFCs with more distant orbits.

C/2012 F6 and C/2013 R1, classified as returning LPCs, share some similarities in their activity patterns with JFCs; they have asymmetry in their slopes with steeper incoming slopes than outgoing slopes, but not to the same extent as JFCs. These two LPCs have an average pre-perihelion $Af\rho$ power law index of -3.0 ± 0.7 and post-perihelion index of -1.9 ± 0.8, the asymmetry is -1.1 ± 1.1. These LPCs have a similar asymmetry pre- and post-perihelion to JFCs but the slopes themselves are shallower than those found in JFCs. However, the third returning LPC in my survey, C/2015 ER_{61}, has the opposite asymmetry with a flatter pre-perihelion slope compared to outbound slope and has a far flatter curve of -0.27 ± 0.02 than the other two LPCs, which is behaviour much more reminiscent of DNCs. The peak $Af\rho$ measured for all three LPCs are varied with C/2015 ER_{61} having activity similar to the most active JFCs before its outburst. C/2012 F6 and C/2013 R1 have peak $Af\rho$ about an order of magnitude greater than JFCs. We should be careful to draw conclusions from a small sample size about homogeneous group properties of returning LPCs. It is possible that these are a varied and inhomogeneous group of bodies, or that C/2015 ER_{61} is in fact a more 'typical' LPC and C/2012 F6 and C/2013 R1 are unusual cases. Whipple (1978) found LPCs to have the same slopes post-perihelion, I do not see such uniform slopes in my limited data. Womack et al. (2021) found a symmetric $Af\rho$ dependence of $r^{-1.5}$ in the LPC C/1995 O1 (Hale-Bopp).

Dynamically new comets have the most variety in their light curves, but overall they have shallow or non-linear slopes pre-perihelion and steep post-perihelion slopes. Due to the variety in the activity trends, the DNCs' activity have been grouped into the following heliocentric distance ranges for calculating the averages: $r < 2$ au, $2 < r < 3$ au, $3 < r < 4$ au and $r > 4$ au. At pre-perihelion distances between 4 and 6 au, the power law index is -0.8 ± 0.6, at pre-perihelion distances between 3 and 4 au the slopes flatten to -0.2 ± 1.6, between 2 and 3 au the slopes flatten further to -0.1 ± 0.1 with C/2013 US_{10} measuring 0.0 ± 0.3 within 2 au pre-perihelion. Post-perihelion, the slopes are much steeper with -1.5 ± 1.2 at heliocentric distances below 3 au, at distances above 3 au the slopes steepen again to -2.7 ± 0.5. C/2009 F4 was measured out to 9 au and mea-

sured a slope of -2.4 ± 0.8, suggesting that the activity trend established in the other comets could continue to large heliocentric distances. Although this is an assumption drawn from one single data point so more observations of DNC at large post-perihelion distances would be needed to confirm this. The asymmetry between the pre- and post-perihelion slopes at distances less than 3 au is 1.4 ± 2.0, these are the only group to display a positive asymmetry (i.e. the comets have a steeper post-perihelion than pre-perihelion slopes). At distances greater than 3 au the asymmetry between the slopes is 2.5 ± 1.7, a much larger asymmetry than seen in JFCs or LPCs. This would suggest that large positive asymmetry between pre- and post-perihelion slopes is an indicator of a DNC, however as demonstrated with the outlier C/2015 ER_{61}, LPCs can display this asymmetry too. Perhaps instead what this could indicate is how processed a cometary surface is. Even though C/2015 ER_{61} is confirmed as a returning LPC (Nakano, 2017), it could be that it is only returning to the inner Solar System for the second or third time and hence will have a far less processed surface more similar to a DNC which is entering the Solar System for the very first time than another LPC which even though it has very long orbital period, it is insignificant compared to the age of the Solar System so could have made many hundreds or thousands of Solar System returns in its lifetime. My findings are supported by Sárneczky et al. (2016), who find that $Af\rho$ is substantially higher than in DNCs than in returning comets and find DNCs have shallow activity slopes. They measured a slope of -0.65 for C/2012 K1 at $r = 5.210$ au pre-perihelion, which is in good agreement with my measured value of -0.56 ± 0.12 between 4.55 and 6.21 au pre-perihelion.

Activity is consistent and predictable in JFCs. They have a steady and consistent rise and fall in activity between orbits indicating the same volatiles are being exposed in each orbit. LPCs have the same overall activity pattern as JFCs since they have undergone a similar amount of processing to the JFCs, though not to the same extent, their slopes are shallower, perhaps indicating more active surface and sublimation of residual volatiles that have been depleted from JFCs. LPCs have higher peak $Af\rho$ values and therefore have much more dust production than JFCs. One LPC showed almost flat incoming slope making it more similar to DNCs than JFCs, perhaps indicating its younger dynamical age. JFC and LPC activity slopes do not show much variation across the orbit within 3 au.

88P and 246P have significantly higher dust production than their fellow JFCs, their measured peak $Af\rho$ values are an order of magnitude larger than other JFCs

however this is still an order of magnitude lower than LPCs or DNCs.

DNCs have initially high and sustained activity giving them a shallow incoming slope which suggest unprocessed surface freely sublimating. Post-perihelion the fall-off is steep and creates a much larger asymmetry between the slopes.

4.3.2 Offset between peak $Af\rho$ and perihelion

I looked to see if a pattern existed in the offset between the time of peak activity and perihelion. Most comets do show a discrepancy between the time of peak $Af\rho$ and the time of perihelion, however there seems to be no pattern or trend in this behaviour, with some comets peaking before perihelion and some after. For some comets an exact time could not be established since measurements were not taken near enough to perihelion so the peak in dust production could not be accurately determined. Of the ones measured: 9P peaked 36 days before perihelion, 46P peaked 4 days after perihelion, 88P peaked 12 days after perihelion, 246P peaks 216 days before perihelion, C/2013 A1 had an outburst 18 days after perihelion and C/2015 ER_{61} had an outburst 35 days before perihelion. For the others, I look to see if the trends indicate whether or not the peak would be before or after perihelion. C/2009 F4 peaks some time 100-200 days before perihelion. C/2009 P1 is hard to judge, the activity is higher pre-perihelion but following the post-perihelion trend back it would seem it peaks post-perihelion. C/2012 F6 and C/2013 R1 looks like they both peak post-perihelion. C/2012 K1 peaks post-perihelion. C/2013 US_{10} is hard to judge but looks very close to perihelion. Having a peak activity before perihelion seems more common within the DNCs with only C/2012 K1 having a peak activity after perihelion and C/2013 A1 outbursting 18 days after perihelion. There does not seem to be an easily identifiable factor that indicates which way the offset is going to be. Most other observers attribute the offset due to seasonal effects on the nucleus and not an inherent evolutionary difference, but this varies comet-to-comet. Gillan et al. (2024) found that JFCs had a tendency to exhibit peak activity after perihelion, with some having peak activity over a year after perihelion.

4.3.3 $Af\rho$ profiles

$Af\rho$ measurements are built on the assumption that the dust outflow rate from an aperture is constant. In order to test the validity of this assumption we can look at the $Af\rho$ profiles for each comet. Figure 4.52 shows an example profile for all comets in my survey, in this you can see the profile varies with aperture radius, the measured $Af\rho$ rise rapidly for smaller radii as FWHM dominates at such small aperture sizes. The profile then plateaus around 5000 km and begins to slowly tail off at larger radii. For an ideal coma with constant outflow the profile should be flat for all aperture sizes, this is not the case for 103P so indicates a non-steady state coma, perhaps the unusual brightness distribution is caused by the icy grains in the coma. 88P, C/2009 F4, C/2009 P1, C/2011 L4, C/2013 US_{10} and C/2015 ER_{61} all have $Af\rho$ profiles that plateau after 5000 km aperture radius and remains constant which indicates $Af\rho$ is a good model for dust production in these cases. The shortcomings in accounting for non-steady state dust flow affects the other comets causing the measured $Af\rho$ to tail off when measuring in bigger apertures, however this tail-off occurs beyond 10 000 km in most cases so

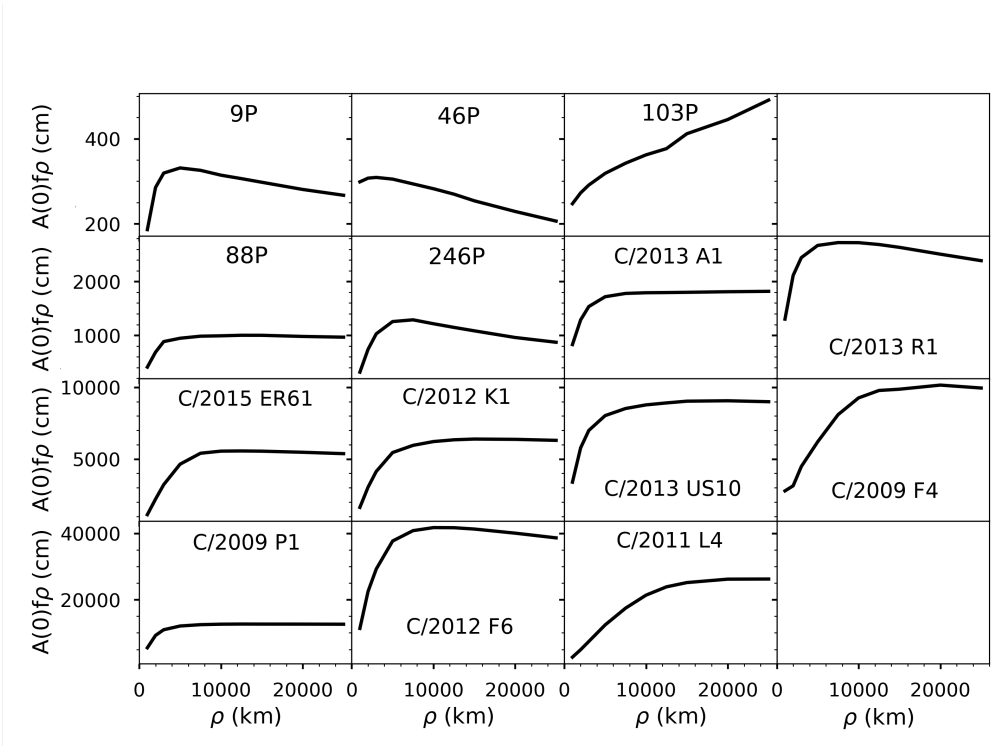

Figure 4.52 $Af\rho$ as a function of aperture radius ρ for all fourteen comets. The profiles are measured in R-band at each targets brightest point, with the exceptions of 103P, C/2009 F4, C/2009 P1 and C/2011 L4 whose $Af\rho$ are measured in the V-band.

$Af\rho$ is a good representation in my interpretation of dust activity.

4.3.4 *Effects on comet colour*

It is important to consider all of possible effects that can alter the colour of a comet's coma when making interpretations about activity. One is the dust-to-gas ratios within the coma. Comets with a lower dust-to-gas ratio will appear bluer in optical wavelengths as the bright emission lines of the gas radicals begin to dominate the dust emissions. These emission lines arise from the photodissociation of gas molecules in the coma, the fluorescence efficiencies of which vary as a function of heliocentric distance. The choice of aperture size can have a strong influence on the measured colours. Colours measured in a fixed angle aperture might appear to show a dependence on geocentric distance if the nuclei and coma have intrinsically different colours, or if the particle properties change with distance from the nucleus. As the geocentric distance changes, the physical size of the aperture will change and thus the colour gradient measured across the coma will also change. In almost every active comet, the photometry is dominated by the dust brightness, and not by the central nucleus. Radial colour variations result from changes in particle properties over time since release from the nucleus, such as dust fragmentation and the loss of embedded volatiles. Sudden changes in colour can also occur from rapid changes in coma composition due to an injection of new material into the coma from outbursts on the comet's surface. The comet can also appear redder at larger phase angles (typically between 30° and 120°) in a process known as phase reddening.

4.3.5 *Dependencies on heliocentric distance*

Figure 4.53 plots the peak measured $Af\rho$ of each comet against heliocentric distance. I do not see a strong dependency of $Af\rho$ with respect to heliocentric distance, Langland-Shula and Smith (2011) suggest there is a weak positive trend but this is not seen in my data. If one ignores the JFCs and only considers the dynamically newer comets, you could argue there is a trend of decreasing $Af\rho$ with increasing r. This is at odds with the findings of Langland-Shula and Smith (2011), but there too few points for me to confidently claim that this trend is real. What is clear is a separation in peak activity between the dynamical classes. JFCs typically have $Af\rho$ on the order of 10^2 cm, 88P and 246P measure larger

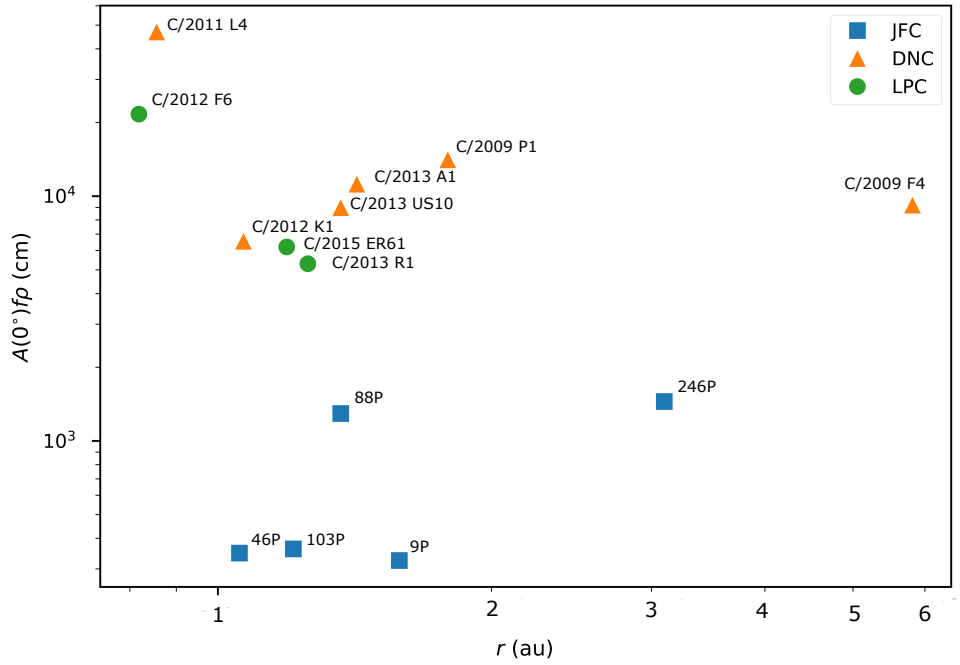

Figure 4.53 Heliocentric distance dependence on the peak measured $Af\rho$ of all fourteen comets.

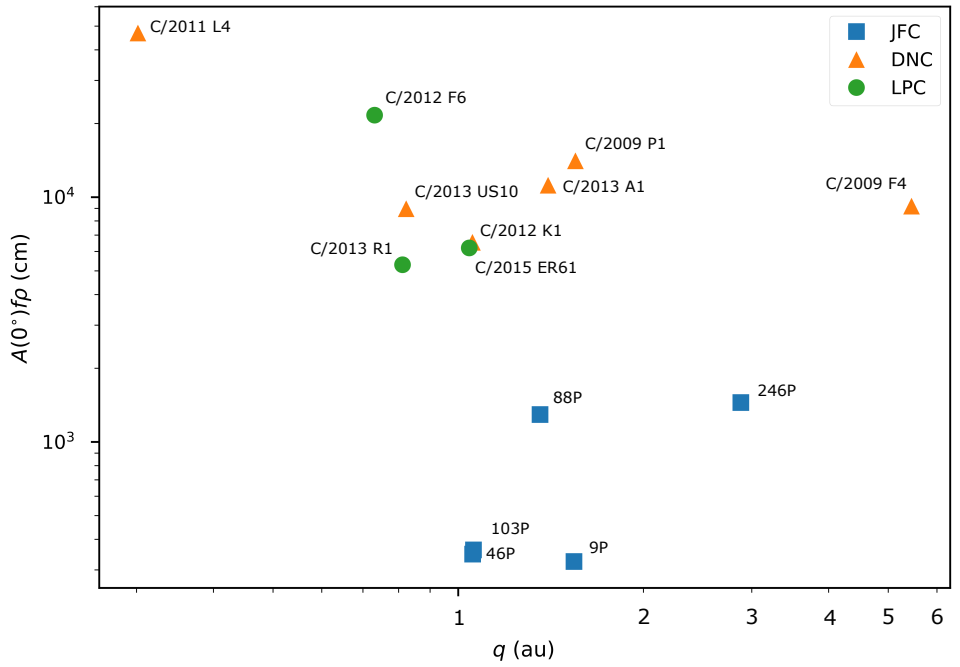

Figure 4.54 Peak measured $Af\rho$ vs. perihelion distance q for all survey comets.

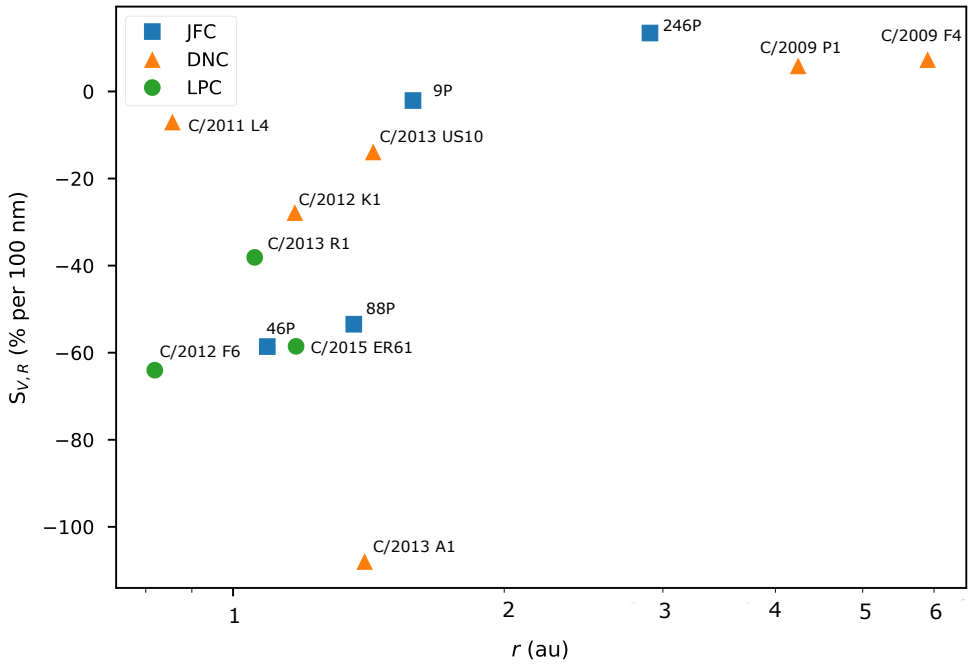

Figure 4.55 The minimum measured $S_{V,R}$ vs. r for all survey comets.

$Af\rho$ being on the order of 10^3 cm. LPCs and DNCs have much higher $Af\rho$ on the order of 10^3 or 10^4 cm. My comets at further distances do not show as large of an $Af\rho$ as measured by Langland-Shula and Smith (2011). Maybe this is not a fair comparison since the other studies only have one or two points per comet whereas we have more complete light curve. C/2011 L4 and C/2012 F6 have high $Af\rho$ at low r, they both show this despite being in different families.

Plotting $Af\rho$ against q (Figure 4.54) shows no obvious trend and might even suggest a negative trend with comets with lower q having higher $Af\rho$, especially when only considering the dynamically newer comets. However, there is such variations between the comets at all distances of q that inferring a trend with any confidence is a stretch.

Figure 4.55 shows that comets with $r < 1.5$ au have bluer colours than others, with JFCs and LPCs having the most extreme spectral slopes, whereas the DNCs show it to a lesser extent. The only exception being C/2011 L4 but this only has one observation in all colour bands. DNCs in general are redder than JFCs or LPCs. Most comets in my sample show decrease in $V - R$ around perihelion within 1.5 au implying increased production of gases.

4.3.6 Time lag between peak dust and gas production

Three comets show significant time differences between peak gas production and peak dust production. 46P has a 24 day gap between the peak in dust production and the peak in gas production. In the outburst of C/2013 A1 the peak in gas production comes 15 days before peak in dust production. For C/2013 R1 it is difficult to gauge the exact difference but it would seem the gas activity peaks before perihelion and dust peaks after perihelion. In all of these cases the gas production peaks before dust production, these are all from different classes so this would suggest that this is not an indicator of ageing. For all other comets with significant colour change in our sample, the peak in dust and gas production occur together.

4.4 Conclusions

- JFCs can be distinguished by their steep pre-perihelion activity slopes and shallower post-perihelion slopes.
- LPCs share similarities to JFCs in that they have steep pre-perihelion slopes followed by shallower post-perihelion, with the exception of C/2015 ER_{61} which had unusually shallow slopes.
- DNCs have shallow incoming slopes in general, although this can vary a lot and they can have unusual non-linear increases in activity. Their post-perihelion slopes are always steep and they have a much larger asymmetry than LPCs or JFCs.
- Across all comets, there seems to be no correlation as to whether the peak of activity occurs before or after perihelion
- LPCs and DNCs generally have $Af\rho$ one to two orders of magnitudes greater than JFCs
- I do not see a strong dependence between heliocentric distance and peak $Af\rho$.
- The spectral slopes of the comets are dependent on distance with comets $r < 1.5$ au having a negative spectral slope between V and R, these colour

changes suggest gas production is significantly increased at lower heliocentric distance compared to larger ones.

- Three comets show a peak in their gas production before the peak in their dust production, which is unlike all the other comets in the sample. These three comets are all in different classes so this change cannot be attributed to ageing.

Chapter 5

A comparison between broadband and narrowband observations of gas activity in comets

It is a long-established fact in comet science that gas emissions of active comets contaminate the broadband filters at the bluer end of the spectrum, i.e. B-, V-bands in the Johnson–Cousins system and g-band in the *ugriz* system (Meech and Svoreň, 2004). Often, a change in the colour of the coma is attributed to production of gases, usually C_2, C_3 and CN. But how accurate is this assumption? Can we put a constraint on how the change in colour relates to the production rates of these gases? In this chapter I will compare my own broadband data that was presented in Chapter 4 with published narrowband data on the same comets and see what comparisons can be made.

5.1 Dust-to-gas ratio

I started by measuring the dust-to-gas ratios of three well-observed comets that were observed by TRAPPIST in both narrowband and broadband filters. The three comets were 46P, C/2012 F6 and C/2013 R1. This was a useful comparison to make because the targets were observed in the broadband and narrowband

filters more or less simultaneously so I had both dust and gas production data across the same period and at similar cadences. Dust-to-gas ratio is defined, in this case, as the ratio of $Af\rho$ to the gas production rate – for my purposes, the OH and CN production rates. Dust-to-gas ratio is a term used widely across comet science that has multiple definitions that can often be confused with one another. In this case, I was looking at a ratio of production rates, using $Af\rho$ as the analogue for dust production rate, and gas production determined from narrowband observations and gas distribution models (e.g. Festou, 1981; Haser, 1957). Dust-to-gas ratio can also describe the ratios of the volumes of dust and gas in the coma, which requires knowledge of factors such as dust size distribution and gas density. Dust-to-gas ratio could even be describing the intrinsic mass or volume ratio of refractory material to ice found in the comet nucleus. This is based on direct observations of the nucleus and is dependent on factors such as porosity. All these definitions are used interchangeably in comet science and are not necessarily directly related to each other, but that is not to say they are completely independent from one another either. For the avoidance of doubt, when I use the term dust-to-gas ratio, I am referring to the ratio of production rates: $Af\rho$-to-Q(OH) or $Af\rho$-to-Q(CN). The $Af\rho$ measurements are my own derived using my calibration methods and the gas production rates are taken from literature – the production rates for 46P, C/2012 F6 and C/2013 R1 were measured by Moulane et al. (2023), Opitom et al. (2015a) and Opitom et al. (2015b) respectively.

5.1.1 46P

The dust-to-gas ratios for 46P, C/2012 F6 and C/2013 R1 are plotted against heliocentric distance in Figures 5.1 and 5.2. 46P had dust-to-OH ratios between 4×10^{-26} and 8×10^{-26} cm s mol^{-1} across its orbit. It had a higher dust-to-gas ratio post-perihelion than pre-perihelion, an increase of about 100 per cent from the lowest pre-perihelion value. A'Hearn et al. (1995) measured the dust-to-gas ratio of 46P at distance of $r = 1.118$ au outbound of 1.32×10^{-26} cm s mol^{-1}, which raises the question as to why I saw higher dust-to-gas ratios in my data. It is unlikely that the dust-to-gas ratio of 46P has changed significantly since 1995 as JFCs typically are well-behaved and their activity does not change drastically from orbit-to-orbit. Knight et al. (2021) found dust-to-gas ratios of 46P of 3×10^{-26} cm s mol^{-1}. Looking at Figure 5.1a, there seems to be trend for increasing dust-to-gas with heliocentric distance but this is likely just the pre-

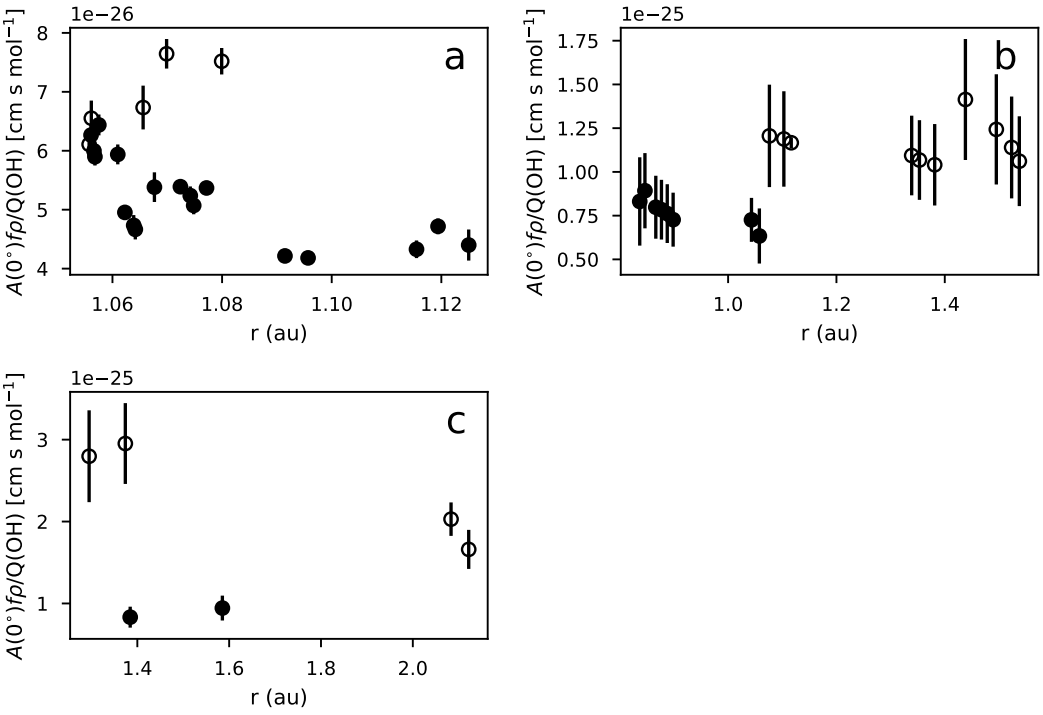

Figure 5.1 Ratio of $Af\rho$ to OH production rates of (a) 46P, (b) C/2012 F6 and (c) C/2013 R1. The filled and unfilled points represent pre- and post-perihelion measurements respectively.

perihelion reddening caused by low phase angle and is therefore a manifestation of the observing geometry.

The dust-to-CN ratio of 46P was asymmetric around perihelion but not to the same extent as the OH rates and the phase angle effect was still present. Pre-perihelion, the dust-to-CN ratio was about 2×10^{-23} to 2.4×10^{-23} cm s mol^{-1}. The dust-to-CN peaked around perihelion but otherwise was flat at larger heliocentric distances. Moulane et al. (2023) saw this pattern and said 46P had a typical dust-to-gas ratio that did not change orbit-to-orbit.

5.1.2 C/2012 F6

C/2012 F6 had dust-to-OH ratios between 6×10^{-26} and 12×10^{-26} cm s mol^{-1}. Like 46P, C/2012 F6 had a higher dust-to-gas ratio post-perihelion than pre-perihelion with an increase of about 100 per cent. The dust-to-CN ratio of C/2012 F6 went from 2.5×10^{-23} cm s mol^{-1} pre-perihelion to 3.5×10^{-23} cm s mol^{-1} post-perihelion, a difference of 40 per cent. As previously discussed in Chapter 4.2.9,

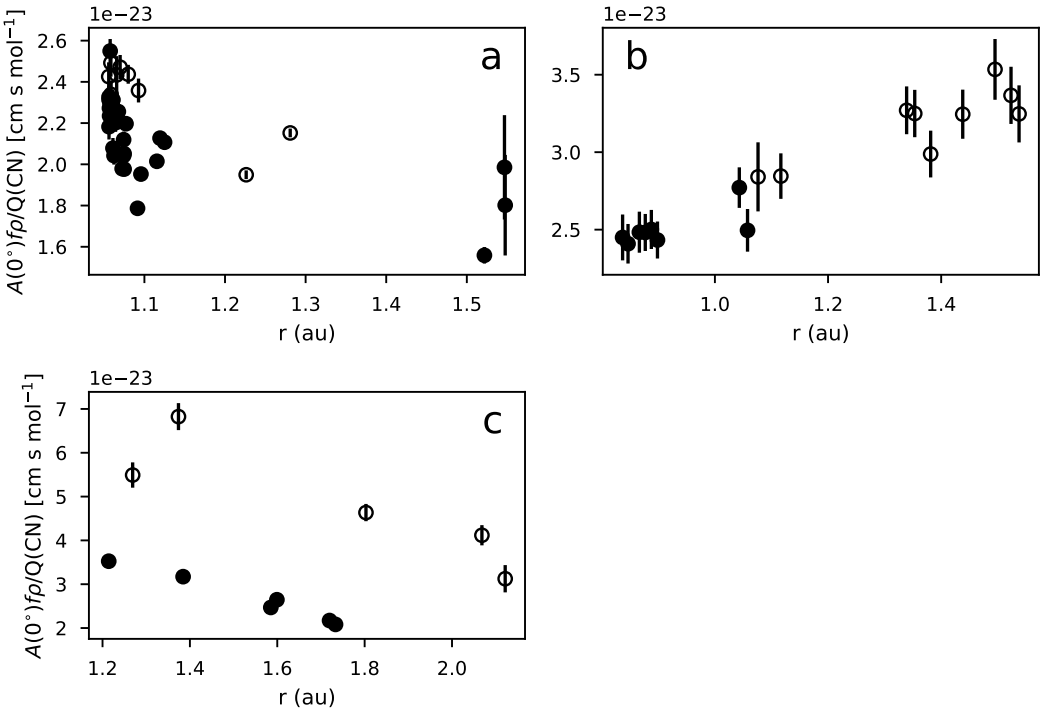

Figure 5.2 Ratio of $Af\rho$ to CN production rates of (a) 46P, (b) C/2012 F6 and (c) C/2013 R1. The filled and unfilled points represent pre- and post-perihelion measurements respectively.

Opitom et al. (2015a) found significant differences between dust and gas activity in C/2012 F6. They found dust-to-gas ratios to be in the range of 1×10^{-26} to 4×10^{-26} cm s mol^{-1}. The difference from the ratios I determined was likely due to the fact Opitom et al. (2015a) measured $Af\rho$ based on narrowband continuum filter observations, which have different calibration methods that may not be as reliable as broadband.

5.1.3 C/2013 R1

C/2013 R1 has dust-to-OH ratios between $10{\times}10^{-26}$ and $30{\times}10^{-26}$ cm s mol^{-1}. C/2013 R1 had a much higher dust-to-OH ratio post-perihelion than pre-perihelion which was much higher than the previous two comets, with a 150–200 per cent increase from pre- to post-perihelion. Opitom et al. (2015b) attributed the higher dust-to-gas ratio to asymmetry in OH production around perihelion. Except for the asymmetry around perihelion, they found that $Af\rho$-to-OH was constant with heliocentric distance. I did not have enough data to confirm this claim although it would seem true from the limited data I had. Opitom et al. (2015b) measured

dust-to-gas ratios pre-perihelion of 5×10^{-26} cm s mol^{-1} and post-perihelion of 20×10^{-26} cm s mol^{-1}, a 400 per cent difference. My measured values of dust-to-gas did not have such a significant increase, although I had a very limited data set. The $Af\rho$ was derived from different methods, when looking at the absolute difference and not percentage change they were similar.

Dust-to-CN ratio seemed to be on an increasing trend pre-perihelion and then decreasing post-perihelion. The dust-to-gas ratio rose from 2×10^{-23} to 4×10^{-23} cm s mol^{-1} before perihelion. Then had a much higher post-perihelion dust-to-gas ratio of 6×10^{-23} cm s mol^{-1}, or possibly as high as 7×10^{-23} cm s mol^{-1}, which then decreased down to 3×10^{-23} cm s mol^{-1}. The difference between peak dust-to-gas ratios was 150 per cent. Opitom et al. (2015b) found CN was not correlated with dust. Like the dust-to-OH ratios, C/2013 R1 seemed to have a much larger asymmetry pre- and post-perihelion compared to the other two comets.

5.1.4 Summary

All three comets showed increased dust-to-gas ratios post-perihelion for both OH and CN. This was easily attributed to the difference in the asymmetry around perihelion between the dust and gas production. In all three comets, asymmetry was much more prominent in the dust production than the gas productions which lead to the higher dust-to-gas ratios (Moulane et al., 2023; Opitom et al., 2015a,b). This was probably due to the expansion rate of gas compared to dust. Dust has a slower expansion rate than the gas and so remains within the viewing aperture for longer than the gas.

C/2013 R1 was the dustiest comet with a peak dust-to-gas ratio of 3×10^{-25} cm s mol^{-1}. This is at odds with trends found by A'Hearn et al. (1995) which found that perihelion distance and dust-to-gas ratio are correlated meaning that 46P, with the largest perihelion distance, would be expected to be the dustiest. That being said, 46P does demonstrate the dust-to-gas ratios that A'Hearn et al. (1995) would expect from a comet of a similar perihelion distance, which would be of the order 10^{-25} cm s mol^{-1}. A'Hearn et al. (1995) also found that, in the ensemble population, dust-to-gas ratios increased with heliocentric distance. In these three comets, I see indications of the opposite trend of larger dust-to-gas ratio at smaller heliocentric distances. This apparent contradiction can be solved since A'Hearn et al. (1995) found that individual comets behaved differently from

the ensemble, as well as the fact that the small number statistics I am working with make it difficult to infer ensemble trends. Another finding of A'Hearn et al. (1995) was that dust-to-gas ratios are independent of dynamical class. I suggest an agreement with this since the two LPCs, C/2012 F6 and C/2013 R1, have noticeably different dust-to-gas ratios, but this is too small a sample size to draw any definitive conclusions of the wider comet population.

My dust-to-gas ratios are in good agreement with published values of these comets.

5.2 Linking colour change to production rates observed by TRAPPIST

I made a comparison of the production rates observed by the TRAPPIST telescopes using the narrowband filters and the colours measured from the broadband observations. The four comets I compared were 46P, C/2012 F6, C/2013 A1 and C/2013 R1, the production rates of which were published by Moulane et al. (2023), Opitom et al. (2015a), Opitom et al. (2016) and Opitom et al. (2015b) respectively.

5.2.1 46P

The C_2, C_3 and CN production rates of 46P are plotted against the $V-R$ colour in Figure 5.3a.

The production rates of all three gases were strongly correlated with the $V-R$ colour, with a higher production rate corresponding to a bluer colour. The production rates were related to $V-R$ with slopes of -1.58 ± 0.14 for C_2, -1.91 ± 0.15 for C_3 and -1.29 ± 0.15 for CN. The correlations for OH were also found to be -1.74 ± 0.20, they are not plotted in Figure 5.3 for ease of presentation due to the large order of magnitude difference in production rate. It was interesting that there was such a strong correlation with OH since OH emissions are not present in these filters. The wavelength of OH emission lines ($\sim$ 3085 Å) would place it firmly in the U-band. This tells us that the different gases are at least partially correlated with each other, but the slopes are not entirely the same so there must be some variations in relative abundance. I found no correlation between the

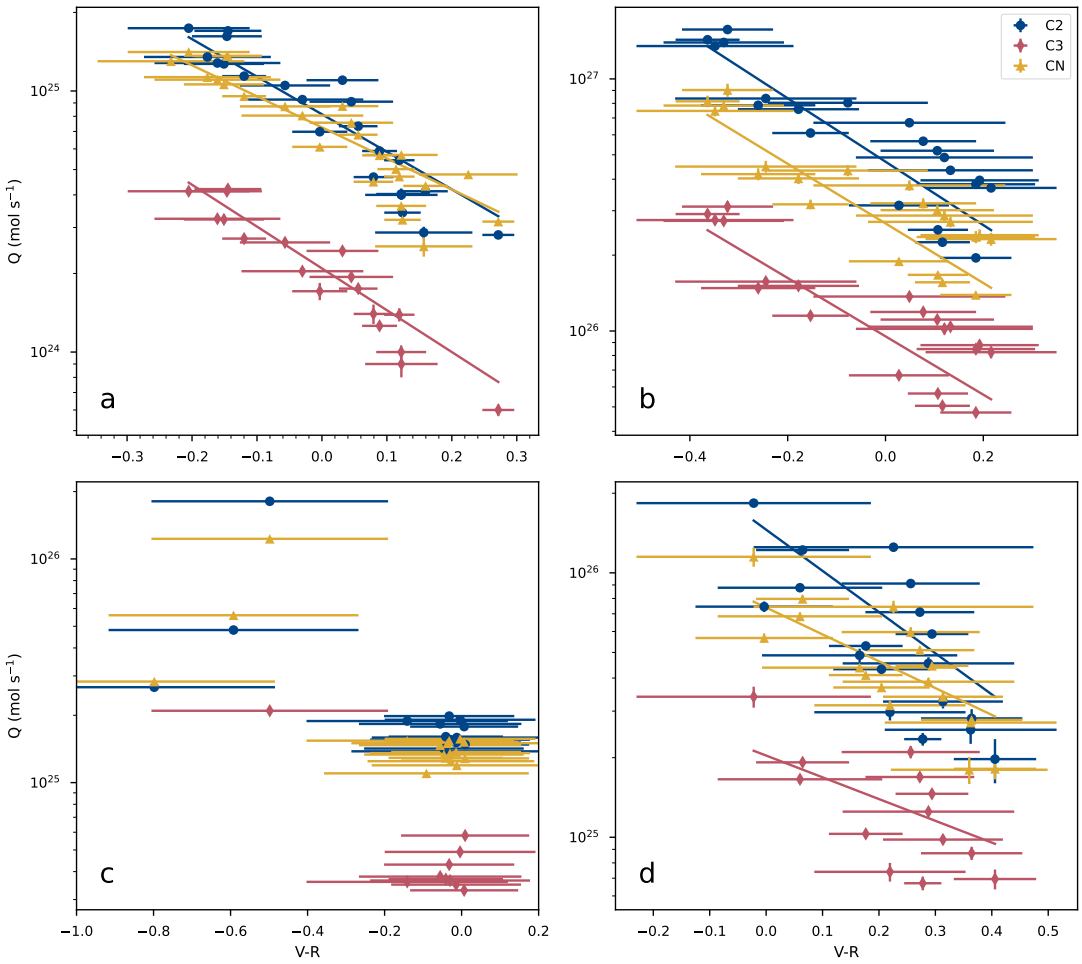

Figure 5.3 Production rates of C_2, C_3 and CN plotted against the $V-R$ colour for comets (a) 46P, (b) C/2012 F6, (c) C/2013 A1 and (d) C/2013 R1. The errors in production rates are too small to be seen on this plot.

production rates and $B-V$ or $R-I$ for 46P for any of the four gases. This was not surprising as I did not expect to see a change, since for $B-V$, both bands were contaminated by gas emissions, and for $R-I$, these bands were free of these contaminants. Since the rates of change of the gases were similar to each other, the colour should not change between those bands.

5.2.2 C/2012 F6

The C_2, C_3 and CN production rates of C/2012 F6 are plotted against the $V-R$ in Figure 5.3b. Again, I find the production rates are strongly correlated in $V-R$ but not $B-V$ or $R-I$. The relationships between production rates and $V-R$ can be described with slopes of -1.10 ± 0.13 for C_2, -0.98 ± 0.12 for C_3, -0.98 ± 0.11 for CN and -1.07 ± 0.08 for OH.

5.2.3 C/2013 A1

The C_2, C_3 and CN production rates of C/2013 A1 are plotted against the $V-R$ in Figure 5.3c. This comet was different in the fact that it had relatively steady activity for most of its apparition then a sudden outburst near perihelion, as such the production rates of each gas remained clustered together in both production rate and colour. The production rates and colours over the orbit were constant within error bars apart from a few points measured during and after the outburst where the production rate was significantly higher. While I cannot plot a trend to this data, we can see that the higher production rates during the outburst do correspond to much bluer colours, implying that higher production rates do decrease $V-R$.

5.2.4 C/2013 R1

The C_2, C_3 and CN production rates of C/2013 R1 are plotted against the $V-R$ colour in Figure 5.3d. The slopes of the production rates with respect to $V-R$ are -2.93 ± 0.79 for C_2, -1.62 ± 0.35 for C_3, -1.75 ± 0.32 for CN and -2.17 ± 0.27 for OH with no correlation between the production rates and $B-V$ or $R-I$ for C/2013 R1.

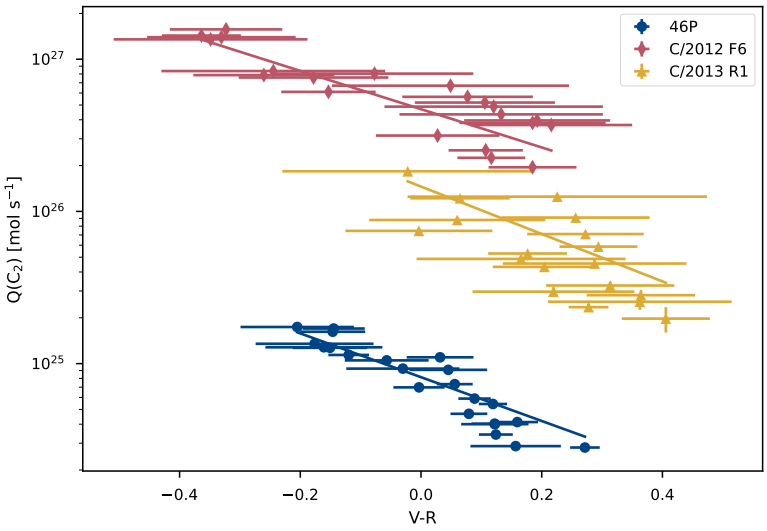

Figure 5.4 Production rates of C_2 plotted against the $V-R$ of 46P, C/2012 F6 and C/2013 R1.

5.2.5 Summary

There was a strong correlation between $V-R$ and C_2, C_3, CN and OH production rates. These correlations were seen in all four of the comets, and trends were calculated for three of them; 46P, C/2012 F6 and C/2013 R1. On initial inspection, the colour change was an indication of production rates and this correlation held true across multiple comets. As demonstrated by the example in Figure 5.4, the comets all had different initial production rates and therefore did not fit on the same line and there was not a unifying relationship that applies to all three comets. The production rates were individual to each comet and prediction from one cannot be used on another without some sort of scaling factor or shift. In order to fit these comets to a common scale, I look at how the $Af\rho$ is related to production rates in the next section.

5.3 Afρ vs. gas production rates

The production rates of C_2, C_3, CN and OH are plotted against $Af\rho$ in Figure 5.5 for the comets 46P, C/2012 F6 and C/2013 A1. It was clear that $Af\rho$, and hence dust production, was strongly correlated with gas production and this relationship was consistent across these three comets. There was a distinct offset

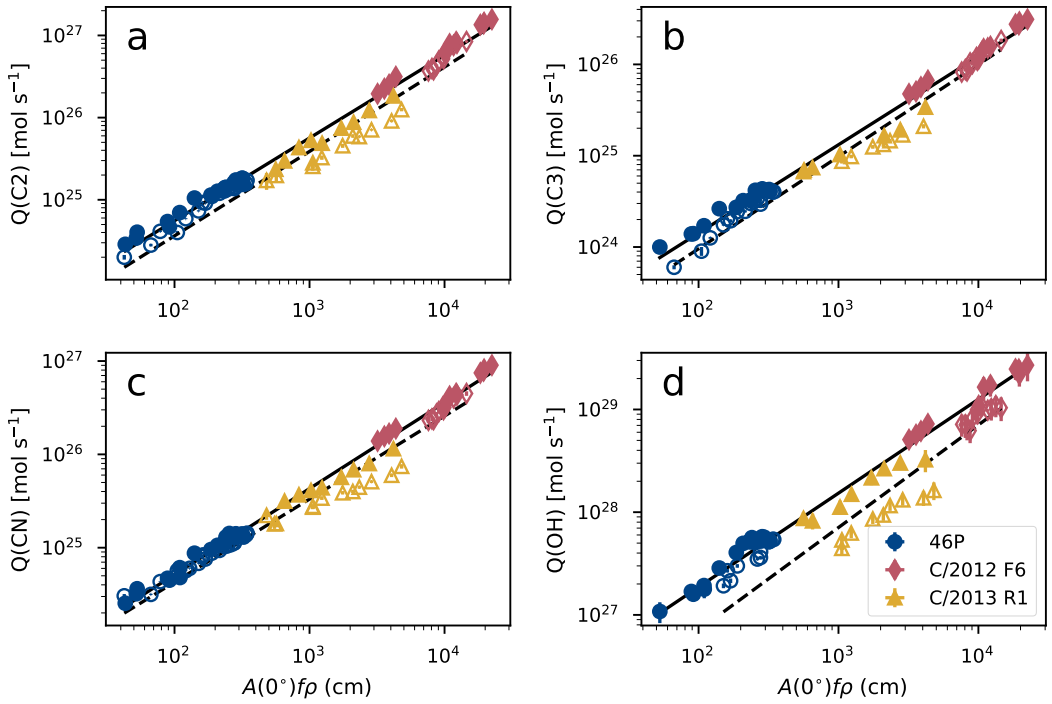

Figure 5.5 Production rates of (a) C_2, (b) C_3, (c) CN and (d) OH against $Af\rho$ of 46P, C/2012 F6 and C/2013 R1. Filled and unfilled points represent pre- and post-perihelion measurements respectively. The solid and dashed lines are the fits pre- and post-perihelion respectively.

between pre- and post-perihelion slopes and this offset was not constant between comets. The offset of C/2013 R1 was much greater than those of either 46P or C/2012 F6. This offset was especially noticeable in the OH data (Figure 5.5d).

The relationships between $Af\rho$ and production rates were found to be:

$$\text{Pre-perihelion} : \log Q(\mathrm{C_2}) = 1.01(\pm 0.02) \log Af\rho + 22.73 \pm 0.06 \tag{5.1}$$

$$\text{Post-perihelion} : \log Q(\mathrm{C_2}) = 1.03(\pm 0.04) \log Af\rho + 22.51 \pm 0.11 \tag{5.2}$$

$$\text{Pre-perihelion} : \log Q(\mathrm{C_3}) = 0.97(\pm 0.02) \log Af\rho + 22.22 \pm 0.07 \tag{5.3}$$

$$\text{Post-perihelion} : \log Q(\mathrm{C_3}) = 1.01(\pm 0.03) \log Af\rho + 21.96 \pm 0.10 \tag{5.4}$$

$$\text{Pre-perihelion} : \log Q(\mathrm{CN}) = 0.92(\pm 0.01) \log Af\rho + 22.87 \pm 0.01 \tag{5.5}$$

$$\text{Post-perihelion} : \log Q(\mathrm{CN}) = 0.89(\pm 0.03) \log Af\rho + 22.85 \pm 0.09 \tag{5.6}$$

$$\text{Pre-perihelion} : \log Q(\mathrm{OH}) = 0.91(\pm 0.02) \log Af\rho + 25.44 \pm 0.06 \tag{5.7}$$

$$\text{Post-perihelion} : \log Q(\mathrm{OH}) = 1.00(\pm 0.07) \log Af\rho + 24.85 \pm 0.23 \tag{5.8}$$

Across all the gases, both pre- and post-perihelion, the relationships are all very close to 1, and overlap in gradient within errors. This implies that the gas production and dust production are directly correlated, supporting the idea that gas and dust production are causally related to one another. These relationships are useful much like the relationship found by Jorda et al. (1991) which can be used for gas production estimations when no spectroscopic data is available. The Jorda et al. (1991) relationship is different is several key ways from the relationships I describe. First off, Jorda et al. (1991) only describes a relationship for water production rate derived from OH measured at radio wavelengths. Secondly, the relationship is for visual magnitudes, a notoriously subjective measurement of total brightness. Whereas my relationships are based on accurately calibrated broadband photometry, which should in theory provide far more accurate relationships.

The more significant offset of C/2013 R1 post-perihelion contributed to the larger uncertainties in the post-perihelion compared to the pre-perihelion slopes. Opitom et al. (2015b) found that C/2013 R1 has significant asymmetry in its gas production, the C_3 and CN gas production of C/2013 R1 had different production rate slopes than the other gases. Although I found that the production rates of these two gases still fit with my relationship, it can be seen by eye that the trends of C_3 and CN for C/2013 R1 do not follow the line as well as C_2 and OH. This difference and evidence from Rosetta about the decoupled dust and CN production rates (Snodgrass et al., 2017) suggests that CN is not a reliable tracer of overall gas production. Opitom et al. (2015b) also saw a large asymmetry in the production rates of OH pre- and post-perihelion, this explains why the production rate lines are so offset post-perihelion for this comet.

While the relationships are strong and well defined, it is worth reiterating that this data is limited to just three comets, which are either JFCs (46P) or returning LPCs (C/2012 F6, C/2013 R1), and it is well-established that these three comets have differing dust-to-gas ratios. Caution should be taken when applying this result to other comets as this might not be representative of the entire population of comets. One might ask does this result hold true for DNCs? I have not found long-term production rate monitoring on DNCs in my sample, but we can make a preliminary comparison to individual production rates of a well-characterised DNC, C/2009 P1. On 2011 October 28, it had production rates of $Q(\mathrm{CN})=5.24\times 10^{26}$ mol s^{-1}, $Q(\mathrm{C_3})=1.01\times 10^{26}$ mol s^{-1} and $Q(\mathrm{C_2})=3.07\times 10^{26}$ mol s^{-1} (Ivanova et al., 2014). Using the relationships I derived and my $Af\rho$ measured 8 days prior

in the V-band, I estimated production rates of $Q(\mathrm{CN})=4.76\pm0.47\times10^{26}$ mol s^{-1}, $Q(\mathrm{C_3})=1.72\pm0.43\times10^{26}$ mol s^{-1} and $Q(\mathrm{C_2})=8.13\pm1.92\times10^{26}$ mol s^{-1}. This was not a good match, especially in the case of $Q(\mathrm{C_2})$ which was out by almost a factor of 3. This is far from a perfect comparison due to the time difference and the fact I only have $Af\rho$ in the V-band which, of course, is contaminated by the very gases I am trying to determine the production rates of. I would have expected this contamination to result in over-estimates in all three production rates, but it was only $Q(\mathrm{C_2})$ that was an over-estimate. Perhaps since this was a DNC, it behaved differently from periodic comets and did not follow the trend I derived. DNCs may have different activity mechanisms by which dust is lifted from the surface and therefore the dust production is not necessarily directly related to the gas production rates. More observations of production rates with coincident broadband observations of DNCs are needed to see if this relationship holds true for a wider population of comets.

5.4 Production rate change vs. colour change

In order to formulate a common relationship between colour and production rates, I shifted the production rates to a common scale so the relationships describe the change in production rate instead of an absolute production rate. This was achieved by using the previously derived $Af\rho$–production rate relationships and the peak measured $Af\rho$ to determine a zero point from which the production rates could be related to one another. The pre-perihelion change in production rates of $\mathrm{C_2}$, $\mathrm{C_3}$, CN and OH are each plotted against $V-R$ in Figure 5.6. From this I got the relationships $\Delta\mathrm{Q(C_2)}=(V-R)^{-1.68\pm0.10}$, $\Delta\mathrm{Q(C_3)}=(V-R)^{-1.53\pm0.10}$, $\Delta\mathrm{Q(CN)}=(V-R)^{-1.29\pm0.12}$ and $\Delta\mathrm{Q(OH)}=(V-R)^{-1.30\pm0.12}$. The changes in production rates between the comets were well correlated with change in colour for the pre-perihelion measurements.

Post-perihelion, the shifted slopes do not match well with one another and there are still significant differences between the production rates of the individual comets, they are plotted in Figure 5.7. C/2012 F6 had a much shallower production rate slope post-perihelion than the other two comets, with slopes from -0.7 to -0.9, which was also much shallower than the average pre-perihelion values. 46P had slopes closer to the pre-perihelion slopes, having slopes -1.5 to -2.4. These were slightly steeper, but I was expecting some sort of asymmetry like those seen in the $Af\rho$ measurements. C/2013 R1 had by far the steepest slopes

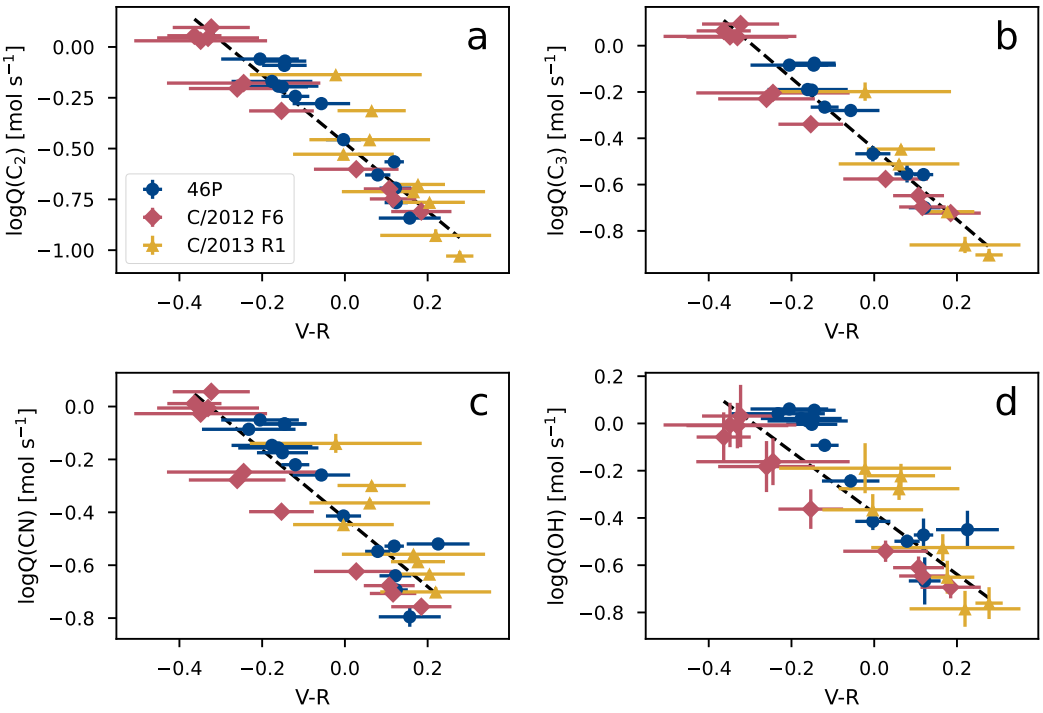

Figure 5.6 The pre-perihelion change in production rates of (a) C_2, (b) C_3, (c) CN and (d) OH plotted against the $V - R$ colour observed in three comets 46P, C/2012 F6 and C/2013 R1.

post-perihelion with slopes in the range of −3.3 to −4.9.

It was not immediately obvious what was causing such differences between the individual comets. In the case of C/2012 F6 post-perihelion, a small decrease in gas production rate corresponded to a significant reddening of the colour implying the gas production was decreasing much faster than the dust. Opitom et al. (2015a) saw in their observations of C/2012 F6 that the dust production decreased at a much slower rate than the gas, they suggested that the gas and dust were decoupled and not related to each other. This could explain why the C/2012 F6 production rate was shallower compared to the other two comets.

Opitom et al. (2015b) found similar rates of change in the gas and dust production post-perihelion in C/2013 R1. Moulane et al. (2023) found that the dust production rate of 46P decreased faster than gas production. This did not seem to line up with what I saw in the colour changes. C/2013 R1 had the steepest dependence on colour post-perihelion, implying the dust production was decreasing faster than the gas but 46P should have been the steepest judging from data by Moulane et al. (2023). It would seem the post-perihelion production rate changes

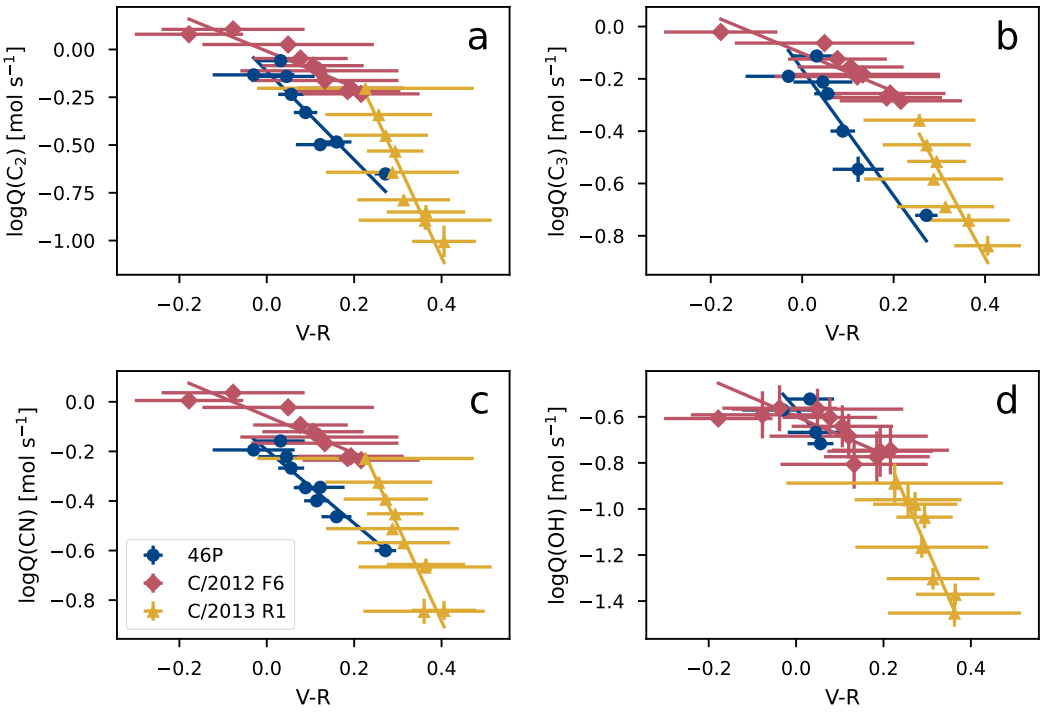

Figure 5.7 The post-perihelion change in production rates of (a) C_2, (b) C_3, (c) CN and (d) OH plotted against the $V - R$ colour observed in three comets 46P, C/2012 F6 and C/2013 R1.

were more difficult to determine purely from the colour change. It also could be due to the escape speed of dust and gas being very different, the dust has a slower expansion speed than the gas so is therefore within the aperture for a longer time than the gas, even as the dust production rate is decreasing. This difference in the speeds could explain why the colour and production rates were not as well correlated between the comets post-perihelion. This leads me to the conclusion that scaling production rates using $Af\rho$ vs. production rate relationship may not be valid post-perihelion and that post-perihelion dust and gas activity are significantly varied between individual comets.

5.5 Comparison to SOHO/SWAN data

Besides the narrowband TRAPPIST data, another source of regular gas production rate data was observations of these comets made by SOHO/SWAN. The water production rates of the comets were determined from observations of the Ly α emitted from neutral atomic hydrogen in cometary coma. The atomic hy-

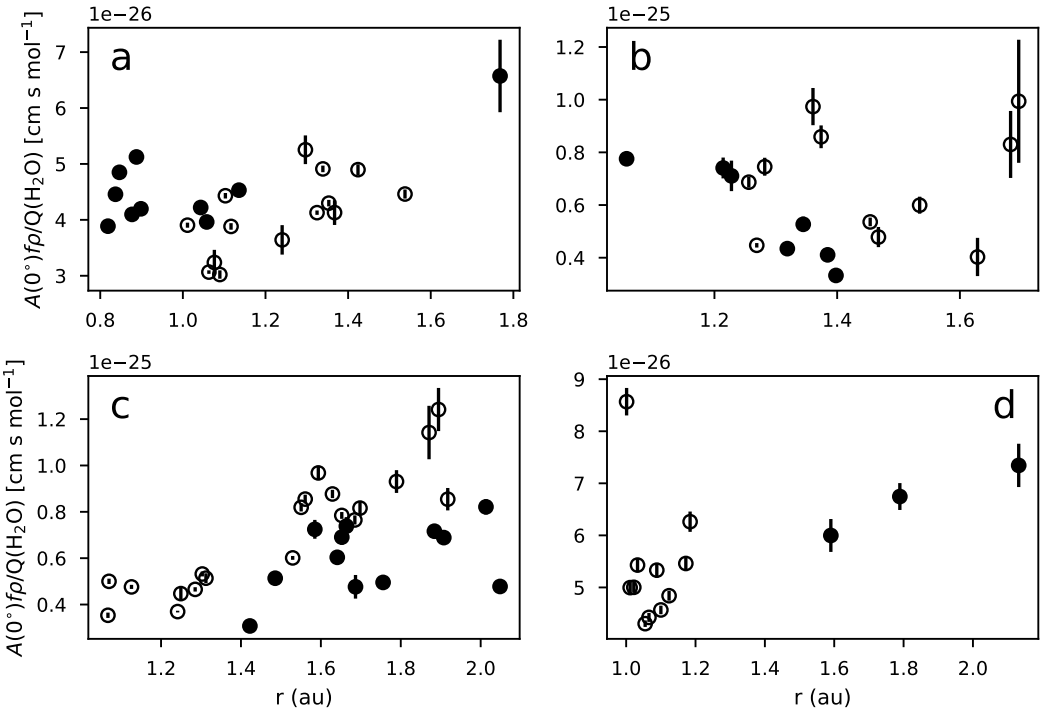

Figure 5.8 Ratio of $Af\rho$ to water production rates measured by SOHO/SWAN of C/2012 F6 (a), C/2013 R1 (b), C/2012 K1 (c) and C/2013 US_{10} (d). The filled and unfilled points represent pre- and post-perihelion measurements respectively.

drogen is produced from the photodissociation of water and can therefore be used to determine water production rates.

The dust-to-gas ratios of four comets, C/2012 F6, C/2012 K1, C/2013 R1 and C/2013 US_{10} are plotted in Figure 5.8. The dust-to-gas ratios did not show variation pre- and post-perihelion like the dust-to-OH or dust-to-CN calculated before.

5.5.1 C/2012 F6

C/2012 F6 had a dust-to-gas ratio of 4×10^{-26} cm s mol^{-1}, which was smaller than those I determined from OH production rates which were closer to 6×10^{-26} cm s mol^{-1}. It was close to the values found by Opitom et al. (2015a) but I did not see a distinct separation of pre- and post-perihelion they saw. The discrepancy in C/2012 F6 dust-to-gas ratios can be explained by the fact that the production rates derived by Combi et al. (2014) did not show the same asymmetry around perihelion as the production rates of Opitom et al. (2015a) did. Therefore, that

is why there was no difference in dust-to-gas ratios pre- and post-perihelion.

5.5.2 C/2013 R1

C/2013 R1 had dust-to-gas ratio of 6×10^{-26} cm s mol^{-1}, with no significant offset pre- and post-perihelion. The upper end of the scatter matched the dust-to-OH ratio of 10×10^{-26} cm s mol^{-1} I determined before, however I did not see the increase to 30×10^{-26} cm s mol^{-1} that was seen in the dust-to-OH ratios.

Again, the explanation for the discrepancy was due to the differences in asymmetry between the two production rates of Opitom et al. (2015b) and Combi et al. (2018). Combi et al. (2018) made a direct comparison to Opitom et al. (2015b) as well as other water production rate determinations made by Paganini et al. (2014) and Biver et al. (2014) – I did not make a comparison to these as there was no overlap with my data. Combi et al. (2018) attributed the differences to the different coma density models used. Opitom et al. (2015b) used a Haser model (Haser, 1957) while Combi et al. (2018) used a 'more appropriate' vectorial model (Festou, 1981) to determine production rates. The differences between these two models was sufficient to explain the factor 2 offset pre-perihelion but post-perihelion the offset was almost a factor 4. The offset in my dust-to-gas ratios between those using OH and H were about a factor 3 post-perihelion.

5.5.3 C/2012 K1

C/2012 K1 showed the same trend as the others with a higher dust-to-gas ratio post-perihelion than pre-perihelion, although the comet has large dust-to-gas ratio pre-perihelion at small heliocentric distances.

5.5.4 C/2013 US$_{10}$

In C/2013 US$_{10}$, I saw far more drastic asymmetry in my $Af\rho$ slopes than the water production in Combi et al. (2018), hence the lower dust-to-gas post-perihelion. This was the only comet that has a lower dust-to-gas post-perihelion than pre-perihelion.

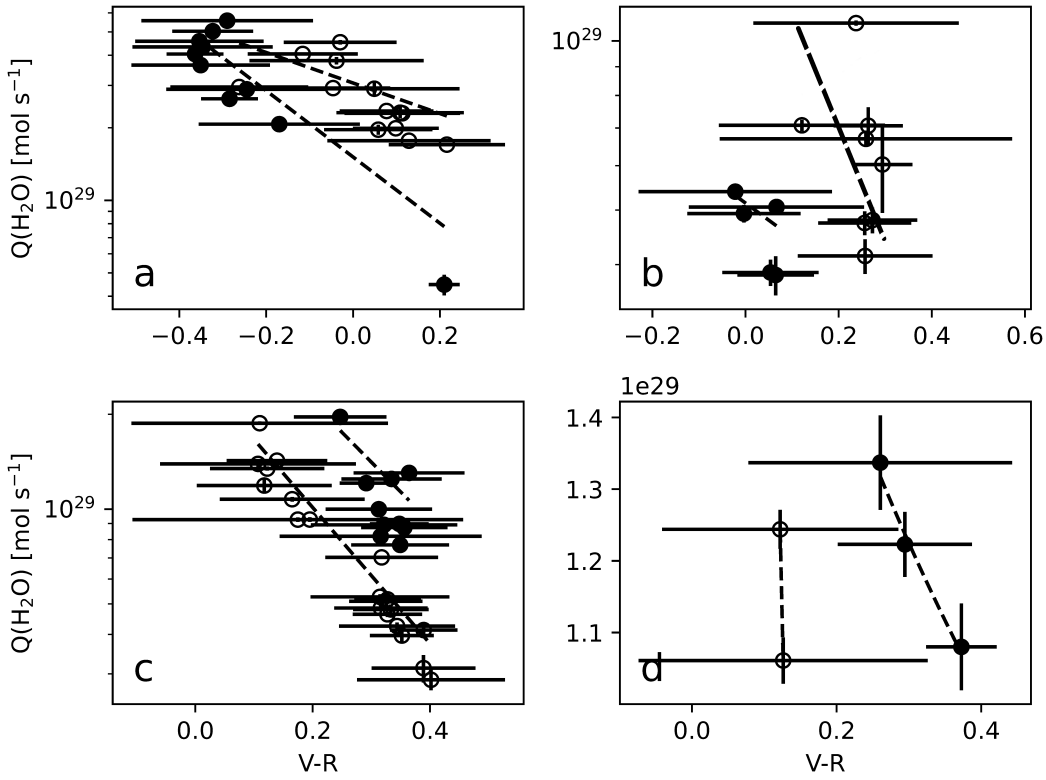

Figure 5.9 The water production rates measured by SOHO/SWAN plotted against $V - R$ for (a) C/2012 F6, (b) C/2013 R1, (c) C/2012 K1 and (d) C/2013 US_{10}. The filled and unfilled points represent pre- and post-perihelion measurements respectively.

5.5.5 Overall trends

The production rates are plotted against $V - R$ in Figure 5.9. They all showed similar relations in so far that an increase in water production slope was correlated with an decrease in colour. They also showed the pre- and post-perihelion offsets that were seen in other comets.

The relationships were:

- C/2012 F6 pre- $(V-R)^{-1.76\pm0.09}$ post- $(V-R)^{-1.25\pm0.31}$
- C/2013 R1 pre- $(V-R)^{-1.44\pm0.75}$ post- $(V-R)^{-2.06\pm1.18}$
- C/2012 K1 pre- $(V-R)^{-4.10\pm1.65}$ post- $(V-R)^{-2.25\pm0.11}$
- C/2013 US_{10} had too few points to fit a good line, but does show a slight trend to blue pre-perihelion.

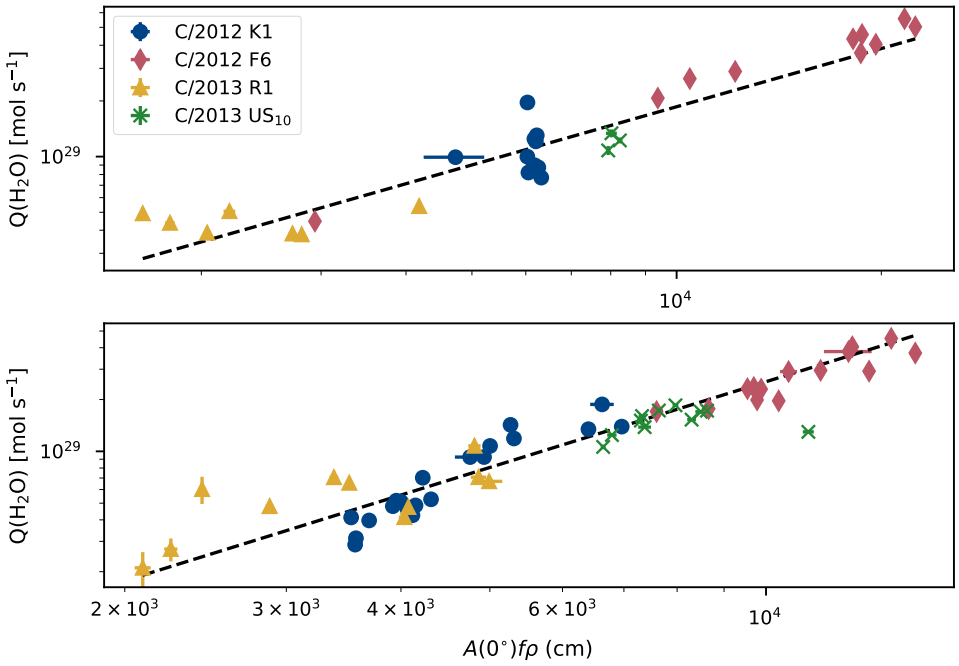

Figure 5.10 The water production rates measured by SOHO/SWAN plotted against $Af\rho$ for comets C/2012 F6, C/2012 K1, C/2013 R1 and C/2013 US_{10} separated into (top) pre- and (bottom) post-perihelion.

The production rate trends were similar to the TRAPPIST narrowband observations in Section 5.4 but were not quite as a nice fit. The slopes were similar in so far as the change in slope was in the right direction but the slopes themselves were not close. Only C/2013 R1 had a slope similar to that found for OH (-2.17 ± 0.27 for OH).

Water production rate against $Af\rho$ is plotted in Figure 5.10. Pre-perihelion the relationship was $\log Q(H_2O) = (1.05 \pm 0.08) \log Af\rho + 25.1 \pm 0.3$ and post-perihelion $\log Q(H_2O) = (1.65 \pm 0.08) \log Af\rho + 22.8 \pm 0.3$. It was interesting to note that there was more scatter in these points than those found when plotted against narrowband production rates (Figure 5.5), and it was also interesting how the slopes pre- and post-perihelion were different, those found using the previous method had both pre- and post-perihelion slopes close to or equal to one, in this case the post-perihelion slope was steeper. The slopes here should in theory be the same as those in equations 5.7 and 5.8 as they were both measuring the production rates of water. The pre-perihelion slopes were in good agreement, but post-perihelion the slope were noticeably off.

5.6 Conclusion

I undertook an investigation into the insights about gas production rates that could be gained purely from broadband data. It was found that the decrease in $V - R$ colour was strongly correlated with an increase in gas production, however this relationship was different for each individual comet. Relationships were found between $Af\rho$ and production rates which held true for each comet which could be used as a rough approximation of gas production rates if one found themselves only presented with broadband data. Using these relationships to set a relative production rate baseline, I found that there was a good correlation between $V - R$ colours and production rates pre-perihelion. Post-perihelion, the individual comets still displayed different trends even after applying this correction. This demonstrates that, post-perihelion, changes in coma colour are not a good indication of changes in gas production rates alone, and other factors, such as asymmetry in the dust and gas production about perihelion, contribute to the change in colour.

These conclusions are drawn from a limited sample and more investigation is necessary to see if these relationships holds true for other comets, especially DNCs. Extrapolating from existing data using the relationships and comparing to published production rates provided inconsistent production rates. A thorough analysis of a larger body of comets is needed to more firmly establish these relationships. And, as always, when we try to establish general relationships for all comets, we are confronted with the possibility that each comet is unique and that there is no way to encapsulate the entire breadth and variety in the population with just a few relationships, and that the only way to truly understand each comet is to study them individually.

Narrowband and spectroscopic observations are still necessary to obtain a full and complete picture of comets, however, the broadband data can provide plenty of insight even when there is an absence of narrowband observations. This is especially useful for observations of comets at high heliocentric distances where spectroscopy and narrowband photometry is more challenging. Broadband observations also have the advantage that broadband calibrations are more trustworthy than narrowband due to the inherent challenges that face narrowband calibrations. Broadband calibrations can just use standard calibration stars or stars in the field and thus gain a more accurate calibration. The advantage of my method is that the calibration and the photometry is reliable.

Chapter 6

Conclusion

I developed a pipeline for the consistent calibration of comet photometry, designed to be flexible enough to work across disparate data sets and instruments. The pipeline would calibrate broadband data to a common photometric system using the calviacat (Kelley et al., 2021b) program. I applied this pipeline to two data sets: the first was the vast set of ground-based observing data of 67P accompanying the Rosetta mission; and the second was TRAPPIST photometry of a broader survey of 14 individual comets.

Application of the pipeline to the 67P data worked well with a processing success rate of ∼83 per cent across the data and allowed me to compile one of the most comprehensive and detailed light curves of a comet. I discovered one outburst on 2015 August 22 with a magnitude increase of ∼0.14 mag. This event confirms the outburst seen in Boehnhardt et al. (2016). Although an in situ outburst was observed during the same period as the brightening event, disparities in the estimates of their surface origins and the differences in scale between the in situ outbursts and the broader coma morphology made it difficult to conclusively link them. Despite the observation of numerous in situ events, no other outbursts were detected in my data. It appears that events of this scale are exceedingly difficult to observe from the ground, and there is still much to uncover in understanding the relationship between large-scale changes in the coma and small-scale nuclear activity.

I then applied the pipeline to archival imaging data of 14 comets observed over the last decade by the TRAPPIST telescopes. I found that different dynamical classes of comets exhibit different dust activity. JFCs can be distinguished by

their steep pre-perihelion activity slopes and shallower post-perihelion slopes. LPCs are similar to JFCs in this regard, except for C/2015 ER_{61}, which had unusually shallow slopes. DNCs generally have shallow incoming slopes, although this can vary from comet-to-comet and the slopes are not always continuous pre-perihelion. DNCs' post-perihelion slopes are always steep and they have a much larger asymmetry than LPCs or JFCs. Across all the comets, there seems to be no correlation as to whether the peak of activity occurs before or after perihelion. LPCs and DNCs generally have $Af\rho$ one to two orders of magnitudes greater than JFCs. I do not see a strong dependence on heliocentric distance and peak $Af\rho$. The spectral slopes of comets depend on distance, with comets at $r < 1.5$ au showing negative spectral slopes between V and R. The gas production is significantly increased at smaller heliocentric distance compared to larger ones. Three comets show a peak in their gas production before the peak in their dust production.

Finally, I investigated if gas production rates could be estimated from broadband data. I found that the decrease in $V - R$ colour is strongly correlated with an increase in gas production, however this relationship was different for each individual comet. I found relationships between $Af\rho$ and gas production rates which were consistent across each comet, offering a rough estimate of gas production when only broadband data is available. Using these relationships to set a relative production rate baseline, I found that there is a good correlation between $V - R$ colours and production rates pre-perihelion. Post-perihelion, the individual comets still displayed different trends even after applying this correction, suggesting that changes in coma colour are not solely indicative of gas production changes. Other factors, such as asymmetry in the dust and gas production about perihelion, contribute to the change in colour post-perihelion.

Through these investigations, I have tested the strengths and limitations of broadband imaging and looked at what it can – and cannot – tell us about cometary activity. The strengths of broadband imaging are:

- Consistent and trustworthy calibration
- Can probe to larger heliocentric distances than narrowband imaging or spectroscopy
- Ideal for long-term and regular monitoring
- Dust activity monitoring can distinguish different dynamical classes

- Essential for characterising future mission targets
- Good for ensemble property determination

Limitations:

- It cannot detect small-scale outbursts
- Gas production insights are limited

6.1 Future work

Weighing up these strengths and limitations, there is still much use and science to be gathered from the ground-based broadband imaging of comets and will remain a vital cornerstone in comet science. Further investigation is needed to validate the activity relationships found in this work, especially those of DNCs which even in my small sample size displayed significant variation in activity between them. Extrapolating from existing data using these relationships led to inconsistent production rate estimates. A comprehensive analysis of a larger comet data set is needed to establish these relationships more conclusively. It is important to acknowledge that each comet is unique, and there may not be a one size fits all approach to understanding them. While narrowband and spectroscopic observations remain crucial for a complete understanding of comets, broadband data can offer valuable insights, especially when narrowband data is lacking, particularly for comets at large heliocentric distances. Broadband calibrations are considered more reliable due to the challenges faced by narrowband calibrations. This method offers trustworthy calibration and photometry. Additionally, this approach holds promise for future studies of comets with instruments like LSST (Jones et al., 2009), which provide extensive data across various distance ranges but only in broadband filters. Current predictions estimate that the number of new Solar System bodies discovered by LSST could be in the millions (Schwamb et al., 2023), such large number statistics will require automated processing and analysis like those described in this thesis. LSST will provide far deeper regular all-sky monitoring than ever before, which should allow for increased detection of comets farther out in the Solar System beyond 5 and 10 au (Bauer et al., 2022). LSST will also increase our sensitivity to interstellar objects. It is hoped we can detect and observe far more LPCs, helping constrain our models of activity

at large heliocentric distances and perhaps even observe the onset of activity of pristine DNCs. Since these observations will be made with broadband filters, it is imperative we fully understand what these filters can tell us about activity at large distances and what it cannot. This knowledge will be essential for selecting targets for follow-up observations or space missions.

Further investigations of comet nuclei are also needed to advance our understanding. The best way to do this is with spacecraft missions, the next one being ESA's Comet Interceptor (Snodgrass and Jones, 2019). A target has not yet been selected for Comet Interceptor, but it is intended to visit a DNC if possible or, if we are lucky, even an interstellar comet. In order to correctly characterise these comets and select a viable target, observations will need to be made of the comets at large heliocentric distance where only broadband observations are possible. Using conclusions derived in this work and similar large population studies, we can determine the type and dynamical age and appropriately select a target. Broadband observations are also much more useful at observing the comet over long periods of time, while the Comet Interceptor will only perform a brief fly-by allowing us to link what we see on the nucleus to longer term changes seen from Earth.

The new era of large surveys will also require an enormous amount of photometry and calibration to be done, which is too large to be done by hand. The pipeline developed for this thesis provide a proof of concept for some sort of automated photometry and calibration method that can consistently calibrate disparate data to one another. My pipeline is primitive and still somewhat specific to the data I had to hand. Many cometary scientists have also developed similar pipelines and methods for calibrating their own data. I think it would be of great benefit for comet science both amateur and professional, to have a standardised calibration pipeline to achieve far more consistent and comparable results across the field.

Bibliography

Agarwal, J. et al. (2017). 'Evidence of sub-surface energy storage in comet 67P from the outburst of 2016 July 03'. *MNRAS*, 469(Suppl_2), pp. s606–s625. doi:10.1093/mnras/stx2386.

A'Hearn, M. F. (2004). 'Cometary science: The present and future', in Festou, M. C., Keller, H. U. and Weaver, H. A. (eds.) *Comets II*, Tuscon: Univ. Arizona Press, pp. 17–22.

A'Hearn, M. F. (2017). 'Comets: Looking ahead'. *Phil. Trans. R. Soc. A*, 375(2097), 20160261. doi:10.1098/rsta.2016.0261.

A'Hearn, M. F. and Millis, R. L. (1980). 'Abundance correlations among comets.' *AJ*, 85, pp. 1528–1537. doi:10.1086/112830.

A'Hearn, M. F. et al. (1984). 'Comet Bowell 1980b'. *AJ*, 89, pp. 579–591. doi:10.1086/113552.

A'Hearn, M. F. et al. (1995). 'The ensemble properties of comets: Results from narrowband photometry of 85 comets, 1976-1992'. *Icarus*, 118(2), pp. 223–270. doi:10.1006/icar.1995.1190.

A'Hearn, M. F. et al. (2005). 'Deep Impact: Excavating comet Tempel 1'. *Science*, 310(5746), pp. 258–264. doi:10.1126/science.1118923.

A'Hearn, M. F. et al. (2011). 'EPOXI at comet Hartley 2'. *Science*, 332(6036), pp. 1396–1400. doi:10.1126/science.1204054.

A'Hearn, M. F. et al. (2012). 'Cometary volatiles and the origin of comets'. *ApJ*, 758(1), p. 29. doi:10.1088/0004-637X/758/1/29.

Altwegg, K. et al. (2015). '67P/Churyumov–Gerasimenko, a Jupiter family comet with a high D/H ratio'. *Science*, 347(6220). doi:10.1126/science.1261952.

Andrienko, Y. S. et al. (2016). 'A photometric and dynamic study of comet C/2013 A1 (Siding Spring) from observations at a heliocentric distance of ∼4.1 au'. *Sol. Syst. Res.*, 50, pp. 102–112. doi:10.1134/S0038094616020015.

Bauer, J. M. et al. (2022). 'Comet science with ground based and space based surveys in the new millennium', in Meech, K. J. and Combi, M. R. (eds.)

Comets III [Preprint], Tuscon: Univ. Arizona Press. doi:10.48550/arXiv.2210.09400.

Benna, M. et al. (2015). 'Metallic ions in the upper atmosphere of Mars from the passage of comet C/2013 A1 (Siding Spring)'. *Geophys. Res. Lett.*, 42(12), pp. 4670–4675. doi:10.1002/2015GL064159.

Bertin, E. and Arnouts, S. (1996). 'SExtractor: Software for source extraction.' *A&AS*, 117, pp. 393–404. doi:10.1051/aas:1996164.

Bertini, I. et al. (2017). 'The scattering phase function of comet 67P/Churyumov–Gerasimenko coma as seen from the Rosetta/OSIRIS instrument'. *MNRAS*, 469(Suppl_2), pp. S404–S415. doi:10.1093/mnras/stx1850.

Bessell, M. S. (1979). 'UBVRI photometry II: The Cousins VRI system, its temperature and absolute flux calibration, and relevance for two-dimensional photometry.' *PASP*, 91(543), p. 589. doi:10.1086/130542.

Bessell, M. S. (1990). 'UBVRI passbands.' *PASP*, 102, pp. 1181–1199. doi:10.1086/132749.

Betzler, A. S. et al. (2020). 'BVR photometry of comets 63P/Wild 1 and C/2012 K1 (PANSTARRS)'. *Ap&SS*, 365(6), 102. doi:10.1007/s10509-020-03814-5.

Biele, J. et al. (2015). 'The landing(s) of Philae and inferences about comet surface mechanical properties'. *Science*, 349(6247), aaa9816. doi:10.1126/science.aaa9816.

Bieler, A. et al. (2015). 'Abundant molecular oxygen in the coma of comet 67P/Churyumov–Gerasimenko'. *Nature*, 526(7575), pp. 678–681. doi:10.1038/nature15707.

Biver, N. et al. (2014). 'Complex organic molecules in comets C/2012 F6 (Lemmon) and C/2013 R1 (Lovejoy): Detection of ethylene glycol and formamide'. *A&A*, 566, L5. doi:10.1051/0004-6361/201423890.

Biver, N. et al. (2022). 'Chemistry of comet atmospheres', in Meech, K. J. and Combi, M. R. (eds.) *Comets III* [Preprint], Tuscon: Univ. Arizona Press. doi:10.48550/arXiv.2207.04800.

Bockelée-Morvan, D. et al. (2010). 'A study of the distant activity of comet C/2006 W3 (Christensen) with Herschel and ground-based radio telescopes'. *A&A*, 518, L149. doi:10.1051/0004-6361/201014655.

Bockelée-Morvan, D. et al. (2015). 'First observations of H_2O and CO_2 vapor in comet 67P/Churyumov–Gerasimenko made by VIRTIS onboard Rosetta'. *A&A*, 583, A6.

Bodewits, D. et al. (2014). 'The evolving activity of the dynamically young comet C/2009 P1 (Garradd)'. *ApJ*, 786(1), 48. doi:10.1088/0004-637X/786/1/48.

Bodewits, D. et al. (2015). 'The pre-perihelion activity of dynamically new comet C/2013 A1 (Siding Spring) and its close encounter with Mars'. *ApJ*, 802(1), L6. doi:10.1088/2041-8205/802/1/L6.

Bodewits, D. et al. (2020). 'The carbon monoxide-rich interstellar comet 2I/-Borisov'. *Nat. Astron.*, 4, pp. 867–871. doi:10.1038/s41550-020-1095-2.

Boehnhardt, H. et al. (2016). 'Mt. Wendelstein imaging of the post-perihelion dust coma of 67P/Churyumov—Gerasimenko in 2015/2016'. *MNRAS*, 462(Suppl_1), pp. S376–S393. doi:10.1093/mnras/stw2859.

Boehnhardt, H. et al. (2017). 'The Philae lander mission and science overview'. *Phil. Trans. R. Soc. A.*, 375(2097), 20160248. doi:10.1098/rsta.2016.0248.

Bouziani, N. and Jewitt, D. (2022). 'Cometary activity beyond the planets'. *ApJ*, 924(1), p. 37. doi:10.3847/1538-4357/ac323b.

Brasser, R. and Morbidelli, A. (2013). 'Oort cloud and scattered disc formation during a late dynamical instability in the Solar System'. *Icarus*, 225(1), pp. 40–49. doi:10.1016/j.icarus.2013.03.012.

Britt, D. et al. (2004). 'The morphology and surface processes of comet 19P/Borrelly'. *Icarus*, 167(1), pp. 45 – 53. doi:10.1016/j.icarus.2003.09.004.

Brownlee, D. et al. (2006). 'Comet 81P/Wild 2 under a microscope'. *Science*, 314(5806), pp. 1711–1716. doi:10.1126/science.1135840.

Cochran, A., Barker, E. and Gray, C. (2012). 'Thirty years of cometary spectroscopy from McDonald Observatory'. *Icarus*, 218(1), pp. 144–168. doi:10.1016/j.icarus.2011.12.010.

Combi, M. R., Harris, W. M. and Smyth, W. H. (2004). 'Gas dynamics and kinetics in the cometary coma: Theory and observations', in Festou, M. C., Keller, H. U. and Weaver, H. A. (eds.) *Comets II*, Tuscon: Univ. Arizona Press, pp. 523–552.

Combi, M. R. et al. (2013). 'Water production rate of comet C/2009 P1 (Garradd) throughout the 2011–2012 apparition: Evidence for an icy grain halo'. *Icarus*, 225(1), pp. 740–748. doi:10.1016/j.icarus.2013.04.030.

Combi, M. R. et al. (2014). 'Water production in comets C/2011 L4 (PanSTARRS) and C/2012 F6 (Lemmon) from observations with SOHO/SWAN'. *AJ*, 147(6), p. 126. doi:10.1088/0004-6256/147/6/126.

Combi, M. R. et al. (2018). 'Water production activity of nine long-period comets from SOHO/SWAN observations of hydrogen Lyman-alpha: 2013–2016'. *Icarus*, 300, pp. 33–46. doi:10.1016/j.icarus.2017.08.035.

Combi, M. R. et al. (2020). 'Comet 41P/Tuttle–Giacobini–Kresak, 45P/Honda–Mrkos–Pajdusakova, and 46P/Wirtanen: Water production activity over 21 yr with SOHO/SWAN'. *Planet. Sci. J.*, 1(3), 72. doi:10.3847/PSJ/abb026.

Cordiner, M. A. et al. (2020). 'Unusually high CO abundance of the first active interstellar comet'. *Nat. Astron.*, 4, pp. 861–866. doi:10.1038/s41550-020-1087-2.

Crismani, M. M. J. et al. (2015). 'Ultraviolet observations of the hydrogen coma of comet C/2013 A1 (Siding Spring) by MAVEN/IUVS'. *Geophys. Res. Lett.*, 42(21), pp. 8803–8809. doi:10.1002/2015GL065290.

Crismani, M. M. J. et al. (2018). 'The impact of comet Siding Spring's meteors on the Martian atmosphere and ionosphere'. *J. Geophys. Res.: Planets*, 123(10), pp. 2613–2627. doi:10.1029/2018JE005750.

Davidsson, B. J. R. et al. (2016). 'The primordial nucleus of comet 67P/Churyumov–Gerasimenko'. *A&A*, 592, A63. doi:10.1051/0004-6361/201526968.

De Sanctis, M. C. et al. (2015). 'The diurnal cycle of water ice on comet 67P/Churyumov–Gerasimenko'. *Nature*, 525(7570), pp. 500–503. doi:10.1038/nature14869.

de Val-Borro, M. et al. (2017). 'Measuring molecular abundances in comet C/2014 Q2 (Lovejoy) using the APEX telescope'. *MNRAS*, 474(1), pp. 1099–1107. doi:10.1093/mnras/stx2802.

Dello Russo, N. et al. (2016). 'Emerging trends and a comet taxonomy based on the volatile chemistry measured in thirty comets with high-resolution infrared spectroscopy between 1997 and 2013'. *Icarus*, 278, pp. 301–332. doi:10.1016/j.icarus.2016.05.039.

Dones, L. et al. (2004). 'Oort cloud formation and dynamics', in Festou, M. C., Keller, H. U. and Weaver, H. A. (eds.) *Comets II*, Tuscon: Univ. Arizona Press, pp. 153–174.

Donn, B. (1989). 'The accumulation and structure of comets'. *IAU Colloq.*, 116(1), p. 335–359. doi:10.1017/S0252921100109753.

Donn, B., Daniels, P. A. and Hughes, D. W. (1985). 'On the structure of the cometary nucleus'. *BAAS*, 17, p. 520.

Edgeworth, K. E. (1943). 'The evolution of our planetary system'. *J. British Astron. Association*, 53, pp. 181–188.

Edgeworth, K. E. (1949). 'The origin and evolution of the Solar System'. *MNRAS*, 109, pp. 600–609. doi:10.1093/mnras/109.5.600.

El-Maarry, M. R. et al. (2019). 'Surface morphology of comets and associated evolutionary processes: A review of Rosetta's observations of 67P/Churyumov–Gerasimenko'. *Space Sci. Rev.*, 215(4), 36. doi:10.1007/s11214-019-0602-1.

Espley, J. R. et al. (2015). 'A comet engulfs Mars: MAVEN observations of comet Siding Spring's influence on the Martian magnetosphere'. *Geophys. Res. Lett.*, 42(21), pp. 8810–8818. doi:10.1002/2015GL066300.

Farnham, T. et al. (2017). 'The resolved nucleus of comet Siding Spring (C/2013 A1) in MRO HiRISE images', *49th Annual DPS Meeting*. Provo, Utah, 15-20 Ocotber.

Farnham, T. L., Kelley, M. S. P. and Bauer, J. M. (2021). 'Early activity in comet C/2014 UN271 Bernardinelli–Bernstein as observed by TESS'. *Planet. Sci. J.*, 2(6), p. 236. doi:10.3847/PSJ/ac323d.

Farnocchia, D. et al. (2014). 'Trajectory analysis for the nucleus and dust of comet C/2013 A1 (Siding Spring)'. *ApJ*, 790(2), 114. doi:10.1088/0004-637X/790/2/114.

Feaga, L. M. et al. (2011). 'Heterogeneity of comet 103P/Hartley 2's gaseous coma', *42nd Lunar and Planetary Science Conference*. The Woodlands, Texas, 7-11 March.

Feaga, L. M. et al. (2013). 'Uncorrelated volatile behavior during the 2011 apparition of comet C/2009 P1 Garradd'. *AJ*, 147(1), p. 24. doi:10.1088/0004-6256/147/1/24.

Ferrín, I. (2010). 'Atlas of secular light curves of comets'. *Planet. Space Sci.*, 58(3), pp. 365–391. doi:10.1016/j.pss.2009.09.026.

Ferrín, I. (2014). 'The location of Oort cloud comets C/2011 L4 Panstarrs and C/2012 S1 ISON on a comet evolutionary diagram'. *MNRAS*, 442(2), pp. 1731–1754. doi:10.1093/mnras/stu820.

Festou, M. C. (1981). 'The density distribution of neutral compounds in cometary atmospheres. I - Models and equations'. *A&A*, 95(1), pp. 69–79.

Festou, M. C., Keller, H. U. and Weaver, H. A. (2004). 'A brief conceptual history of cometary science', in Festou, M. C., Keller, H. U. and Weaver, H. A. (eds.) *Comets II*, Tuscon: Univ. Arizona Press, pp. 3–16.

Fink, U. (2009). 'A taxonomic survey of comet composition 1985–2004 using CCD spectroscopy'. *Icarus*, 201(1), pp. 311–334. doi:10.1016/j.icarus.2008.12.044.

Fink, U. and Rubin, M. (2012). 'The calculation of Afρ and mass loss rate for comets'. *Icarus*, 221(2), pp. 721–734. doi:10.1016/j.icarus.2012.09.001.

Fink, U. et al. (2016). 'Investigation into the disparate origin of CO_2 and H_2O outgassing for comet 67/P'. *Icarus*, 277, pp. 78–97. doi:https://doi.org/10.1016/j.icarus.2016.04.040.

Fornasier, S. et al. (2016). 'Rosetta's comet 67P/Churyumov–Gerasimenko sheds its dusty mantle to reveal its icy nature'. *Science*, 354(6319), pp. 1566–1570. doi:10.1126/science.aag2671.

Fougere, N. et al. (2016). 'Three-dimensional direct simulation Monte-Carlo modeling of the coma of comet 67P/Churyumov–Gerasimenko observed by the VIRTIS and ROSINA instruments on board Rosetta'. *A&A*, 588, A134. doi:10.1051/0004-6361/201527889.

Fraser, W. C. et al. (2022). 'The transition from the Kuiper Belt to the Jupiter-family (comets)', in Meech, K. J. and Combi, M. R. (eds.) *Comets III* [Preprint], Tuscon: Univ. Arizona Press. doi:10.48550/arXiv.2210.16354.

Fulle, M. (2004). 'Motion of cometary dust', in Festou, M. C., Keller, H. U. and Weaver, H. A. (eds.) *Comets II*, Tuscon: Univ. Arizona Press, pp. 565–575.

Garcia, R. and Gil-Hutton, R. (2021). 'Photometry of four long-period comets'. *Planet. Space Sci.*, 206, 105308. doi:10.1016/j.pss.2021.105308.

Garcia, R. S., Gil-Hutton, R. and García-Migani, E. (2020). 'Observational results for five short-period and five long-period comets'. *Planet. Space. Sci.*, 180, 104779. doi:10.1016/j.pss.2019.104779.

Gardener, D., Snodgrass, C. and Ligier, N. (2022). 'Searching for outbursts in the ground-based photometry of 67P/Churyumov–Gerasimenko'. *MNRAS*, 517(3), pp. 4305–4316. doi:10.1093/mnras/stac2995.

Gicquel, A. et al. (2015). 'The evolution of volatile production in comet C/2009 P1 (Garradd) during its 2011–2012 apparition'. *ApJ*, 807(1), 19. doi:10.1088/0004-637X/807/1/19.

Gillan, A. F. et al. (2024). 'Dust production rates in Jupiter-family comets: A two year study with ATLAS photometry'. *Planet. Sci. J.*, 5(1), 25. doi:10.3847/PSJ/ad1394.

Giorgini, J. D. et al. (1996). 'JPL's on-line Solar System data service'. *BAAS*, 28(3), 25.04.

Gombosi, T. I. and Houpis, H. L. F. (1986). 'An icy-glue model of cometary nuclei'. *Nature*, 324(6092), pp. 43–44. doi:10.1038/324043a0.

Grewing, M., Praderie, F. and Reinhard, R. (eds.) (1988). *Exploration of Halley's Comet*. Heidelberg: Springer Berlin.

Groussin, O. et al. (2015). 'Temporal morphological changes in the Imhotep region of comet 67P/Churyumov–Gerasimenko'. *A&A*, 583, A36. doi:10.1051/0004-6361/201527020.

Grün, E. et al. (2016). 'The 2016 Feb 19 outburst of comet 67P/CG: An ESA Rosetta multi-instrument study'. *MNRAS*, 462(Suppl_1), pp. S220–S234. doi:10.1093/mnras/stw2088.

Guido, E. et al. (2013). 'Comet C/2013 R1 (Lovejoy)'. *Cent. Bureau Electron. Telegrams*, 3649(1).

Gunn, J. E. et al. (1998). 'The Sloan Digital Sky Survey photometric camera'. *AJ*, 116(6), p. 3040. doi:10.1086/300645.

Gurnett, D. A. et al. (2015). 'An ionized layer in the upper atmosphere of Mars caused by dust impacts from comet Siding Spring'. *Geophys. Res. Lett.*, 42(12), pp. 4745–4751. doi:10.1002/2015GL063726.

Guzik, P. et al. (2019). 'Initial characterization of interstellar comet 2I/Borisov'. *Nat. Astron.*, 4(1), p. 53–57. doi:10.1038/s41550-019-0931-8.

Halley, E. (1705). *Astronomiae Cometicae Synopsis*. Oxford.

Hanner, M. S. (1996). 'Composition and optical properties of cometary dust'. *IAU Colloq.*, 150, p. 367–376. doi:10.1017/S0252921100501870.

Hanner, M. S. et al. (1981). 'On the definition of albedo and application to irregular particles'. *A&A*, 104(1), pp. 42–46.

Hansen, K. C. et al. (2016). 'Evolution of water production of 67P/Churyumov–Gerasimenko: An empirical model and a multi-instrument study'. *MNRAS*, 462(Suppl_1), pp. S491–S506. doi:10.1093/mnras/stw2413.

Harker, D. E. et al. (2011). 'Mid-infrared spectrophotometric observations of fragments B and C of comet 73P/Schwassmann–Wachmann 3'. *AJ*, 141(1), 26. doi:10.1088/0004-6256/141/1/26.

Hartley, M. (1986). 'Comet Hartley (1986c)'. *IAU Circ.*, 4197(1).

Haser, L. (1957). 'Distribution d'intensité dans la tête d'une comète'. *Bull. Soc. R. Sci. Liege*, 43, pp. 740–750.

Hills, J. G. (1981). 'Comet showers and the steady-state infall of comets from the Oort cloud.' *AJ*, 86, pp. 1730–1740. doi:10.1086/113058.

Holmberg, J., Flynn, C. and Portinari, L. (2006). 'The colours of the Sun'. *MNRAS*, 367(2), pp. 449–453. doi:10.1111/j.1365-2966.2005.09832.x.

Honkova, M. et al. (2013). '2013 US10'. *MPEC*, 2013-V05.

Hormuth, F. et al. (2004). 'Comet P/2004 F3 (NEAT)'. *IAU Circ.*, 8313(2).

Howell, E. and Kowal, C. (1981). 'Comet Howell (1981k)'. *IAU Circ.*, 3631(1).

Hsieh, H. H. (2017). 'Asteroid-comet continuum objects in the solar system'. *Phil. Trans. R. Soc. A*, 375(2097), 20160259. doi:10.1098/rsta.2016.0259.

Hässig, M. et al. (2015). 'Time variability and heterogeneity in the coma of 67P/Churyumov–Gerasimenko'. *Science*, 347(6220), aaa0276. doi:10.1126/science.aaa0276.

Ivanova, A. V., Borisenko, S. A. and Andreev, M. V. (2014). 'Photometric studies of comet C/2009 P1 (Garradd) before the perihelion'. *Sol. Syst. Res.*, 48(5), pp. 375–381. doi:10.1134/S0038094614050025.

Ivanova, O., Borysenko, S. and Golovin, A. (2014). 'Photometry of comet C/2011 L4 (PANSTARRS) at 4.4–4.2au heliocentric distances'. *Icarus*, 227, pp. 202–205. doi:10.1016/j.icarus.2013.08.026.

Ivanova, O. et al. (2017). 'Polarimetry, photometry, and spectroscopy of comet C/2009 P1 (Garradd)'. *Icarus*, 284, pp. 167–182. doi:10.1016/j.icarus.2016.11.014.

Jehin, E. et al. (2011). 'TRAPPIST: TRAnsiting Planets and PlanetesImals Small Telescope'. *The Messenger*, 145, pp. 2–6.

Jester, S. et al. (2005). 'The Sloan Digital Sky Survey view of the Palomar-Green bright quasar survey'. *AJ*, 130(3), pp. 873–895. doi:10.1086/432466.

Jewitt, D. (2004). 'From cradle to grave: The rise and demise of the comets', in Festou, M. C., Keller, H. U. and Weaver, H. A. (eds.) *Comets II*, Tuscon: Univ. Arizona Press, pp. 659–676.

Jewitt, D. (2015). 'Color systematics of comets and related bodies*'. *AJ*, 150(6), 201. doi:10.1088/0004-6256/150/6/201.

Jewitt, D. and Hsieh, H. H. (2022). 'The asteroid-comet continuum', in Meech, K. J. and Combi, M. R. (eds.) *Comets III* [Preprint], Tuscon: Univ. Arizona Press. doi:10.48550/arXiv.2203.01397.

Jewitt, D. and Luu, J. (1993). 'Discovery of the candidate Kuiper belt object 1992 QB_1'. *Nature*, 362(6422), pp. 730–732. doi:10.1038/362730a0.

Jewitt, D. and Meech, K. J. (1986). 'Cometary grain scattering versus wavelength, or, "What color is comet dust?"'. *ApJ*, 310, p. 937. doi:10.1086/164745.

Jewitt, D. et al. (2017). 'A comet active beyond the crystallization zone'. *ApJ*, 847(2), p. L19. doi:10.3847/2041-8213/aa88b4.

Jewitt, D. et al. (2021). 'Cometary activity begins at Kuiper belt distances: Evidence from C/2017 K2'. *AJ*, 161(4), p. 188. doi:10.3847/1538-3881/abe4cf.

Johnson, H. L. and Morgan, W. W. (1953). 'Fundamental stellar photometry for standards of spectral type on the revised system of the Yerkes spectral atlas.' *ApJ*, 117, p. 313. doi:10.1086/145697.

Jones, G. H. et al. (2017). 'Cometary science after Rosetta'. *Phil. Trans. R. Soc. A*, 375(2097), 20170001. doi:10.1098/rsta.2017.0001.

Jones, R. L. et al. (2009). 'Solar System science with LSST'. *Earth Moon Planets*, 105, pp. 101–105. doi:10.1007/s11038-009-9305-z.

Jorda, L., Crovisier, J. and Green, D. W. E. (1991). 'The correlation between water production rates and visual magnitudes in comets', *Asteroids, Comets, Meteors 1991*. Flagstaff, Arizona, 24-28 June.

Jorda, L. et al. (2016). 'The global shape, density and rotation of comet 67P/Churyumov–Gerasimenko from preperihelion Rosetta/OSIRIS observations'. *Icarus*, 277, pp. 257–278. doi:10.1016/j.icarus.2016.05.002.

Kaib, N. A. and Volk, K. (2022). 'Dynamical population of comet reservoirs', in Meech, K. J. and Combi, M. R. (eds.) *Comets III* [Preprint], Tuscon: Univ. Arizona Press. doi:10.48550/arXiv.2206.00010.

Kamel, L. (1992). 'The comet light curve atlas. The comet light curve catalogue/atlas. III - The atlas'. *A&AS*, 92(1), pp. 85–149.

Kareta, T. et al. (2023). 'Ice, ice, maybe? Investigating 46P/Wirtanen's inner coma for icy grains'. *Planet. Sci. J.*, 4(5), 85. doi:10.3847/PSJ/accc28.

Keller, H. U. (1989). 'Comets - Dirty snowballs or icy dirtballs?', in Hunt, J. J. and Guyenne, T. D. (eds.) *Physics and Mechanics of Cometary Materials*, pp. 39–45.

Keller, H. U. et al. (1986). 'First Halley Multicolour Camera imaging results from Giotto'. *Nature*, 321, pp. 320–326. doi:10.1038/321320a0.

Kelley, M. S. P. and Lister, T. (2019). 'mkelley/calviacat'. doi:10.5281/zenodo.2635840.

Kelley, M. S. P. et al. (2014). 'A study of dust and gas at Mars from comet C/2013 A1 (Siding Spring)'. *ApJ*, 792(1), L16. doi:10.1088/2041-8205/792/1/L16.

Kelley, M. S. P. et al. (2021a). 'Apparent outburst of comet 67P/Churyumov–Gerasimenko'. *The Astronomer's Telegram*, 15053, p. 1.

Kelley, M. S. P. et al. (2021b). 'Six outbursts of comet 46P/Wirtanen'. *Planet. Sci. J.*, 2(4), p. 131. doi:10.3847/psj/abfe11.

Kiss, C. et al. (2015). 'Comet C/2013(Siding Spring) as seen with the Herschel Space Observatory'. *A&A*, 574, L3. doi:10.1051/0004-6361/201425127.

Knight, M. M. and Schleicher, D. G. (2013). 'The highly unusual outgassing of comet 103P/Hartley 2 from narrowband photometry and imaging of the coma'. *Icarus*, 222(2), pp. 691–706. doi:10.1016/j.icarus.2012.06.004.

Knight, M. M., Schleicher, D. G. and Farnham, T. L. (2021). 'Narrowband observations of comet 46P/Wirtanen during its exceptional apparition of 2018/19. II. Photometry, jet morphology, and modeling results'. *Planet. Sci. J.*, 2(3), 104. doi:10.3847/PSJ/abef6c.

Knight, M. M. et al. (2017). 'Gemini and Lowell observations of 67P/Churyumov-Gerasimenko during the Rosetta mission'. *MNRAS*, 469(Suppl_2), pp. S661–S674. doi:10.1093/mnras/stx2472.

Knollenberg, J. et al. (2016). 'A mini outburst from the nightside of comet 67P/Churyumov–Gerasimenko observed by the OSIRIS camera on Rosetta'. *A&A*, 596, A89. doi:10.1051/0004-6361/201527744.

Kresák, L. (1985). 'Aging of comets and their evolution into asteroids', *The Evolution of the Small Bodies of the Solar System*. Lake Como, Italy, 16-20 May.

Królikowska, M. and Dybczyński, P. A. (2020). 'The catalogue of cometary orbits and their dynamical evolution'. *A&A*, 640, A97. doi:10.1051/0004-6361/202038451.

Kron, R. G. (1980). 'Photometry of a complete sample of faint galaxies.' *ApJS*, 43, pp. 305–325. doi:10.1086/190669.

Kuiper, G. P. (1951). 'On the origin of the Solar System'. *Proc. Natl. Acad. Sci.*, 37(1), pp. 1–14. doi:10.1073/pnas.37.1.1.

Lamy, P. L. et al. (2004). 'The sizes, shapes, albedos, and colors of cometary nuclei', in Festou, M. C., Keller, H. U. and Weaver, H. A. (eds.) *Comets II*, Tuscon: Univ. Arizona Press, pp. 223–264.

Lang, D. et al. (2010). 'Astrometry.net: Blind astrometric calibration of arbitrary astronomical images'. *AJ*, 139(5), pp. 1782–1800. doi:10.1088/0004-6256/139/5/1782.

Langland-Shula, L. E. and Smith, G. H. (2011). 'Comet classification with new methods for gas and dust spectroscopy'. *Icarus*, 213(1), pp. 280–322. doi:10.1016/j.icarus.2011.02.007.

Laufer, D., Kochavi, E. and Bar-Nun, A. (1987). 'Structure and dynamics of amorphous water ice'. *Phys. Rev. B*, 36(17), pp. 9219–9227. doi:10.1103/physrevb.36.9219.

Levison, H. F. (1996). 'Comet taxonomy', in Rettig, T. and Hahn, J. M. (eds.) *Completing the Inventory of the Solar System*, vol. 107 of *Astronomical Society of the Pacific Conference Series*, pp. 173–191.

Levison, H. F. et al. (2010). 'Capture of the Sun's Oort cloud from stars in its birth cluster'. *Science*, 329(5988), pp. 187–190. doi:10.1126/science.1187535.

Li, J.-Y. et al. (2014). 'Constraining the dust coma properties of comet C/Siding Spring (2013 A1) at large heliocentric distances'. *ApJ*, 797(1), L8. doi:10.1088/2041-8205/797/1/L8.

Lister, T. et al. (2022). 'The LCO Outbursting Objects Key Project: Overview and year 1 status'. *Planet. Sci. J.*, 3(7), 173. doi:10.3847/PSJ/ac7a31.

Lyttleton, R. A. (1951). 'On the structure of comets and the formation of tails'. *MNRAS*, 111, p. 268. doi:10.1093/mnras/111.3.268.

Marcus, J. N. (2007). 'Forward-scattering enhancement of comet brightness. I. Background and model'. *Int. Comet Q.*, 29, pp. 39–66.

Massironi, M. et al. (2015). 'Two independent and primitive envelopes of the bilobate nucleus of comet 67P'. *Nature*, 526(7573), pp. 402–405. doi:10.1038/nature15511.

Mazzotta Epifani, E. et al. (2016). 'Photometry of the Oort cloud comet C/2009 P1 (Garradd): Pre-perihelion observations at 5.7 and 2.5au'. *Planet. Space Sci.*, 132, pp. 23–31. doi:10.1016/j.pss.2016.07.007.

McGlynn, T. A. and Chapman, R. D. (1989). 'On the nondetection of extrasolar comets'. *ApJ*, 346, L105. doi:10.1086/185590.

McKay, A. J. et al. (2015). 'Evolution of H_2O, CO, and CO_2 production in Comet C/2009 P1 Garradd during the 2011–2012 apparition'. *Icarus*, 250, pp. 504–515. doi:10.1016/j.icarus.2014.12.023.

McNaught, R. H. and Garradd, G. J. (2009). 'Comet C/2009 P1 (Garradd)'. *Cent. Bureau Electron. Telegrams*, 1908, p. 1.

McNaught, R. H., Sato, H. and Williams, G. V. (2013). 'Comet C/2013 A1 (Siding Spring)'. *Cent. Bureau Electron. Telegrams*, 3368, p. 1.

McNaught, R. H. et al. (2009). 'Comet C/2009 F4 (McNaught)'. *IAU Circ.*, 9032(1).

Meech, K. et al. (2009). 'Activity of comets at large heliocentric distances pre-perihelion'. *Icarus*, 201(2), pp. 719–739. doi:10.1016/j.icarus.2008.12.045.

Meech, K. J. (1999). 'Chemical and physical aging of comets', in Svoren, J., Pittich, E. M. and Rickman, H. (eds.) *IAU Colloq. 173: Evolution and Source Regions of Asteroids and Comets*, p. 195.

Meech, K. J. (2017). 'Setting the scene: What did we know before Rosetta?' *Phil. Trans. R. Soc. A*, 375(2097), 20160247. doi:10.1098/rsta.2016.0247.

Meech, K. J., Jewitt, D. and Ricker, G. R. (1986). 'Early photometry of comet P/Halley: Development of the coma'. *Icarus*, 66(3), pp. 561–574. doi:10.1016/0019-1035(86)90091-6.

Meech, K. J. and Svoreň, J. (2004). 'Using cometary activity to trace the physical and chemical evolution of cometary nuclei', in Festou, M. C., Keller, H. U. and Weaver, H. A. (eds.) *Comets II*, Tuscon: Univ. Arizona Press, pp. 317–335.

Meech, K. J. et al. (2011a). 'Deep Impact, Stardust-NExT and the behavior of Comet 9P/Tempel 1 from 1997 to 2010'. *Icarus*, 213(1), pp. 323–344. doi:10.1016/j.icarus.2011.02.016.

Meech, K. J. et al. (2011b). 'EPOXI: Comet 103P/Hartley 2 observations from a worldwide campaign'. *ApJ*, 734(1), L1. doi:10.1088/2041-8205/734/1/L1.

Meech, K. J. et al. (2017). 'Beginning of activity in long-period comet C/2015 ER61 (PANSTARRS)'. *AJ*, 153(5), p. 206. doi:10.3847/1538-3881/aa63f2.

Moulane, Y. et al. (2023). 'Activity and composition of the hyperactive comet 46P/Wirtanen during its close approach in 2018'. *A&A*, 670, A159. doi:10.1051/0004-6361/202244779.

Mumma, M. J. and Charnley, S. B. (2011). 'The chemical composition of comets—Emerging taxonomies and natal heritage'. *ARA&A*, 49(1), pp. 471–524. doi:10.1146/annurev-astro-081309-130811.

Mumma, M. J., Weissman, P. R. and Stern, S. A. (1993). 'Comets and the origin of the Solar System - Reading the Rosetta Stone', in Levy, E. H. and Lunine, J. I. (eds.) *Protostars and Planets III*, Tuscon: Univ. Arizona Press, pp. 1177–1252.

Nakano, S. (2017). *Nakano note 3379*. Available at: `https://www.oaa.gr.jp/~oaacs/nk/nk3379.htm` (Accessed: 26 May 2023).

Nesvorný, D. et al. (2017). 'Origin and evolution of short-period comets'. *ApJ*, 845(1), 27. doi:10.3847/1538-4357/aa7cf6.

Oort, J. H. (1950). 'The structure of the cloud of comets surrounding the Solar System and a hypothesis concerning its origin'. *Bull. Astron. Inst. Netherlands*, 11, pp. 91–110.

Opitom, C. et al. (2015a). 'TRAPPIST monitoring of comet C/2012 F6 (Lemmon)'. *A&A*, 574, A38. doi:10.1051/0004-6361/201424582.

Opitom, C. et al. (2015b). 'TRAPPIST photometry and imaging monitoring of comet C/2013 R1 (Lovejoy): Implications for the origin of daughter species '. *A&A*, 584, A121. doi:10.1051/0004-6361/201526427.

Opitom, C. et al. (2016). 'Long-term activity and outburst of comet C/2013 A1 (Siding Spring) from narrow-band photometry and long-slit spectroscopy'. *A&A*, 589, A8. doi:10.1051/0004-6361/201527628.

Opitom, C. et al. (2017). 'Ground-based monitoring of comet 67P/Churyumov–Gerasimenko gas activity throughout the Rosetta mission'. *MNRAS*, 469(Suppl_2), pp. S222–S229.

Opitom, C. et al. (2019). 'First observations of an outbursting comet with the MUSE integral-field spectrograph'. *A&A*, 628, A128. doi:10.1051/0004-6361/201833960.

'Oumuamua ISSI Team (2019). 'The natural history of 'Oumuamua'. *Nat. Astron.*, 3, pp. 594–602. doi:10.1038/s41550-019-0816-x.

Paganini, L. et al. (2012). 'The chemical composition of CO-rich comet C/2009 P1 (Garradd) at $R_{\rm h}$ = 2.4 and 2.0 au before perihelion*'. *ApJ*, 748(1), L13. doi:10.1088/2041-8205/748/1/L13.

Paganini, L. et al. (2014). 'C/2013 R1 (Lovejoy) at IR wavelengths and the variability of CO abundances among Oort cloud comets'. *ApJ*, 791(2), p. 122. doi:10.1088/0004-637X/791/2/122.

Pajola, M. et al. (2017). 'The pristine interior of comet 67P revealed by the combined Aswan outburst and cliff collapse'. *Nat. Astron.*, 1(5), p. 0092. doi: 10.1038/s41550-017-0092.

Pätzold, M. et al. (2016). 'A homogeneous nucleus for comet 67P/Churyumov–Gerasimenko from its gravity field'. *Nature*, 530(7588), pp. 63–65. doi:10.1038/nature16535.

Picazzio, E. et al. (2014). 'Spectroscopic study of comet 9P/Tempel 1 .' *Astron. Astrophys. Trans.*, 28(3), pp. 293–306.

Prialnik, D. and Bar-Nun, A. (1992). 'Crystallization of amorphous ice as the cause of Comet P/Halley's outburst at 14 au'. *A&A*, 258(2), pp. L9–L12.

Prialnik, D. and Jewitt, D. (2022). 'Amorphous ice in comets: Evidence and consequences', in Meech, K. J. and Combi, M. R. (eds.) *Comets III* [Preprint], Tuscon: Univ. Arizona Press. doi:10.48550/arXiv.2209.05907.

Protopapa, S. et al. (2018). 'Icy grains from the nucleus of comet C/2013 US_{10} (Catalina)'. *ApJ*, 862(2), L16. doi:10.3847/2041-8213/aad33b.

Protopapa, S. et al. (2021). 'Nondetection of water-ice grains in the coma of comet 46P/Wirtanen and implications for hyperactivity'. *Planet. Sci. J.*, 2(5), 176. doi:10.3847/PSJ/ac135a.

Reach, W. T., Kelley, M. S. and Vaubaillon, J. (2013). 'Survey of cometary CO_2, CO, and particulate emissions using the Spitzer Space Telescope'. *Icarus*, 226(1), pp. 777–797. doi:10.1016/j.icarus.2013.06.011.

Reinhard, R. (1986). 'The Giotto encounter with comet Halley'. *Nature*, 321, pp. 313–318. doi:10.1126/science.232.4748.353.

Restano, M. et al. (2015). 'Effects of the passage of Comet C/2013 A1 (Siding Spring) observed by the Shallow Radar (SHARAD) on Mars Reconnaissance Orbiter'. *Geophys. Res. Lett.*, 42(12), pp. 4663–4669. doi: 10.1002/2015GL064150.

Roll, R. and Witte, L. (2016). 'Rosetta lander Philae: Touch-down reconstruction'. *Planet. Space Sci.*, 125, pp. 12 – 19. doi:10.1016/j.pss.2016.02.005.

Rosenbush, V. et al. (2021). 'Photometry and polarimetry of comet 46P/Wirtanen in the 2018 apparition'. *MNRAS*, 503(3), pp. 4297–4308. doi:10.1093/mnras/stab585.

Roth, N. X. et al. (2021). 'Leveraging the ALMA Atacama Compact Array for cometary science: An interferometric survey of comet C/2015 ER61 (PanSTARRS) and evidence for a distributed source of carbon monosulfide'. *ApJ*, 921(1), 14. doi:10.3847/1538-4357/ac0441.

Saki, M. et al. (2021). 'Chemical composition of outbursting comet C/2015 ER61 (PanSTARRS)'. *AJ*, 162(4), 145. doi:10.3847/1538-3881/abfcbd.

Sato, H. et al. (2012). 'Comet C/2012 K1 (Panstarrs)'. *Cent. Bureau Electron. Telegrams*, 3112, p. 1.

Schleicher, D. G. (2007). 'Deep Impact's target Comet 9P/Tempel 1 at multiple apparitions: Seasonal and secular variations in gas and dust production'. *Icarus*, 190(2), pp. 406–422. doi:10.1016/j.icarus.2007.04.013.

Schleicher, D. G. (2010). *Composite Dust Phase Function for Comets*. Available at: `https://asteroid.lowell.edu/comet/dustphase.html` (Accessed: 28 June 2022).

Schleicher, D. G. and Bair, A. N. (2011). 'The composition of the interior of comet 73P/Schwassmann-Wachmann 3: Results from narrowband photometry of multiple components'. *AJ*, 141(6), 177. doi:10.1088/0004-6256/141/6/177.

Schleicher, D. G. and Farnham, T. L. (2004). 'Photometry and imaging of the coma with narrowband filters', in Festou, M. C., Keller, H. U. and Weaver, H. A. (eds.) *Comets II*, Tuscon: Univ. Arizona Press, pp. 449–469.

Schleicher, D. G., Millis, R. L. and Birch, P. V. (1998). 'Narrowband photometry of comet P/Halley: Variation with heliocentric distance, season, and solar phase angle'. *Icarus*, 132(2), pp. 397–417. doi:10.1006/icar.1997.5902.

Schneider, N. M. et al. (2015). 'MAVEN IUVS observations of the aftermath of the comet Siding Spring meteor shower on Mars'. *Geophys. Res. Lett.*, 42(12), pp. 4755–4761. doi:10.1002/2015GL063863.

Schwamb, M. E. et al. (2023). 'Tuning the Legacy Survey of Space and Time (LSST) observing strategy for solar system science'. *ApJS*, 266(2), p. 22. doi:10.3847/1538-4365/acc173.

Seligman, D. Z. et al. (2023). 'Dark comets? Unexpectedly large nongravitational accelerations on a sample of small asteroids'. *Planet. Sci. J.*, 4(2), p. 35. doi:10.3847/PSJ/acb697.

Sharma, K. et al. (2021). 'Outbursts of comet 67P/Churyumov–Gerasimenko'. *Res. Notes of the AAS*, 5(12), 277. doi:10.3847/2515-5172/ac3ee4.

Shepard, M. K. (2017). *Introduction to Planetary Photometry*. Cambridge: Cambridge University Press. doi:10.1017/9781316443545.

Snodgrass, C. and Jones, G. H. (2019). 'The European Space Agency's Comet Interceptor lies in wait'. *Nat. Commun.*, 10, 5418. doi:10.1038/s41467-019-13470-1.

Snodgrass, C. et al. (2011). 'The size distribution of Jupiter family comet nuclei'. *MNRAS*, 414(1), pp. 458–469. doi:10.1111/j.1365-2966.2011.18406.x.

Snodgrass, C. et al. (2013). 'Beginning of activity in 67P/Churyumov–Gerasimenko and predictions for 2014-2015'. *A&A*, 557, A33. doi:10.1051/0004-6361/201322020.

Snodgrass, C. et al. (2016a). 'Distant activity of 67P/Churyumov–Gerasimenko in 2014: Ground-based results during the Rosetta pre-landing phase'. *A&A*, 588, A80. doi:10.1051/0004-6361/201527834.

Snodgrass, C. et al. (2016b). 'The perihelion activity of comet 67P/Churyumov–Gerasimenko as seen by robotic telescopes'. *MNRAS*, 462(Suppl_1), pp. S138–S145. doi:10.1093/mnras/stw2300.

Snodgrass, C. et al. (2017). 'The 67P/Churyumov–Gerasimenko observation campaign in support of the Rosetta mission'. *Phil. Trans. R. Soc. A*, 375(2097), 20160249. doi:10.1098/rsta.2016.0249.

Soderblom, L. A. et al. (2002). 'Observations of comet 19P/Borrelly by the Miniature Integrated Camera and Spectrometer aboard Deep Space 1'. *Science*, 296(5570), pp. 1087–1091. doi:10.1126/science.1069527.

Solontoi, M. et al. (2012). 'Ensemble properties of comets in the Sloan Digital Sky Survey'. *Icarus*, 218(1), pp. 571–584. doi:10.1016/j.icarus.2011.10.008.

Stevenson, R. et al. (2014). 'NEOWISE observations of comet C/2013 A1 (Siding Spring) as it approaches Mars'. *ApJ*, 798(2), L31. doi:10.1088/2041-8205/798/2/L31.

Sunshine, J. M. et al. (2012). 'The distribution of water ice on comet 103P/Hartley 2', *Asteroids, Comets, Meteors 2012*. Niigata, Japan, 16-20 May.

Sánchez–Cano, B. et al. (2020). 'Mars' ionospheric interaction with comet C/2013 A1 Siding Spring's coma at their closest approach as seen by Mars Express'. *J. Geophys. Res.: Space Phys.*, 125(1), e2019JA027344. doi:10.1029/2019JA027344.

Sárneczky, K. et al. (2016). 'Activity of 50 long-period comets beyond 5.2 au'. *AJ*, 152(6), p. 220. doi:10.3847/0004-6256/152/6/220.

Thomas, N. (2020). *An Introduction to Comets: Post-Rosetta Perspectives*. Cham: Springer. doi:10.1007/978-3-030-50574-5.

Tisserand, F.-F. (1896). *Traité de Mécanique Céleste IV*. Paris: Gauthier-Villars.

Tonry, J. L. et al. (2012). 'The Pan-STARRS1 photometric system'. *ApJ*, 750(2), p. 99. doi:10.1088/0004-637x/750/2/99.

Tonry, J. L. et al. (2018). 'The ATLAS all-sky stellar reference catalog'. *ApJ*, 867(2), 105. doi:10.3847/1538-4357/aae386.

Tricarico, P. et al. (2014). 'Delivery of dust grains from comet C/2013 A1 (Siding Spring) to Mars'. *ApJ*, 787(2), L35. doi:10.1088/2041-8205/787/2/L35.

Tubiana, C. et al. (2015). '67P/Churyumov–Gerasimenko: Activity between March and June 2014 as observed from Rosetta/OSIRIS'. *A&A*, 573, A62. doi:10.1051/0004-6361/201424735.

van Biesbroeck, G. (1948). 'Comet notes: Comet 1948 b (Wirtanen); Comet 1947 n'. *Popular Astron.*, 56, p. 164.

Velichko, S. F. and Andreev, M. V. (2018). 'Photometry of comet C/2009 P1 (Garradd) before and after perihelion'. *Odessa Astron. Publ.*, 30, p. 196. doi: 10.18524/1810-4215.2018.31.144748.

Veverka, J. et al. (2013). 'Return to comet Tempel 1: Overview of Stardust-NExT results'. *Icarus*, 222(2), pp. 424 – 435. doi:10.1016/j.icarus.2012.03.034.

Villanueva, G. et al. (2012). 'A multi-instrument study of comet C/2009 P1 (Garradd) at 2.1au (pre-perihelion) from the Sun'. *Icarus*, 220(1), pp. 291–295. doi:10.1016/j.icarus.2012.03.027.

Vincent, J.-B. et al. (2016). 'Summer fireworks on comet 67P'. *MNRAS*, 462(Suppl_1), pp. S184–S194. doi:10.1093/mnras/stw2409.

Von Rosenvinge, T. T., Brandt, J. C. and Farquhar, R. W. (1986). 'The International Cometary Explorer mission to comet Giacobini-Zinner'. *Science*, 232(4748), pp. 353–356. doi:10.1126/science.232.4748.353.

Wainscoat, R. et al. (2011). 'Comet C/2011 L4 (Panstarrs)'. *IAU Circ.*, 9215(1).

Weaver, H. A. et al. (1999). 'Post-perihelion HST observations of comet Hale-Bopp (C/1995 O1)'. *Icarus*, 141(1), pp. 1–12. doi:10.1006/icar.1999.6159.

Weissman, P. R. (1986). 'Are cometary nuclei primordial rubble piles?' *Nature*, 320(6059), pp. 242–244. doi:10.1038/320242a0.

Whipple, F. L. (1950). 'A comet model. I. The acceleration of Comet Encke'. *ApJ*, 111, pp. 375–394. doi:10.1086/145272.

Whipple, F. L. (1978). 'Cometary brightness variation and nucleus structure'. *Moon Planets*, 18(3), pp. 343–359. doi:10.1007/BF00896489.

Williams, G. V. (2011a). 'Comet C/2011 L4 (PANSTARRS)'. *MPEC*, 2011-L33.

Williams, G. V. (2011b). 'Comet C/2012 F6 (Lemmon)'. *MPEC*, 2012-F88.

Williams, G. V. (2013). 'Observations and orbits of comets'. *MPEC*, 2013-V48.

Womack, M. et al. (2021). 'The visual lightcurve of comet c/1995 O1 (Hale–Bopp) from 1995 to 1999'. *Planet. Sci. J.*, 2(1), p. 17. doi:10.3847/PSJ/abd32c.

Wooden, D. H., Ishii, H. A. and Zolensky, M. E. (2017). 'Cometary dust: The diversity of primitive refractory grains'. *Phil. Trans. R. Soc. A*, 375, 20160260. doi:10.1098/rsta.2016.0260.

Woodward, C. E. et al. (2015). 'SOFIA infrared spectrophotometry of comet C/2012 K1 (Pan-STARRS)'. *ApJ*, 809(2), 181. doi:10.1088/0004-637X/809/2/181.

Woodward, C. E. et al. (2021). 'The coma dust of comet C/2013 US_{10} (Catalina): A window into carbon in the solar system'. *Planet. Sci. J.*, 2(1), 25. doi: 10.3847/PSJ/abca3e.

Yang, B. et al. (2014). 'Multi-wavelength observations of comet C/2011 L4 (Pan-STARRS)'. *ApJ*, 784(2), L23. doi:10.1088/2041-8205/784/2/L23.

Yang, B. et al. (2018). 'Isotopic ratios in outbursting comet C/2015 ER61'. *A&A*, 609, L4. doi:10.1051/0004-6361/201732100.

Ye, Q.-Z. and Hui, M.-T. (2014). 'An early look of comet C/2013 A1 (Siding Spring): Breathtaker or nightmare?' *ApJ*, 787(2), 115. doi:10.1088/0004-637X/787/2/115.

Yeomans, D., Giorgini, J. and Chesley, S. (2005). 'The history and dynamics of comet 9P/Tempel 1'. *Space Sci. Rev.*, 117, pp. 123–135. doi: 10.1007/s11214-005-3392-6.

Zaprudin, B. et al. (2015). 'Optical observations of comet 67P/Churyumov–Gerasimenko with the Nordic Optical Telescope. Comet activity before the solar conjunction'. *A&A*, 583, A10. doi:10.1051/0004-6361/201525703.

Zaprudin, B. et al. (2017). 'Solar-insolation-induced changes in the coma morphology of comet 67P/Churyumov–Gerasimenko. Optical monitoring with the Nordic Optical Telescope'. *A&A*, 604, A3. doi:10.1051/0004-6361/201730475.

Zheltobryukhov, M. et al. (2020). 'Monitoring polarization in comet 46P/Wirtanen'. *MNRAS*, 498(2), pp. 1814–1825. doi:10.1093/mnras/staa2469.

Zhen-Tao, X., Stephenson, F. R. and Yao-Tiao, J. (1995). 'Astronomy on oracle bone inscriptions'. *QJRAS*, 36, p. 397.